UNIVERSITY OF CALIFORNIA
RIVERSIDE

Search for Charged B Meson Decays to a Charged Kaon or Pion, a Tau, and an Electron or Muon Using the *BABAR* Detector

A Dissertation submitted in partial satisfaction
of the requirements for the degree of

Doctor of Philosophy

in

Physics

by

Gil Matias Vitug

August 2011

Dissertation Committee:

Professor Owen R. Long, Chairperson
Professor J. William Gary
Professor John Ellison

The Dissertation of Gil Matias Vitug is approved:

Committee Chairperson

University of California, Riverside

Acknowledgments

Thank you to my wife, Pattaraporn Vitug, for her patience, devotion, and inspiration. Thank you mom, for believing in me and, to my father, for giving me the strength and will to endure. Thanks to the Sithalaphurk family for their faith and support, and allowing me the responsibility of keeping their beloved daughter happy. Thanks to Glenn, Noriel, John, May, and their families, I hope you forgive me for being distant for so many years, the loss of your love and support would make anything I do not worth it. To my mentor and advisor, Owen Long, you have shared with me so much knowledge, I hope one day I may be able to truly thank you.

To SLAC and the *BABAR* collaboration for allowing me to fulfill this dream. Especially to John William (Bill) Gary, Feng Liu, Lei Zhang, Stephen Foulkes, Bob Messner*, Henry Band, Mark Convery, Philippe Grenier, and Benjamin Shen*. Thank you for sharing your guidance, knowledge, help, and support. To my review committee members: Tim Gershon, Dana Lindemann, and David Lopes Pegna. Thanks for your sincere effort in trying to make sense of my analysis document. To the leptonic b & c decay analysis working group members: Silke Nelson, Guglielmo De Nardo, Matt Bellis, and Stephen Sekula. Thank you for great feedback, in the face of my pedantic presentations. To *BABAR* friends and colleagues: Hulya Atmacan, Elizabeth Mullin, Tae-Min Hong, Ryan White, Kyle Knoepfel, Elisabetta Baracchini, Valentina Santoro, Gigi Cibinetto, Antonio Petrella, Viola Sordini, Nichola Arnaud, and Alessandro Gaz. A global collaboration can be intimidating, thanks for making it more friendly. To Donna Hernandez, Raymond Lo, Kathryn Webb, and Toni Campos, thanks for your concern and help related to SLAC and *BABAR* issues.

To the UCR community, especially to the physics faculty: John Baez, Robert Clare, Bipin Desai, John Ellison, Gail Hanson, Ernest Ma, Umar Mohideen, Stephen Wimpenny, and Jose Wudka. Our world is so much more an interesting place, thank you for the enlightenment. To the UCR staff: Derek Beving, Herb Kuehne, Luci Pacocha, Jack Reid, and Will Sundquist. Thanks for being helpful with needs related to UCR. To my friends and colleagues at UCR, especially: Vincent Ugarte, Kaoru Kamiya, Mark Padilla, Shih-Chuan Kao, Arun Luthra, and Ferdinando Giordano. Thanks for all the great conversations, experiences, and lending an ear in times of struggle.

To Joe MacDonald, William Suarez, and Mike Kaiser, you will always be my best friends. I hope you forgive me for taking you for granted. I would also like to thank the wonderful people I had the good fortunate of meeting on this journey. To Roberta Bernett, Jody and Roger Lawler, Mark and Seth Farrell, and Roxanne Nilan. Thank you for sharing your home with me, I wish you the best in life.

To my family and friends...

ABSTRACT OF THE DISSERTATION

Search for Charged B Meson Decays to a Charged Kaon or Pion, a Tau, and an Electron or Muon Using the *BABAR* Detector

by

Gil Matias Vitug

Doctor of Philosophy, Graduate Program in Physics
University of California, Riverside, August 2011
Professor Owen R. Long, Chairperson

We present a search for the lepton-flavor-violating decays $B^{\pm} \to h^{\pm}\tau\ell$ ($h = K, \pi$; $\ell = e, \mu$) using the full *BABAR* dataset, which corresponds to 471.9 million $B\bar{B}$ pairs. The search uses a sample of events where one B meson (the "tag" B) is fully reconstructed in one of several hadronic final states. Using the tag-B momentum and the reconstructed h and ℓ, we are able to fully reconstruct the τ 4-momentum. The reconstructed τ mass is our main discriminant against combinatoric background. The measured upper limits on the branching fractions at the 90% confidence level are on the order of 10^{-5}.

Contents

List of Figures

List of Tables

Chapter 1

Introduction

1.1 Physics Motivation/Theory

There are indications that the standard model (SM) of electroweak interactions is incomplete. Observations of neutrino oscillations in atmospheric [1], solar [2], reactor [3] and accelerator [4, 5] neutrino experiments suggest the occurrence of lepton flavor violation in the neutral sector. Experiments involving neutrinoless double-beta decay may provide the best sensitivity for direct observation of lepton flavor violation in the neutral lepton sector [6]. From the *BABAR* experiment, evidence of $D^0 - \bar{D}^0$ mixing has been presented, which may be larger than the expected SM predictions [7]. Glashow-Iliopoulos-Maiani (GIM) suppressed box diagrams for $\Delta C = 2$ interactions involve quark masses and explain why Δm_D is much smaller than Δm_K [8]. Flavor non-conserving models with multiple Higgs doublets have potential to account for larger $D^0 - \bar{D}^0$ mixing [9]. These results seem to suggest that observation of lepton flavor violation in the charged sector may be just on the horizon.

Tree-level flavor changing neutral currents (FCNC) in the quark sector are forbidden in the SM [10]. However, higher order processes are allowed in *down*-type FCNCs, which is observed in some measured decays rates ($\Delta S = 1$ & $\Delta B = 1$); $\mathcal{B}F(K_L^0 \to \mu^+\mu^-) = (6.87 \pm 0.11) \times 10^{-9}$), $\mathcal{B}F(K^+ \to \pi^+\nu\bar{\nu}) = (1.5^{+1.3}_{-0.9}) \times 10^{-10}$), and $\mathcal{B}F(B^+ \to K^+\ell^+\ell^-) = (5.3 \pm 1.1) \times 10^{-7}$ and mass splittings ($\Delta S = 2$ & $\Delta B = 2$); $\Delta m_{K^0} = m_{K_L^0} - m_{K_S^0} = (3.483 \pm 0.006) \times 10^{-12}\ MeV/c^2$ and $\Delta m_{B^0} = m_{B_H^0} - m_{B_L^0} = (3.337 \pm 0.033) \times 10^{-10}\ MeV/c^2$ [11]. At the *BABAR* experiment, searches for lepton flavor violation in the charged leptonic sector have yielded upper limits on branching fractions for $\tau^- \to \ell^- K_S^0$ and $\tau^- \to \ell^-(\rho^0, K^{*0}, \bar{K}^{*0}, \phi)$ between $(0.8 - 18.2) \times 10^{-8}$ [12] and $\tau^- \to \ell^-\ell^+\ell^-$ between $(1.8 - 3.3) \times 10^{-8}$ at the 90% confidence level [13]. Lepton flavor violation in the charged sector has not been observed.

Grand unified theories (GUT) suggest that "...leptons and quarks must lie together in the same irreducible representations of..." a larger symmetry group and some gauge fields may carry lepton number and quark number [14]. Tree-level FCNC for quarks and leptons are assumed to be identical at the grand unification scale. It is well beyond the scope of this experimental study to go over the intricacy of grand unified theories [15].

Extensions of the SM allow for FCNCs with the addition of another Higgs doublet. Decays with couplings involving the 3rd generation may provide the best chance of detection [16]. Arguments paraphrasing the motivation of a search for rare three-body B-meson decays involving τ's in the context of grand unification presented by Sher & Yuan is reiterated below [16]. To try and avoid confusion, the notation is the same: If an additional Higgs doublet is included in the SM and only neutral currents are considered, the Yukawa

coupling components in the Lagrangian can be generalized as

$$(\lambda_{ija}\bar{d}'_{iL}d'_{jR}\phi_a + \lambda_{ijb}\bar{d}'_{iL}d'_{jR}\phi_b) + H.c.\ ,$$

where d'_i represents the three *down*-type quarks, ϕ_a and ϕ_b are complex neutral fields and the λ_{ijk} are arbitrary. This generalization can be applied to the *up*-type quarks and charged leptons as well, but will be ignored to simplify the arguments. Two new scalar fields H and ϕ can be defined as

$$H \equiv cos\beta\phi_a + sin\beta\phi_b,\ \phi \equiv -sin\beta\phi_a + cos\beta\phi_b\ ,$$

by using a rotation transformation of ϕ_a and ϕ_b by some angle β. The angle is defined $tan\beta \equiv v_b/v_a$, such that the real components of the Higgs fields acquire vacuum expectation values v_a and v_b. The real components of H and ϕ have vacuum expectation values $v = \sqrt{v_a^2 + v_b^2}$ and zero, respectively. The Yukawa couplings in the Lagrangian are transformed in terms of the new fields:

$$(f_{ij}\bar{d}'_{iL}d'_{jR}H + g_{ij}\bar{d}'_{iL}d'_{jR}\phi) + H.c.\ ,$$

where f_{ij} and g_{ij} are still arbitrary and that the mass matrix is given by $M_{ij} = f_{ij}v$. After diagonalization, the terms of the quark mass eigenstates become

$$\begin{aligned}[m_d\bar{d}_L d_R(\sqrt{2}H/v) + m_s\bar{s}_L s_R(\sqrt{2}H/v) + \\ m_s\bar{b}_L b_R(\sqrt{2}H/v) + h_{ij}\bar{d}_{iL}d_{jR}\phi] + H.c.\ ,\end{aligned} \tag{1.1}$$

where a natural coupling (h_{ij}) to the new scalar ϕ field component appears, which does not contribute to symmetry breaking or to the quark or lepton masses. Notice the new H field is the Higgs field of the SM.

Moreover, by assuming mixing between the H field and ϕ field are small, it is found that the H field is identical to the SM-Higgs field and the complex field ϕ is composed of a scalar ϕ_S and a pseudoscalar ϕ_P, such that the scalar couples as

$$\frac{h_{ij}}{\sqrt{2}}\bar{d}_i d_j \phi_S$$

and the pseudoscalar couples as

$$\frac{h_{ij}}{\sqrt{2}}\bar{d}_i \gamma_5 d_j \phi_P$$

with similar terms for the leptons. It is assumed that the h_{ij} is Hermitian, for simplicity.

Furthermore, this leads to tree-level FCNCs through the exchange of these extra scalars, with rates in general proportional to $h_{ij}^2 h_{kl}^2/m_\phi^4$. Our work is dedicated to searches involving three-body $B \to h\tau\ell$ decays. Three-body B decays are determined to occur only through the exchange of the scalar field (ϕ_S). Therefore, discussion of the pseudoscalar field (which occurs mostly in two-body processes) will try to be avoided.

Sher and Yuan continue to argue that the value of the coupling constants, h_{ij}^{quark} for the *down* -type sector and h_{ij}^{lepton} for the lepton sector should be arbitrary. Extensions of the SM, with multiple Higgs doublets, remove tree-level FCNCs by assuming coupling constants are of the order of the gauge coupling (g). By doing this, the mass scale of FCNCs are unnaturally large citing bounds using the form $m_S h_{ij}/g$. The argument that Yukawa couplings are comparable to the gauge coupling is used by many theorists, but is strongly criticized by Cheng and Sher [9]. They instead argue that the fermion mass structure has an hierarchical structure and show if no fine-tuning is assumed by requiring only one doublet per generation, the Yukawa couplings are of the form

$$h_{ij}^{\text{quark}} = \sqrt{(g_y)_i (g_y)_j}\ , \tag{1.2}$$

where $(g_y)_d = m_d\sqrt{2}/v$, $(g_y)_s = m_s\sqrt{2}/v$, and $(g_y)_b = m_b\sqrt{2}/v$ are the coefficients of the transformed Yukawa terms: $\bar{d}_L d_R H$, $\bar{s}_L s_R H$, and $\bar{b}_L b_R H$ in equation 1.1, respectively. Similarly, these terms arise for leptons as well. The coupling h_{ij} of the additional scalar to b and s quarks is then not of order unity, but instead is of order of the geometric mean of the Yukawa couplings, $(g_y)_b$ and $(g_y)_s$, which retains the Kobayashi-Maskawa (KM) angles without fine-tuning.

In addition, dimensionless couplings for quarks and leptons can be defined as

$$\eta_{ij}^{\text{quark}} \equiv \frac{h_{ij}^{\text{quark}}}{(g_y)_b} \, , \eta_{ij}^{\text{lepton}} \equiv \frac{h_{ij}^{\text{lepton}}}{(g_y)_\tau} \, . \tag{1.3}$$

Experimental bounds calculated from earlier theories assume $\eta_{ij} = 1$, which result in the flavor-changing Higgs mass of $\approx 150\ TeV$ [9]. By substituting equation 1.2 into equation 1.3, the "most natural value" for the couplings are $\eta_{ij}^{\text{quark}} = \sqrt{m_i m_j}/m_b$ and $\eta_{ij}^{\text{lepton}} = \sqrt{m_i m_j}/m_\tau$, which results in a more reasonable flavor-changing Higgs mass of $\approx 1\ TeV$. At the GUT scale, we expect $\eta_{ij}^{\text{quark}} = \eta_{ij}^{\text{lepton}}$. Therefore, a B-meson decaying to $K\tau\mu$, $K\tau e$, $\pi\tau\mu$, and $\pi\tau e$ should result in branching fractions sensitive to η_{bs}^4, $\eta_{bs}^2\eta_{bd}^2$, $\eta_{bd}^2\eta_{bs}^2$, and η_{bd}^4, respectively, assuming these "natural" couplings and GUT scale energies, and may be within reach at the B-factories.

Quark-level FCNC transitions to LFV processes include, $b \to s\tau\ell$ and $b \to d\tau\ell$, where the primary lepton, $\ell = e$ or μ, comes directly from our signal B decay. Possible Feynman diagrams for $b \to s\tau\ell$ and $b \to d\tau\ell$ transitions are shown in Figure 1.1(a) for a tree-level diagram and Figures 1.1(b) and 1.1(c) which involve higher order diagrams and result in branching fractions which might as well be forbidden in the SM, but are technically allowed, on the order of $\mathcal{BF} \propto \left(\frac{m_\nu}{m_W}\right)^2$. The first experimental search for decay modes of this

type was done for the $B^+ \to K^+\tau\mu$ decay, with an upper limit on the branching fraction of 7.7×10^{-5} at the 90% confidence level using the Feldman-Cousins method from the *BABAR* runs 1-4 dataset ($347.3 fb^{-1}$ at the $\Upsilon(4S)$ resonance) [18]. The best experimental constraint of decays of this type involve the $B_s \to \mu^+\mu^-$ search, where the CDF collaboration has set an upper limit on the branching fraction of $< 5.8 \times 10^{-8}$ at the 95% confidence level [20].

Using again Sher & Yuan notation, we can write branching fractions proportional to their "most natural" values. Therefore, $\mathcal{B}F(B_s \to \mu^+\mu^-) \propto \eta_{bs}^2\eta_{\mu\mu}^2$ and $\mathcal{B}F(B^+ \to K^+\tau\mu) \propto \eta_{bs}^2\eta_{\tau\mu}^2$. The ratio between branching fractions and the experimental limit on the $B_s \to \mu^+\mu^-$ decay gives us an idea of the sensitivity needed to be competitive for NP searches at the GUT scale. Table 1.1 provides a summary of the branching fractions for each signal decay mode search in terms of η_{ij} and sensitivities necessary to be competitive with the $B_s \to \mu^+\mu^-$ upper limit. The best chance at improving the constraint on NP, using the *BABAR* dataset may come from the $B^+ \to K^+\tau\mu$ search. The full *BABAR* dataset should improve the current upper limit of $\mathcal{B}F(B^+ \to K^+\tau\mu) < 7.7 \times 10^{-5}$ and put constraints on similar decays that have never been attempted before. There are also possible enhancements that could come from unknown parameters, buried in these GUT scale couplings that could be interesting, but we do not discuss them here.

Sher & Yuan also provide an estimate for determining the bound on the mass of the scalar exchange particle from upper limits on the signal branching fraction. We provide a summary of these bounds if we assume hypothetical upper limits from the expected *BABAR* sensitivity, in Table 1.2. It seems that the best decay process to study for determining these bounds are from the $B^+ \to K^+\tau\ell$; $\ell = e, \mu$ modes.

Branching fraction proportional to dimensionless parameter	Ratio of $\mathcal{B}F$(signal):$\mathcal{B}F(B_s \to \mu^+\mu^-)$ where $\eta_{ij}^{\text{quark}} = \eta_{ij}^{\text{lepton}}$ at GUT scale	NP sensitivity to be competitive with $\mathcal{B}F(B_s \to \mu^+\mu^-)$
$\mathcal{B}F(B^+ \to K^+\tau\mu) \propto \eta_{bs}^2\eta_{\tau\mu}^2$	$\eta_{\tau\mu}^2/\eta_{\mu\mu}^2 = m_\tau/m_\mu \approx 17$	$< 1.0 \times 10^{-6}$
$\mathcal{B}F(B^+ \to K^+\tau e) \propto \eta_{bs}^2\eta_{\tau e}^2$	$\eta_{\tau e}^2/\eta_{\mu\mu}^2 = (m_\tau m_e)/m_\mu^2 \approx 1/12.6$	$< 4.6 \times 10^{-9}$
$\mathcal{B}F(B^+ \to \pi^+\tau\mu) \propto \eta_{bd}^2\eta_{\tau\mu}^2$	$\eta_{\tau e}^2/\eta_{\mu\mu}^2 = (m_\tau m_e)/m_\mu^2 \approx 1/12.6$	$< 4.6 \times 10^{-9}$
$\mathcal{B}F(B^+ \to \pi^+\tau e) \propto \eta_{bd}^2\eta_{\tau e}^2$	$\eta_{\tau e}^4/(\eta_{\tau\mu}^2\eta_{\mu\mu}^2) = (m_\tau m_e^2)/m_\mu^3 \approx 3.7 \times 10^{-4}$	$< 2.1 \times 10^{-11}$
$\mathcal{B}F(B_s \to \mu^+\mu^-) \propto \eta_{bs}^2\eta_{\mu\mu}^2$	1	$< 5.8 \times 10^{-8}$

Table 1.1: Summary of sensitivities needed to improve NP constraints. Best experimental constraint on NP parameters of this type set by CDF collaboration with $B_s \to \mu^+\mu^-$ result. To be competitive, we need to set upper limits on the order of the last column, derived using the relationship between Yukawa couplings and dimensionless parameters discussed in text.

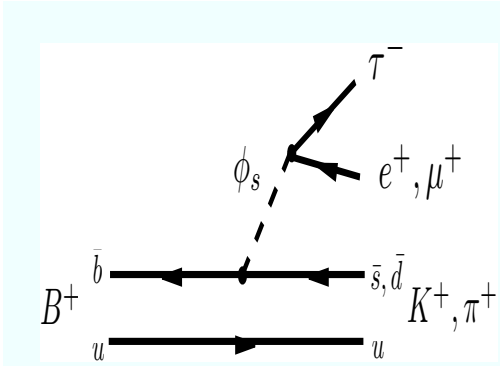

(a) NP tree level LFV FCNC: $B^+ \to h^+ \tau \ell$; $h = K, \pi$; $\ell = e, \mu$.

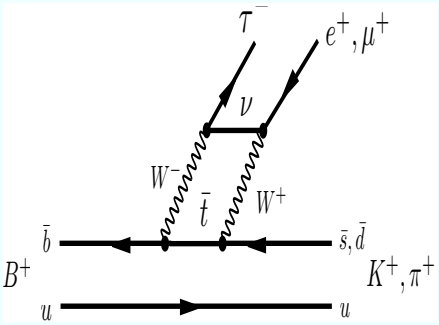

(b) SM box diagram LFV FCNC, assumes neutrino mixing.

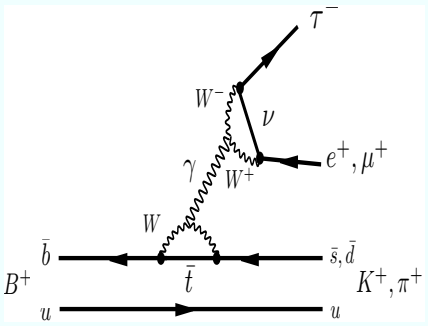

(c) SM QED penguin with "mixed" coupling of a photon with two W propagators, also assumes neutrino mixing.

Figure 1.1: Possible Feynman diagrams.

From the work of Black *et al.* on $\tau - \mu$ flavor violation [17], we can estimate the energy scale for flavor-changing operators. They determined that the branching fraction on B decays involving $h\tau\mu$; $h = K, \pi$ is proportional to Λ^{-4}, where Λ is the energy scale for NP. They predicted NP energy scales in flavor-changing operators of > 2.6 TeV and > 2.2 TeV,

Decay process	Expected upper limit	Bound $\times(m_S/m_W)^4$
$B^+ \to K^+\tau\mu$	(7.7×10^{-5}) [1]	$\eta^4_{\mu\tau} < 7.7$
$B^+ \to \pi^+\tau\mu$	7.7×10^{-5}	$\eta^2_{e\tau}\eta^2_{\mu\tau} < 770$
$B^+ \to K^+\tau e$	7.7×10^{-5}	$\eta^2_{\mu\tau}\eta^2_{e\tau} < 7.7$
$B^+ \to \pi^+\tau e$	7.7×10^{-5}	$\eta^4_{e\tau} < 770$

Table 1.2: Bounds on flavor-changing couplings from three-body B decays estimated using the Sher & Yuan calculation [16], with expected *BABAR* sensitivity, in column 2. Estimated bounds can provide method for determining mass of the scalar exchange particle, m_S, in Figure 1.1(a).

assuming a branching fraction of 5%, for the $B \to K\tau\mu$ and $B \to \pi\tau\mu$ decays, respectively. The NP energy scale in flavor-changing operators has been pushed to > 13 TeV, from the initial *BABAR* $B \to K\tau\mu$ search which yielded an upper limit branching fraction of $< 7.7 \times 10^{-5}$ at the 90% C.L. Assuming the same sensitivity for the $B \to \pi\tau\mu$ search, we can push the NP energy scale to > 11 TeV. With the full *BABAR* dataset, we expect a sensitivity on the $B \to K\tau\mu$ branching fraction of 1.3×10^{-5}, which would push the NP energy scale to > 20 TeV. Black *et al.* does not provide an estimate for determining the NP energy scale from $B \to h\tau e$; $h = K, \pi$ operators, couplings between the third and first generations.

The Type III two-Higgs-doublet-model using the Cheng and Sher *ansatz* [9] can be excluded: in the leptonic sector, perhaps in the next three years from failure to observe the signal $\mu \to e\gamma$ at the MEG experiment (unless cancellation between the scalar and pseudoscalar occurs); in the quark sector, a pseudoscalar mass in the range $100-200\ GeV/c^2$ is problematic in $B^0 - \bar{B}^0$ and $B^0_s - \bar{B}^0_s$ mixing, and an observation of the signal $B_s \to \mu\mu$ would be expected; or also in the quark sector, a branching ratio of $< 10^{-3}$ for a $t \to ch$ signature, if h is light [21]. Any of the three scenarios above, would rule out the Type III two-

Higgs-doublet-model. For other tree-level flavor-changing neutral-current models and their predictions, see the discussion on BGL, MFV, and Two-Higgs Leptonic Minimal Flavour Violation also summarized from Branco, Ferreira, Lavoura, Rebelo, Sher, and Silva [21].

Chapter 2

PEP-II and the *BABAR* Detector

2.1 Introduction

The primary goal of the *BABAR* experiment is to study CP-violation in neutral B meson decays. In order to achieve this goal, copious amounts of B mesons must be created (of order 100 million events) in a relatively clean event reconstruction environment. This led to the design of a high luminosity asymmetric B Factory, colliding electrons and positrons head on just above the $\Upsilon(4S)$ center of mass resonance, 10.58 GeV. The electrons and positrons are accelerated to 9.0 GeV and 3.1 GeV, respectively, which provide a Lorentz boost to the $\Upsilon(4S)$ resonance of $\beta\gamma = 0.56$. The $\Upsilon(4S)$ is boosted in the forward direction and decays to $B\bar{B}$ pairs $> 96\%$ of the time; B^+B^- 51.6% of the time and $B^0\bar{B}^0$ 48.4% of the time [11]. This boost provides the necessary vertex separation, that can be measured using silicon vertex detector technology, between neutral B mesons for time-dependent CP asymmetry measurements.

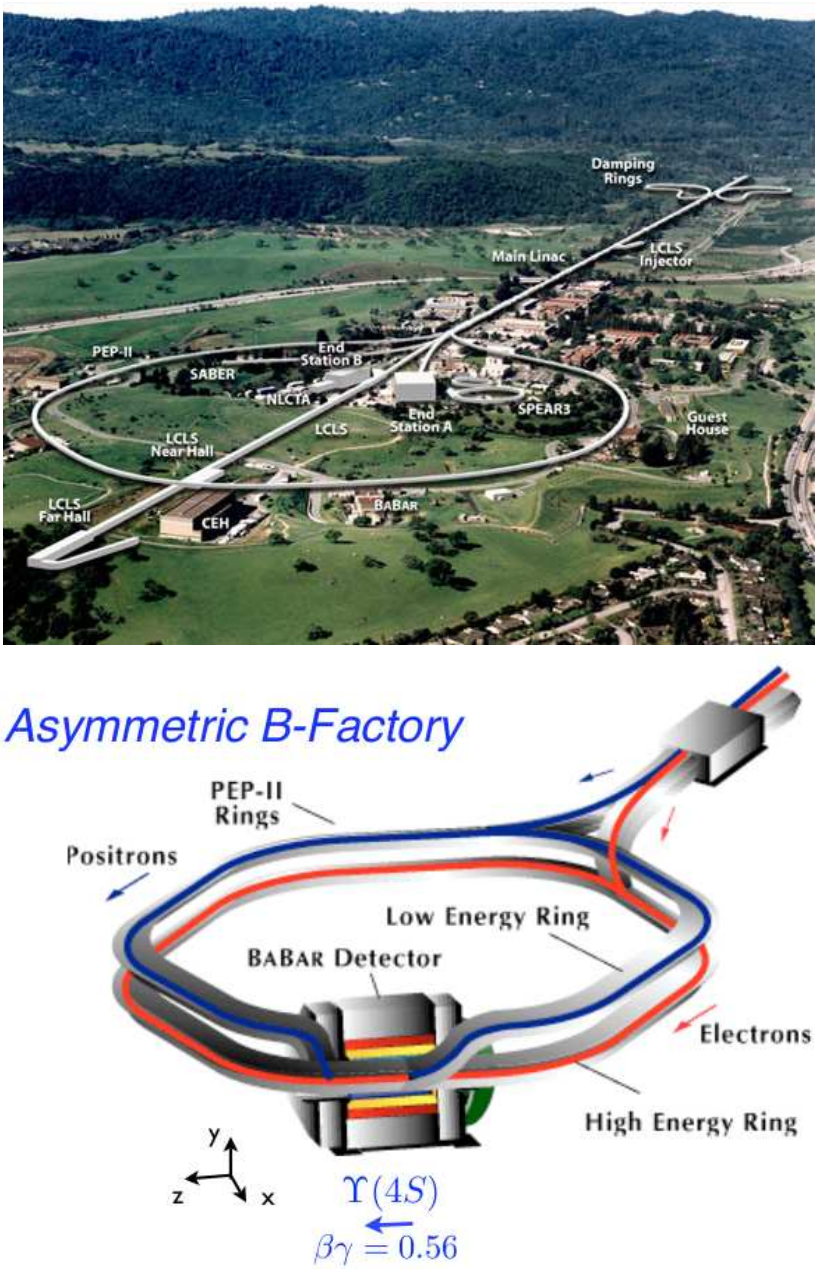

Figure 2.1: Aerial view of SLAC-NAL annotated with accelerator and detector facilities (top) [22]. Schematic of asymmetric B-Factory and placement of *BABAR* detector with HER electron and LER positron directions indicated (bottom) [23].

Other types of studies are performed using the high event yield (precision measurements) from the B Factory. A better name may be the Flavor Factory. The average production cross sections of other processes at the $\Upsilon(4S)$ resonance are provided in Table 2.1. Precision measurements of decays involving bottom and charm mesons, τ leptons,

Cross-section (nb)	
$e^+e^- \to b\bar{b}$	1.05
$e^+e^- \to c\bar{c}$	1.30
$e^+e^- \to s\bar{s}$	0.35
$e^+e^- \to u\bar{u}$	1.39
$e^+e^- \to d\bar{d}$	0.35
$e^+e^- \to \tau^+\tau^-$	0.94
$e^+e^- \to \mu^+\mu^-$	1.16
$e^+e^- \to e^+e^-$	≈ 40

Table 2.1: Production cross sections at 10.58 GeV within the *BABAR* fiducial region [24].

and searches of rare decays are studied. In our analysis, we focus on reconstruction of $\Upsilon(4S)$ decays to charged B mesons. In the following, we overview features of the Positron-Electron Project (PEP II) storage ring and the *BABAR* detector. For the entire *BABAR* detector, we briefly discuss each subsystem and highlight particle identification performance in the event reconstruction.

2.2 PEP II Asymmetric Collider

SLAC, formerly known as the Stanford Linear Accelerator Center located in Menlo Park, CA, has been renamed the SLAC National Accelerator Laboratory, one of only three DOE national accelerator laboratories [1]. An aerial photograph of the facility annotated

[1]Fermi National Accelerator Laboratory and Thomas Jefferson National Accelerator Laboratory are the others.

with accelerator and detector facilities can be seen in Figure 2.1. The two-mile long linear accelerator (Linac), crossing what eventually became the 280 Interstate Freeway running nearly perpendicular to the Santa Cruz Mountains, injects the PEP-II storage rings; high energy ring (HER) with electrons and low energy ring (LER) with positrons.

In Figure 2.2, a schematic overview of the linac and PEP-II is provided. The e-gun and damping rings provide the source of electron bunches which are accelerated in the linac. Half of the electron bunches are accelerated and feed into a tungsten target, resulting in electron-positron production. These positrons are collected into the second damping ring before being accelerated from the linac. The electron and positron bunches are then injected into the HER and LER, respectively. Table 2.2 provides a summary

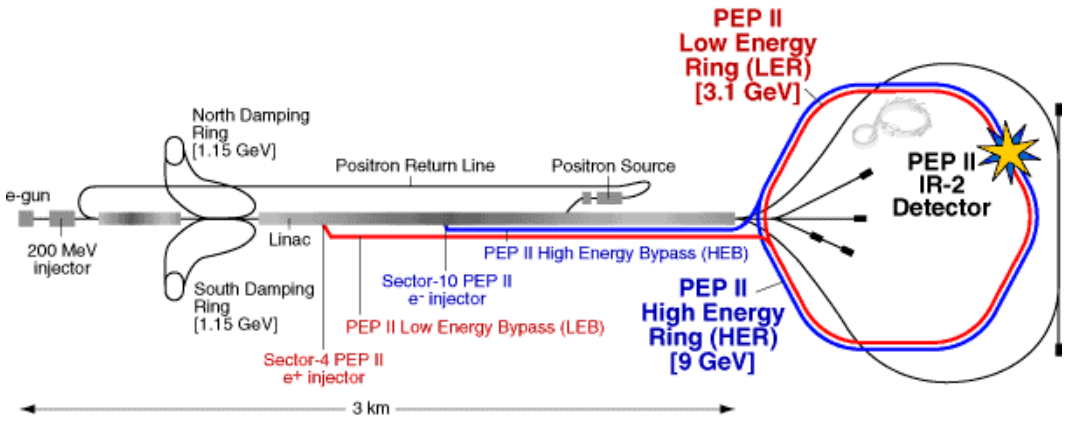

Figure 2.2: Schematic of the linac and PEP-II [25].

of PEP-II beam parameters for typical operations during the first year, design, and best performances. Beams circulate in opposite direction and collide at the interaction point, where the *BABAR* detector sits, housed in the interaction region (IR-2) facility, just to the right of the Collider Experimental Hall in Figure 2.1 (top). Figure 2.1(bottom) provides

Parameters	1st Year	Design	Best
Energy HER/LER (GeV)	9.0/3.1	9.0/3.1	9.0/3.1
Current HER/LER (A)	0.7/1.3	0.75/2.15	2.07/3.21
Number of bunches	553-829	1658	1732
Bunch spacing (ns)	6.3-10.5	4.2	4.2
σ_{Lx} (μm)	120	110	-
σ_{Ly} (μm)	5.6	3.3	-
σ_{Lz} (mm)	9	9	-
Luminosity (10^{33} cm^{-2}s^{-1})	2.5	3	12
Luminosity (pb^{-1}/day)	120	135	911

Table 2.2: PEP-II beam parameters for typical first year operations [26], design, and best performances [27]. σ_L is defined as the luminous region RMS size of the bunches.

a cartoon schematic of the asymmetric B Factory, PEP-II rings, HER and LER, *BABAR* detector orientation, and the forward boost of the $\Upsilon(4S)$ resonance.

BABAR collected data from 2000-2008, completing a total of seven runs (runs 1-6 at the $\Upsilon(4S)$ resonance, with run 7 split at the $\Upsilon(2S)$ and $\Upsilon(3S)$ resonances). The highest instantaneous luminosity reached by the PEP-II collider is 1.2×10^{34} cm^{-2}s^{-1}, well above the design luminosity. PEP-II has delivered 557 fb^{-1}, while *BABAR* has recorded 531.43 fb^{-1}. This analysis is concerned with data at the $\Upsilon(4S)$ resonance, where *BABAR* has recorded 432.89 fb^{-1}. The off-peak integrated luminosity recorded at *BABAR* is 53.85 fb^{-1}. PEP-II officially turned off on April 7, 2008. Figure 2.3 has a complete breakdown of the integrated luminosity year-by-year. In the following sections, we give a brief overview of each *BABAR* sub-detector.

2.3 *BABAR* Detector Overview

The boosted $\Upsilon(4S)$ resonance provided by PEP-II requires an asymmetric detector design to optimize the detector acceptance, particularly for spatial resolution requirements

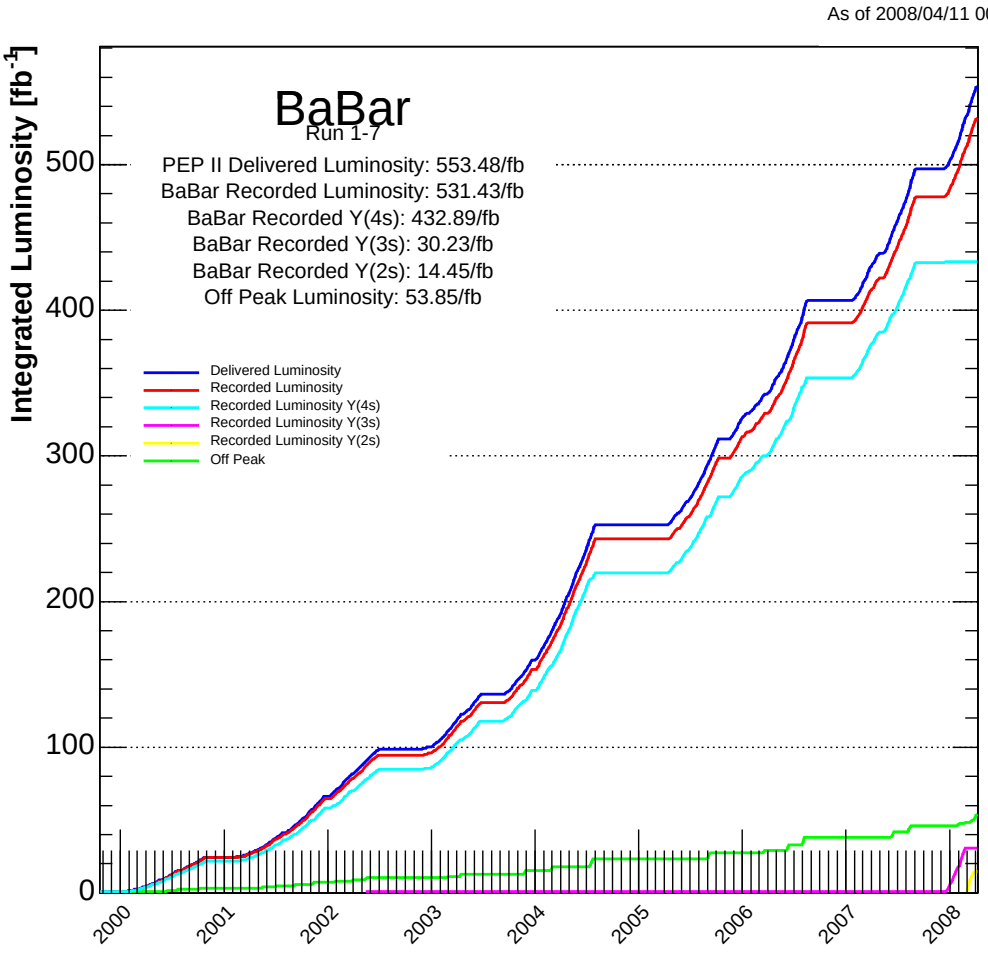

Figure 2.3: Integrated luminosity runs 1-7 [28].

to untangle $B^0 - \bar{B}^0$ mixing. The *BABAR* detector has been designed to [24]:

- maximize the acceptance in the center-of-mass system.
- accommodate machine components near the region of the interaction point, where special beam optics are necessary for the high luminosity event rates.

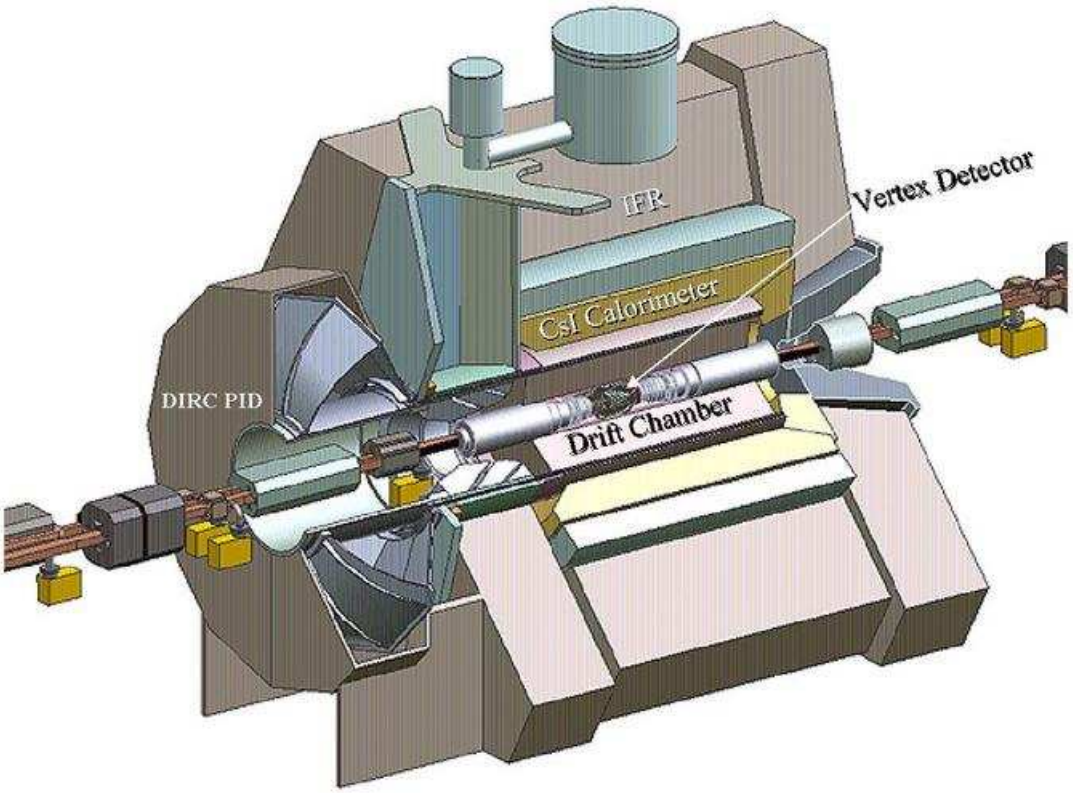

Figure 2.4: 3D schematic of the *BABAR* detector with subsystems labeled [29].

- provide excellent vertex resolution, especially in the z-axis, to help discriminate bottom, charm, and light quark vertices.
- identify tracks from charged particles within the transverse momenta range of ≈[0.060,4.00] GeV.
- discriminate stable particles (e, μ, π, K, and p) over a wide range of kinematics, especially for $\pi - K$ resolution at momenta between (2-4) GeV.
- distinguish γs from π^0s within the energy range [0.02, 5] GeV.
- possibly provide neutral hadron (K_L^0) identification.

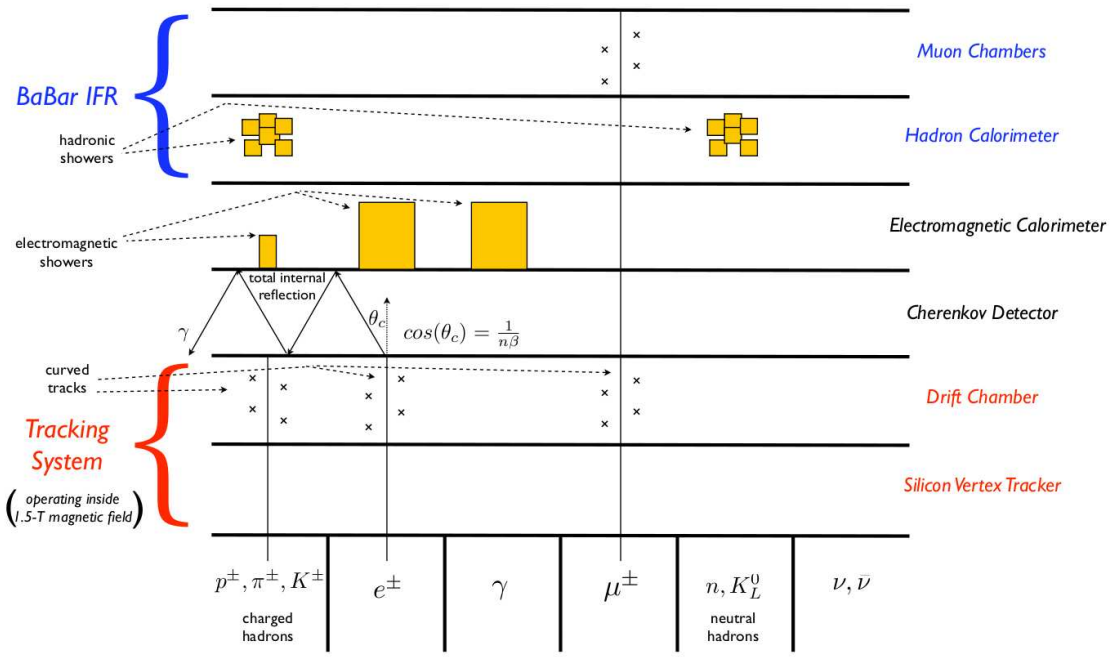

Figure 2.5: Cartoon of particle flow via each sub-detector.

Figure 2.5 provides a cartoon summary of the particle flow of each sub-detector. The tracking system is composed of the Silicon Vertex Detector (SVT) and the Drift Chamber (DCH), both operating within the 1.5 Tesla superconducting solenoid which curves the trajectories of charged particles. The SVT provides the precision vertexing on charged tracks and the only subsystem capable of tracking low-energy particles. The DCH provides momentum measurements of charged particles and particle identification through ionization energy loss per unit length measurements. It has been designed to minimize multiple scattering effects. The Cherenkov detector, or DIRC, is designed to provide additional charged hadron particle identification for tracks passing the DCH. The Cesium Iodide Electromagnetic Calorimeter, or EMC, measures energy deposits from neutral and charged particles

and is designed to account for the Lorentz boost with barrel and forward endcap components. Also the EMC provides photon, electron, and neutral hadron identification. The Instrumented Flux Return, or IFR, provides muon identification down to approximately 600 MeV and possibly neutral hadron (K_L^0) identification.

A detailed schematic of the longitudinal and transverse profile of the *BABAR* detector is provided in Figure 2.6. A detailed discussion of the *BABAR* detector is found in [26, 27].

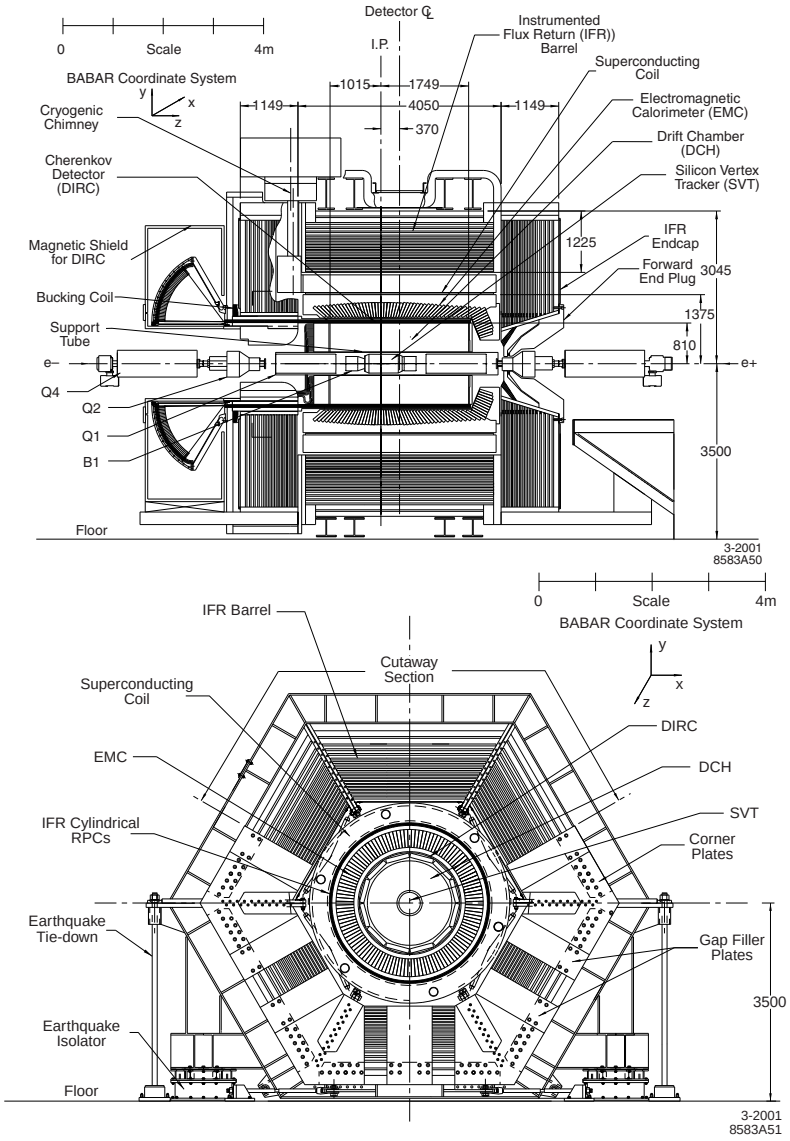

Figure 2.6: Detailed schematics of the *BABAR* detector: longitudinal (top) and endcap (bottom) views [26].

2.4 Silicon Vertex Tracker

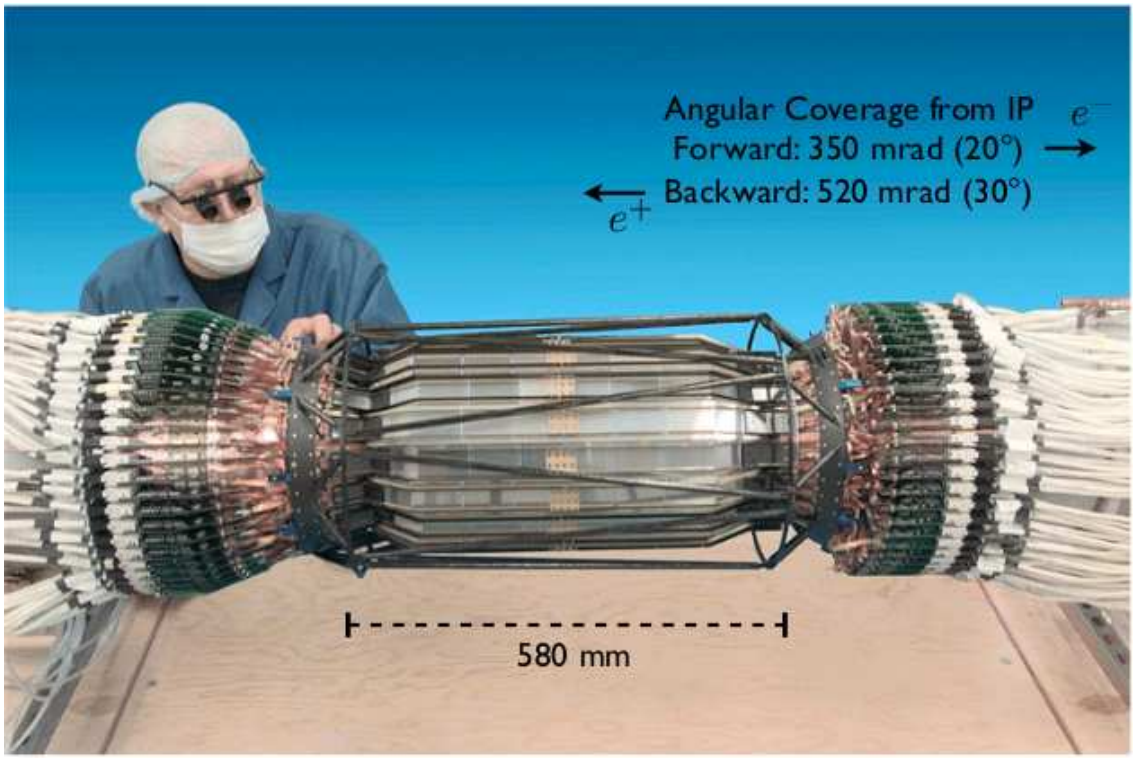

Figure 2.7: Photo of Silicon Vertex Tracker in quality control and prior to installation [30].

The subsystem closest to the beam pipe is the silicon vertex tracker (SVT), a five layer double-sided silicon strip detector, designed to measure angles and position of charged particles from the interaction point. The three inner layers provide position and angle information for measuring the vertex position, while the outer fourth and fifth layers provide coordinate and angle information to link the SVT tracks with the drift chamber subsystem tracks. Figure 2.8 provides longitudinal and transverse views of SVT cross-sections.

Because of the vicinity closest to the beam pipe, the SVT is mechanically designed

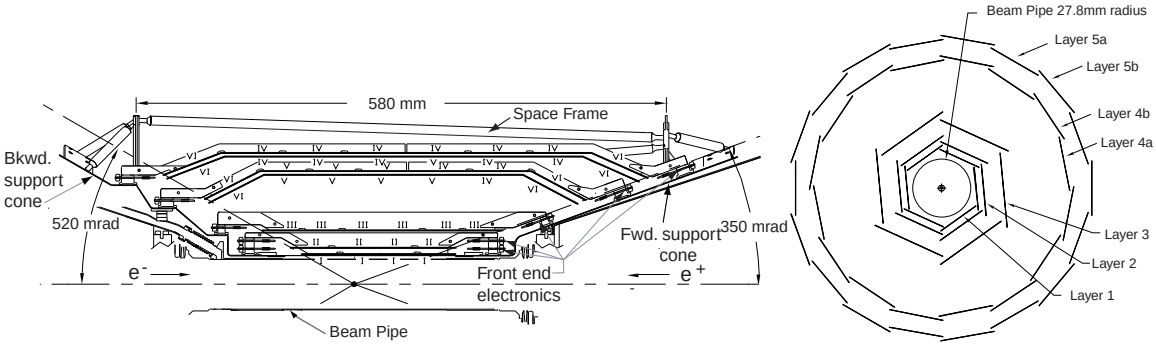

Figure 2.8: Silicon Vertex Tracker schematics: longitudinal (r-z) and transverse (x-y) cross-sections [26].

to minimize multiple scattering in the extrapolation of the vertex. Therefore, this requires reducing the inactive material in the acceptance volume by placing the readout electronics at the ends of the silicon strip detector modules, see Figure 2.7. Another design requirement, because of high radiation doses from high luminosities, is for the system to withstand a lifetime radiation dose of 2 Mrad over ten years. The SVT must be reliable, because it is not accessible during routine shutdowns.

We can determine the momentum of the charged track, $p = qrB$, by measuring the bend radius, r, knowing the magnetic field strength, B, and determining charge, q, by the direction of curvature. For low momentum tracks, the SVT is the only subsystem that provides information, especially in the case of $D^* \to D\pi$ decays which provides momentum resolution for the slow pion. It has a z-axis vertexing resolution of 80μm and has the sole reconstruction information for charged particles with transverse momentum below 120 MeV (not reaching the DCH). For our analysis the SVT helps with track reconstruction in our control sample, in $D^* \to D\pi$ decays with slow charged pions and in our hadronic tagged B reconstructions.

2.5 Drift Chamber

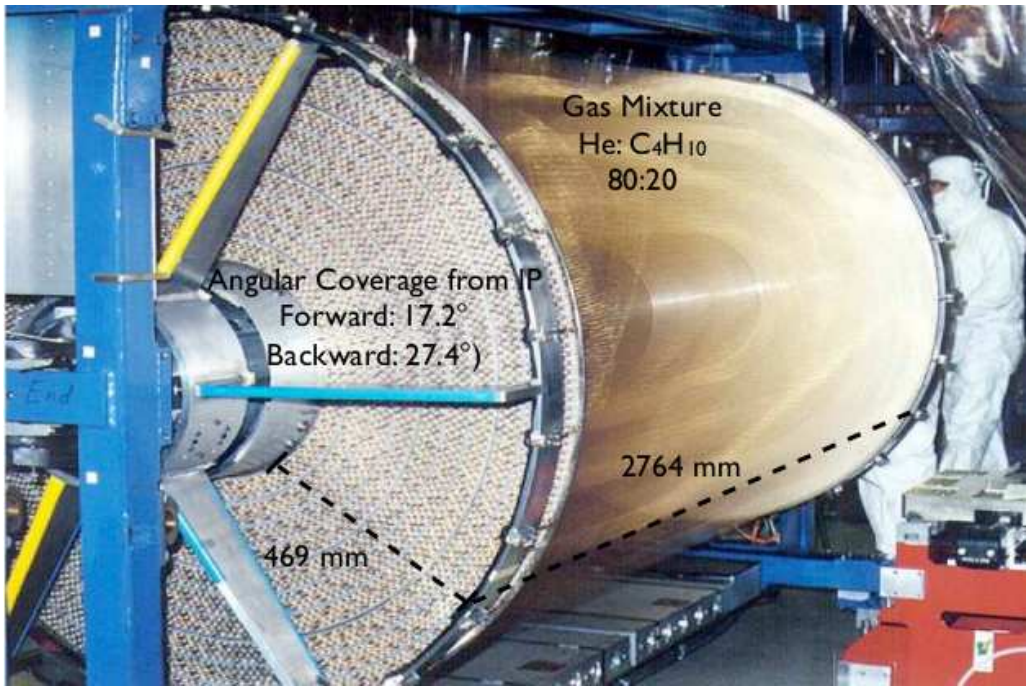

Figure 2.9: Drift Chamber photo with sense wires connected, prior to installation [32].

The drift chamber (DCH) is the second part of the *BABAR* tracking system. The 40 cylindrical layer subsystem principally measures momentum of charged particles, ensuring high reconstruction efficiency for charged tracks with transverse momentum approximately above 120 MeV. It provides a charged particle trigger and measures ionization loss, dE/dx, for particle identification. The energy deposited per unit length curves versus momentum in Figure 2.11 allows us to identify charged particles much better than the SVT alone. The DCH also provides vertexing from long-lived hadrons, such as the $K_S \to \pi^+\pi^-$ decays, well within the acceptance region. The DCH sub-detector is crucial for this analysis.

The DCH provides 140 μm of spatial resolution, averaged over the hexagonal cells

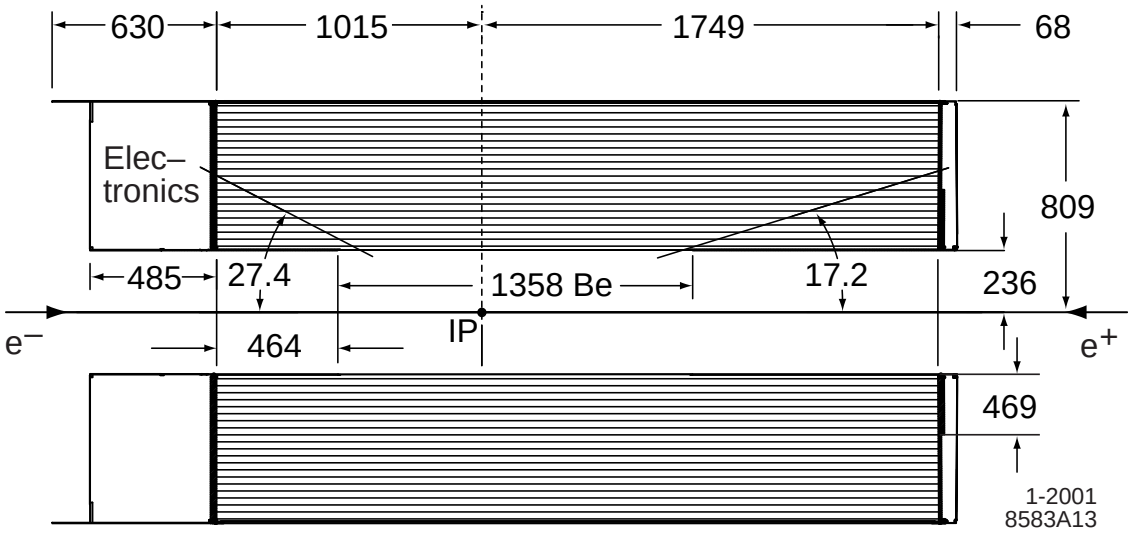

Figure 2.10: Schematic of cross-sectional view of the DCH with angular resolutions in degrees and spatial dimensions in mm (bottom) [33].

in the azimuthal-radial plane. The acceptance region of the DCH is shown in the left of Figure 2.10, consistent with the SVT acceptance in the azimuth. In order to minimize multiple scattering, the nominal gas mixture while recording data is (He:Isobutane 80:20) setting the high voltage of the sense wires to roughly 1960 Volts, allowing the DCH to operate in avalanche mode. As high energy particles propagate through the gas mixture electrons are liberated and accelerated to the sense wire by high voltage, forming a build-up or avalanche of electric charge. The dissipation of this electric charge lasts for approximately 10-500 ns, providing timing information to the front-end electronics for readout. There are 7104 cells, with typical cell dimensions of 1.2×1.8 cm^2. The mechanical structure of the DCH is constructed with light materials (inner cylinder: 1 mm thick beryllium 0.28% radiation lengths, outer cylinder: 2 layers of carbon fiber on Nomex core 1.5% radiation lengths, and forward endcap: 12 mm thick aluminum in the acceptance region to account for the

forward boost) with read-out electronics mounted near the rear and forward endplates of the subsystem, to minimize multiple scattering at the interface between adjacent sub-detectors. The magnetic field within the DCH is 1.5 Tesla.

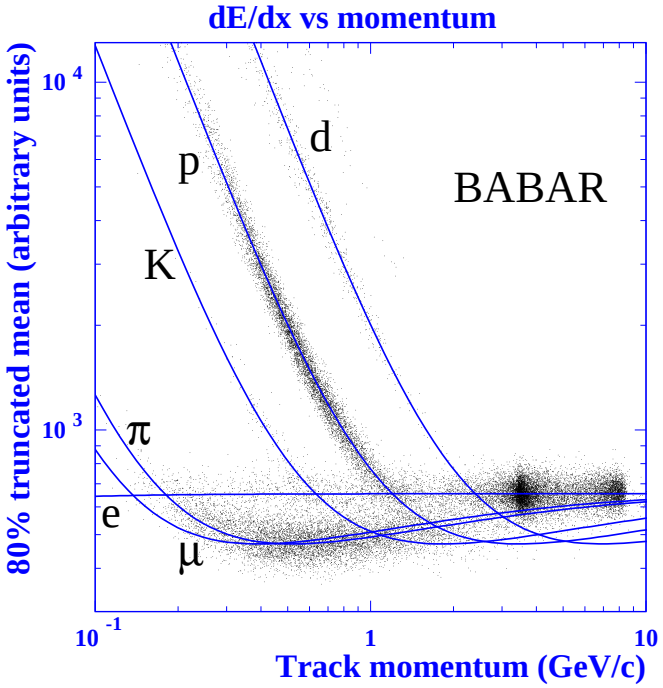

Figure 2.11: Energy loss per unit length (dE/dx) versus Momentum for particle identification in the DCH [26].

The drift chamber electronics is designed to not degrade performance of the chamber by more than 10%. The electronics provides hit information from all 7104 channels to the Level 1 Trigger at a sample rate of 3.75 MHz. The system should maintain good performance even in cases of large background conditions during collisions. The signal-cell efficiency in the trigger signal should be greater than 95%.

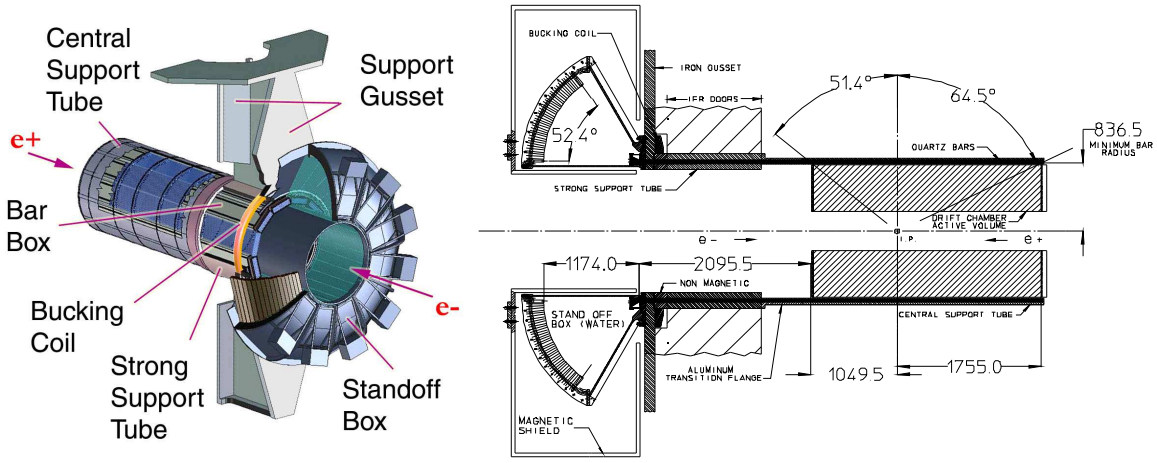

Figure 2.12: Schematic of DIRC crystal, with path of internally reflected light reaching phototubes housed in stand-off box (left) [26] and actual picture of quartz crystal (right) [32].

2.6 Detector of Internally Reflected Cherenkov Light

The *BABAR* Cherenkov detector, or DIRC, is designed to separate pions and kaons with momenta from approximately $0.5 - 4.5$ GeV, particularly in the range [2.0-4.0] GeV where charged hadrons have similar dE/dx. It is the next subsystem after the DCH, going radially out from the interaction point. A 3D DIRC support structure diagram (left) and schematic layout (right) is provided in Figure 2.12.

The angle between the track trajectory and cone of Cherenkov radiation is the Cherenkov angle (θ_c). The measurement of the Cherenkov angle, in conjunction with knowing the track angle and momentum from the DCH, allows us to determine the particle mass. This provides better particle identification rather than only relying on dE/dx from the DCH and SVT. The Cherenkov angle can be determined from, $cos(\theta_c) = \frac{1}{n\beta}$, where $n = 1.473$ is the index of refraction of the material (quartz) through which the Cherenkov light propagates and $\beta = \frac{v}{c}$, where v is the velocity of the track propagating across the material and

c is the speed of light in vacuum. Figure 2.13 provides a detailed schematic of the quartz bar and the stand-off box that house the phototube detectors.

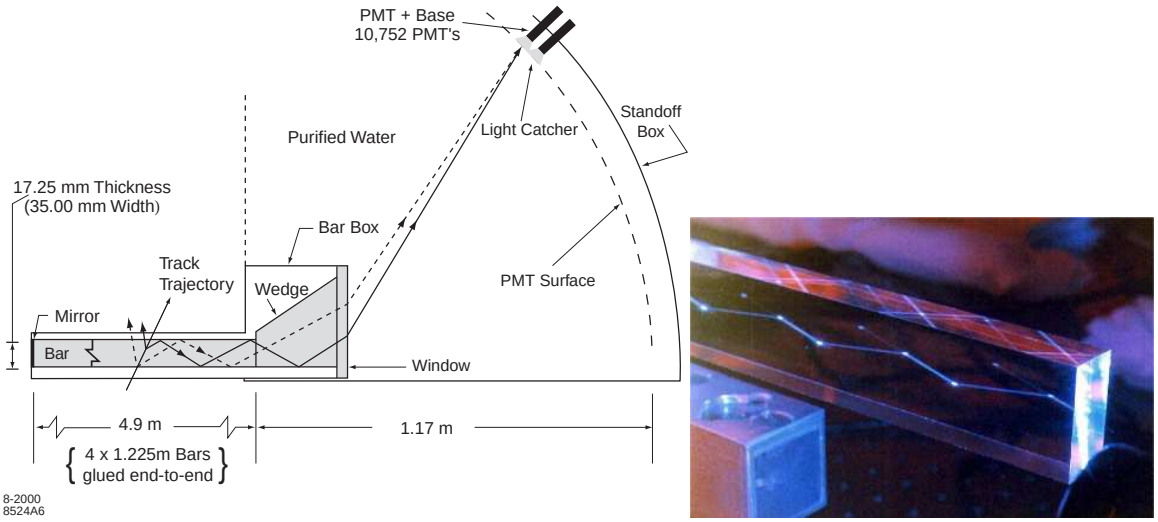

Figure 2.13: 3D diagram of DIRC support structure (left) and longitudinal cross section schematic (right) [26].

The DIRC is composed of 144 quartz bars arranged in a 12-sided polygon around the beam line. The quartz bar dimensions are 1.7 cm thick, 3.5 cm wide, and 490 cm long. As a charged particle passes through the quartz bar, Cherenkov light is totally internally reflected and guided to a region in the backward endcap of the *BABAR* detector where approximately 11,000 conventional 2.5 cm diameter phototubes detect the angle of the light (in the stand-off box). From the position of this phototube, θ_c is determined.

The DIRC coverage is 87% in the polar angle from the center-of-mass frame and 93% in the azimuthal (due to gaps between quartz bars). In a 1.5 T magnetic field with an internal radius of 80 μm, only particles with transverse momentum greater than $\approx$250 MeV from the interaction point can reach the DIRC quartz bars. The probability for a real kaon in the DIRC acceptance to pass kaon hypothesis is of order 95% or larger for all momenta

greater than ≈460 MeV. The fraction of pions misidentified as kaons is less than 3% for tracks with momenta measured up to ≈3 GeV. Figure 2.14 shows the separation power of Cherenkov angle versus lab frame momentum of charged particles.

Kaon and pion PID resolution is very important for precision measurements and without the DIRC, the quality of this analysis and many others would not be possible. Notice that the pion vs. muon identification is not very good. The probability of correctly assigning a muon within the DIRC acceptance is $>$ 80% for track momenta less than ≈750 MeV and 95% for track momenta at 500 MeV. Muon reconstruction with larger momenta require the IFR (see section 2.8).

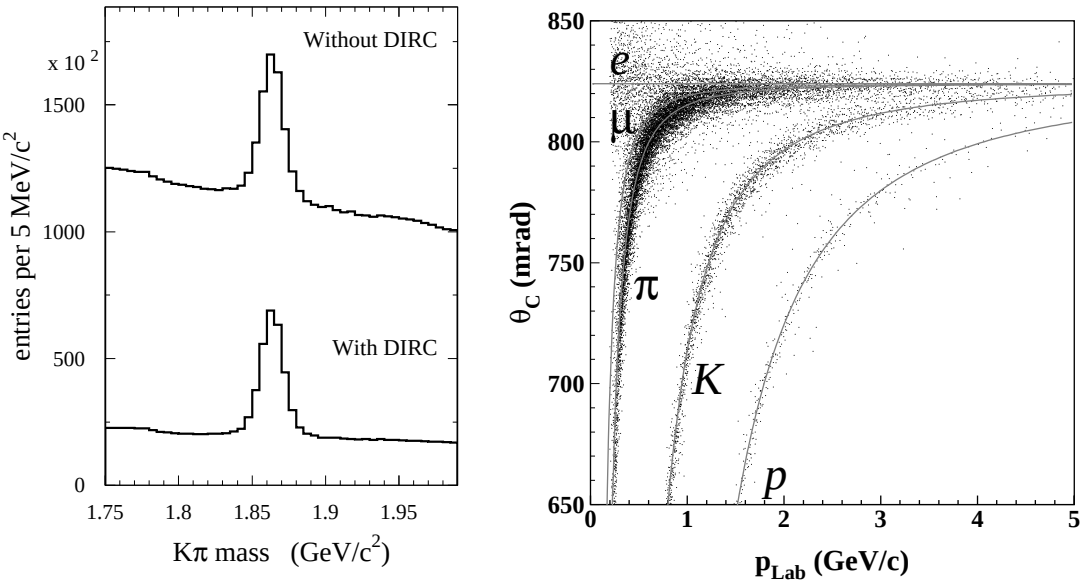

Figure 2.14: D^0 reconstruction using $K\pi$ invariant mass with and without DIRC information (left). DIRC particle separation: $\theta_{\rm C}$ versus $p_{\rm lab}$ (right). Note the $K-\pi$ separation [33].

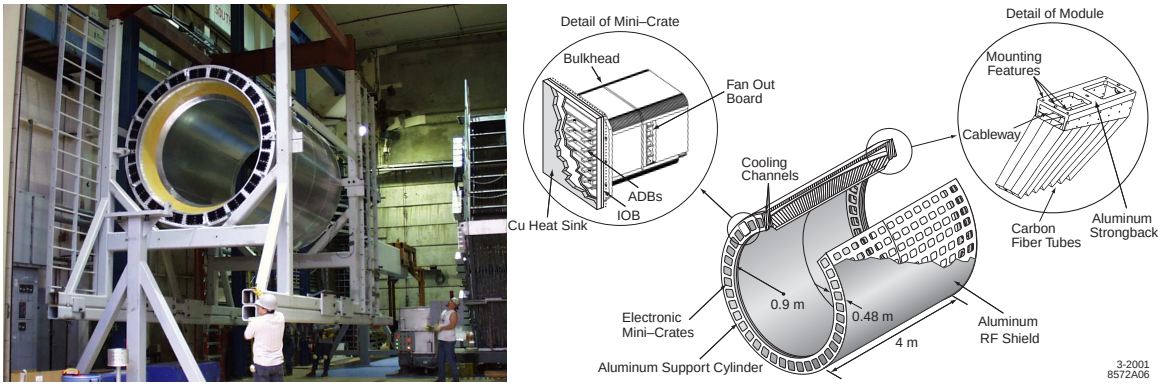

Figure 2.15: Photograph of EMC barrel prior to installation (left) with detailed schematic of support structure components (right) [34].

2.7 Electromagnetic Calorimeter

The electromagnetic calorimeter (EMC) is designed to measure QED processes in the range 20 MeV to 4 GeV, with excellent shower, energy, and angular resolution efficiency. Another function is to detect neutral hadrons such as π^0s and ηs, along with other radiative processes. Track hits from charged particles also deposit energy into the EMC. We use the EMC to identify electrons directly coming from a charged B meson, or from a secondary hadronic τ decays involving π^0s. Neutral particle detection in our tagged side reconstruction is also important. Signal searches, where the secondary τ decays leptonically, should result in zero residual energy in the calorimeter after fully reconstructing the event.

Below, we highlight some key points of the EMC subsystem. For details, please see the NIM paper on the *BABAR* detector [26]. Design considerations for the EMC require reliable operation for a lifetime of ten years, exposed to high temperatures and compatible with a 1.5 T magnetic field. Temperature and radiation exposure must be continually monitored during operations, with calibrations of electronics and energy response over the

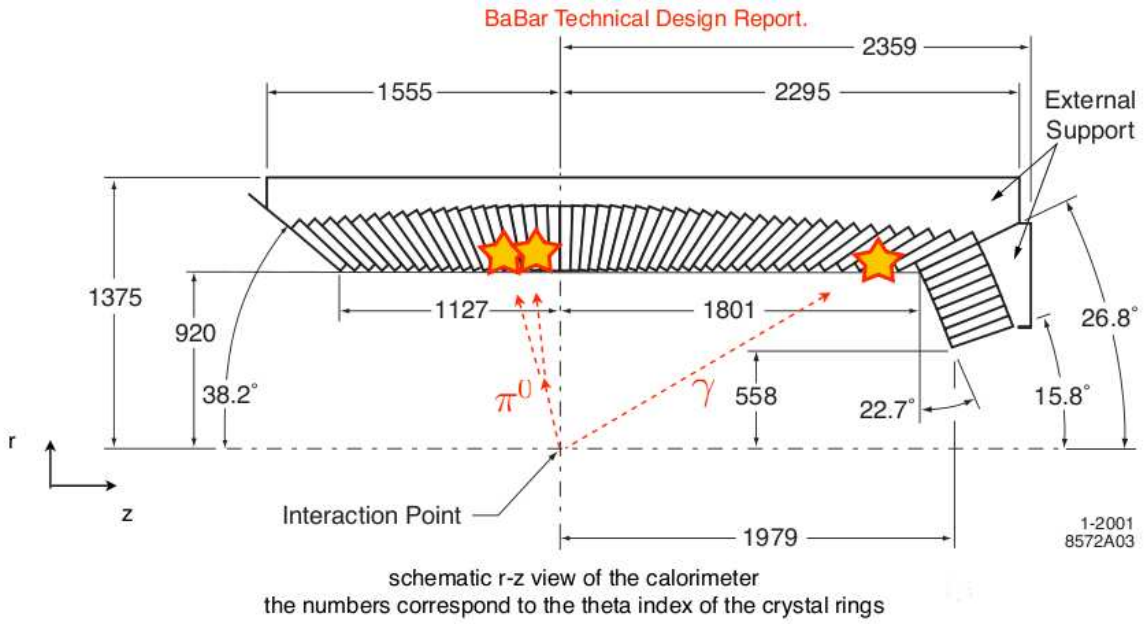

Figure 2.16: EMC geometry schematic (in mm) of CsI(Tl) crystal arrangement (γ and π^0 illustration superimposed) [26].

full dynamic range regularly performed. The EMC is designed with 6580 thallium-doped cesium iodide crystals CsI(Tl) in the barrel and forward endcap, finely segmented to provide a hermetic, total-absorption calorimeter. Silicon photodiodes read-out the energy deposited into the crystals, matched to the spectrum of scintillation light.

The energy resolution of a homogeneous crystal calorimeter is determined from the sum of two terms added in quadrature:

$$\frac{\sigma_E}{E} = \frac{a}{\sqrt[4]{E(GeV)}} \oplus b, \tag{2.1}$$

where E and σ_E is the energy of a photon and its RMS error, measured in GeV. The angular resolution is determined by the transverse crystal size and the distance from the interaction

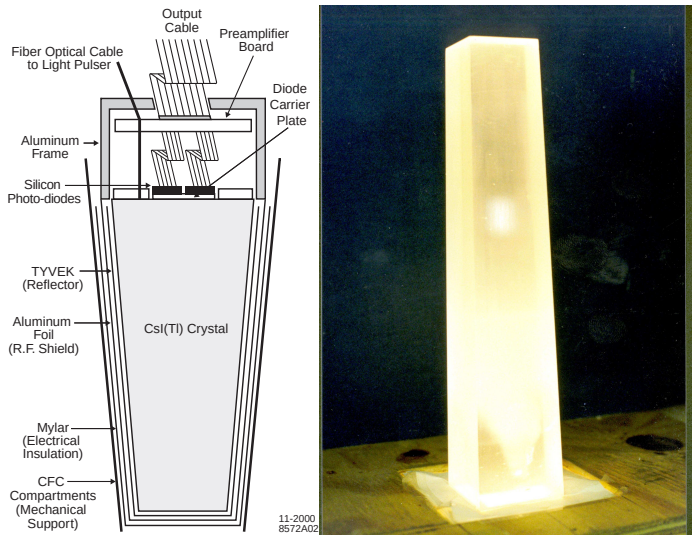

Figure 2.17: Detailed schematic of wrapped CsI(Tl) crystal (left) [26] with a photograph of an unwrapped crystal illuminated by a light bulb (right) [34].

point, parameterized as a sum of an energy dependent term and a constant:

$$\sigma_\theta = \sigma_\phi = \frac{c}{\sqrt{E(GeV)}} + d, \tag{2.2}$$

where E is again the energy measured, in GeV. The energy dependent term a is accounts for fluctuations in photon statistics, but is also impacted by electronic and beam-generated background noise. The constant term b is dominant at energies > 1 GeV and results from non-uniformity in light collection, leakage or absorption from non-crystalline material and uncertainty in calibrations. Other uncertainties come from operating conditions, such as variations in temperature, electronic gain noise, and radiation damage. The energy resolution parameters a and b, for ideal conditions are close to 1-2%. The angular resolution of a few mrad corresponds to resolution parameters $c \approx 3$ mrad and $d \approx 1$ mrad. Ideal conditions are apparently hardly ever met [26].

CsI(Tl) has an intrinsic efficiency for detecting photons of near 100%, losing only

a few MeV in energy. Detailed characteristics of CsI(Tl) crystals are provided in Table 2.3. A schematic of a wrapped CsI(Tl) crystal with a photograph of an unwrapped crystal illuminated by a lightbulb in shown in Figure 2.17.

Properties	CsI(Tl)
Radiation length (cm)	1.85
Molière Radius (cm)	3.6
Absorption Length for 5 GeV pions (cm)	41.7
Density (g/cm^3)	4.53
$dE/dx\|_{mip}$ (MeV/cm)	5.6
Light Yield (Photons/ MeV$\times 10^3$)	40-50
Light Yield Temperature Coef. (%/degC)	0.1
Peak Emission (nm)	565
Refractive Index at Emission Maximum	1.79
Decay Time (ns)	940
Hygroscopic	slight
Radiation Hardness (rad)	$10^3 - 10^4$

Table 2.3: Properties of Thallium-doped Cesium Iodide [24].

A schematic of the EMC layout and assembly is provided in Figures 2.15 and 2.16. The EMC has full coverage in the azimuthal and has a range of [15.8°, 141.8°] resulting in a coverage of solid-angle of 90% in the center-of-mass frame. Reconstruction distributions of the $\gamma\gamma$ invariant mass is provided in Figure 2.18.

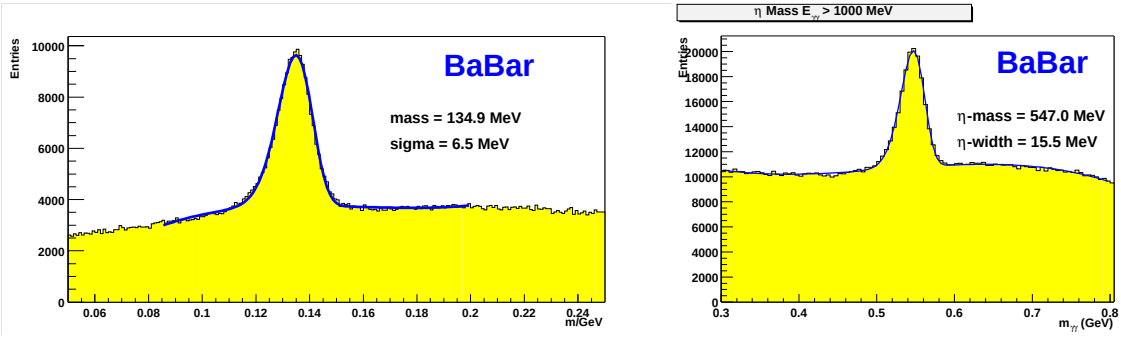

Figure 2.18: $\gamma\gamma$ invariant mass distributions of π^0 (left) and η (right) with the EMC [35].

2.8 Instrumented Flux Return

The instrumented flux return (IFR) is the last subsystem from the interaction point and is designed to identify muons and neutral hadrons (in tandem with the calorimeter), such as K_L^0 and neutrons over a wide range of momenta and angles. Muon detection is equally as important as electron detection in this analysis, in which the IFR detects muons to below 1 GeV. Our analysis requires the detection of muons in our control sample and in our signal mode reconstructions. The IFR is a large iron structure that secures the superconducting solenoid and was initially instrumented with Resistive Plate Chambers (RPCs) in the central part (barrel) and two plugs (endcaps), but eventually replaced with Limited Streamer Tubes (LSTs) in the barrel. The solid angle coverage of the IFR excludes 300 mrad in the forward direction and 400 mrad in the backward direction.

The IFR was initially segmented with 18 plates of iron, a total thickness of 65 cm in the barrel and 60 cm in the endcaps, surrounding the solenoidal coil and all other sub-detectors covering a total active area of approximately 2000 m^2. There are six barrel sectors (sextants) housing roughly 342 RPC/LST modules and four half end doors housing 432 RPC modules. The iron in the barrel and endcaps act as a flux return of the 1.5 T inner magnetic field. Between the gaps of the iron house RPCs operating in streamer mode. Eventually, the iron in the barrel was replaced with brass and instrumented with LSTs, due to the performance degradation of the RPCs. A novel feature of the *BABAR* IFR is that it has a graded segmentation of absorber (with the outer layer thickest) for better performance; muon identification at low momentum and K_L^0 detection. Below, we will discuss some of the specifications of the RPCs and LSTs.

2.8.1 Resistive-Plate Chambers

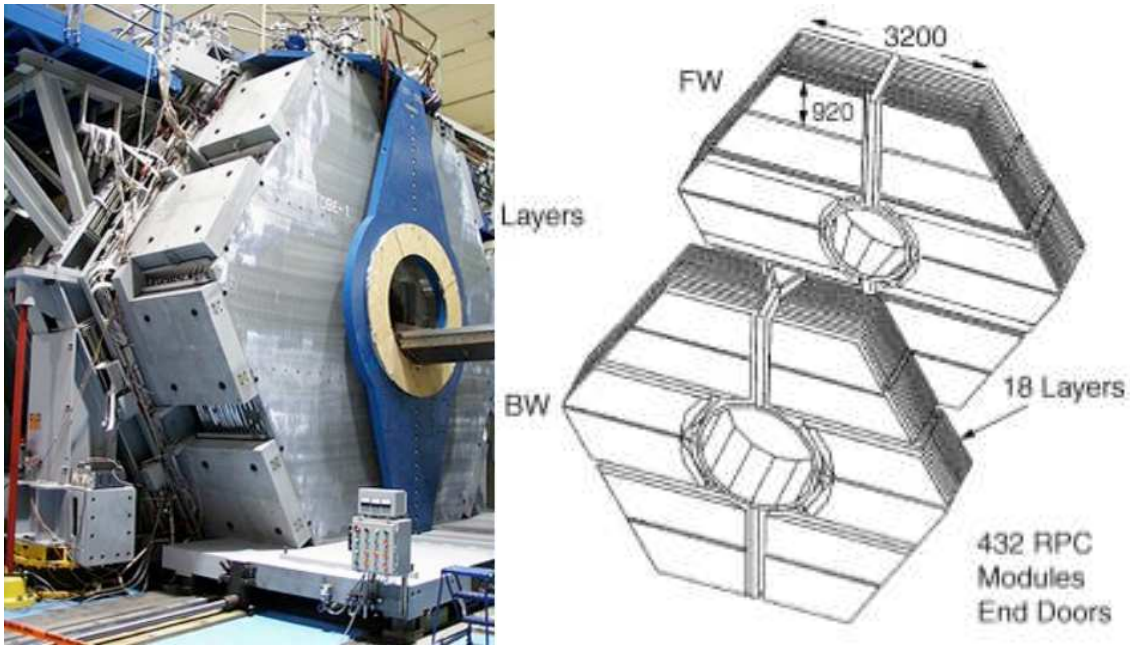

Figure 2.19: Photograph of IFR forward endcap (left) with schematic of the forward and backward endcap modules (right).

In the last days of running, only the forward and backward endcaps of the magnetic flux return were instrumented with resistive plate chambers (RPCs). RPCs detect streamers from ionizing particles in an active volume filled with a gas mixture of Argon, Freon 134A ($C_2H_2F_4$), and Isobutane with approximate ratios 57:39:5, respectively via capacitive couplings held at roughly 8000 V. Figure 2.19 (right) is a schematic of the forward and backward endcap structure. Figure 2.20 provides a schematic of the RPC module cross section. The cross section shows two bakelite (phenolic polymer) sheets, 2 mm-thick and separated by a gap of 2 mm filled with the gas mixture.

The RPC design is intended to create a uniform electric field permeating the gas mixture volume. As an ionizing particle traverses this medium, the liberated electrons create

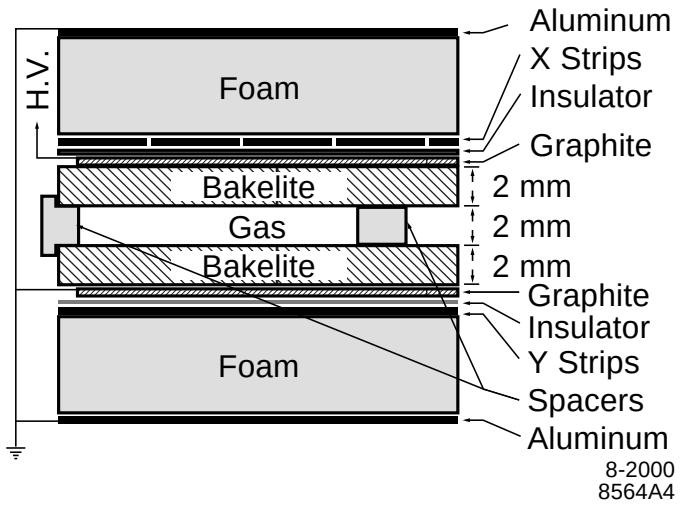

Figure 2.20: Typical RPC module cross section [26].

an avalanche of charge from nearby gas growing into a streamer, or electrical discharge. The potential change from the streamer is readout via the X-Y (horizontal and vertical) strips through a 2000 Ω resistor connected as an input to Front End readout Cards (FECs). The benefits of the this system is simple, low cost construction, the possibility of odd shape coverage with minimal dead space, large signals with fast response typically 1-2 ns. Each FEC can readout 16 channels each. From each FEC, the signals are sent to the Front End Electronics for further processing.

Relatively early within the start of the experiment, it was apparent that the IFR muon detection system was deteriorating rapidly, typically from 90% response to as low as 10% in some modules. Apparently, due to poor curing of the linseed oil intended to provide a smooth surface to create a uniform electric field within the gas mixture volume of the RPCs. The operating temperatures for *BABAR* in the IFR region resulted in defects

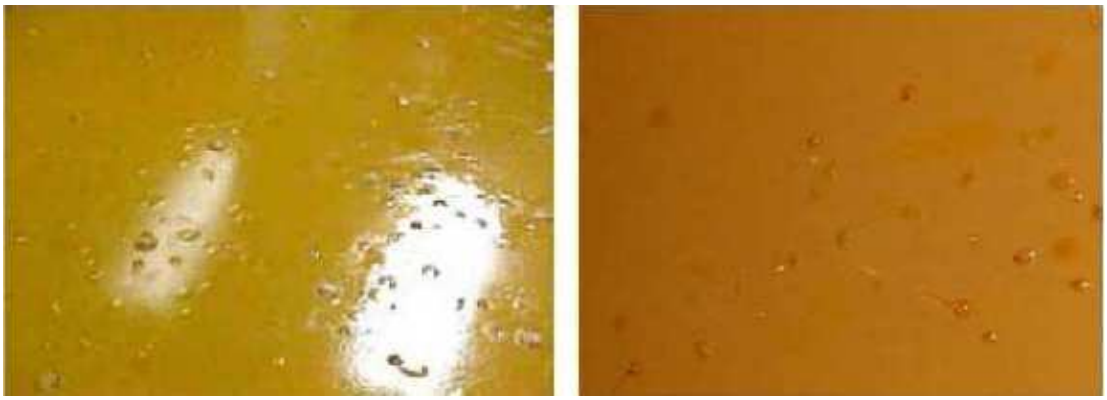

Figure 2.21: Photographs of linseed oil coating defects for high temperatures; cause of RPC degradation.

of the linseed oil coating creating increased dark current rates (electric discharges from non-smooth surfaces), see Figure 2.21. This eventually led to the decision to upgrade the barrel with limited streamer tube technology. The forward and backward endcaps remained as RPCs; the forward endcaps were retrofitted with new RPCs in 2002 with some modules operating in avalanche mode and backward endcaps left alone due to low response rates from the boost.

For service work at *BABAR* , I assisted Henry Band with converting the RPC front-end electronics cards (FEC) to readout avalanche mode operations. Streamer operation for the RPCs ran at a approximately 8000 V, while avalanche mode operations ran at approximately 9200 V. In the electronics readout, the FEC capacitance was increased to accommodate the larger avalanche signals from the gas response. My duties, required the change-out of hundreds of FECs for proper electronics readout. Other duties involved quality control of the FEC prior to installation and monitoring of occupancies after installation.

2.8.2 Limited Streamer Tubes

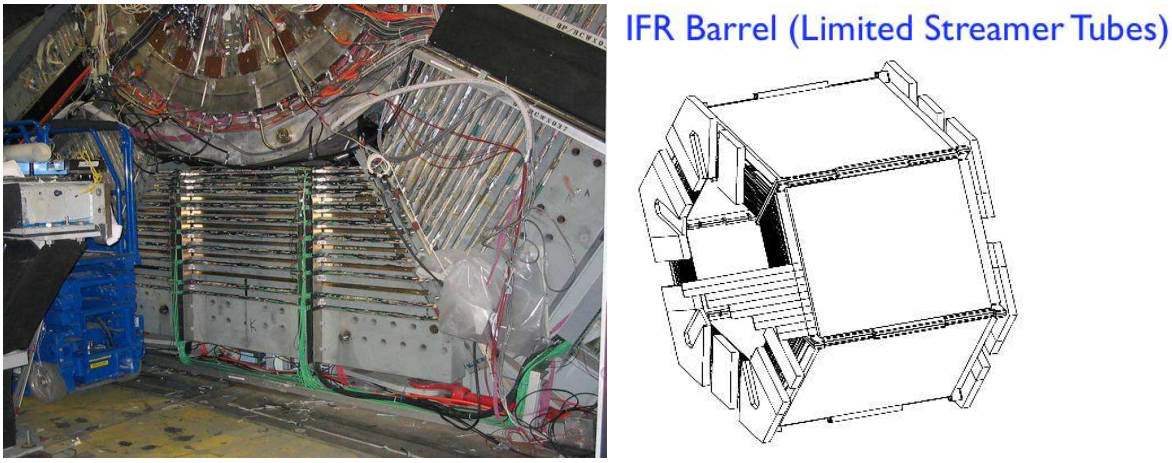

Figure 2.22: Photograph of Limited Streamer Tubes after installation in the IFR barrel (left) and schematic of full IFR barrel structure (right).

At the end of data collection, the barrel of the the IFR was fully instrumented with limited streamer tubes (LSTs). The upgrade was necessary due to degradation in efficiency of the original RPCs over time [36]. The replacement was done in two stages; in 2004, the top and bottom sextants (see left Figure 2.22); and in 2006, the rest of the barrel.

In the summer of 2006, I participated in the LST muon detector upgrade, therefore below is a brief summary of my duties. My first hands-on experience with high energy particle detectors involved participation in the z-plane fabrication, simply helping with laminating the Mylar foil. The next job involved labor intensive work, preparing the high voltage (HV) cables for transport from the Collider Hall (CEH) to the interaction region (IR II) where the *BABAR* detector was located. More labor intensive work involved help with coordinating the HV installation and connection to the LST modules, which involved running cables all throughout the *BABAR* structure. Other miscellaneous duties involved

help with fabrication and installation of gas tubes for the digital bubblers. For details of the LST module construction, please see Menges *et al.* [36].

After installation, the LST modules are no longer accessible, therefore strict quality control systems in all phases of the IFR upgrade were established. Components of the LST modules were fabricated in Italy, assembled at Princeton University and the Ohio State University, then installed at SLAC. For each phase of the trip, quality control tests were performed. Modules that failed were due to problems associated with flakes from graphite paint in the cells or impurities in the sense wire and were removed if it could not be repaired. HV conditioning tests were performed to insure currents did not exceed 500 nA for voltages between 4900-5900 V. HV channels were tested using single rates, our what were known as plateau curves; performing cosmic ray studies with HV intervals of 100 V, from 4900-5900 V, using 100 second intervals for each step, see Figure 2.23. Good modules were determined to have long and flat plateau response characteristics.

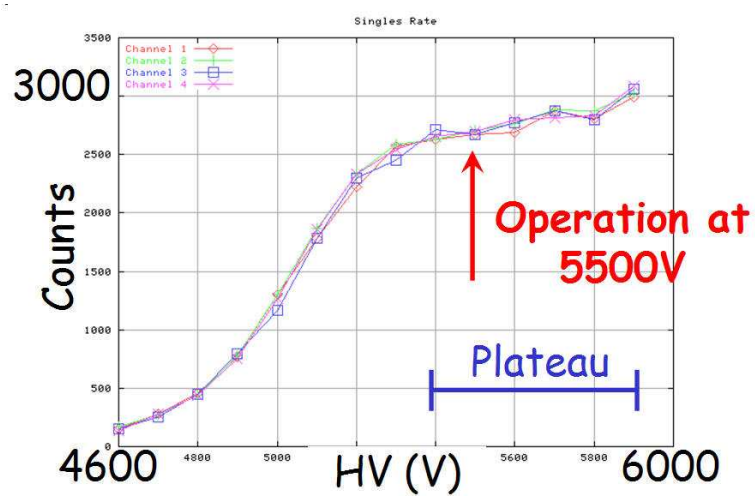

Figure 2.23: LST plateau curves for high voltage optimization [37].

The RPCs and iron were replaced with 12 layers of LSTs and 6 layers of brass. The brass compensated for any lose of absorption material after upgrade requirements where iron was removed. The LSTs consist of a PVC comb of eight cells with dimensions, 15 mm×17 mm, approximately 3.5 m long, encased in a PVC sleeve, with a 100 μm gold-plated beryllium-copper wire running down the center of each cell. Each cell of the comb is grounded, covered with graphite and the sense wire is generally held at 5500 V. The LST gas mixture consists of argon, isobutane, and carbon dioxide with a ratio of roughly 3:8:89, respectively [36] and operates in streamer mode. The signal is readout directly from the wires through AC-coupled electronics and from $z-$strips running perpendicular to the tubes, capacitively coupled to the wires.

A comparison of the RPC versus LST performance using the pion rejection rate and muon efficiency for two ranges of the muon momentum is given in Figure 2.24. This analysis uses a neural network based muon selection algorithm [36] As a charged particle

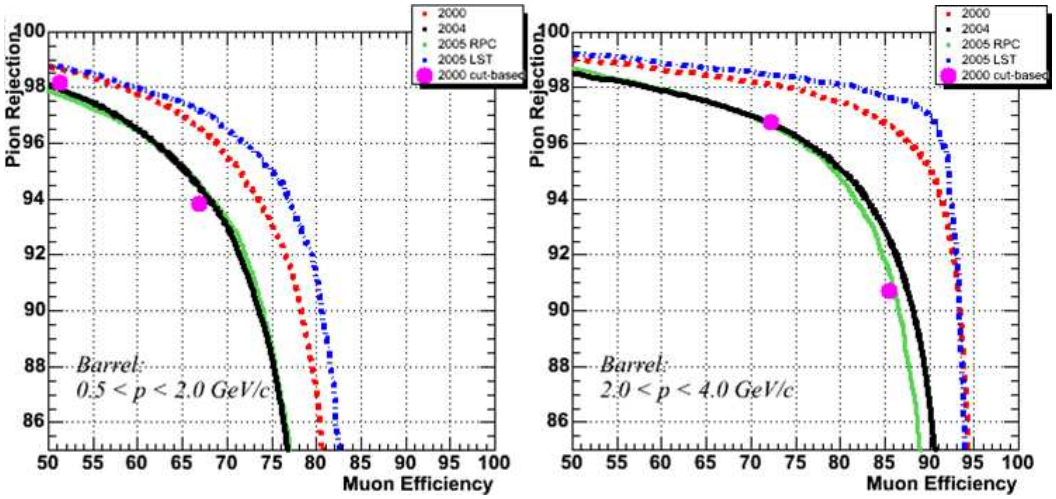

Figure 2.24: Comparison of IFR performance after LST upgrade [37].

moves through a gas-filled cell, a single wire set at 5500 V senses a streamer build up from the ionized gas. The readout from the wire allows for the ϕ direction measurement, while simultaneously a z-plane signal is induced, orthogonally situated. The ϕ and z coordinates coupled with the corresponding layer provide the 3D location hit in the track reconstruction. An image of the first muon track reconstructed, from cosmic ray data is shown in Figure 2.25.

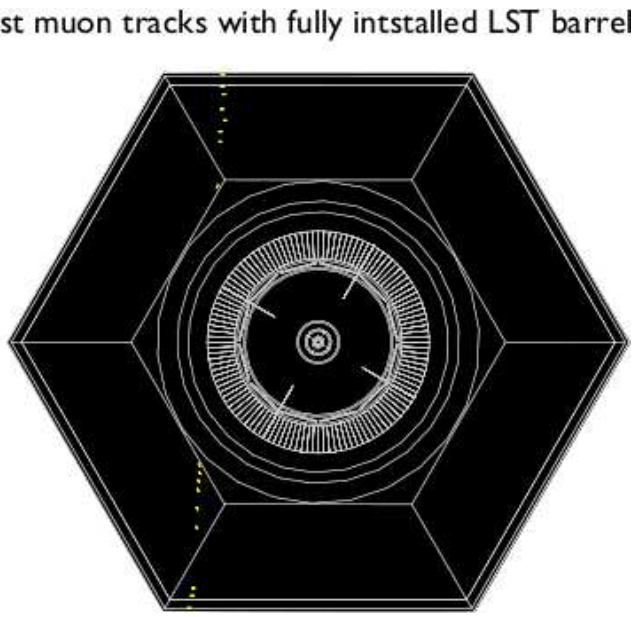

Figure 2.25: First muons of the new all limited streamer tube barrel.

2.9 Trigger and Data Acquisition

2.9.1 Trigger Level 1 and Level 3

The basic function of the trigger system is to select events of interest rejecting background, keeping the total event rate under 120 Hz for storage purposes, and contribut-

ing no more than 1% dead-time. There are two levels to the *BABAR* trigger: primarily from hardware Level 1 (L1) and software after event assembly Level 3 (L3). The L1 trigger is designed to achieve very high efficiency, with digitized signals coming directly from Front End Electronics (FEE) of the DCH, EMC, and IFR. The DCH is triggered if there are at least two tracks in an event: one long track with transverse momentum greater than 180 MeV and one short track with $p_t > 120$ MeV. The EMC is triggered if two clusters are both reconstructed with energy deposits above the the threshold efficient for muons. The two subsystem triggers allow for good independent cross-calibration of the trigger efficiency. The IFR trigger is designed to trigger on $\mu^+\mu^-$ and cosmic rays, mostly for diagnostic purposes.

A Global Level 1 Trigger (GLT) processes a summary of trigger objects on the position and energy of particles every 134 ns, ϕ-maps for the DCH and EMC triggers and hit topologies for the IFR trigger. This summary is passed to the Fast Control and Timing System (FCTS) for the final trigger decision. The total rate for this open trigger was simulated to be about 16 KHz at $\times 10$ nominal beam backgrounds, much greater than specification requirements of 2 KHz, with a fixed latency window of 11-12μs after an e^+e^- collision. The trigger rate can be reduced by requiring various other conditions which provides for a very robust triggering system. Cross sections, production rates, and trigger rates are provided in Table 2.4 [26].

The L3 trigger which runs on a unix based farm of commercial processors receives the output from the L1 trigger and reduces the event rate down to approximately 100 Hz with a flexible combination of tools to reduce backgrounds while keeping physics events. L3 identifies and flags the special events necessary for luminosity determination, diagnostics,

Event type $e^+e^- \rightarrow$	Cross section (nb)	Production Rate (Hz)	Level 1 Trigger Rate (Hz)
$b\bar{b}$	1.1	3.2	3.2
other $q\bar{q}$	3.4	10.2	10.1
e^+e^-	$\approx$53 [2]	159	156
$\mu^+\mu^-$	1.2	3.5	3.1
$\tau^+\tau^-$	0.9	2.8	2.4

Table 2.4: Cross sections, production and trigger rates for principle processes at 10.58 GeV with instantaneoud luminosity $3 \times 10^{33}\text{cm}^{-2}\text{s}^{-1}$.

and calibration purposes by refining and augmenting the L1 conditions. The L3 algorithms can require better DCH tracking (vertexing resolution) and EMC clustering filters. The L3 output information is lastly stored on tapes in collections which are retrieved later for high-level analysis by groups or users.

2.9.2 Data Acquisition

Data acquisition systems are responsible for transport of event data from the Front End Electronics to mass storage with minimum dead-time. For a layout of the data acquisition system, see Figure 2.26. For a detailed discussion of the *BABAR* data acquisition system, see [26, 27].

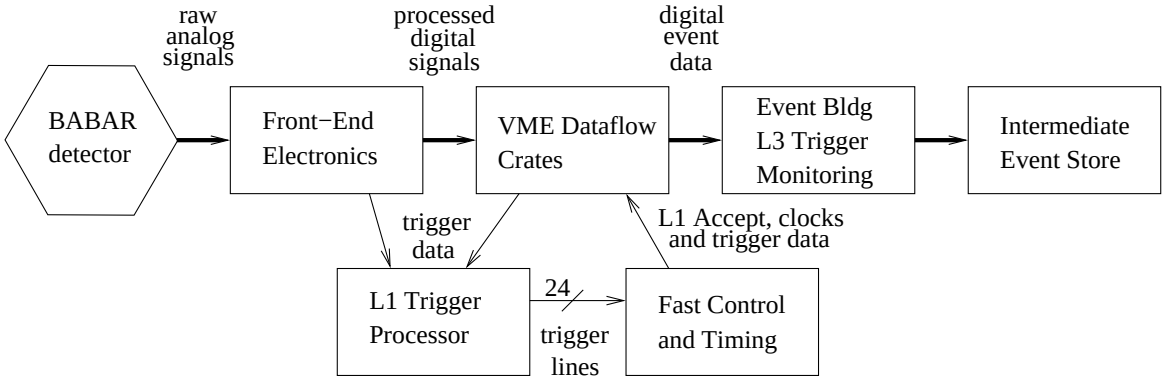

Figure 2.26: Layout of *BABAR* data acquisition system [26, 27].

Chapter 3

Analysis of $B^+ \to h^+\tau\ell$; $h = K, \pi$;

$\ell = e, \mu$

3.1 Overview

Assuming the existence of tree-level FCNCs and lepton flavor violation, the three-body $B^+ \to K^+\tau\mu(e)$ search will help constrain parameters between third and second (third and second/first) generations by either a measurement or setting an upper limit on the branching fraction, which is proportional to η_{bs}^4 ($\eta_{bs}^2\eta_{bd}^2$) assuming Sher & Yuan notation [16]. For the three-body $B^+ \to \pi^+\tau\mu(e)$ search, the third and first/second (third and first) generation couplings are constrained in the branching fraction, proportional to $\eta_{bs}^2\eta_{bd}^2$ (η_{bd}^4). Searches for decays $B^+ \to K^+\tau e$, $B^+ \to \pi^+\tau\mu$, and $B^+ \to \pi^+\tau e$ have never before been attempted.

We perform each analysis independently from $e^+e^- \to \Upsilon(4S) \to B^+B^-$ decays,

where one charged B-meson decay ($B_{\rm tag}$) is fully reconstructed from a large set of possible hadronic states. The $B_{\rm tag}$ meson is reconstructed in $B^- \to D^{(*)0}X^-$ modes; where $D^{(*)0}$ is reconstructed as $D^0\gamma$, $D^0\pi^0$, or D^0 and D^0 is reconstructed in the $K^-\pi^+$, $K^-\pi^+\pi^-\pi^+$, $K^-\pi^+\pi^0$, and $K^0_S\pi^+\pi^-$ channels. The K^0_S candidates are reconstructed in the $\pi^+\pi^-$ channel, while π^0 candidates are reconstructed in the $\gamma\gamma$ channel. X^- represents a system of charged and neutral hadrons where intermediate resonance states are ignored but constrained by combinatoric conditions: $n_1\pi^\pm$, $n_2K^\pm$, $n_3K^0_S$, and $n_4\pi^0$; where $n_1 + n_2 \leq 5$, $n_3 \leq 2$, and $n_4 \leq 2$; where the total charge must equal -1. In the *BABAR* collaboration, this is known as the B recoil technique [40]. In the rest of the $e^+e^- \to \Upsilon(4S) \to B^+B^-$ event, we require three track candidates presumably from the signal B decay.

In the $\Upsilon(4S)$ center-of-mass (CM) frame of reference, we fully reconstruct the τ invariant mass using information from the $B_{\rm tag}$ candidate and the kinematics of two other track candidates, with the hypothesis that the excluded track is from the τ decay. We use the reconstructed $B_{\rm tag}$ 3-momentum and replace the $B_{\rm tag}$ energy with a more precise CM beam energy of one beam ($E_{\rm beam}$), the measured 3-momenta of the h and ℓ tracks, and mass substituted energies for the h and ℓ candidates, to compute the τ invariant mass:

$$\begin{aligned}
\vec{p}_{B_{\rm sig}} &= -\vec{p}_{B_{\rm tag}} \\
\vec{p}_\tau &= \vec{p}_{B_{\rm sig}} - \vec{p}_h - \vec{p}_\ell \quad (h = K, \pi; \ell = e, \mu) \\
E_\tau &= E_{\rm beam} - E_h - E_\ell \\
m_\tau &= \sqrt{E_\tau^2 - \vec{p}_\tau^{\,2}}. \qquad (3.1)
\end{aligned}$$

Since our signal produces neutrinos only from the τ decay, we expect no missing energy if the τ invariant mass is properly reconstructed. We use particle identification selection criteria

to determine whether the track excluded in the τ invariant mass calculation is identified as an electron, muon, or charged pion. A cartoon of the $\Upsilon(4S) \to B_{\rm tag}B_{\rm sig}$ decay in the CM frame with possible track momenta is shown in Figure 3.1.

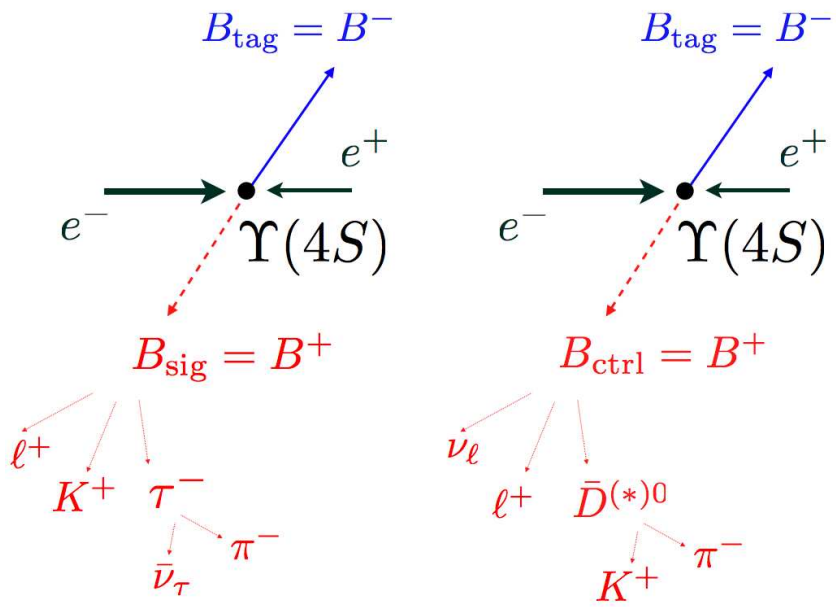

Figure 3.1: Cartoon of $e^+e^- \to \Upsilon(4S) \to B^+B^-$ decays for a signal (left) and control (right) mode in the $\Upsilon(4S)$ center-of-mass frame of reference.

Signal candidate events are categorized into three τ decay channels. In *BABAR* literature, these channels are known as "1-prong" τ decays: $\tau \to e\nu\nu$, $\tau \to \mu\nu\nu$, and $\tau \to (n\pi^0)\pi\nu$ where $n = 0, 1, 2, \&3$. A signal event candidate can also be categorized by accounting for the charge of the $B_{\rm tag}$ candidate and the charge of the primary lepton, defined as the lepton that presumably decayed directly from a signal B decay.

Since our signal searches transition through a charged B-meson resonance, continuum events from $e^+e^- \to q\bar{q}$; $q = u, d, s, \&c$ and $e^+e^- \to \tau^+\tau^-$ must be rejected. We compute an energy substituted mass for the $B_{\rm tag}$ candidate, again using the beam energy in the

CM frame of reference and the $B_{\rm tag}$ 3-momentum, such that $m_{\rm ES} = \sqrt{E^2_{\rm beam} - |\vec{p}_{\rm tag}|^2}$, which peaks at the B-meson invariant mass. A large component of $e^+e^- \rightarrow \Upsilon(4S) \rightarrow B^+B^-$ background for our signals come from semileptonic $b \rightarrow c$ transitions, where a neutral D-meson resonance is observed. To account for this background, we compute an invariant mass of two signal track candidates; one identified as a kaon with opposite sign charge as the charge of the $B_{\rm tag}$ candidate and one track with opposite sign charge as the kaon candidate - assumed to be a pion. A non-negligible source of B^+B^- background from a charmonium resonance is observed, from $B^+ \rightarrow c\bar{c}\ h^+$; $c\bar{c} \rightarrow \ell^+\ell^-$ decays, where $\ell = e$ or μ and $h = K$ or π depending on the signal search. The invariant mass of two oppositely charged tracks, assuming either both are electrons or muons is computed.

To reject additional combinatoric background, we compute a likelihood ratio from other discriminating variables, where a simple cut on each variable would be less than optimal. A likelihood ratio function combines inputs from lepton track particle identification quality, residual energies in the EMC, and an event shape topology variable to separate contunuum-like events from B^+B^- events. An optimization on the likelihood ratio is performed, using the average expected upper limit on the signal branching fraction as the optimization metric.

Our searches are performed using a cut-and-count strategy, where the event selection is optimized in an unbiased way. This is done by not looking at the data in the range where our signal search is expected to peak. In data, we ignore events in the range $m(\tau) \in [1.60, 1.95]\ GeV/c^2$ but not in our generated signal MC samples, where the signal is observed to peak. This technique is known as a blind analysis. To estimate the expected SM

background in the blinded data sample of a particular signal search, we use a data-driven technique. After applying all event selection requirements to our data and SM Monte Carlo samples, we compute the expected SM background in data by taking the product of the total number of events outside the $m(\tau)$ signal window in data and the ratio of the total number of events inside-to-outside the signal window using SM Monte Carlo as a function of the minimum likelihood ratio discriminant. After unblinding, any excess in the total number of events in the signal window from the expected SM background will tell us if a signal exist, or not.

The sensitivity of finding signal modes of these types can be determined using the event yield of a control sample ($B^- \to D^{(*)0}\ell^-\bar{\nu}$; $D^{*0} \to D^0(\gamma, \pi^0)$; $D^0 \to K^-\pi^+$; $\ell = e$ or μ) with identical, or nearly identical, final state signal topology. We avoid systematic uncertainties associated with event reconstruction of the signal and the control modes, since event selection requirements are similar. The D^0 resonance provides a nice clean reconstruction of our control mode. Since there is only one neutrino in the control mode decay, we can determine the 3-momentum of the neutrino in the CM frame from the kinematics of the $B_{\rm tag}$ candidate and the three other track candidates in the rest of the event, $\vec{p}\nu = \vec{p}_{\rm tag} - \vec{p}_K - \vec{p}_\pi - \vec{p}_\ell$. By assuming a massless neutrino, energy of the neutrino (E_ν) can be inferred. Again using the beam energy of one beam ($E_{\rm beam}$) in the CM frame - as a replacement of the $B_{\rm tag}$ energy, we can compute the difference in the energies of the rest of the event assuming the control mode is fully reconstructed using,

$$\Delta E^{(D\ell\nu)} = E_K + E_\pi + E_\ell + E_\nu - E_{\rm beam}. \tag{3.2}$$

A cartoon of the $\Upsilon(4S)$ decaying into a $B_{\rm tag}$ candidate and a control mode candidate in the

CM frame with possible kinematics is shown in Figure 3.1.

An unbinned maximum likelihood fit is performed on $\Delta E^{(D\ell\nu)}$ using data to determine the control mode event yield. A peak at zero in $\Delta E^{(D\ell\nu)}$ accounts for events from the $B^- \to D^0\ell^-\bar{\nu}$; $D^0 \to K^-\pi^+$; $\ell = e$ or μ decay. Events from $B^- \to D^{*0}\ell^-\bar{\nu}$; $D^{*0} \to D^0(\gamma, \pi^0)$; $D^0 \to K^-\pi^+$; $\ell = e$ or μ decays are observed to peak approximately 200 MeV below zero, due to missing energy from a γ or π^0 in the event.

3.2 Data and Monte Carlo Samples

The results presented in this analysis are based on the *BABAR* $\Upsilon(4S)$ on-resonance data sample, where the PEP-II asymmetric storage ring collides e^+e^- at the center-of-mass energy of 10.58 GeV, collecting a total integrated luminosity of $428.99 fb^{-1}$, during six phases of running (Runs 1-6) between October 1999 - September 2007. Simulated Monte Carlo samples help model expected standard model backgrounds while simulated signal Monte Carlo samples help optimize event selection. All event samples were processed using consistent environment conditions, in the *BABAR* analysis-51 Release 24 software package framework. A summary of the properties of our analysis samples consisting of the total number of events generated (N_{gen}), the detector cross-sections (σ), the equivalent total integrated luminosities ($\mathcal{L}$), and the scale factors to properly compare simulated standard model MC samples with data are given in Table 3.1.

Sample	$N_{gen}(M)$	$\sigma(nb)$	Equiv $\mathcal{L}(fb^{-1})$	scale factor
Generic B^+B^-	708.762	0.55	1288.66	0.3329
Generic $B^0\bar{B}^0$	717.995	0.55	1305.45	0.3286
Generic $c\bar{c}$	1128.544	1.30	868.11	0.4942
Generic $q\bar{q}$; $q = u, d, \& s$	1618.347	2.09	774.33	0.5540
Generic $\tau^+\tau^-$	680.713	0.90	756.35	0.5672
$B^\pm \to K^\pm\tau\mu$, $B_{\rm tag}$ Generic	5.769	-na-	-na-	-na-
$B^\pm \to K^\pm\tau e$, $B_{\rm tag}$ Generic	6.449	-na-	-na-	-na-
$B^\pm \to \pi^\pm\tau e/\mu$, $B_{\rm tag}$ Generic	11.630	-na-	-na-	-na-
$B^\pm \to \pi^\pm\tau e/\mu$, $B_{\rm tag}$ Cocktail	0.429	-na-	-na-	-na-
$B^\pm \to K^\pm\tau e/\mu$, $B_{\rm tag}$ Cocktail	0.429	-na-	-na-	-na-
$B^\pm \to D^{(*)0}\ell\nu$, $B_{\rm tag}$ Cocktail	0.812	-na-	-na-	-na-
On-resonance data	6711.96	-na-	428.99	1.0000

Table 3.1: Properties of analysis samples: on-resonance data, standard model MC, signal mode MC, and control mode MC. Generic samples decay via known SM processes. Cocktail samples are generated with a mix of hadronic SM processes in order to enhance the *BABAR* B-tagging algorithm yield.

3.3 Reconstruction and Event Selection

3.3.1 $B_{\rm tag}$ pre-selection skim

The analysis technique for our signal searches require a $B_{\rm tag}$ candidate be fully reconstructed. Using the B recoil technique, tagged B-meson candidates that decay hadronically (discussed earlier) are reconstructed using the *BABAR* `BSemiExcl` software skim package [40]. Because of combinatoric reconstruction, multiple $B_{\rm tag}$ candidates are possible. Each $B_{\rm tag}$ candidate is ranked by mode reconstruction purity, where the best $B_{\rm tag}$ candidate with the highest mode purity is chosen. If more than one candidate has the same mode purity, the $B_{\rm tag}$ candidate with $\Delta E = E_{\rm tag} - E_{\rm beam}$ closest to zero is chosen. The event yield after skimming for the $B_{\rm tag}$ reconstruction is provided in Table 3.2. Later, we explicitly require the $B_{\rm tag}$ mode purity to be greater than 10% for all signal and control mode reconstructions. To ensure the $B_{\rm tag}$ 3-momentum is properly reconstructed, we use

Sample	$N_{skim}(M)$	Skim efficiency (%)
Generic B^+B^-	50.159	7.1
Generic $B^0\bar{B}^0$	44.793	6.2
Generic $c\bar{c}$	64.583	5.7
Generic $q\bar{q}$; $q = u, d, \& s$	54.772	3.4
Generic $\tau^+\tau^-$	0.132	$\approx$0.0
$B^\pm \to K^\pm\tau\mu$, $B_{\rm tag}$ Generic	0.257493	4.5
$B^\pm \to K^\pm\tau e$, $B_{\rm tag}$ Generic	0.242980	3.8
$B^\pm \to \pi^\pm\tau e/\mu$, $B_{\rm tag}$ Generic	0.427613	3.7
$B^\pm \to \pi^\pm\tau e/\mu$, $B_{\rm tag}$ Cocktail	0.087539	20.4
$B^\pm \to K^\pm\tau e/\mu$, $B_{\rm tag}$ Cocktail	0.087734	20.5
$B^\pm \to D^{(*)0}\ell\nu$, $B_{\rm tag}$ Cocktail	0.161571	19.9
On-resonance data	97.592	1.5

Table 3.2: Summary of B-tagging yields after *BABAR* hadronic skimming algorithm applied to analysis samples: on-resonance data, standard model MC, signal mode MC, and control mode MC. Generic samples decay via known SM processes. Cocktail samples are generated with a mix of hadronic SM processes in order to enhance the *BABAR* B-tagging algorithm yield.

a truth matching technique in MC to estimate the percentage of miss reconstructed tagged B-mesons and assume the same percentage in data.

The $B_{\rm tag}$ track reconstruction quality requires a track candidate have a distance of closest approach of 2.5 cm within the beam pipe (z-axis) and 1.5 cm within the transverse plane (xy-plane) of the IP. The track minimum transverse momentum is 0.05 GeV/c, with maximum momentum less than 10 GeV/c. Radiated photons from bremsstrahlung processes are recovered by adding the *BABAR* software package `CompositionSequences/CompHllSequence` to our analysis framework. Studies on kinematic variables involving electron candidates with bremsstrahlung recovery resulted in better performance.

3.3.2 Signal-side track reconstruction

Recall at the end of section 3.3.1, the requirements on the B_{tag} track quality. For our signal B-meson track candidates, we require the same level of track quality for three track candidates not overlapping B_{tag} tracks. We account for extra track candidates that pass weaker track quality requirements, and consider them later in event selection as track multiplicity. If only three signal-side track candidates pass at the weaker track quality requirement, we do not consider additional tracks in the event. This redundancy allows for possible improvements in signal efficiency.

3.3.3 General preselection

We perform four independent signal searches; two where the primary hadron is a kaon ($B^+ \to K^+\tau\ell$) and two where the primary hadron is a pion ($B^+ \to \pi^+\tau\ell$); each with $\ell = e$ or μ. After processing all event samples for B_{tag} reconstruction, a general preselection is performed. We require the following, for all signal searches:

- Skip any event if the charges of the best reconstructed B_{tag} candidate and reconstructed B_{sig} candidate are the same, where the B_{sig} charge is the net charge of our three signal-side tracks.

- Reject any event where the best B_{tag} charge is neutral.

- Reject any event if the B_{sig} candidate has a charge magnitude of 3.

- Require all best B_{tag} candidates have mode purity greater than 10% [19].

In sections 3.3.4 and 3.3.5, we discuss additional preselection criteria specific to the $B^- \to K^-\tau\ell$ and $B^- \to \pi^-\tau\ell$ ($\ell = e$ or μ) analyses, respectively. The signal-side track assignments require two fundamentally different particle mass assignment algorithms. Table 3.3 provides a mini glossary of terminology used throughout this paper for reference.

Table 3.3: Mini Glossary of Terminology:

primary	track identified to originate from $B_{\rm sig}$, not from τ
secondary	track identified to originate from τ, not from $B_{\rm sig}$
$Q_{\rm sig}$	charge of $B_{\rm sig}$ candidate
$Q_{\rm tag}$	charge of $B_{\rm tag}$ candidate
Q_ℓ	charge of primary lepton candidate
same-sign	charge relative to $B_{\rm sig}$ candidate
opposite-sign	
trkss1	randomly chosen, first of two possible tracks with the same-sign as $Q_{\rm sig}$
trkss2	randomly chosen, second of two possible tracks with same-sign as $Q_{\rm sig}$
trkos	only signal-side track candidate with opposite-sign as $Q_{\rm sig}$

3.3.4 Kaon signal modes - preselection and τ channel categorization

Additional preselection requirements for the $B^+ \to K^+\tau\mu$ and $B^+ \to K^+\tau e$ analyses are summarized below:

- The signal $K^\pm$ candidate must have the opposite charge of the $B_{\rm tag}$ candidate.
- There must be exactly two tracks that are not the signal $K^\pm$ or $B_{\rm tag}$ tracks, with net charge equal to zero.
- One of the non-kaon tracks must be identified as a muon in the $B^+ \to K^+\tau\mu$ analysis or an electron in the $B^+ \to K^+\tau e$ analysis.

Considering charge combinatorics of our three signal-side track candidates, the best signal kaon candidate is chosen to have the highest *BABAR* kaon particle identification

quality. If two tracks with the same-sign charge have equivalent kaon PID quality, the track with the lower lab frame momentum is assigned our best kaon candidate, which resulted in better signal purity reconstruction [19].

The primary lepton candidate, coming directly from a signal B decay, must be identified from one of the two remaining tracks. For the $B^+ \to K^+\tau\mu$ analysis, if only one of these two tracks is identified as a muon, then the primary lepton is this track. If both remaining tracks are identified as muons, then we assign primary and secondary lepton tracks based on the combination that gives a reconstructed τ invariant mass closest to 1.777 GeV/c^2 [39]. For the $B^+ \to K^+\tau e$ analysis, we follow a similar recipe.

Once the kaon and primary lepton candidates are assigned, we need to determine the mass identity of the track excluded in the τ invariant mass calculation. The excluded track is presumably from the τ decay. The "1-prong" τ decay channels are categorized here. By default, the τ track candidate is assumed to be a pion, categorizing the event into the $\tau \to \pi(n\pi^0)\nu$ channel. We re-assign the event to the $\tau \to e\nu\nu$ channel if the τ track candidate can be identified as an electron. If the τ track is not identified as an electron, we check if it can be identified as a muon. If it is identified as a muon, then the event is re-assigned into the $\tau \to \mu\nu\nu$ channel.

3.3.5 Pion signal modes - preselection and τ channel categorization

Additional preselection for the $B^+ \to \pi^+\tau\mu$ and $B^+ \to \pi^+\tau e$ analyses is discussed below:

- Skip any event if *both* track candidates, with the same-sign charge as the $B_{\rm sig}$ candi-

date, are identified as muons for the $B^+ \to \pi^+\tau\mu$ analysis. Two same-sign muons are not allowed for our signal reconstruction. One same-sign pion track must be in the $B_{\rm sig}$ reconstruction. For the $B^+ \to \pi^+\tau e$ analysis, likewise, two same-sign electron tracks must also be skipped.

- Skip any event if none of the three signal tracks can be identified as a muon (electron) for the $B^+ \to \pi^+\tau\mu(e)$ analysis. There must be a lepton in the signal-side track reconstruction.

The algorithm for making signal-side track assignments in the $B^+ \to \pi^+\tau\ell$ analyses is different from the signal kaon mode reconstruction because of a second pion from hadronic $\tau \to \pi(n\pi^0)\nu$ decays. Consider, as an example, signal-side track assignments in the $B^- \to \pi^-\tau\mu$ search. First, we isolate the primary muon in the event by assuming its charge has the same-sign as the $B_{\rm tag}$ charge. The charge configuration may look like $B^- \to \pi^-\tau^-\mu^+; B^+_{\rm tag}$, note $Q_\mu = Q_{\rm tag}$. For this configuration, the τ daughter track must be negative. If this is the case, we can reconstruct the signal in three different combinations:

- $\pi^-e^-\mu^+$ - by requiring only one track candidate be identified as an electron with the same-sign charge as the $B_{\rm sig}$ candidate and requiring the remaining track candidate not be identified as a muon nor an electron. These events are assigned to the $\tau \to e\nu\nu$ decay channel. The track with opposite-sign charge as the $B_{\rm sig}$ charge is therefore identified as the primary muon.

- $\pi^-\mu^-\mu^+$ - by requiring only one same-sign track candidate be identified as a muon and again requiring the remaining same-sign track not be identified as a muon nor an electron. The remaining same-sign track must be the primary pion. Events passing

these criteria are assigned to the $\tau \to \mu\nu\nu$ decay channel. Since two muons with opposite charge are reconstructed in this channel, the primary and secondary muon track assignment is decided using the combination which give a reconstructed τ invariant mass closest to 1.777 GeV/c^2 [39].

- $\pi^-\pi^-\mu^+$ - if neither same-sign track candidates are identified as leptons, then the positively charged muon candidate must be the primary muon from the signal B decay. Therefore, we assume both same-sign track candidates are pions. Because there are two pions in the event, our primary pion is again decided using the combination with reconstructed τ invariant mass closest to 1.777 GeV/c^2. These events are assigned to our signal $\tau \to (n\pi^0)\pi\nu$ decay channel.

If the track candidate with opposite-sign charge as the B_{sig} charge is not identified as a muon and only one same-sign track candidate is identified as a muon, then we assign the same-sign track as the primary muon ($B^- \to \pi^-\tau^+\mu^-$). The track with opposite-sign charge as the B_{sig} charge must be assumed to come from the τ decay, because of charge conservation. If instead the track with opposite-sign charge as the B_{sig} charge is identified as an electron, the final state combinatorics should look like $\pi^-e^+\mu^-$ and the event is dumped into the $\tau \to e\nu\nu$ channel. If the opposite-sign track and the remaining same-sign track fail to be identified as leptons, then we assume the final state combinatorics should look like $\pi^-\pi^+\mu^-$. This event is dumped into the $\tau \to \pi(n\pi^0)\nu$ channel, where the remaining same-sign track is assigned to be the primary pion.

Table 3.4 provides a summary of preselection signal MC efficiencies and standard model MC background yields.

Sample	$K^-\tau e$	$K^-\tau\mu$	$\pi^-\tau e$	$\pi^-\tau\mu$
$N_{\rm gen}$	6.449 M	5.768 M	5.815 M	5.815 M
$N_{\rm pre}$	10247	10479	12643	7872
$\epsilon_{\rm tag} \times \epsilon_{\rm sig}$	0.159%	0.182%	0.217%	0.135%
$N_{\rm B^+B^-}$	63921	96649	152506	94110
$N_{\rm B^0\bar{B}^0}$	10121	19923	44947	26114
$N_{\rm uds}$	9703	73742	46271	46684
$N_{\rm c\bar{c}}$	28263	106201	98091	71233
$N_{\tau^+\tau^-}$	54	85	572	153
$N_{\rm BG}$	112062	296600	342387	238294

Table 3.4: Signal efficiencies and Monte Carlo background yields after preselection. Generic background MC yields are luminosity weighted.

3.3.6 Separating backgrounds by semileptonic B and D decays

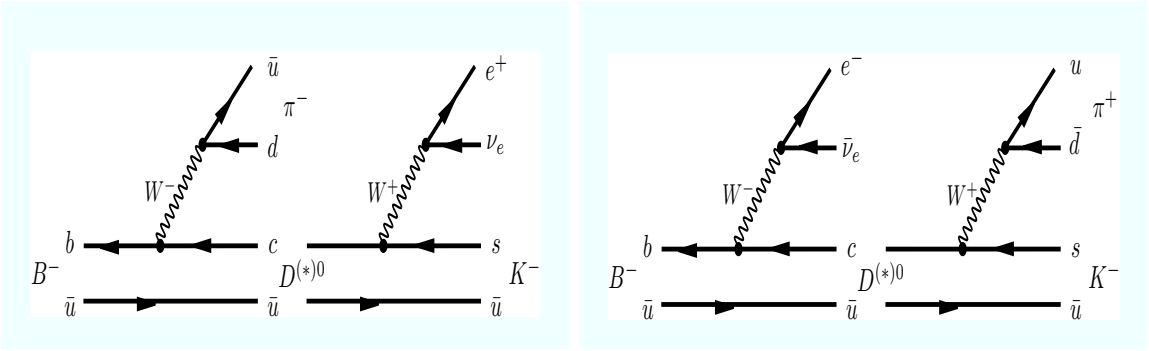

Figure 3.2: Left - Standard Model background from semileptonic charm decays: $B^- \to D^{(*)0}\pi^-; D^{(*)0} \to K^- e^+ \nu_e$. Right - Standard Model background from semileptonic bottom decays: $B^- \to D^{(*)0} e^- \bar{\nu}_e; D^{(*)0} \to K^-\pi^+$.

We can use the primary lepton and $B_{\rm tag}$ charge correlations of a signal B decay to help further categorize backgrounds coming from B^+B^- processes, for each signal search. By careful examination of Feynman diagrams of dominant background decay processes, shown in Figure 3.2, we notice we can exploit the correlation between the primary lepton charge (Q_ℓ) and $B_{\rm tag}$ charge ($Q_{\rm tag}$) to separate background contributions via semileptonic

B decays and semileptonic D decays. Notice in Table 3.5, background from the hadronic decay $B^- \to D^0\pi^-; B^+_{\rm tag}$, where the D^0 decays semileptonically, requires the charges of the lepton and $B_{\rm tag}$ candidates be the same ($Q_\ell = Q_{\rm tag}$). Likewise, for background from the semileptonic B decay $B^- \to D^0\ell^-\bar{\nu}_\ell; B^+_{\rm tag}$ where the D^0 decays hadronically, the charges of the lepton and $B_{\rm tag}$ candidates require $Q_\ell = -Q_{\rm tag}$. Therefore, each signal search can be broken into six independent search channels; based on the "1-prong" τ decays and also on the charge of the τ candidate, relative to the charge of the $B_{\rm sig}$, or $B_{\rm tag}$, candidate. Explicitly, if the charge of the $B_{\rm sig}$ candidate is negative, we isolate our search parameters into the six channels: $\tau^- \to e^-\nu\nu$, $\tau^- \to \mu^-\nu\nu$, $\tau^- \to \pi^-\nu$, $\tau^+ \to e^+\nu\nu$, $\tau^+ \to \mu^+\nu\nu$, and $\tau^+ \to \pi^+\nu$.

$B^\pm \to \pi^\pm\tau\ell$	Dirty: $Q_\ell = Q_{\rm tag}$	Clean: $Q_\ell = -Q_{\rm tag}$
Signal:	$B^- \to \pi^-\tau^-\ell^+; B^+_{\rm tag}$	$B^- \to \pi^-\tau^+\ \ell^-; B^+_{\rm tag}$
Background:	semileptonic D decay	semileptonic B decay
	$B^- \to D^0\pi^-; B^+_{\rm tag}$	$B^- \to D^0\ell^-\bar{\nu}_\ell; B^+_{\rm tag}$
	$D^0 \to K^-\ell^+\nu_\ell$	$D^0 \to K^-\pi^+$

Table 3.5: Example of signal primary lepton & $B_{\rm tag}$ charge configurations, relative to backgrounds from semileptonic B & D decays.

Figure 3.3 provides an example of invariant mass distributions of kaon and pion tracks with opposite charge for the $B^+ \to \pi^+\tau e;\ B^-_{\rm tag};\ \tau^\pm \to \pi^\pm\nu$ channels. On the left (right), we require $Q_e = Q_{\rm tag}$ ($Q_e = -Q_{\rm tag}$). The top distributions are stacked histograms of luminosity-weighted SM background MC samples overlapped with on-resonance data, while the bottom distributions are signal histograms from our $B^\pm \to \pi^\pm\tau e/\mu$ Monte Carlo sample. Notice a large D^0 resonance in the SM distributions when $Q_\ell = -Q_{\rm tag}$ (top right Figure 3.3) at $m(K\pi)$=1.86 GeV. If we remove events below 1.95 GeV (slightly above the D^0 resonance),

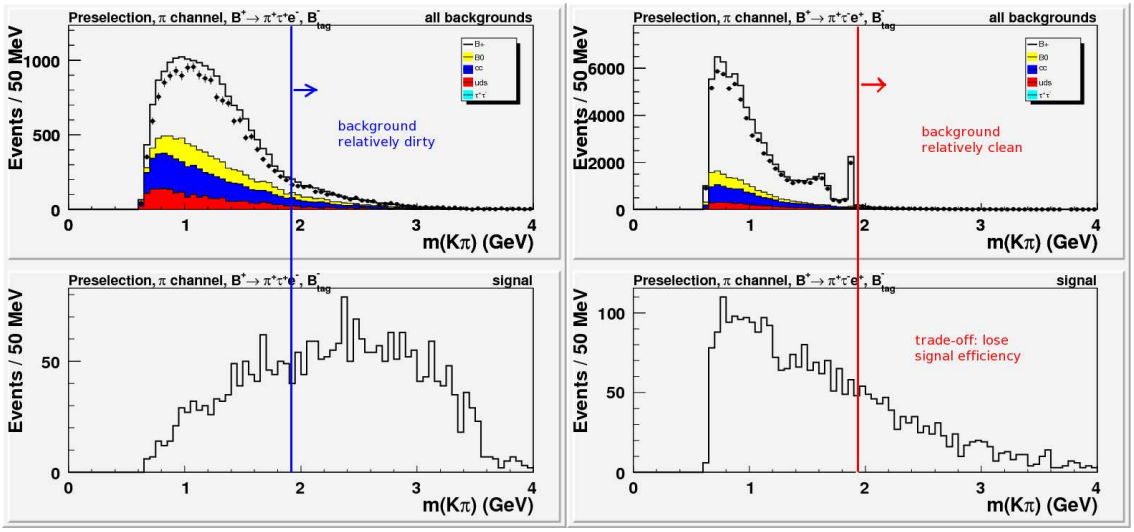

Figure 3.3: Background (top) and signal (bottom) $m(K\pi)$ distributions for the $B^{\pm} \to \pi^{\pm}\tau e$ analysis, after requiring $Q_e = Q_{\rm tag}$ (left) and $Q_e = -Q_{\rm tag}$ (right) for the $\tau \to \pi(n\pi^0)\nu$ channel only. Just above the D^0 resonance in the background distributions are indicated at 1.95 GeV with a solid blue (red) line for the "dirty" ("clean") channel.

a huge amount of background is removed, and compared to the remaining $Q_\ell = Q_{\rm tag}$ background, is relatively "clean." For the rest of this paper, we refer to distributions requiring $Q_\ell = -Q_{\rm tag}$ as "clean" and $Q_\ell = Q_{\rm tag}$ as "dirty", likewise these backgrounds contain semileptonic B decays and semileptonic D decays, respectively.

Furthermore, we observe in the signal MC distributions for the $\tau^{\pm} \to \pi^{\pm}\nu$ channels, while requiring $Q_\ell = -Q_{\rm tag}$ is "clean" in terms of background reduction, the trade-off is a loss in signal efficiency after removing events below 1.95 GeV, as seen in Figure 3.3. Table 3.6 provides a breakdown of the signal efficiencies after requiring the Q_ℓ and $Q_{\rm tag}$ correlations. Note that $N_{\rm rec}^{\rm (sig)}$ represents the number of signal events passing the $B_{\rm tag}$ reconstruction, while $N_{m(K\pi)}^{\rm pre}$ represents the number of signal events passing preselection, $B_{\rm tag}$ $m_{\rm ES} > 5.27$ GeV, $B_{\rm tag}$ mode purity $> 10\%$, but before the $m(K\pi) > 1.95$ GeV

($N^{\rm post}_{m(K\pi)}$ after $m(K\pi) > 1.95$ GeV) requirements. $\epsilon^{\rm (sig)}_{\rm rel}$ is the relative efficiency defined as ratio of signal efficiencies before and after the $m(K\pi) > 1.95$ GeV requirement. These event selection variables are discussed further in the following section 3.3.8

	"clean" $Q_\ell = -Q_{\rm tag}$				"dirty" $Q_\ell = Q_{\rm tag}$			
Sample	$K\tau e$	$K\tau\mu$	$\pi\tau e$	$\pi\tau\mu$	$K\tau e$	$K\tau\mu$	$\pi\tau e$	$\pi\tau\mu$
$N^{\rm (sig)}_{\rm rec}$	15677	14429	13313	13702	12659	12541	11734	12471
$N^{\rm pre}_{m(K\pi)}$	3988	4079	2129	2586	4105	4022	1894	2678
$N^{\rm post}_{m(K\pi)}$	1453	1461	737	825	2529	2521	1236	1939
$\epsilon^{\rm pre}_{m(K\pi)}$	25.4%	28.3%	16.0%	18.9%	32.4%	32.1%	16.1%	21.5%
$\epsilon^{\rm post}_{m(K\pi)}$	9.3%	10.1%	5.5%	6.0%	20.0%	20.1%	10.5%	15.5%
$\epsilon^{\rm (sig)}_{\rm rel}$	36.6%	35.7%	34.4%	31.7%	61.7%	62.6%	65.2%	72.1%

Table 3.6: Signal efficiency breakdown after requiring Q_ℓ and $Q_{\rm tag}$ correlations, with event selection.

Table 3.7 provides a breakdown of background yields after requiring Q_ℓ and $Q_{\rm tag}$ correlations. Note that $N^{\rm pre}_{\rm xxx}$ represents the number of Generic luminosity weighted `xxx` MC events passing preselection, $B_{\rm tag}$ $m_{\rm ES} > 5.27$ GeV, $B_{\rm tag}$ mode purity $> 10\%$, but before the $m(K\pi) > 1.95$ GeV ($N^{\rm post}_{\rm xxx}$ after $m(K\pi) > 1.95$ GeV) requirements. $N^{\rm pre}_{\rm BG}$ represents the combined number of background `xxx` MC events. The $\epsilon^{\rm (BG)}_{\rm rel}$ represents relative efficiency, defined as $N^{\rm post}_{\rm BG}/N^{\rm pre}_{\rm BG}$. A pseudo-purity ($\epsilon^{\rm post}_{m(K\pi)}/N^{\rm post}_{\rm BG}$) is computed using $\epsilon^{\rm post}_{m(K\pi)}$ in Table 3.6. No significant benefit between "clean" and "dirty" pseudo-purity is suggested.

3.3.7 Blinding technique

Event selection is optimized in this analysis, by blinding, or ignoring events with the invariant mass of the τ in the range [1.60,1.95] GeV, from all samples. One exception is made in the $m(\tau)$ background MC distributions, which is needed to help estimate the

	"clean" $Q_\ell = -Q_{\rm tag}$				"dirty" $Q_\ell = Q_{\rm tag}$			
Sample	$K\tau e$	$K\tau\mu$	$\pi\tau e$	$\pi\tau\mu$	$K\tau e$	$K\tau\mu$	$\pi\tau e$	$\pi\tau\mu$
$N^{\rm pre}_{\rm B^+B^-}$	32088	38929	68844	43777	9829	17362	18095	10191
$N^{\rm pre}_{\rm B^0\bar{B}^0}$	1269	2142	6382	3794	900	1706	3587	2034
$N^{\rm pre}_{\rm uds}$	683	6210	4585	4830	878	5490	2838	2542
$N^{\rm pre}_{\rm c\bar{c}}$	2304	8355	9383	7009	1851	7579	5131	3587
$N^{\rm pre}_{\tau^+\tau^-}$	3	7	56	24	5	11	32	12
$N^{\rm pre}_{\rm BG}$	36347	55643	89250	59434	13463	32148	29683	18366
post $m(K\pi) > 1.95$ GeV								
$N^{\rm post}_{\rm B^+B^-}$	138	370	503	476	301	578	1809	1330
$N^{\rm post}_{\rm B^0\bar{B}^0}$	9	37	47	36	78	129	510	383
$N^{\rm post}_{\rm uds}$	80	1022	385	489	92	868	310	504
$N^{\rm post}_{\rm c\bar{c}}$	153	771	440	399	159	722	582	565
$N^{\rm post}_{\tau^+\tau^-}$	1	2	5	8	0	5	7	5
$N^{\rm post}_{\rm BG}$	381	2202	1380	1408	630	2302	3218	2787
$\epsilon^{\rm BG}_{\rm rel}(\%)$	1.0	4.0	1.5	2.4	4.7	7.2	10.8	15.2
pseudo-purity								
$\epsilon^{\rm post}_{m(K\pi)}/N^{\rm post}_{\rm BG}$ (%)	0.024	0.005	0.004	0.004	0.032	0.009	0.003	0.006

Table 3.7: Breakdown of background yields after requiring Q_ℓ and $Q_{\rm tag}$ correlations, with event selection. The pseudo-purity suggests no significant benefit between "clean" and "dirty" channels.

ratio of events inside-to-outside the signal region. This is the only time when the cut is not made.

3.3.8 Summary of event selection

In the following, we define the final event selection parameters and requirements specific to each signal search, for each τ decay channel. Distributions comparing on-resonance data overlaid with luminosity weighted background MC and signal MC samples are placed in the Appendix, for all six channels, where the top-two rows represent $Q_\ell = -Q_{\rm tag}$, or "clean" modes, and the bottom-two rows represent $Q_\ell = Q_{\rm tag}$, or "dirty"

modes. To the left are the $\tau^{\pm} \to e^{\pm}\nu\nu$ channels, in the middle are the $\tau^{\pm} \to \mu^{\pm}\nu\nu$ channels, and to the right are the $\tau^{\pm} \to \pi^{\pm}(n\pi^0)\nu$ channels. All signal searches require the following event selection:

- preselection
- $m(K\pi) > 1.95$ GeV - keeps possible signal events only slightly above the D^0 resonance.
- $c\bar{c}$ vetoes (on appropriate channels) - removes events in the range $m(\ell^+\ell^-) \in [3.03, 3.14]$ GeV and $m(\ell^+\ell^-) \in [3.60, 3.75]$ GeV with $\ell = e$ or μ around the $J/\psi(1S)$ and $\psi(2S)$ resonances, respectively.
- γ-conversion vetoes on the $h\tau e$ modes (electron and pion channels only) - excludes $\gamma \to e^+e^-$ conversions in matter, by keeping events with $m(e^+e^-) > 0.10$ GeV.
- $B_{\rm tag}$ $m_{\rm ES} > 5.27$ GeV - removes most of the continuum background, focusing on events that transition through $\Upsilon(4S) \to B\bar{B}$.
- kaon and proton PID vetoes - removes events if any signal-side track is identified as a proton and removes events if any of the two non primary hadron track candidates is identified as a kaon.
- track multiplicity equal to zero - explicitly requires only three good quality signal-side tracks in the event.

Specific for $B \to \pi\tau\ell$ modes, we also require:

- kaon PID veto on the kaon candidate in the $m(K\pi)$ calculation - since $m(K\pi)$ is computed independent of $B \to \pi\tau\ell$ signal reconstruction, we require no signal-side

track be identified as a kaon.

- kaon PID veto on the primary pion candidate - again, requires no signal-side track be identified as a kaon.

- minimum pion PID on the primary pion candidate - requires the primary pion track be identified as a pion.

Note all distributions in Appendices B-F, labeled **post $m(K\pi)$ cut** are a result of the above event selection, but exclude requirements on the parameter being presented.

The $m(K\pi)$ cut

If we consider the $B \to K\tau e$ analysis, where backgrounds that produce nearly identical final state topologies are illustrated below:

$$\begin{array}{cc} B^- \to D^0 e^- \bar{\nu}_e & B^- \to K^- \tau^+ e^- \\ D^0 \to K^- \pi^+ & \tau^+ \to \pi^+ \bar{\nu}_\tau \\ D^0 \to K^- \ell^+ \nu_\ell & \tau^+ \to \ell^+ \nu_\ell \bar{\nu}_\tau \ . \end{array}$$

The final state topology of a semileptonic B (top left) with a hadronic D decay (middle left) is similar in topology as in the signal $B \to K\tau e$ (top right) with τ decaying to a positive pion and τ-anti-neutrino (middle right). The particle composition and charge correlation are identical, except for anti-neutrino flavor. When we have a semileptonic D^0 decay involving a kaon (bottom left), the final state topology is again similar if the signal decay of the τ is purely leptonic (bottom right), again ignoring anti-neutrino flavor. By trying to reconstruct the D^0 resonance from the invariant mass of the kaon candidate, with same-sign charge as the $B_{\rm sig}$ candidate, combined with a track of opposite charge, assuming it is a pion, we can remove roughly (87-99)% of all SM backgrounds by keeping only events with the mass

distribution, $m(K\pi) > 1.95\ GeV$, just above the D^0 resonance. An example is given in Figure 3.4.

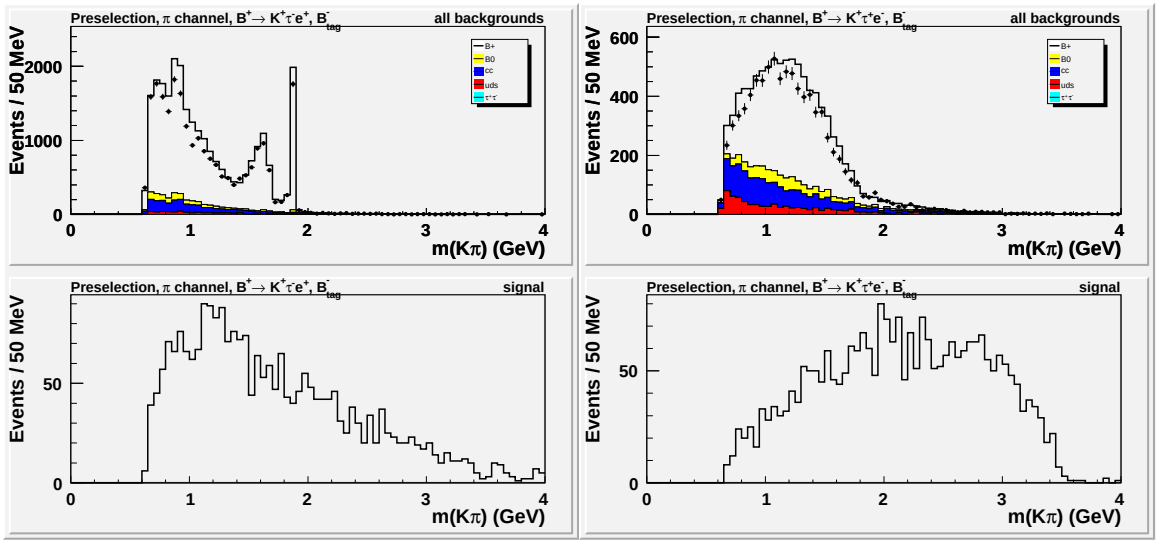

Figure 3.4: Invariant mass of a kaon with a track of opposite charge, assuming it's a pion for the "clean" (left) and "dirty" (right) $B^+ \to K^+\tau e$; $\tau \to \pi(n\pi^0)\nu$ channels. SM background MC overlaid with on-resonance data points (top) and signal MC (bottom).

In Appendix A, we show all $m(K\pi)$ distributions after preselection. Figures A.1 and A.2 show $m(K\pi)$ distributions for the "clean" and "dirty" $K\tau\mu$ plots, respectively. Figures A.3 and A.4 show $m(K\pi)$ distributions for the "clean" and "dirty" $K\tau e$ plots, respectively. Figures A.5 and A.6 show $m(K\pi)$ distributions for "clean" and "dirty" $\pi\tau\mu$ plots, respectively. Figures A.7 and A.8 show $m(K\pi)$ distributions for the "clean" and "dirty" $\pi\tau e$ plots, respectively.

The overall trend observed is that the "dirty" modes have larger relative backgrounds after the $m(K\pi) > 1.95$ GeV requirement but better signal efficiency. The trade-off in background rejection and signal efficiency between the "clean" and "dirty" modes ultimately balance each other in the expected branching fraction limits. No significant benefit

between either channels.

The $m(\mu\mu)$ $c\bar{c}$ vetoes

In Appendix B, we show the $m(\mu\mu)$ distributions post $m(K\pi)$ cut. $m(\mu\mu)$ is computed with two tracks of opposite charge (assuming they are muons) where neither can be the primary hadron (K or π) candidate, depending on the analysis. For the $B \to K\tau\mu$ signal search, a source of B background comes from $B \to (c\bar{c})K$; $(c\bar{c}) \to \mu\mu$ decays. See Figure 3.5 for an example. For the $B \to \pi\tau\mu$ signal search, a smaller source of B background

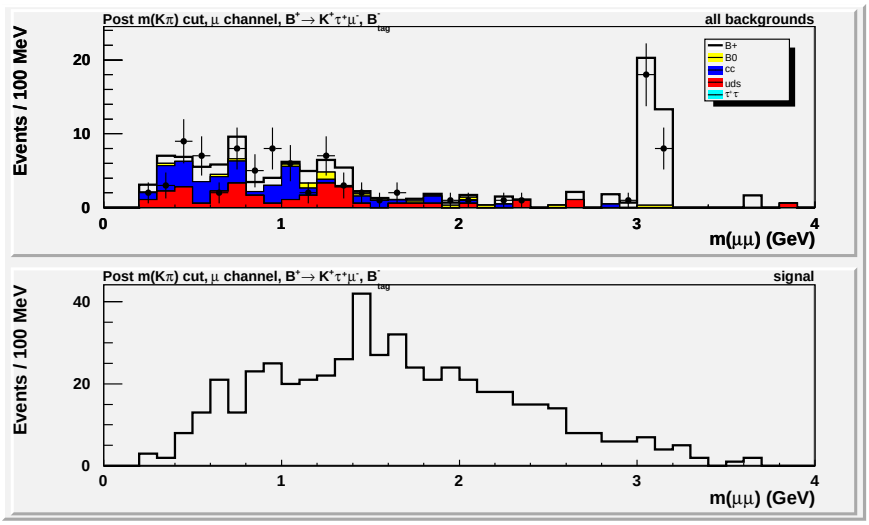

Figure 3.5: Invariant mass distributions of two muon candidates with opposite charge for our "dirty" $K\tau\mu$; $\tau \to \mu\nu\nu$ channel, post $m(K\pi)$ cut. SM background MC overlaid with on-resonance data points (top) and signal MC (bottom). Observe a significant charmonium peak near the J/ψ resonance at 3.10 GeV.

from $B \to (c\bar{c})\pi$; $(c\bar{c}) \to \mu\mu$ decays is also observed. The $(c\bar{c}) \to \mu\mu$ veto rejects events with $m(\mu\mu)$ in the range [3.03,3.14] GeV and [3.60,3.75] GeV around the $J/\psi(1S)$ and $\psi(2S)$ resonances, respectively. This is applied to the μ and π channels, only. The enhancement in the π channel is assumed to come from a higher probability of a real muon faking a pion,

in the particle identification algorithm.

Figure B.1 shows the muon and pion channels for both "clean" (left) and "dirty" (right) $K\tau\mu$ modes post $m(K\pi)$ cuts. Figure B.2 shows the muon and pion channels for both "clean" (left) and "dirty" (right) $\pi\tau\mu$ modes also post $m(K\pi)$ cuts.

The $m(ee)$ $c\bar{c}$ and γ-conversion vetoes

In Appendix C, we show the $m(ee)$ distributions post $m(K\pi)$ cut. We compute $m(ee)$ with two tracks of opposite charge (assumed to be electrons) where neither can be the primary hadron candidate; neither the kaon in the $K\tau e$ reconstruction nor the pion in the $\pi\tau e$ reconstruction. We remove sources of B background observed from $B \to (c\bar{c})h$; $(c\bar{c}) \to ee$ decays for the respective signal searches, by rejecting events with $m(ee)$ in the range [3.03,3.14] GeV and [3.60,3.75] GeV around the $J/\psi(1S)$ and $\psi(2S)$ resonances again, respectively. These vetoes are applied in the e and π channels only. See Figure 3.6, for an example. No sign of peaking in the π channel is observed, therefore we could easily make this requirement only in the e channel. But, we include this requirement in the π channel anyway.

γ-conversions in material can fake signal decays with final states Kee and πee also. In $B\bar{B}$ & continuum MC samples peaking near $m(ee) = 0$ is observed. Recall no peaking in the π channel is observed near the $c\bar{c}$ resonances, therefore one would expect not to see γ-conversions in the π channel either. This is not the case, γ-conversion peaks are observed in the background MC for both e and π channels. We therefore require $m(ee) > 0.1$ GeV in the e and π channels.

Figure C.1 shows the electron and pion channels for the "clean" (top-two) and

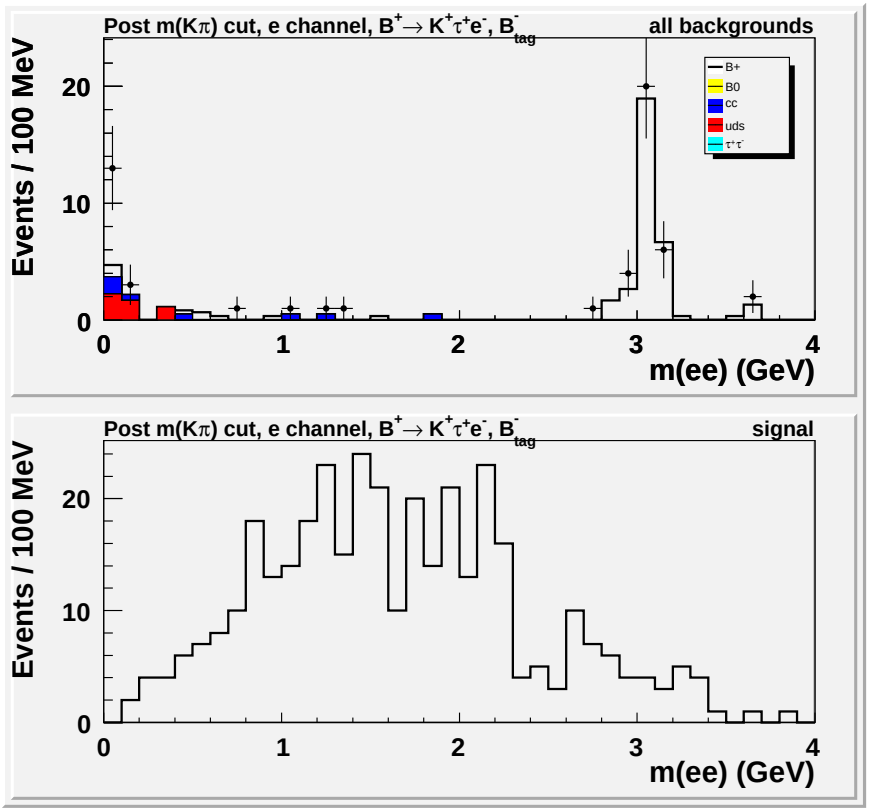

Figure 3.6: Invariant mass distributions of two electron candidates of opposite charge for our "dirty" $K\tau e$; $\tau \to e\nu\nu$ channel, post $m(K\pi)$ cut. SM background MC overlaid with on-resonance data points (top) and signal MC (bottom). Observe significant charmonium and γ-conversion peaks near the J/ψ resonance and zero. A small $\psi(2S)$ resonance at 3.69 GeV is also observed.

"dirty" (bottom-two) $K\tau e$ modes post $m(K\pi)$ cuts. Figure C.2 shows the electron and pion channels for the "clean" (top-two) and "dirty" (bottom-two) $\pi\tau e$ modes post $m(K\pi)$ cuts.

The $B_{\rm tag}$ $m_{\rm ES}$ cut

In Appendix D, we show the $B_{\rm tag}$ $m_{\rm ES}$ distributions post $m(K\pi)$ cut. We require the $B_{\rm tag}$ $m_{\rm ES}$ be greater than 5.27 GeV for all signal modes. In general, the agreement

between the on-resonance data and the standard model background Monte Carlo is fair. An excess in the expected background Monte Carlo compared to data in some channels is observed. But, this disagreement should not affect final background estimates since we use a data-driven technique. See Figure 3.7 for an example.

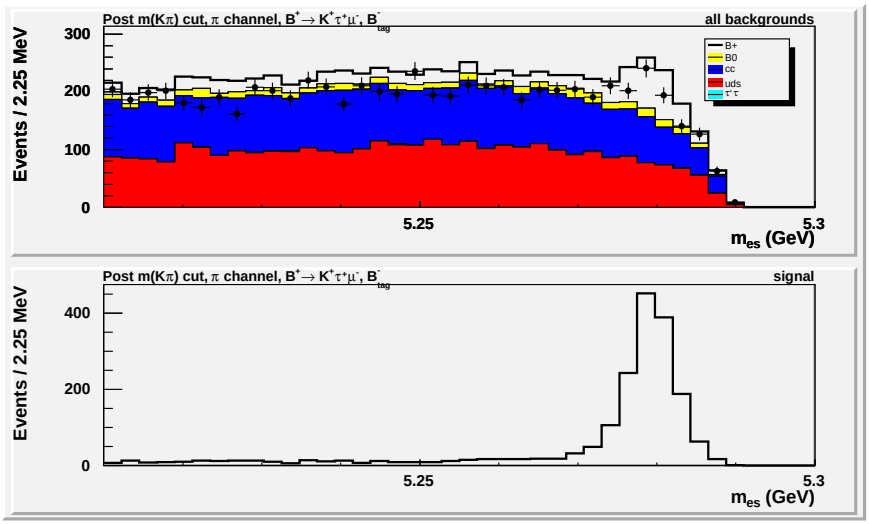

Figure 3.7: Distributions of $B_{\rm tag}$ $m_{\rm ES}$ for the "dirty" $K\tau\mu$; $\tau \to \pi(n\pi^0)\nu$ channel, SM background MC overlaid with on-resonance data (top) and signal MC (bottom), post $m(K\pi)$ cut. $B_{\rm tag}$ $m_{\rm ES} > 5.27$ GeV keeps most of our signal while removing non-peaking background.

Figure D.1 shows $m_{\rm ES}$ distributions for the "clean" (top-two) and "dirty" (bottom-two) $K\tau\mu$ search for all τ channels. Figure D.2 shows $m_{\rm ES}$ distributions for the "clean" (top-two) and "dirty" (bottom-two) $K\tau e$ search for all τ channels. Figure D.3 shows $m_{\rm ES}$ distributions for the "clean" (top-two) and "dirty" (bottom-two) $\pi\tau\mu$ search for all τ channels. Figure D.4 shows $m_{\rm ES}$ distributions for the "clean" (top-two) and "dirty" (bottom-two) $\pi\tau e$ search for all τ channels.

Kaon and proton PID vetoes

Kaon and proton particle identification vetoes for signal-side tracks are required. The kaon veto removes any event where either the primary lepton or the secondary tau track candidates are identified as kaons, using a very tight kaon particle identification algorithm, provided by the *BABAR* collaboration [41]. The proton veto removes any event where either the primary hadron, primary lepton, or the secondary tau track candidates are identified as a proton, using a very tight proton selection algorithm, also provided by *BABAR* collaborators [42]. The particle identification quality of these selectors can be ranked from `veryloose`, `loose`, `tight`, to `verytight` or numerically, from 1 to 4, respectively, where a selection quality of 0 does not pass the lowest selection quality, `veryloose`. Events from signal MC samples rarely have `verytight` proton or kaon particle identification quality in the appropriate signal-side track reconstruction, but small amounts of background MC events are observed to pass `verytight` levels of PID quality. These events are removed in our final event selection.

Track selection and quality

Like with our $B_{\rm tag}$ track reconstruction quality, our signal-side track quality requires a track candidate have a distance of closest approach of 2.5 cm within the beam pipe (z-axis) and 1.5 cm within the transverse plane (xy-plane) of the IP. A more stringent requirement includes that the track minimum transverse momentum be 0.05 GeV/c, with maximum momentum less than 10 GeV. The less stringent track reconstruction, known in *BABAR* as the `GoodTracksVeryLoose` selection criteria, only requires a track candidate

have a distance of closest approach of 2.5 cm within the beam pipe and 1.5 cm within the transverse plane of the IP [44]. Nearly all signal and background track multiplicities are consistent with zero. We require the multiplicity of the GTVL-only tracks to be zero for each signal search.

Kaon PID veto on kaon candidate in $m(K\pi)$ calculation; $\pi\tau\ell$ modes only

Since the $\pi\tau\ell$ signal searches should not have a kaon in the final state reconstruction, but we use the $B^- \to D^0\ell^-\bar{\nu}$; $D^0 \to K^-\pi^+$ control sample to determine the signal branching fraction, a kaon from the $m(K\pi)$ calculation may persist in an event. Since this calculation is independent of the $B \to \pi\tau\ell$ event reconstruction, we can remove all events with a signal-side track identified as a kaon. Recall *BABAR* particle identification quality for kaon selectors can be ranked from `veryloose`, `loose`, `tight`, to `verytight` or numerically, from 1 to 4, respectively, where a selection quality of 0 does not pass the lowest selection quality, `veryloose`. We observe a few events with kaon candidates passing `verytight` PID criteria in the background distributions, but with very few in signal. We veto events if this kaon candidate passes the kaon `verytight` PID criteria. The systematic uncertainty associated with this requirement is discussed in section 4.2.2.

Kaon PID veto on primary pion candidate; $\pi\tau\ell$ modes only

The kaon particle identification veto on the primary pion candidate can be easily appended to the proton and kaon PID veto section discussed earlier. By making this requirement, we exclude all possible real kaon tracks from the signal-side track reconstruction. We do not observe events with primary pion candidates passing the *BABAR* kaon `verytight`

selection criteria in background or signal MC samples, post $m(K\pi)$ cut. We veto events if the kaon PID level of the primary pion candidate passes the kaon `verytight` PID criteria anyway.

Minimum pion PID on primary pion candidate; $\pi\tau\ell$ modes only

Recall in section 3.3.5, that essentially, the primary pion candidate is determined after selecting the primary lepton from the signal-side tracks and that the primary pion must have the same-sign charge as the $B_{\rm sig}$ candidate. Here we explicitly require the primary pion candidate be identified as a pion, using the *BABAR* `veryloose` pion identification selection criteria [42]. In Appendix E, we show distributions of the pion PID levels on the primary pion candidate post $m(K\pi)$ cut.

Figure E.1 shows the pion PID level of the primary pion candidate for the $\pi\tau\mu$ search for all τ decay channels. Figure E.2 shows the pion PID level of the primary pion candidate for the $\pi\tau e$ search for all τ decay channels.

3.3.9 The $m(\tau)$ signal region

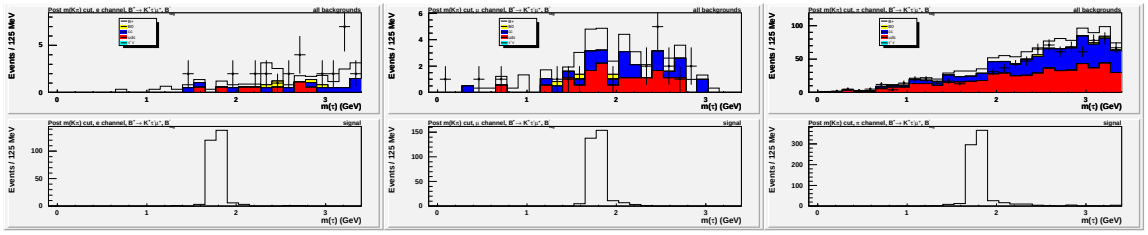

Figure 3.8: Distributions of the reconstructed τ invariant mass for the electron (left), muon (middle), & pion (right) channels, post $m(K\pi)$ cut for our "clean" $K\tau\mu$ search. Data is blinded in the range [1.65,1.90] GeV, while SM background MC is observed with a very broad, smooth distribution (top). Signal MC peaks sharply at 1.777 GeV (bottom).

Recall from section 3.1, the τ invariant mass is calculated using equation 3.1. See Figure 3.8 for an example. The τ invariant mass distributions provide a simple signal window where we determine signal efficiencies and background estimates for each signal search. From an optimization study using the best expected average upper limit on the signal branching fraction as an optimization metric, we determine that a 120 MeV signal window centered at 1.777 GeV works for all signal searches. The signal window optimization method is discussed in section 4.1.4.

In Appendix F, we show the $m(\tau)$ distributions post $m(K\pi)$ cut with the on-resonance data blinded in the range $m(\tau) \in$[1.60,1.95] GeV. Figures F.1, F.2, F.3, and F.4 show $m(\tau)$ distributions for all τ decay channels for the $K\tau\mu$, $K\tau e$, $\pi\tau\mu$, and $\pi\tau e$ searches, respectively. In general, the background shape agreement between data and MC is good, but the normalization is sometimes off, especially in the pion signal analyses. Again, since background estimates are obtained from the data sideband, we are not dependent of the MC normalization, but only the shape of the distributions. This is discussed further in section 4.1.3.

3.4 Combinatoric background rejection

3.4.1 Likelihood ratio construction

Additional discriminating variables help suppress combinatoric background, but a simple cut on individual discriminants is below optimal. We combine the lepton track identification quality, residual energies in the calorimeter, and event shape variables into a

likelihood ratio function using the relationship:

$$L_R \;=\; \frac{\prod_i P_s(x_i)}{\prod_i P_s(x_i) + \prod_i P_b(x_i)}, \tag{3.3}$$

where the product is over discriminating input variables x_i. $P_s(x_i)$ and $P_b(x_i)$ are probability density functions modeled from signal and SM luminosity weighted background MC distributions, after requiring all previous event selection criteria with the $m(\tau)$ signal window blinded in the background distributions. Signal-like events tend towards 1, while high probability background events peak towards 0. The final likelihood ratio requirements are determined for each τ decay channel, using the expected average upper limit on the branching fraction as an optimization metric, discussed in section 4.1.4. The definitions of the additional discriminating variables are:

- $\boldsymbol{|\cos\theta_{\mathbf{thr}}|}$: The absolute value of the cosine of the angle between the $B_{\rm tag}$ thrust axis and the thrust axis of the remainder of the event, where the thrust axis is the axis that maximizes $\sum_i \hat{a}\cdot\vec{p}_i$, for a set of momenta.

- $\boldsymbol{\sum E_{\mathbf{cal}}}$: The scalar sum of the neutral cluster energy in the event from the calorimeter that is not associated with the $B_{\rm tag}$ and bremsstrahlung photons or signal-side daughters (3 tracks). Also referred to as $E_{\rm extra}$, in other *BABAR* analyses.

- **Primary lepton PID quality**: For $h\tau\mu(e)$ signal searches, the muon (electron) PID level of the track identified as the muon (electron) coming directly from the signal B decay.

- **Secondary lepton PID quality**: The lepton PID level of the track assigned to come from the tau decay, either an electron or muon.

We parameterize the $|\cos\theta_{\rm thr}|$ and $\sum E_{\rm cal}$ distributions with polynomials using a least χ^2. The primary and secondary lepton PID qualities are in bins from $0 \rightarrow 4$, or from `loosest` to `tightest` PID selector quality, respectively. All likelihood ratio inputs are normalized to unity.

3.4.2 Inputs to likelihood ratio discriminant

Parameterization of $|cos(\theta_{\rm thr})|$ and $\sum E_{\rm cal}$ distributions

The signal and background Monte Carlo distributions for the $|cos(\theta_{\rm thr})|$ and $\sum E_{\rm cal}$ inputs are parameterized with probability density functions, found in Appendix I Figures I.1, I.2, I.3, and I.4 for the $\pi\tau\mu$, $\pi\tau e$, $K\tau\mu$, and $K\tau e$ searches, respectively. The $|cos(\theta_{\rm thr})|$ background MC samples in general peak closer to 1 due to jet-like topologies from continuum processes, while event shapes going through an $\Upsilon(4S)$ resonance are more uniformly distributed. The signal MC event shape is also more uniformly distributed, making it useful as an input to the likelihood ratio function. One example is found on the right in Figure 3.9. See Appendix H for all $|cos(\theta_{\rm thr})|$ distributions, post $m(K\pi)$ cut.

The $\sum E_{\rm cal}$ distributions require a minimum energy threshold of 50 MeV for all clusters in the barrel (with polar angle $\cos\theta < 0.8942$) and a minimum energy threshold of 100 MeV in the forward region of the detector. A single bin below zero on the horizontal axis is off-set from the other events, to emphasize that this is where signals may be found if no additional π^0s, presumably from a hadronic τ decay are present. It is exactly the $\sum E_{\rm cal} = 0$ bin. The residual energy is a useful discriminating variable because it peaks closer to zero in signal MC samples, while distributed away from zero in the background

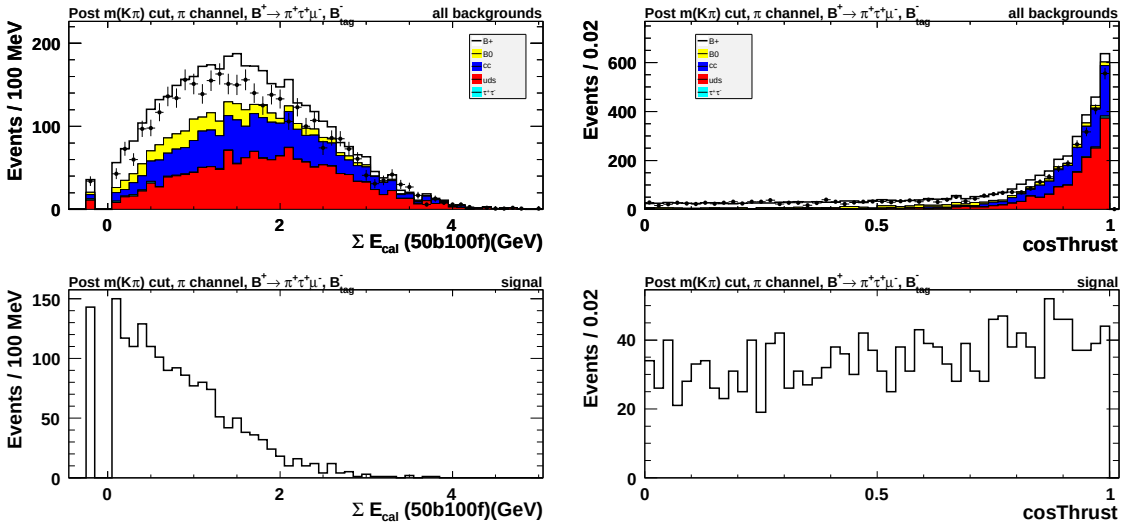

Figure 3.9: Distributions of the $\sum E_{\rm cal}$ (left) and $|cos(\theta_{\rm thr})|$ (right) for the "dirty" $\pi\tau\mu$; $\tau \to \pi(n\pi^0)\nu\nu$ channel, post $m(K\pi)$ cut. SM background overlaid with on-resonance data (top) and signal MC (bottom).

samples. Note in pion channel signal MC distributions, a broad tail above 2 GeV is observed from hadronic τ decays with multiple π^0s. An example is given on the left in Figure 3.9. See Appendix G for all $\sum E_{\rm cal}$ distributions, post $m(K\pi)$ cut.

Distributions of the primary lepton PID quality

The primary lepton PID levels are discrete inputs to the likelihood ratio, normalized to the integrated number of events for a particular channel. The *BABAR* collaboration has developed many particle identification algorithms, with varying levels of quality. The algorithms used below identify electrons, pions, and protons using an Error Correction Output Code Multiclass Classifier (`KM`) [42] and muons using a Bagger Decision Tree (`BDT`) [43]. For the $h\tau\mu$ modes, the primary muon candidate PID level correspond to bins of selection quality: 4=`muBDTVeryTight`, 3=`muBDTTight`, 2=`muBDTLoose`, and 1=`muBDTVeryLoose`. For

the $h\tau e$ modes, the primary electron candidate PID level correspond to bins of selection quality: 4=`eKMVeryTight`, 3=`eKMTight`, 2=`eKMLoose`, and 1=`eKMVeryLoose`.

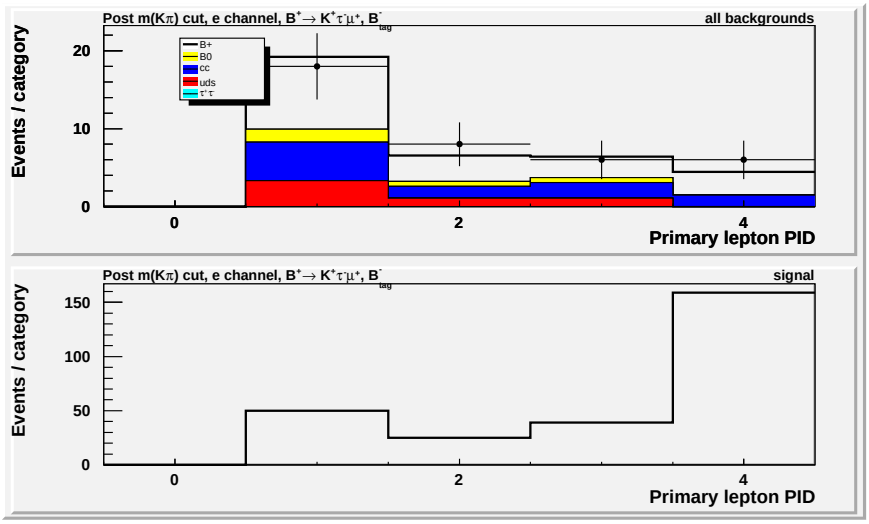

Figure 3.10: Distributions of muon PID quality for the primary lepton candidate in the "clean" $K\tau\mu$; $\tau \to e\nu\nu$ channel. Bins correspond to the following PID quality: 1=`muBDTVeryLoose`, 2=`muBDTLoose`, 3=`muBDTTight`, 4=`muBDTVeryTight`. SM background MC overlaid with on-resonance data (top) and signal MC (bottom).

Figure 3.10 provides an example. In Appendix J Figures J.1 and J.2, we present the primary lepton PID level distributions for the $K\tau\mu$ and $\pi\tau\mu$ modes, respectively. We normalize the primary muon PID level distributions before including them as inputs to the likelihood ratio, in the $h\tau\mu$ analyses. For the $h\tau e$ signal modes, more often than not, the primary lepton candidate in the background and signal samples pass at a `VeryTight` PID quality, making it a poor discriminating variable. We exclude it from the likelihood ratio, but instead require the minimum electron PID quality be `VeryTight` for the $h\tau e$ analyses, see Appendix J Figures J.3 and J.4.

Distributions of the secondary lepton PID quality

Similar to the primary lepton PID quality, the secondary lepton PID quality is also used as a discrete input to the likelihood ratio function, except that the lepton candidate is assumed to come from the tau decay. An example is shown in Figure 3.11. The electron

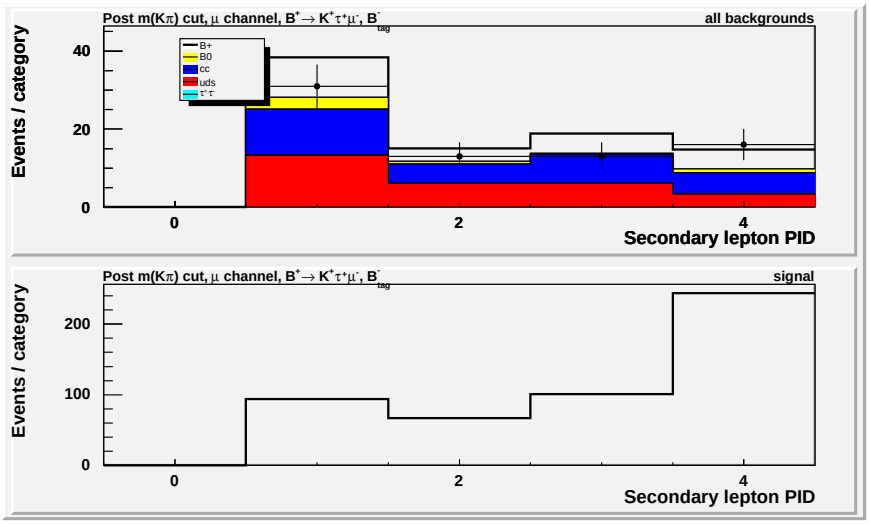

Figure 3.11: Distribution of muon PID quality for the secondary lepton PID candidate in the "dirty" $K\tau\mu$; $\tau \to \mu\nu\nu$ channel. The muon bins correspond to the following PID quality: 1=`muBDTVeryLoose`, 2=`muBDTLoose`, 3=`muBDTTight`, 4=`muBDTVeryTight`. SM background MC overlaid with on-resonance data (top) and signal MC (bottom).

bins correspond to the following PID quality: 1=`eKMVeryLoose`, 2=`eKMLoose`, 3=`eKMTight`, 4=`eKMVeryTight` [42], while muon bins correspond to the following: 1=`muBDTVeryLoose`, 2=`muBDTLoose`, 3=`muBDTTight`, 4=`muBDTVeryTight` [43]. In the muon channels, we observe secondary lepton tracks passing low PID quality in background but higher PID quality in signal. For the $h\tau\mu$ modes, we include it as an input to the likelihood ratio function for muon channels only, see Appendix K Figures K.1 and K.2. The electron channels are observed to not discriminate well, events in background and signal MC are identified passing mostly

at the `VeryTight` PID criteria. In the $h\tau e$ searches, the secondary lepton PID level is not a good discriminating variable, therefore we exclude it as an input to the likelihood ratio function for all channels. The secondary electron candidate is identified with a `VeryTight` PID quality in all signal searches, but is not necessarily explicitly required in the event selection. A summary of inputs used in the respective likelihood ratio funtions is found in section 3.4.3.

3.4.3 Likelihood ratio outputs

Inputs to the likelihood ratio functions and lepton PID quality requirements are are summarized below:

- $\boldsymbol{K\tau\mu}$: $|cos(\theta_{\rm thr})|$, $\sum E_{\rm cal}$, primary lepton PID level, and secondary lepton PID level (muon channel only).
- $\boldsymbol{K\tau e}$: $|cos(\theta_{\rm thr})|$ and $\sum E_{\rm cal}$ only, but require `VeryTight` primary and secondary electron PID.
- $\boldsymbol{\pi\tau\mu}$: $|cos(\theta_{\rm thr})|$, $\sum E_{\rm cal}$, primary lepton PID level, and secondary lepton PID level (muon channel only) but require `VeryTight` secondary electron PID.
- $\boldsymbol{\pi\tau e}$: $|cos(\theta_{\rm thr})|$ and $\sum E_{\rm cal}$ only, but require `VeryTight` primary and secondary electron PID.

Figure 3.12 provides an example of likelihood ratio distributions. Outputs of all likelihood ratio distributions are found in Appendix L Figures L.1, L.2, L.3, and L.4 for the $K\tau\mu$, $K\tau e$, $\pi\tau\mu$, and $\pi\tau e$, respectively (recall event selection requirements summarized in section 3.3.8).

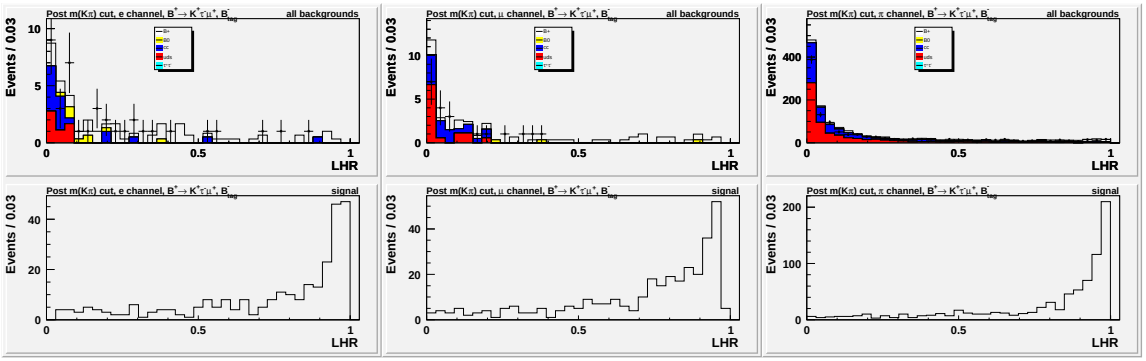

Figure 3.12: Likelihood ratio distributions for our "clean" $K\tau\mu$ electron (left), muon (center), and pion (right) channels. SM background MC overlaid with on-resonance data (top) and signal MC (bottom). Notice, very good discriminating power.

We observe good data and MC agreement. The optimal minimum likelihood ratio cuts are discussed in section 4.1.4.

3.5 The ($B \to D^{(*)0}\ell\nu$; $D^0 \to K^-\pi^+$; $\ell = e$ or μ) control samples

3.5.1 Signal branching fraction normalization

The $D^0 \to K^-\pi^+$ background in the range $m(K\pi) \in$ [1.845,1.885] GeV provides a nice clean control sample, to normalize our signal search branching fractions. In the $B^\pm \to h^\pm\tau\mu$; ($h = K$ or π) analyses, the control sample requires a muon in the final state: $B \to D^{(*)0}\mu\nu$; $D^0 \to K^-\pi^+$. In the $B^\pm \to h^\pm\tau e$; ($h = K$ or π) analyses, the control sample requires an electron in the final state: $B \to D^{(*)0}e\nu$; $D^0 \to K^-\pi^+$.

The yield of a reconstructed $B \to f$ transition can be obtained from a general tagging technique that reconstructs the other $B_{\rm tag}$ in the event, where f represents the non-

tag side reconstruction. For our analysis, f is $h\tau\ell$ ($h = K$ or π and $\ell = e$ or μ) for our signal search or $D\ell\nu$ ($\ell = e$ or μ) for our control/normalization. We use the *BABAR* BSemiExcl reconstruction algorithm, mentioned earlier, for our B tagging. From the tag yield or the number of events with a reconstructed $B_{\rm tag}$ ($N_{\rm tag}$), the known or assumed branching fraction ($\mathcal{B}_f$), and the final state signal efficiency (ϵ_f), we can essentially determine any $B \to f$ yield from the following formula:

$$N_f = N_{\rm tag}\ \mathcal{F}_f^{\rm tag}\ \epsilon_f \tag{3.4}$$

$$N_f = N_{\rm tag}\ \left(\frac{\epsilon_{\rm tag}^f}{\epsilon_{\rm tag}^X}\right)\ \mathcal{B}_f\ \epsilon_f. \tag{3.5}$$

The fraction of events with a $B \to f$ transition in the sample, after requiring a reconstructed $B_{\rm tag}$ is the symbol $\mathcal{F}_f^{\rm tag}$. It is approximately equal to $\left(\frac{\epsilon_{\rm tag}^f}{\epsilon_{\rm tag}^X}\right)\ \mathcal{B}_f$, if we assume the $B \to f$ yield is much, much smaller than the expected yield of all events where we exclude the final state reconstruction, $B \to X$ decays [19]. Notice we need to include the tag efficiency ($\epsilon_{\rm tag}^f$), assuming that the signal sample is enriched with a particular $B \to f$ transition, based on how the non-$B_{\rm tag}$ is persisted in the sample.

We show later in our sensitivity measurements that $\epsilon_{\rm tag}^f$ is dependent on the final state topology of the MC sample, but it is not significant. The $\epsilon_{\rm tag}^X$ is the tag efficiency assuming a $B \to X$ candidate, where X represents events with non-f final states on the signal side. We determine $\epsilon_{\rm tag}^f$ from the ratio of the number of reconstructed tagged B's to the total number of generated B's in dedicated signal Monte Carlo samples found in Table 3.1. The control mode $\epsilon_{\rm tag}^f$ is determined from the Generic B^+B^- sample within the range $m(K\pi) \in$ [1.845,1.885] GeV, where the other $B_{\rm tag}$ meson decays via the transitions and probabilities defined by the standard model. We avoid measuring $\epsilon_{\rm tag}^X$, since it cancels

in the branching fraction normalization.

The number of reconstructed control and signal modes can be determined using equation 3.5:

$$N_{D\ell\nu} = N_{\rm tag} \left(\frac{\epsilon_{\rm tag}^{D\ell\nu}}{\epsilon_{\rm tag}^{X}} \right) \mathcal{B}_{D\ell\nu}\, \epsilon_{D\ell\nu} \tag{3.6}$$

$$N_{h\tau\ell} = N_{\rm tag} \left(\frac{\epsilon_{\rm tag}^{h\tau\ell}}{\epsilon_{\rm tag}^{X}} \right) \mathcal{B}_{h\tau\ell}\, \epsilon_{h\tau\ell} \tag{3.7}$$

where $\epsilon_{D\ell\nu}$ and $\epsilon_{h\tau\ell}$ are the control and signal reconstruction efficiencies, respectively. Taking the ratio of equations 3.6 to 3.7 and rearranging, we get the signal branching fraction to be

$$\mathcal{B}_{h\tau\ell} = \left(\frac{N_{h\tau\ell}}{N_{D\ell\nu}} \right) \left(\frac{\epsilon_{\rm tag}^{D\ell\nu}}{\epsilon_{\rm tag}^{h\tau\ell}} \right) \left(\frac{\epsilon_{D\ell\nu}}{\epsilon_{h\tau\ell}} \right) \mathcal{B}_{D\ell\nu}. \tag{3.8}$$

The beauty of using the branching ratio of our signal and control mode branching fractions is that the tag yield ($N_{\rm tag}$) and $\epsilon_{\rm tag}^{X}$ cancel. Using this normalization, we avoid explicit measurement of the tag yield and the systematic errors associated with it.

3.5.2 Control sample reconstruction

In addition to preselection, the $B \to D^{(*)0}\ell\nu$; $D^0 \to K^-\pi^+$; with $\ell = e$ or μ control samples are reconstructed with similar event selection, as used in the $B \to K\tau\ell$ reconstruction found in section 3.3.8, but replace the $m(\tau)$ mass window, minimum likelihood ratio, and $m(K\pi) > 1.95$ GeV requirements with $m(K\pi) \in [1.845,1.885]$ GeV. If we require the $B_{\rm tag}$ $m_{\rm ES} > 5.27$ GeV, a nice clean peak from the D^0 resonance is observed in $m(K\pi)$. Figure 3.13 shows the $B_{\rm tag}$ $m_{\rm ES}$ (left) and $m(K\pi)$ (right) distributions excluding the $B_{\rm tag}$ and $m(K\pi)$ requirements, respectively.

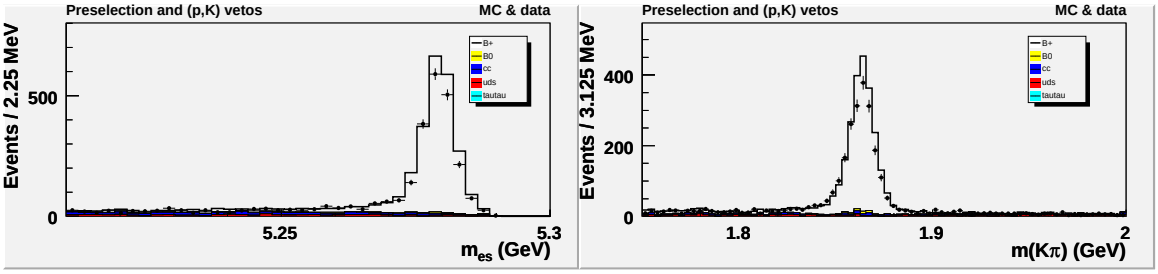

Figure 3.13: $B_{\rm tag}$ $m_{\rm ES}$ (left) and $m(K\pi)$ (right) distributions with $B \to D^{(*)0}\mu\nu$; $D^0 \to K^-\pi^+$ event reconstruction requirements, excluding $B_{\rm tag}$ $m_{\rm ES} > 5.27$ GeV and $m(K\pi) \in$ [1.845,1.885] GeV, respectively.

The track used to compute $m(K\pi)$, with opposite sign charge of the kaon, must be the track assumed to come from the τ decay, i.e. *not* the primary lepton in the signal reconstruction. By requiring that one of the non kaon tracks be identified as a muon (electron) in the $h\tau\mu(e)$ track assignments and requiring $m(K\pi) \in$ [1.845,1.885] GeV, this is done implicitly. Recall by requiring $Q_\ell = -Q_{\rm tag}$, in order to reconstruct $D^0 \to K^-\pi^+$ properly, the semileptonic B decay must have the charge configuration: $B^- \to D^0\ell^-\bar{\nu}_\ell$. There was some $De\nu$ peaking background contamination in the control sample from events where the pion, from $D^0 \to K^-\pi^+$, fakes the primary muon and the "τ track" is an electron. To remove this background we require that the primary muon candidate is not used in the $m(K\pi)$ calculation. The control sample yield from $B^- \to D^{(*)0}\ell^-\bar{\nu}_\ell$; $D^0 \to K^-\pi^+$ is used to normalize the $B^- \to \pi^-\tau\ell$ searches as well. Since systematic uncertainties associated with kaon and pion PID reconstruction between the control and signal mode normalization do not cleanly cancel, as in the $K\tau\ell$ modes, this systematic must be accounted for which is discussed in section 4.2.2.

3.5.3 Control sample ΔE fit yields

The reconstruction of the $D^0\ell\nu$ control decays are complete except for the neutrino. The momentum of the $D^0\ell\nu$ candidate is known to be equal and opposite that of the $B_{\rm tag}$ candidate in the center-of-mass frame, recall Figure 3.1. The momentum of the missing neutrino can be accurately inferred assuming correct track reconstruction. This allows $D^0\ell\nu$ candidates to be fully reconstructed, using the formula

$$\Delta E = E_K + E_\pi + E_\ell + E_\nu - E_{\rm beam}, \tag{3.9}$$

where E_ν is the magnitude of the three-momentum of the reconstructed missing neutrino, assuming $m_\nu = 0$.

Figure 3.14 shows the reconstructed ΔE distributions for the $D^{*0}\mu\nu$ (left column) and $D^{*0}e\nu$ (right column) candidates. The three rows show different ΔE resolutions to help emphasize the components that make up each control mode sample. There are three components visible: one centered near zero from events with a D^0 resonance (dashed), one asymmetric peak approximately one π mass below zero from D^{*0} resonances (dotted), and a much broader distribution mostly from D^{**}-type and $D\pi$ events (dash-dotted).

The plan again is to normalize signal yields with a primary muon (electron) in the final state using the $D^{(*)}\mu(e)\nu$ control sample fit yield. Recall from equation 3.8 that the signal efficiency for the $D^{(*)}\ell\nu$ control reconstruction, $\epsilon_{D\ell\nu}$, is needed. For signal in the $m(\tau)$ reconstruction, it is crucial that the $B_{\rm tag}$ momentum in the center-of-mass ($\vec{p}^*$) frame be properly measured. If the $B_{\rm tag}$ candidate is missing a low-energy neutral that does not mis-reconstruct $\vec{p}^*$ too poorly, the $m(\tau)$ reconstruction will still be okay. For this reason we define the signal efficiency for the control sample reconstruction ($\epsilon_{D\ell\nu}$) in terms

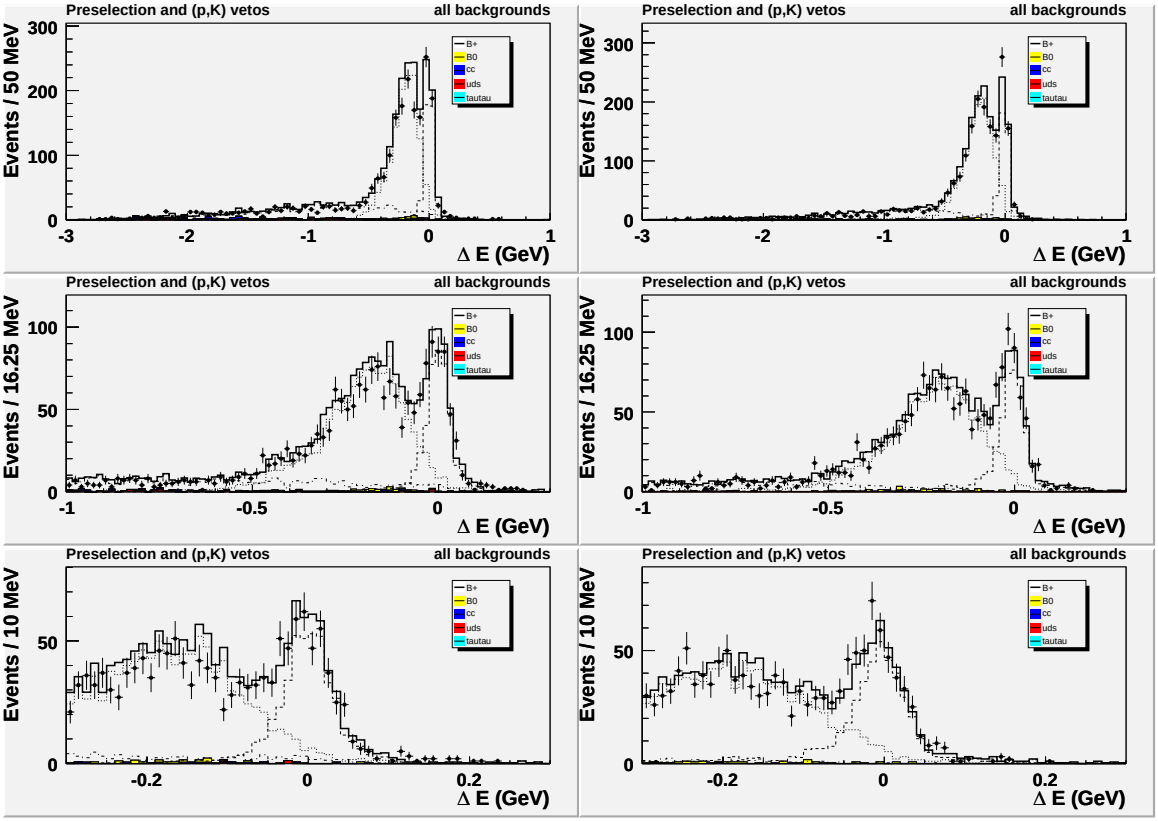

Figure 3.14: Distributions of ΔE for the $B \to D^{(*)0}\mu\nu$ (left) and $B \to D^{(*)0}e\nu$ (right) control samples. All events require $B_{\rm tag}$ $m_{\rm ES} > 5.27$ GeV and $m(K\pi) \in$ [1.845,1.885] GeV. Dashed (dotted) histograms are candidates truth matched with a D^0 (D^{*0}) in the event. Dash-dotted histograms are candidates reconstructed as D^{**}-type events. Points with error bars are from on-resonance data. Data and MC agree very well.

of events where $\Delta p^* \equiv |\vec{p}^*_{\rm true} - \vec{p}^*_{\rm rec}|$ is less than 0.1 GeV, where $\vec{p}^*_{\rm true}$ is the truth matched CM frame momentum and $\vec{p}^*_{\rm rec}$ is the reconstructed CM momentum for the $B_{\rm tag}$ candidate. This should be okay since we believe the Monte Carlo is well modeled in the control sample.

Figure 3.15 shows the Δp^* distributions for Generic B^+B^- events (top), events with a $D^{(*)}\mu\nu$ decay (middle), and events with a signal decay (bottom). Nearly all of the events with $B_{\rm tag}$ properly reconstructed have $\Delta p^* < 0.1$ GeV. We truth match track candidates used to compute $p^*_{\rm true}$ by checking if all tracks properly originate from the same $B_{\rm tag}$ decay. Notice that the red distributions in Figure 3.15 represent truth matched events that are not properly reconstructed. The fraction of events that are estimated in MC allow us to correct for the fraction of events properly reconstructed in data. The signal efficiencies after considering the fraction of events properly reconstructed from the $D^*e\nu$ and $D^*\mu\nu$ control samples are given in Table 3.8. Studies of correlations between Δp^* and $B_{\rm tag}$ $m_{\rm ES}$ were performed, showing no strong correlations, see 2-D plots in Appendix M.

Mode	N^0	$N_{\rm rec}$	$N'_{\rm rec}$	$f_{\rm good}$	$\epsilon_{\rm D\ell\nu}$
$D\mu\nu$	3047	1457	1330	$(91.3 \pm 0.7)\%$	$(43.6 \pm 0.9)\%$
$D^*\mu\nu$	8586	4358	3762	$(86.3 \pm 0.5)\%$	$(43.8 \pm 0.5)\%$
$De\nu$	3030	1460	1316	$(90.1 \pm 0.8)\%$	$(43.4 \pm 0.9)\%$
$D^*e\nu$	8311	4342	3676	$(84.7 \pm 0.5)\%$	$(44.2 \pm 0.5)\%$

Table 3.8: Fraction of properly reconstructed tag yield and reconstruction efficiencies from the $D^{(*)}\ell\nu$ control modes using the Generic B^+B^- MC sample. N^0 is the number of events with $B_{\rm tag}$ $m_{\rm ES} > 5.27$ GeV, $B_{\rm tag}$ mode purity $> 10\%$, and $\Delta p^* < 0.1$ GeV before the signal-side pre selection. $N_{\rm rec}$ is the number of $D^{(*)}\ell\nu$ candidates reconstructed with event selection discussed in section 3.5.2. $N'_{\rm rec}$ is the same as $N_{\rm rec}$ with $\Delta p^* < 0.1$ GeV added. The fraction of properly reconstructed $B_{\rm tag}$, $f_{\rm good}$, is defined as $N'_{\rm rec}/N_{\rm rec}$. The reconstruction efficiency, $\epsilon_{\rm D\ell\nu}$, is defined as $N'_{\rm rec}/N^0$.

We perform a three component fit on the ΔE distributions for each control sample ($D^{(*)}\mu\nu$ and $D^{(*)}e\nu$). The fit parameters for the three ΔE distributions are obtained

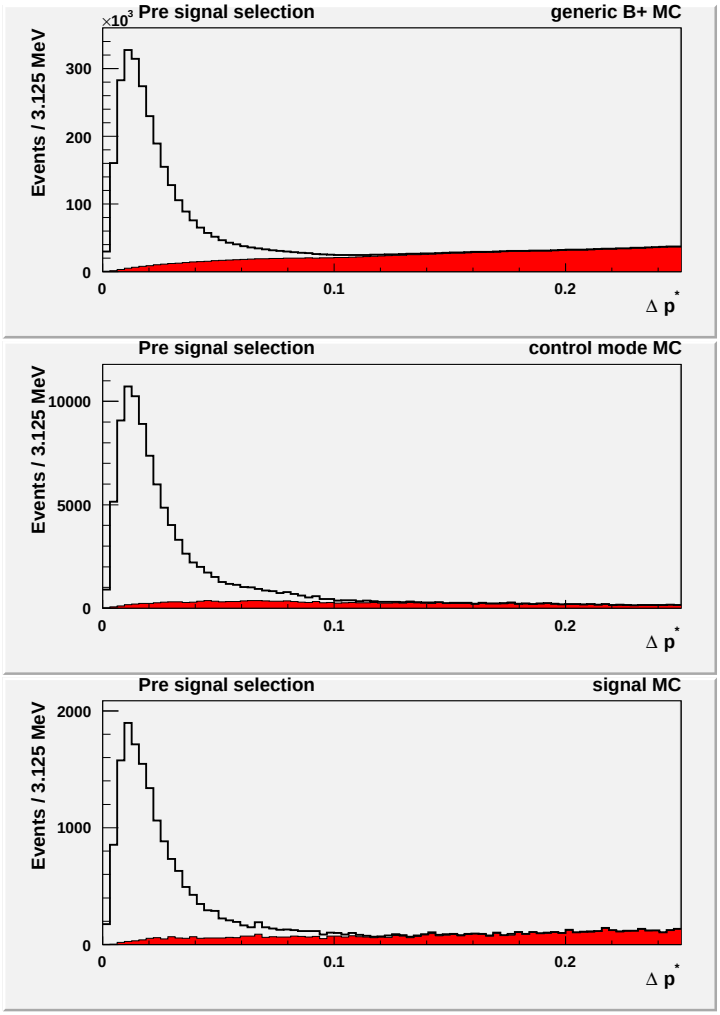

Figure 3.15: Distributions of $\Delta p^* = |\vec{p}^*_{\rm true} - \vec{p}^*_{\rm rec}|$ for the $B_{\rm tag}$ meson in Generic B^+B^- MC (top), $D\mu\nu$ control MC (middle), and signal MC (bottom). The solid red component of the distributions is from events where the $B_{\rm tag}$ meson was *not* truth matched (i.e. not properly reconstructed).

using luminosity-weighted standard model MC samples. The three ΔE distributions are fit separately to obtain the functional forms of the distributions using an unbinned maximum likelihood fit. We categorize the three components based on how the charmed meson resonances are reconstructed: D^0, D^{*0}, and D^{**} (which include $D^{**}\ell\nu$ events and all other non-D^0 and non-D^{*0} backgrounds). Figure 3.16 shows the three individual generic Monte Carlo ΔE distributions (top row) and the corresponding functional forms of the fits (bottom row) for the $D^{(*)}\mu\nu$ control sample. Figure 3.17 shows the same except for the $D^{(*)}e\nu$ control sample.

Figure 3.18 shows our combined fit parameters determined from MC projected onto on-resonance data. For the $D^{(*)}\mu\nu$ control sample, we found that a double gaussian (with a core gaussian mean and width allowed to vary) fit the D^0 shape best. For the $D^{*0}\mu\nu$ contributions, we found that a composite of two PDFs (a gaussian and a crystal ball combined with a relative fraction allowed to vary) performed best, where the gaussian mean and width were also allowed to vary. For the D^{**} contributions, we found that a composite of two PDFs (a bifurcated gaussian with another gaussian) performed best, where the additional gaussian was necessary to model a real bump from contributions in $B^- \to D^0\pi^-$; $D^0 \to K^-\pi^+$ decays, where a pion is misidentified as a muon and the neutrino is not reconstructed, and from $B^+ \to D_s^+ D^0$; $D_s^+ \to \mu\nu$ decays, and $B^- \to D^0 K^-$ decays [19]. For the above, the yields from the fit parameters were also allowed to vary.

For the $D^{(*)}e\nu$ control sample, the yields from the three fit components were also allowed to vary. For the $D^0 e\nu$ shapes, we found that a composite of two PDFs (a gaussian and a crystal ball) performed best, if the gaussian mean and width were allowed

to vary and the relative fraction of the composite PDFs were held fixed. For the $D^{*0}e\nu$ contributions, we again found that a composite of two PDFs (a gaussian and a crystal ball) performed best, allowing the gaussian mean and width to vary. We found that a bifurcated gaussian performed best on the "other" non-D^0 and non-D^{*0} decays, or D^{**}-type components. Table 3.9 provides the yields, on the above fits.

Component	Fit yield (yield varied)	Fit yield (shape varied)	Fraction with $\Delta p^* < 0.1$ GeV	Corrected yield
$D\mu\nu$	481 ± 26	513 ± 38	0.913	468 ± 35
$D^*\mu\nu$	1257 ± 41	1234 ± 49	0.863	1065 ± 43
other$_\mu$	653 ± 31	645 ± 32	-na-	-na-
$De\nu$	516 ± 28	484 ± 46	0.901	436 ± 41
$D^*e\nu$	1337 ± 43	1368 ± 58	0.847	1159 ± 49
other$_e$	361 ± 25	362 ± 29	-na-	-na-

Table 3.9: Results of the on-resonance unbinned maximum likelihood fits to ΔE using the $D^{(*)}\mu\nu$ and $D^{(*)}e\nu$ samples are shown here. The yield varied column shows the results by varying the 3 yield parameters, shape parameters fixed. In the shape varied column, shape parameters are allowed to vary also. The shape varied yields are corrected by the fraction of properly reconstructed $B_{\rm tag}$ candidates, using truth matched information.

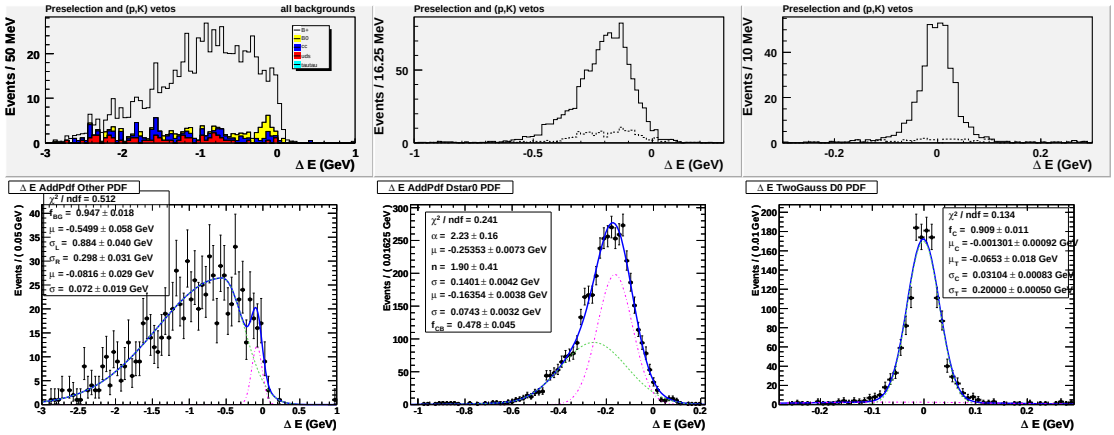

Figure 3.16: Distributions (top row) and fits (bottom row) of ΔE for the three components of the $D^{(*)}\mu\nu$ sample ΔE fit: other (left), $D^*\mu\nu$ (middle), and $D\mu\nu$ right. In the top middle and top right plots, the dashed distribution is for events with $\Delta p^* > 0.1$ GeV, which indicates that the $B_{\rm tag}$ meson was not properly reconstructed. All events are required to have $m_{\rm es} > 5.27$ GeV for $B_{\rm tag}$ and $m(K\pi)$ in the range [1.845,1.885] GeV.

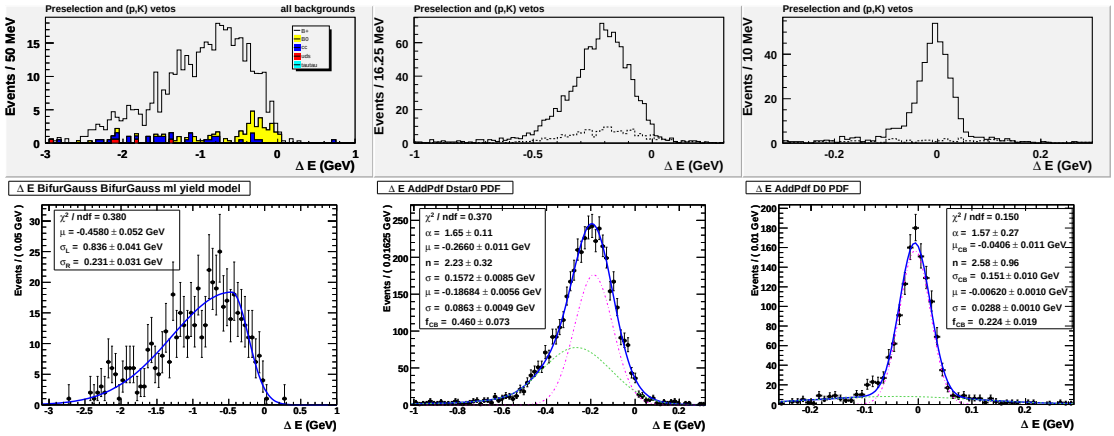

Figure 3.17: Distributions (top row) and fits (bottom row) of ΔE for the three components of the $D^{(*)}e\nu$ sample ΔE fit: other (left), $D^*e\nu$ (middle), and $De\nu$ right. In the top middle and top right plots, the dashed distribution is for events with $\Delta p^* > 0.1$ GeV, which indicates that the $B_{\rm tag}$ meson was not properly reconstructed. All events are required to have $m_{\rm es} > 5.27$ GeV for $B_{\rm tag}$ and $m(K\pi)$ in the range [1.845,1.885] GeV.

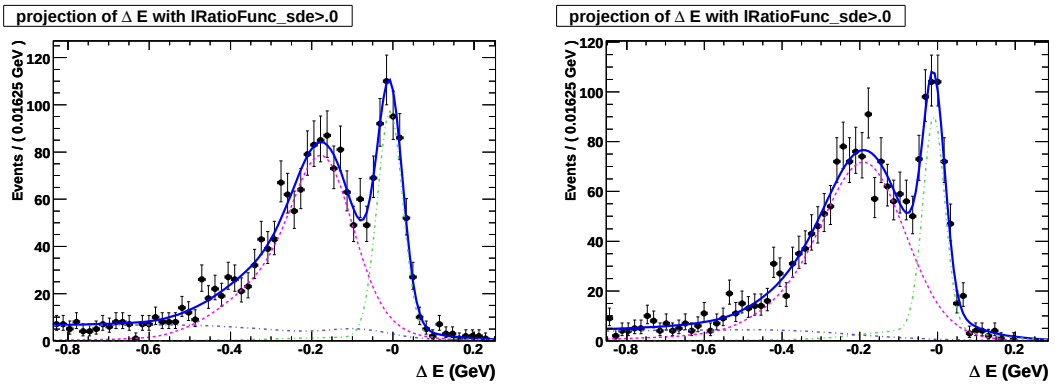

Figure 3.18: Projections of the three-component ΔE fit onto data for the $B \to D^{(*)0}\mu\nu$ (left) and $B \to D^{(*)0}e\nu$ (right) control sample yields. All events are required to have the $B_{\rm tag}$ $m_{\rm ES} > 5.27$ GeV and $m(K\pi) \in$[1.845,1.885] GeV.

3.5.4 Common sensitivity from control sample

We define our so-called sensitivity, S, by rearranging equation 3.8,

$$\mathcal{B}_{h\tau\ell} = \frac{N_{h\tau\ell}}{N_{D\ell\nu}\left(\frac{\epsilon_{\rm tag}^{h\tau\ell}}{\epsilon_{\rm tag}^{D\ell\nu}}\right)\left(\frac{\epsilon_{h\tau\ell}}{\epsilon_{D\ell\nu}}\right)\left(\frac{1}{\mathcal{B}_{D\ell\nu}}\right)}, \tag{3.10}$$

or written as $\mathcal{B}_{h\tau\ell} = \frac{N_{h\tau\ell}}{S}$, where

$$S \equiv N_{D\ell\nu}\left(\frac{\epsilon_{\rm tag}^{h\tau\ell}}{\epsilon_{\rm tag}^{D\ell\nu}}\right)\left(\frac{\epsilon_{h\tau\ell}}{\epsilon_{D\ell\nu}}\right)\left(\frac{1}{\mathcal{B}_{D\ell\nu}}\right). \tag{3.11}$$

If we factor out the signal efficiency, such that $S = \epsilon_{h\tau\ell}S_0$ where

$$S_0 \equiv \frac{N_{D\ell\nu}}{\mathcal{B}_{D\ell\nu}}\left(\frac{\epsilon_{\rm tag}^{h\tau\ell}}{\epsilon_{\rm tag}^{D\ell\nu}}\right)\left(\frac{1}{\epsilon_{D\ell\nu}}\right), \tag{3.12}$$

we can define a sensitivity, S_0, common to the respective τ decay channel.

If we ignore background for the moment and the signal branching fraction is not zero, the number of expected events in the signal region is $N_{h\tau\ell} = \mathcal{B}_{h\tau\ell}S$. In order to extract an upper limit on the signal branching fractions at the 90% confidence level, we investigate the R.Barlow frequentist method [45]. Because we cannot ignore backgrounds, the number of expected events in the $m(\tau)$ signal window must be

$$\mu = N_{h\tau\ell} + b, \tag{3.13}$$

or

$$\mu = \mathcal{B}_{h\tau\ell}S + b, \tag{3.14}$$

where b is the expected number of background events in the corresponding $m(\tau)$ signal window.

We investigated what happens to the $B_{\rm tag}$ efficiency if the signal-side $B_{\rm sig}$ MC samples are enriched with a particular final state topology. The common sensitivity factor (S_0) from Equation 3.12 is

$$S_0 \equiv \frac{N_{D\ell\nu}}{\mathcal{B}_{D\ell\nu}} \left(\frac{\epsilon_{\rm tag}^{h\tau\ell}/\epsilon_{\rm tag}^{D\ell\nu}}{\epsilon_{D\ell\nu}} \right),$$

which again is common to all τ decay channels. The tag efficiency ratios ($\epsilon_{\rm tag}^{h\tau\ell}/\epsilon_{\rm tag}^{D\ell\nu}$) are expected to be 1, if the $B_{\rm tag}$ reconstruction efficiency is independent of the signal-side final state topology of the sample. The measured $B_{\rm tag}$ reconstruction efficiency for each signal MC sample is found in Table 3.10. The computed tag efficiency ratios ($\epsilon_{\rm tag}^{h\tau\ell}/\epsilon_{\rm tag}^{D\ell\nu}$) are found in Table 3.11. The control mode fit yield, $N_{De\nu}$ and $N_{D\mu\nu}$, values corrected with MC truth $B_{\rm tag}$ reconstruction are found in Table 3.9. The control mode signal efficiency, $\epsilon_{De\nu}$ and $\epsilon_{D\mu\nu}$, values are found in Table 3.8. Our control sample branching fractions are [39]:

- $\mathcal{B}(B^- \to D^0 \ell^- \bar{\nu}) = (2.24 \pm 0.11)\%$
- $\mathcal{B}(B^- \to D^{*0} \ell^- \bar{\nu}) = (5.68 \pm 0.19)\%$
- $\mathcal{B}(D^0 \to K^- \pi^+) = (3.91 \pm 0.05)\%$.

The $D^0\ell\nu$ and $D^{*0}\ell\nu$ control samples give eight independent measures of S_0, dependent on the signal mode final state, $h\tau\ell$ for $h = K, \pi$ and $\ell = e, \mu$. The common sensitivities with corrected tag efficiency ratios are presented in Table 3.12. From correlations between the $D\ell\nu$ and $D^*\ell\nu$ control channels, we compute weighted average sensitivities found in Table 3.13. These sensitivities are consistent, within measured uncertainties, regardless of final state topology. The weighted average common sensitivities are used in the expected upper limit calculations in Appendix P.

Sample	$N_{\rm gen}$	$N_{\rm rec}$	$\epsilon_{\rm tag}$
Generic $B^{\pm}$	2×708.762M	3.048M	$(0.215 \pm 0.000)\%$
$K\tau\mu$, Generic $B_{\rm tag}$	5.769M	14,172	$(0.246 \pm 0.002)\%$
$\pi\tau\mu$, Generic $B_{\rm tag}$	11.63M$\times$0.5	14,072	$(0.242 \pm 0.002)\%$
$D^{(*)0}\mu\nu$, Generic $B_{\rm tag}$	2$\times$708.762M$\times$0.00322	11,633	$(0.255 \pm 0.002)\%$
$K\tau\mu$, $B_{\rm tag}$ cocktail	429k$\times$0.5	26,396	$(12.31 \pm 0.07)\%$
$\pi\tau\mu$, $B_{\rm tag}$ cocktail	429k$\times$0.5	26,243	$(12.23 \pm 0.07)\%$
$D^{(*)0}\mu\nu$, $B_{\rm tag}$ cocktail	812k$\times$0.5 $\times$ 0.0841/0.1085	42,047	$(13.36 \pm 0.06)\%$
$K\tau e$, Generic $B_{\rm tag}$	6.449M	15,747	$(0.244 \pm 0.002)\%$
$\pi\tau e$, Generic $B_{\rm tag}$	11.63M$\times$0.5	14,069	$(0.242 \pm 0.002)\%$
$D^{(*)0}e\nu$, Generic $B_{\rm tag}$	2$\times$708.762M$\times$0.00322	11,341	$(0.248 \pm 0.002)\%$
$K\tau e$, $B_{\rm tag}$ cocktail	429k$\times$0.5	26,500	$(12.35 \pm 0.07)\%$
$\pi\tau e$, $B_{\rm tag}$ cocktail	429k$\times$0.5	26,681	$(12.44 \pm 0.07)\%$
$D^{(*)0}e\nu$, $B_{\rm tag}$ cocktail	812k$\times$0.5 $\times$ 0.0841/0.1085	42,617	$(13.54 \pm 0.06)\%$

Table 3.10: Reconstruction efficiency of the $B_{\rm tag}$ candidate for signal and control sample ($D^{(*)0}\ell\nu$) Monte Carlo. The "other" B meson is forced to decay as a cocktail, or mix of hadronic $B_{\rm tag}$ modes, designed to enhance tag efficiency. $N_{\rm gen}$ is the estimated number of generated B-mesons in the sample, while $N_{\rm rec}$ is the number of reconstructed tagged B's with $m_{\rm ES} > 5.27$ GeV, $\Delta p^* < 0.1$ GeV, and mode purity $> 10\%$. Recall that Generic samples decay via SM processes and probabilities.

Tag efficiency ratios	$(\epsilon_{\rm tag}^{K\tau e}/\epsilon_{\rm tag}^{De\nu})$	$(\epsilon_{\rm tag}^{\pi\tau e}/\epsilon_{\rm tag}^{De\nu})$	$(\epsilon_{\rm tag}^{K\tau\mu}/\epsilon_{\rm tag}^{D\mu\nu})$	$(\epsilon_{\rm tag}^{\pi\tau\mu}/\epsilon_{\rm tag}^{D\mu\nu})$
$B_{\rm tag}$ decays generically	0.983 ± 0.012	0.974 ± 0.012	0.964 ± 0.012	0.950 ± 0.012
$B_{\rm tag}$ decays via cocktail	0.912 ± 0.007	0.919 ± 0.007	0.921 ± 0.007	0.916 ± 0.007
Tag efficiency ratio in S_0	0.983 ± 0.072	0.974 ± 0.057	0.964 ± 0.045	0.950 ± 0.036

Table 3.11: Tag efficiency ratios for signal modes, $B \to h\tau\ell$ with $h = K, \pi$ and $\ell = e, \mu$, and control modes, $B \to D\ell\nu$ with $\ell = e, \mu$, respectively. We define our statistical error as the error when the $B_{\rm tag}$ decays generically. We define a systematic error as the difference in the tag efficiency ratio when the $B_{\rm tag}$ decays generically and when the $B_{\rm tag}$ decays via the cocktail sample. In the bottom row, the systematic and statistical errors are added in quadrature and are used in our common sensitivity calculations in Table 3.12.

$D^0\mu\nu$ channel	$S_0^{K\tau\mu} = \frac{(468\pm35)}{(0.000876\pm0.000044)}\frac{(0.964\pm0.045)}{(0.436\pm0.009)}$	$S_0^{K\tau\mu}$	$= (11.81 \pm 1.22) \times 10^5$
$D^{*0}\mu\nu$ channel	$S_0^{K\tau\mu} = \frac{(1065\pm42)}{(0.002221\pm0.000080)}\frac{(0.964\pm0.045)}{(0.438\pm0.005)}$	$S_0^{K\tau\mu}$	$= (10.55 \pm 0.76) \times 10^5$
$D^0\mu\nu$ channel	$S_0^{\pi\tau\mu} = \frac{(468\pm35)}{(0.000876\pm0.000044)}\frac{(0.950\pm0.036)}{(0.436\pm0.009)}$	$S_0^{\pi\tau\mu}$	$= (11.63 \pm 1.16) \times 10^5$
$D^{*0}\mu\nu$ channel	$S_0^{\pi\tau\mu} = \frac{(1065\pm42)}{(0.002221\pm0.000080)}\frac{(0.950\pm0.036)}{(0.438\pm0.005)}$	$S_0^{\pi\tau\mu}$	$= (10.40 \pm 0.69) \times 10^5$
$D^0e\nu$ channel	$S_0^{K\tau e} = \frac{(436\pm41)}{(0.000876\pm0.000044)}\frac{(0.983\pm0.072)}{(0.434\pm0.009)}$	$S_0^{K\tau e}$	$= (11.27 \pm 1.49) \times 10^5$
$D^{*0}e\nu$ channel	$S_0^{K\tau e} = \frac{(1159\pm49)}{(0.002221\pm0.000080)}\frac{(0.983\pm0.072)}{(0.442\pm0.005)}$	$S_0^{K\tau e}$	$= (11.59 \pm 1.07) \times 10^5$
$D^0e\nu$ channel	$S_0^{\pi\tau e} = \frac{(436\pm41)}{(0.000876\pm0.000044)}\frac{(0.974\pm0.057)}{(0.434\pm0.009)}$	$S_0^{\pi\tau e}$	$= (11.17 \pm 1.39) \times 10^5$
$D^{*0}e\nu$ channel	$S_0^{\pi\tau e} = \frac{(1159\pm49)}{(0.002221\pm0.000080)}\frac{(0.974\pm0.057)}{(0.442\pm0.005)}$	$S_0^{\pi\tau e}$	$= (11.48 \pm 0.94) \times 10^5$

Table 3.12: Common sensitivities for all signal modes, after including tag efficiency ratios provided the signal-side is enriched with signal-type topologies or control-type topologies.

	Combined Common Sensitivities	Correlation Coefficients
$S_0^{K\tau\mu}$	$(10.88 \pm 0.69) \times 10^5$	0.11
$S_0^{\pi\tau\mu}$	$(10.72 \pm 0.60) \times 10^5$	0.01
$S_0^{K\tau e}$	$(11.50 \pm 1.05) \times 10^5$	0.23
$S_0^{\pi\tau e}$	$(11.39 \pm 0.81) \times 10^5$	0.09

Table 3.13: Weighted average common sensitivities (normalization) for all signal modes, where correlations between $D^0\ell\nu$ and $D^{*0}\ell\nu$ common sensitivities are included.

Chapter 4

Results

4.1 Limit calculation

The signal branching fraction upper limit at the 90% confidence level for rare processes is calculated based on the number of observed events, background estimates, signal efficiencies, common sensitivities, and their associated uncertainties using the R. Barlow [45] and Feldman-Cousins [46] methods. These values are determined from our event selection, optimized minimum likelihood ratio cuts, and our $m(\tau)$ signal window. The Barlow method also provides a technique for combining the limits for multiple channels in the same experiment. To ensure non-negative branching fraction upper limits, we include the Feldman-Cousins approach as well. We present branching fraction upper limits combining the three τ decay channels for the "clean" and "dirty" signal modes, separately. The limit calculator macros designed for these specifications were developed for the original $B^{\pm} \to K^{\pm}\tau\mu$ search [19] and are used in this analysis as well.

In the following, we briefly discuss the R. Barlow method in section 4.1.1 and

the Feldman-Cousins method in section 4.1.2. A breakdown of signal efficiencies for each event selection requirement is given in Appendix N Tables N.1 -N.8 for all signal modes. Data-driven background estimates are discussed in section 4.1.3. Table 4.1 provides a summary of our optimized minimum likelihood ratio cuts and associated parameters to estimate expected backgrounds (b_i) for all signal modes. In section 4.1.4, we discuss our optimization procedure for the $m(\tau)$ signal window and minimum likelihood ratio cuts.

4.1.1 R. Barlow method

The R. Barlow limit is calculated rearranging equation 4.1, such that the branching fraction is

$$\mathcal{B}_{h\tau\ell} = \frac{1}{\epsilon_{h\tau\ell} S_0}(n_{\text{obs}} - b), \tag{4.1}$$

where μ is replaced with n_{obs}, the number of observed events after unblinding, and S is replaced with $\epsilon_{h\tau\ell} S_0$, where S_0 is determined from equation 3.12 with final common sensitivities found in Table 3.13 and $\epsilon_{h\tau\ell}$ is the final signal reconstruction efficiency found in Appendix N.

For a given value on $\mathcal{B}_{h\tau\ell}$, toy studies are used to randomly generate Gaussian distributions with measured uncertainties on $\epsilon_{h\tau\ell} \pm \Delta\epsilon_{h\tau\ell}$, $S_0 \pm \Delta S_0$, and $b \pm \Delta b$. Since the expected number of observed events should be low, our expected outcome should be based on Poisson statistics. Consider a Poisson distribution for a single τ channel,

$$\mathcal{L} = \frac{\mu^n e^{-\mu}}{n!}, \tag{4.2}$$

where $\mu = \mathcal{B}\epsilon S_0 + b$ is the mean computed from sampling the toy distributions discussed above and n is the number of observed events. The value of $\mathcal{B}$ is scanned for increasing

values starting from zero. The 90% upper limit is the value of $\mathcal{B}$ for which 10% of all measurements would give $n \leq n_{\rm obs}$.

For multiple channels, the Poisson likelihood becomes

$$\mathcal{L} = \prod_i \frac{\mu_i^{n_i} e^{-\mu_i}}{n_i!} \tag{4.3}$$

and R. Barlow recommends using $\partial \ln\mathcal{L}/\partial\mathcal{B} = 0$ to combine multiple channels, maximizing the signal branching fraction. For a detailed discussion, please see [45, 19].

4.1.2 Feldman-Cousins method

The Feldman-Cousins method for determining upper limits for a particular confidence range was developed to fix high-energy physics problems concerning proper assignment of coverage from unphysical results. There were two objectives; one associated with avoiding Bayesian interval construction, and at the same time fixing the problem of unphysical results (in our case, measurements of negative branching fractions). They introduce a new element, using a particular choice of ordering based on a ratio of likelihoods, as opposed to just one likelihood as is commonly used. A confidence interval is determined using the ratio,

$$R = P(n|\mu)/P(n|\mu_{\rm best}), \tag{4.4}$$

where $\mu_{\rm best}$ is the mean value from Poisson statistics which maximizes $P(n|\mu)$. This "ranking", or ordering, of likelihoods for various outcomes and means provides a non-Bayesian approach to fixing the problem of unphysical branching fractions, due to fluctuations where the number of observed events turns out to be less than expected background, $n_{\rm obs} - b$. For a detailed discussion, please see [46, 19]. The Feldman-Cousins upper limits on our signal

search branching fractions are found in the last column of Table 4.6.

4.1.3 Background estimation

We estimate the number of expected background events in the $m(\tau)$ signal window using a data-driven method, by taking the total number of background in data *outside* the signal window and multiplying it by the *ratio* of background events (inside / outside) from MC. The bin-by-bin values as a function of minimum likelihood ratio cut for the pion channel in our "dirty" $K\tau\mu$ analysis are shown in Figure 4.1(a). The (inside / outside) background ratio is fairly stable, which we assume is constant as a function of minimum likelihood cut. The plots of the number of background events outside the signal window vs minimum likelihood ratio cut show the Monte Carlo expectation (red) and on-resonance data (blue). The data / Monte Carlo agreement is not bad here. This data-driven background estimate is performed for all signal searches.

As an aside, if the data / Monte Carlo normalization agreement in the number of background events outside the signal region vs minimum likelihood ratio cut is bad, we assume this is still okay as long as the data / Monte Carlo shape is in agreement. In some cases this becomes a concern, especially in the case when the minimum likelihood ratio cut results in the uncertainty in the background estimate to be zero. This occurs in cases of very low statistics, when the LHR distribution runs out of data while there is still some background in MC. We have found that slightly relaxing, or excluding the minimum LHR cut keeps the optimization metric fairly unchanged.

Table 4.1 gives a summary of parameters used to estimate expected background, after final event selection and minimum likelihood ratio requirements using a 120 MeV $m(\tau)$

signal window. The "BG ratio" column is the ratio of the number of background events after all selection cuts inside / outside the $m(\tau)$ signal window (see example Figure 4.1(a) bottom). The average values and uncertainties of the background ratios are determined by-eye. The "$N_{\rm bg}$ out" columns are the number of background events after all selection cuts outside the $m(\tau)$ signal window, for MC and on-resonance data. The "b_i sig. win." column is the predicted number of background events in the $m(\tau)$ signal window after all selection cuts using the "BG ratio" and "$N_{\rm bg}$ out" from data. The final signal efficiencies ($\epsilon_{\rm sig}$) are also provided.

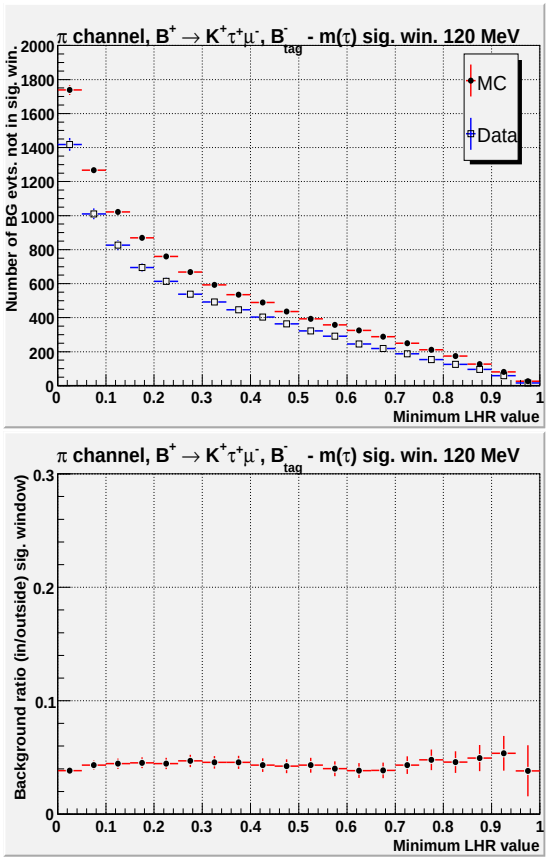

(a) Top: Background outside $m(\tau)$ signal window versus minimum likelihood ratio cut on-resonance data (blue) and standard model MC (red). Bottom: Background ratio in/outside signal window versus minimum likelihood ratio cut using MC, approximately flat at 0.05 ± 0.01. Product of top and bottom provide estimate of expected background for the corresponding minimum likelihood ratio cut (bin-by-bin).

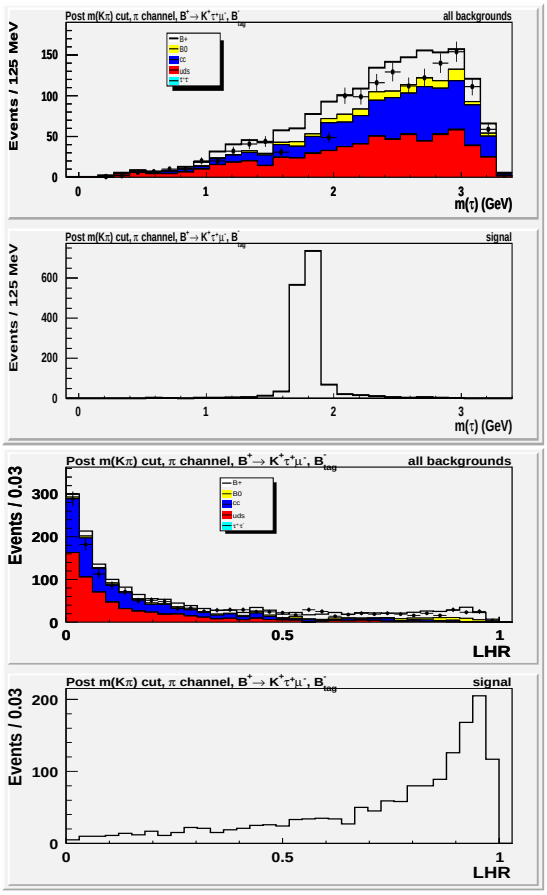

(b) The $m(\tau)$ (top-two) and likelihood ratio (bottom-two) distributions are provided, to help illustrate background estimates for this channel. Points with error bars in the top first and third distributions are on-resonance data. Bottom second and fourth distributions are signal MC.

Figure 4.1: Example of data-driven background estimate for the "dirty" $K\tau\mu$; $\tau \to \pi(n\pi^0)\nu$ channel in the 120 MeV $m(\tau)$ signal window.

Channel	LHR cut	BG ratio (sig.win./out)	$N_{\rm bg}$ out (MC)	$N_{\rm bg}$ out (data)	b_i sig.win. (data)	$\epsilon_{\rm sig}$
"Clean" $B^+ \to \pi^+\tau^-\mu^+, B^-_{\rm tag}$:						
electron	0.25	0.02 ± 0.01	89.2 ± 5.5	55 ± 7.4	0.9 ± 0.6	2.28 ± 0.17
muon	0.50	0.11 ± 0.04	30.2 ± 3.3	10 ± 3.2	1.1 ± 0.4	2.86 ± 0.19
pion	0.90	0.04 ± 0.01	155.0 ± 7.3	93 ± 9.6	3.3 ± 0.9	2.83 ± 0.19
"Dirty" $B^+ \to \pi^+\tau^+\mu^-, B^-_{\rm tag}$:						
electron	0.25	0.012 ± 0.003	223.2 ± 8.7	171 ± 13.1	2.1 ± 0.5	3.83 ± 0.22
muon	0.50	0.04 ± 0.01	128.5 ± 6.6	89 ± 9.4	3.6 ± 0.9	4.82 ± 0.25
pion	0.75	0.05 ± 0.01	571.8 ± 14.1	512 ± 22.6	25.6 ± 2.6	9.12 ± 0.33
"Clean" $B^+ \to \pi^+\tau^-e^+, B^-_{\rm tag}$:						
electron	0.25	0.05 ± 0.03	3.8 ± 1.2	1 ± 1.0	0.05 ± 0.03	1.95 ± 0.16
muon	0.25	0.03 ± 0.01	44.0 ± 3.9	16 ± 4.0	0.40 ± 0.16	2.76 ± 0.19
pion	0.25	0.04 ± 0.01	262.8 ± 9.9	172 ± 13.1	6.02 ± 1.38	5.75 ± 0.27
"Dirty" $B^+ \to \pi^+\tau^+e^-, B^-_{\rm tag}$:						
electron	0.50	0.03 ± 0.01	39.7 ± 3.6	31 ± 5.57	1.0 ± 0.4	2.87 ± 0.19
muon	0.25	0.01 ± 0.01	292.8 ± 10.1	247 ± 15.7	3.0 ± 1.2	4.55 ± 0.24
pion	0.75	0.07 ± 0.03	101.5 ± 5.8	82 ± 9.1	5.7 ± 2.5	3.68 ± 0.22
"Clean" $B^+ \to K^+\tau^-\mu^+, B^-_{\rm tag}$:						
electron	0.00	0.02 ± 0.01	23.1 ± 3.0	22 ± 4.7	0.4 ± 0.2	2.57 ± 0.18
muon	0.25	0.08 ± 0.05	11.3 ± 1.9	4 ± 2.0	0.3 ± 0.2	3.23 ± 0.20
pion	0.90	0.05 ± 0.02	46.0 ± 4.2	39 ± 6.2	1.8 ± 0.8	4.07 ± 0.23
"Dirty" $B^+ \to K^+\tau^+\mu^-, B^-_{\rm tag}$:						
electron	0.25	0.03 ± 0.01	8.6 ± 1.7	5 ± 2.2	0.2 ± 0.1	3.66 ± 0.22
muon	0.90	0.06 ± 0.03	3.8 ± 1.2	3 ± 1.7	0.2 ± 0.1	3.61 ± 0.22
pion	0.75	0.05 ± 0.01	211.5 ± 8.7	153 ± 12.4	6.9 ± 1.5	9.10 ± 0.33
"Clean" $B^+ \to K^+\tau^-e^+, B^-_{\rm tag}$:						
electron	0.00	0.10 ± 0.02	14.2 ± 2.2	6 ± 2.5	0.57 ± 0.12	2.17 ± 0.16
muon	0.40	0.03 ± 0.01	6.3 ± 1.5	4 ± 2.0	0.10 ± 0.04	2.70 ± 0.18
pion	0.50	0.05 ± 0.02	48.9 ± 4.3	33 ± 5.7	1.48 ± 0.50	4.81 ± 0.24
"Dirty" $B^+ \to K^+\tau^+e^-, B^-_{\rm tag}$:						
electron	0.25	0.10 ± 0.06	5.7 ± 1.4	8 ± 2.8	0.80 ± 0.48	2.78 ± 0.18
muon	0.50	0.05 ± 0.02	7.3 ± 1.6	3 ± 1.7	0.14 ± 0.06	3.20 ± 0.19
pion	0.50	0.04 ± 0.01	162.8 ± 7.5	132 ± 11.5	4.62 ± 1.32	8.74 ± 0.31

Table 4.1: Summary of background estimates (b_i) and signal efficiencies ($\epsilon_{\rm sig}$) for all τ decay channels using a 120 MeV $m(\tau)$ signal window with final event selection and optimal minimum likelihood ratio cuts used to compute expected backgrounds in Appendix P.

4.1.4 Optimization

We performed a 2-D optimization varying the $m(\tau)$ signal window range and the minimum likelihood ratio cut. Our optimization metric for each channel is the expected average branching fraction upper limit at the 90% confidence level using the R.Barlow method for individual τ decay channels. The optimization for each parameter is performed by holding the other parameter fixed when performing the limit calculation.

$m(\tau)$ signal window optimization

We selected various $m(\tau)$ signal window ranges centered about the nominal τ invariant mass of 1.777 GeV: [1.60,1.95], [1.65,1.90], [1.677,1.877], [1.702,1.852], [1.717,1.837], & [1.727,1.827] GeV. We plot the expected average branching fraction upper limits vs. the $m(\tau)$ signal window for fixed minimum likelihood ratio cuts: 0.0, 0.25, 0.50, 0.75, & 0.90 for the $\pi\tau\ell$ searches and 0.0, 0.25, 0.40, 0.50, 0.75, & 0.90 for the $K\tau\ell$ searches. A parabolic shape would be good, indicating the choice of signal window range is significant, while a flat shape would indicate a weak dependence on the choice of signal window range. The plots can be found in Appendix O. Our study shows a very weak dependence on the $m(\tau)$ signal window range and that a 120 MeV window in the range [1.717,1.837] GeV is optimal for all signal searches.

Minimum likelihood ratio cut optimization

In Figure 4.2, we provide detailed information on the relative signal efficiency (top), expected number of background events outside the signal region (2nd down), ratio of background inside to outside the signal region (3rd down), and the expected average

upper limit branching fraction at the 90% confidence level using the R. Barlow method as a function of minimum likelihood ratio cut. The minimum likelihood ratio cut is incremented from [0.00,1.00] in units of 0.05 (20 bins). We find the optimal minimum likelihood ratio cuts are 0.25, 0.25, 0.25 for the electron, muon, and pion channels, respectively in the "clean" $\pi\tau e$ search. These minimum likelihood ratio cuts correspond to the lowest average signal branching fraction computed using the R. Barlow method. The expected number of background events outside the signal region and ratio of background inside to outside the signal region should correspond to the results provided in Table 4.1 for the "clean" $\pi\tau e$ mode. Our optimal minimum likelihood ratio cuts are signal mode dependent. These cuts are also summarized in Table 4.1.

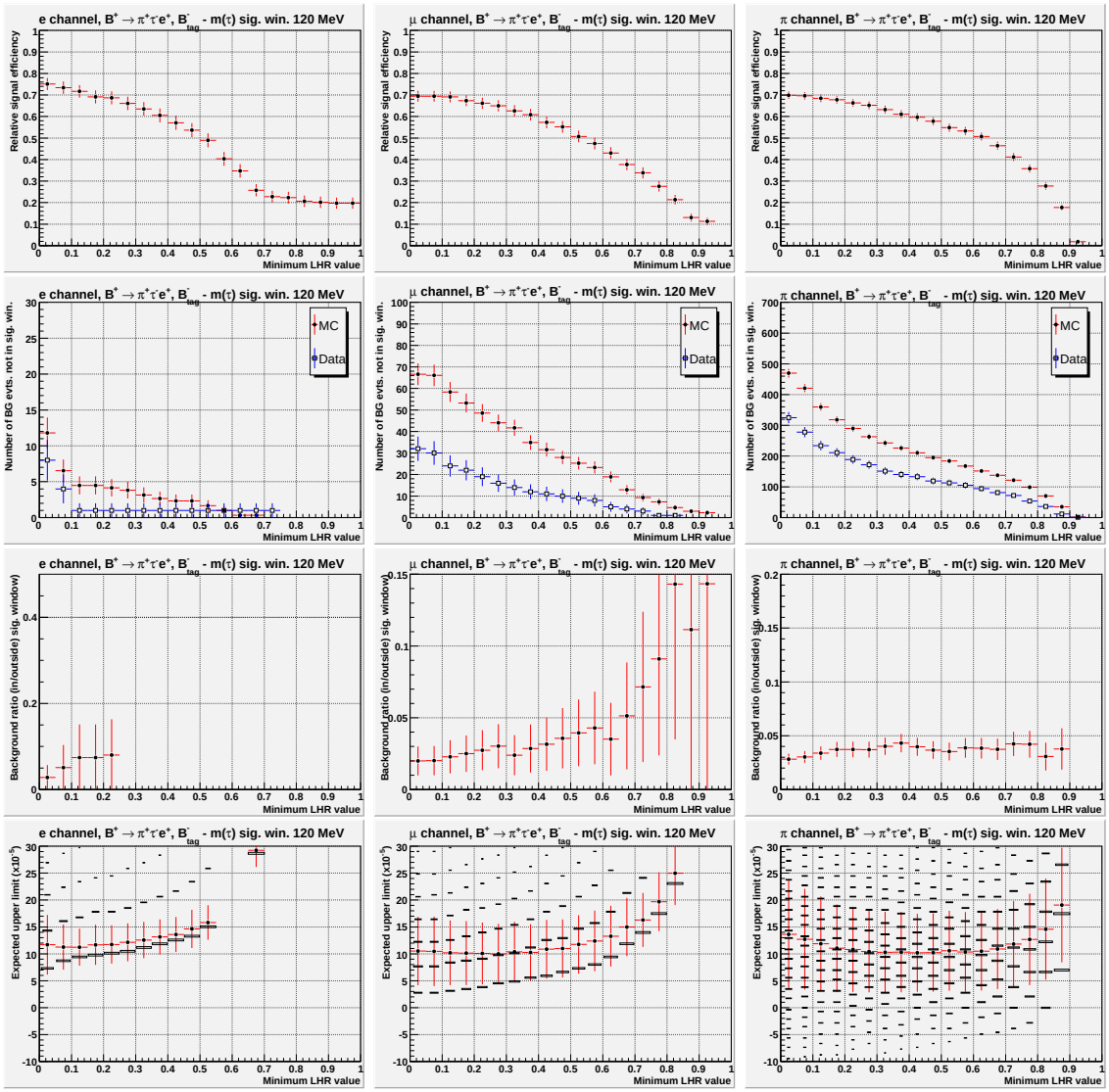

Figure 4.2: **"Clean" $\pi\tau e$**: Graphs of the relative signal efficiency (top), expected number of background events *outside* the signal region (2nd down), ratio of background events inside / outside the signal region (3rd down), and the expected 90% confidence level upper limit (using the Barlow method) on the signal branching fraction (bottom) as a function of the minimum likelihood ratio cut for the **electron** (left), **muon** (middle), and **pion** (right) channels, with a simplified 120 MeV optimal signal window for all τ decay channels. The points with bars in the bottom plots show the average value and RMS of the set of expected upper limits for that particular minimum likelihood ratio value.

4.2 Systematic Uncertainties

We perform systematic uncertainty studies on the signal efficiency ($\epsilon_{\rm sig}$), after the minimum likelihood ratio cut, and on the common sensitivity (S_0), in the control sample normalization. The signal efficiency systematic arises from the fact that the minimum LHR cut is not applied in our control sample. The common sensitivity systematic arises only in the $\pi\tau\ell$ searches, due to the kaon in the control sample and a pion in the signal reconstruction. In the $\pi\tau\ell$ searches, we include additional kaon and pion vetoes in the signal reconstruction. We argue that a K vs π PID efficiency systematic on the common sensitivity should account for any additional systematics not already removed in the normalization using our control sample. Since we estimate background using on-resonance data from the $m(\tau)$ signal window sideband after minimum likelihood ratio cuts, we do not compute a systematic uncertainty on the expected background. The result of the systematic uncertainty studies are given below.

Table 4.2 provides a summary of the total absolute error, which include statistical and systematic errors added in quadrature, for each signal efficiency after applying systematic variations to the likelihood ratio inputs. A breakdown of the total relative errors can be found in Tables 4.3 and 4.4, for the $K\tau\ell$ and $\pi\tau\ell$ signal efficiencies, respectively. These total absolute errors go directly into our limit calculation.

The last row in Table 4.5 provides the systematic uncertainty associated with our common sensitivity, evaluated from the $D\mu\nu$ and $De\nu$ control samples. We add total statistical (found in Table 3.12) and systematic uncertainties on the common sensitivity in quadrature. The total absolute error must be included in the final limit calculation as well.

4.2.1 Systematic error on likelihood ratio cut efficiency

In this section, we discuss the method of evaluating the systematic uncertainty on the efficiency of the minimum likelihood ratio cut. A brief explanation of the variations on each input component in the likelihood ratio calculation is given below. For background PDF inputs to the likelihood ratio, we switch from using luminosity-weighted Monte Carlo samples (as our nominal source) to the on-resonance $m(\tau)$ blinding window data sideband. There is one variation per channel (e, μ, & π) for each of the likelihood ratio inputs: $\sum E_{\rm cal}$, $|cos(\theta_{\rm thr})|$, primary lepton PID level ($h\tau\mu$ modes only), and secondary lepton PID level (μ channels only and completely excluded in both $\pi\tau e$ modes). For signal MC PDF inputs, we vary each channel holding everything else fixed. Here is a summary:

- $\sum \mathbf{E}_{\rm cal}$: We vary the amount of events with exactly $\sum E_{\rm cal} = 0$ by $\pm$ the magnitude of the difference between the nominal value from signal MC and the data semi-leptonic double-tag sample (absolute). We also use the data semi-leptonic double-tag sample to replace the signal MC shape. The semi-leptonic double tag is obtained from our control sample, within $m(K\pi) \in [1.845, 1.885]$ GeV. Details are found in Appendix Q.

- $|\mathbf{cos}(\theta_{\rm thr})|$: We use a flat line (uniform) as the variation from the nominal signal PDF.

- **primary lepton PID level**: We vary each bin of the distribution by $\pm 2.5\%$ (absolute) for the `VL`, `L`, and `T` categories and $\pm 3.2\%$ for the `VT` category. The four variations are then added in quadrature. Applied in $h\tau\mu$ modes only.

- **secondary lepton PID level**: Same as variations in primary lepton PID systematic. Applied in μ channels only and completely excluded in both $\pi\tau e$ modes.

The deviations from each variation described above is added in quadrature for each channel.

The results of total absolute error on the signal efficiency, from variations in likelihood ratio inputs, is given in Table 4.2 The largest systematic uncertainties are observed in the "clean" $\pi\tau e$ and "clean" $K\tau e$ electron channels of 41.4% and 40.2%, respectively. We observe on the order of 20% in the "dirty" $\pi\tau e$ pion channel, "dirty" $K\tau\mu$ muon channel, and "clean" and "dirty" $K\tau e$ muon channels.

A breakdown of the signal efficiency likelihood ratio input systematics are found in Table 4.3 and Table 4.4 for $K\tau\ell$ and $\pi\tau\ell$ modes, respectively. We observe that the largest systematic errors, in general, come from our variations in the modeling of background for the $\sum E_{\text{cal}}$ and $|cos(\theta_{\text{thr}})|$ distributions.

	"Clean"			"Dirty"		
Total Absolute Error	electron	muon	pion	electron	muon	pion
$\pi\tau\mu$	0.18%	0.39%	0.24%	0.25%	0.32%	0.57%
$\pi\tau e$	0.81%	0.31%	0.31%	0.34%	0.36%	0.99%
$K\tau\mu$	0.19%	0.36%	0.38%	0.30%	0.70%	0.50%
$K\tau e$	0.16%	0.56%	0.59%	1.12%	0.70%	1.19%

Table 4.2: Summary of total absolute errors on ϵ_{sig}, from variations in likelihood ratio inputs.

	"Clean"			"Dirty"		
	electron	muon	pion	electron	muon	pion
Variation			$K\tau\mu$			
sig, primary μ PID	0.0%	1.1%	2.9%	1.6%	3.0%	0.9%
sig, secondary ℓ PID	0.0%	0.7%	0.0%	0.0%	2.2%	0.0%
sig, $\sum E_{\rm cal}$ zero bin	0.0%	0.4%	1.0%	0.4%	0.4%	0.1%
sig, $\sum E_{\rm cal}$ polynomial	0.0%	1.3%	4.6%	0.0%	0.8%	2.2%
sig, $\lvert\cos(\theta_{\rm thr})\rvert$	0.0%	0.0%	2.3%	0.4%	0.8%	1.9%
bkg, $\sum E_{\rm cal}$	0.0%	7.2%	0.3%	1.8%	10.6%	1.6%
bkg, $\lvert\cos(\theta_{\rm thr})\rvert$	0.0%	5.9%	3.6%	2.5%	14.8%	2.4%
bkg, primary μ PID	0.0%	0.8%	2.6%	0.4%	2.3%	0.4%
bkg, secondary ℓ PID	0.0%	0.0%	0.0%	2.2%	0.8%	0.0%
total systematic error	0.0%	9.5%	7.5%	4.2%	18.8%	4.2%
MC statistical error	6.8%	6.4%	5.7%	5.6%	6.2%	3.6%
total relative error	±6.8%	±11.5%	±9.4%	±7.0%	±19.8%	±5.5%
total absolute error	±0.19%	±0.36%	±0.38%	±0.30%	±0.70%	±0.50%
Variation			$K\tau e$			
sig, primary e PID	0.0%	0.0%	0.0%	0.0%	0.0%	0.0%
sig, secondary ℓ PID	0.0%	1.5%	0.0%	0.0%	4.5%	0.0%
sig, $\sum E_{\rm cal}$ zero bin	0.0%	0.0%	0.3%	2.3%	2.2%	0.5%
sig, $\sum E_{\rm cal}$ polynomial	0.0%	2.3%	2.8%	1.3%	1.9%	3.4%
sig, $\lvert\cos(\theta_{\rm thr})\rvert$	0.0%	0.5%	1.0%	0.0%	0.4%	2.3%
bkg, $\sum E_{\rm cal}$	0.0%	7.7%	1.5%	17.2%	3%	2.5%
bkg, $\lvert\cos(\theta_{\rm thr})\rvert$	0.0%	17.2%	7.6%	35.6%	19%	4.2%
bkg, primary e PID	0.0%	5.0%	7.6%	2.6%	6.7%	11.6%
bkg, secondary ℓ PID	0.0%	0.9%	0.0%	0.0%	1.9%	0.0%
total systematic error	0.0%	19.7%	11.3%	39.7%	21.1%	13.2%
MC statistical error	7.4%	6.7%	5.0%	6.5%	5.9%	3.5%
total relative error	±7.4%	±20.8%	±12.4%	±40.2%	±21.9%	±13.7%
total absolute error	±0.16%	±0.56%	±0.59%	±1.12%	±0.70%	±1.19%

Table 4.3: $K\tau\ell$ Systematic error on the signal likelihood ratio cut efficiency. Unless stated otherwise, all errors are relative (i.e. $\delta\epsilon_{\rm sig}/\epsilon_{\rm sig}$).

		"Clean"			"Dirty"	
	electron	muon	pion	electron	muon	pion
Variation			$\pi\tau\mu$			
sig, primary μ PID	1.6%	1.5%	3.3%	1.9%	1.5%	2.6%
sig, secondary ℓ PID	0.0%	2.3%	0.0%	0.0%	0.8%	0.0%
sig, $\sum E_{\rm cal}$ zero bin	0.0%	0.7%	0.7%	1.0%	0.3%	0.7%
sig, $\sum E_{\rm cal}$ polynomial	0.0%	1.9%	2.4%	1.4%	1.9%	3.7%
sig, $\lvert\cos(\theta_{\rm thr})\rvert$	1.8%	0.5%	0.0%	1.7%	0.6%	1.0%
bkg, $\sum E_{\rm cal}$	0.0%	1.4%	1.4%	0.0%	2.8%	0.1%
bkg, $\lvert\cos(\theta_{\rm thr})\rvert$	0.6%	11.3%	2.9%	0.3%	1.7%	1.2%
bkg, primary μ PID	1.2%	0.9%	1.4%	0.0%	0.3%	1.6%
bkg, secondary ℓ PID	0.0%	0.9%	0.0%	0.3%	0.3%	0.0%
total systematic error	2.7%	12.0%	5.4%	3.1%	4.2%	5.1%
MC statistical error	7.5%	6.6%	6.8%	5.8%	5.2%	3.6%
total relative error	±8.0%	±13.7%	±8.7%	±6.6%	±6.7%	±6.2%
total absolute error	±0.18%	±0.39%	±0.24%	±0.25%	±0.32%	±0.57%
Variation			$\pi\tau e$			
sig, primary e PID	0.0%	0.0%	0.0%	0.0%	0.0%	0.0%
sig, secondary ℓ PID	0.0%	0.0%	0.0%	0.0%	0.0%	0.0%
sig, $\sum E_{\rm cal}$ zero bin	0.7%	1.0%	0.2%	3.6%	0.6%	1.9%
sig, $\sum E_{\rm cal}$ polynomial	0.0%	1.0%	1.9%	1.9%	3.6%	7.0%
sig, $\lvert\cos(\theta_{\rm thr})\rvert$	0.7%	1.0%	0.5%	5.6%	0.9%	1.8%
bkg, $\sum E_{\rm cal}$	22.8%	2.4%	0.2%	2.3%	1.5%	12.5%
bkg, $\lvert\cos(\theta_{\rm thr})\rvert$	33.1%	4.9%	0.5%	1.9%	0.9%	4.0%
bkg, primary e PID	4.1%	2%	1.9%	2.3%	2.1%	21.6%
bkg, secondary ℓ PID	3.4%	6.3%	0.0%	6.1%	3.6%	0.0%
total systematic error	40.6%	8.7%	2.8%	10.0%	5.9%	26.4%
MC statistical error	8.2%	6.9%	4.7%	6.6%	5.3%	6.0%
total relative error	±41.4%	±11.1%	±5.5%	±12.0%	±7.9%	±27.1%
total absolute error	±0.81%	±0.31%	±0.31%	±0.34%	±0.36%	±0.99%

Table 4.4: $\pi\tau\ell$ Systematic error on the signal likelihood ratio cut efficiency. Unless stated otherwise, all errors are relative (i.e. $\delta\epsilon_{\rm sig}/\epsilon_{\rm sig}$).

4.2.2 K vs π PID efficiency systematic on sensitivity - $\pi\tau\ell$ modes

We perform an unbinned maximum likelihood fit on ΔE distributions, reconstructing D^0 & D^{*0} fit yields (recall subsection 3.5.3 - Control Sample ΔE Fit Yields) requiring various combinations of hadron or no hadron PID. The ratio of PID efficiencies using Monte Carlo and on-resonance samples allow us to extract a systematic uncertainty on our common sensitivity, S_0. We account for this systematic by comparing kaon PID efficiency with pion PID efficiency, $\frac{\epsilon_{\text{KPID}}}{\epsilon_{\pi\text{PID}}}$, using a ratio of on-resonance data to MC,

$$R_{\text{syst}} = \frac{\epsilon_{\text{KPID}}^{(\text{onres})}/\epsilon_{\pi\text{PID}}^{(\text{onres})}}{\epsilon_{\text{KPID}}^{(\text{MC})}/\epsilon_{\pi\text{PID}}^{(\text{MC})}}. \tag{4.5}$$

The kaon vs. pion PID efficiency systematic is necessary for $B^+ \to \pi^+\tau\ell$ searches only. The deviation from 1.000 along with the propagated uncertainty added in quadrature is how we define this systematic. See Table 4.5 for a summary of the kaon vs. pion PID efficiency systematics and the sum of D^0 & D^{*0} ΔE fit yields with shape parameters allowed to vary. Details are found in Appendix R.

Shape & Yield Varied from ΔE Fits	$\text{MC}_{D\mu\nu}$ $(D^0 + D^{*0})$	$\text{Onres}_{D\mu\nu}$ $(D^0 + D^{*0})$	$\text{MC}_{De\nu}$ $(D^0 + D^{*0})$	$\text{Onres}_{De\nu}$ $(D^0 + D^{*0})$
$N_{\text{KPID}\pi\text{PID}} = N^0\epsilon_{\text{K}}\epsilon_{\pi}$	1656	1473	1670	1568
$N_{\text{KPID}} = N^0\epsilon_{\text{K}}$	1663	1480	1679	1577
N^0 (No hadron PID)	1762	1595	1816	1710
ϵ_{K} (%)	94.4 ± 0.5	92.8 ± 0.6	92.5 ± 0.6	92.2 ± 0.6
ϵ_{π} (%)	99.6 ± 0.2	99.5 ± 0.2	99.5 ± 0.2	99.4 ± 0.2
$\epsilon_{\text{K}}/\epsilon_{\pi}$ (%)	94.8 ± 0.6	93.2 ± 0.7	93.0 ± 0.6	92.8 ± 0.7
R_{syst}	0.984 ± 0.009		0.998 ± 0.010	
K vs. π PID ϵ_{syst}	1.8%		1.0%	

Table 4.5: kaon vs. pion PID efficiency systematic (ϵ_{syst}) with shape and yield fit parameters varied (deviation from 1.000 and uncertainty added in quadrature).

4.3 Final results

Our unblinded results are summarized in Table 4.6, which are consistent with no new physics. The estimated backgrounds are consistent with standard model expectations and the upper limits on the branching fractions for these signal searches using the R. Barlow and Feldman-Cousins methods at the 90% confidence levels are as such. The unblinded τ invariant mass distributions are found in Figures 4.3-4.6. Log likelihood scans are provided in Figures 4.7-4.8, for the number of observed events with Poisson means using the R. Barlow method, where the maximum value of the likelihood determines our signal branching fraction $\mathcal{B}$, as the "central value". 1-sigma positive and negative errors are determined from 0.5 of the log likelihood scan where $\mathcal{B}$ is our central value, using the number of observed events found after unblinding.

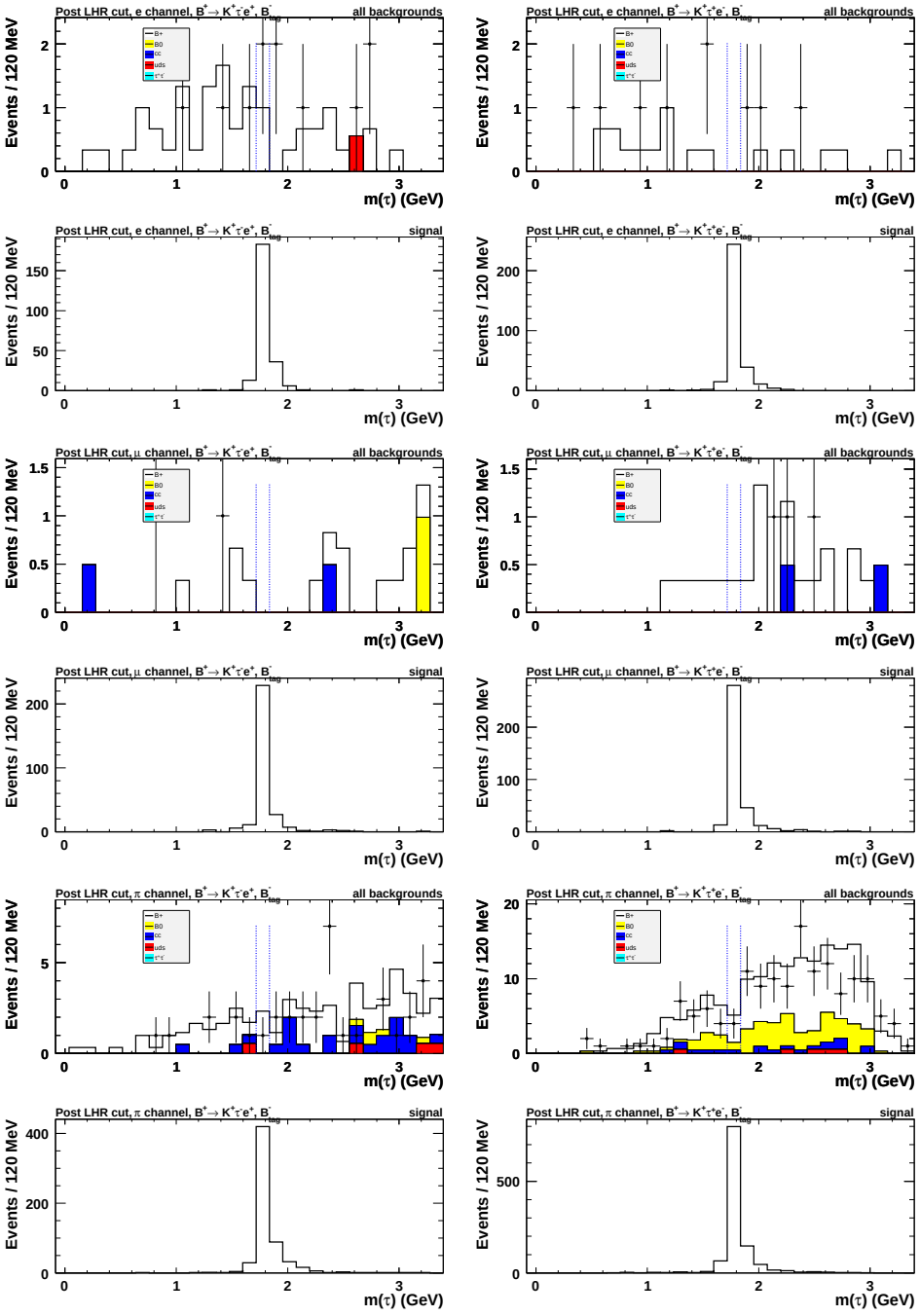

Figure 4.3: Unblinded $m(\tau)$ distributions after final event selection for "clean" (left) and "dirty" (right) $\boldsymbol{K\tau e}$ signal searches. Number of observed events consistent with SM expectations.

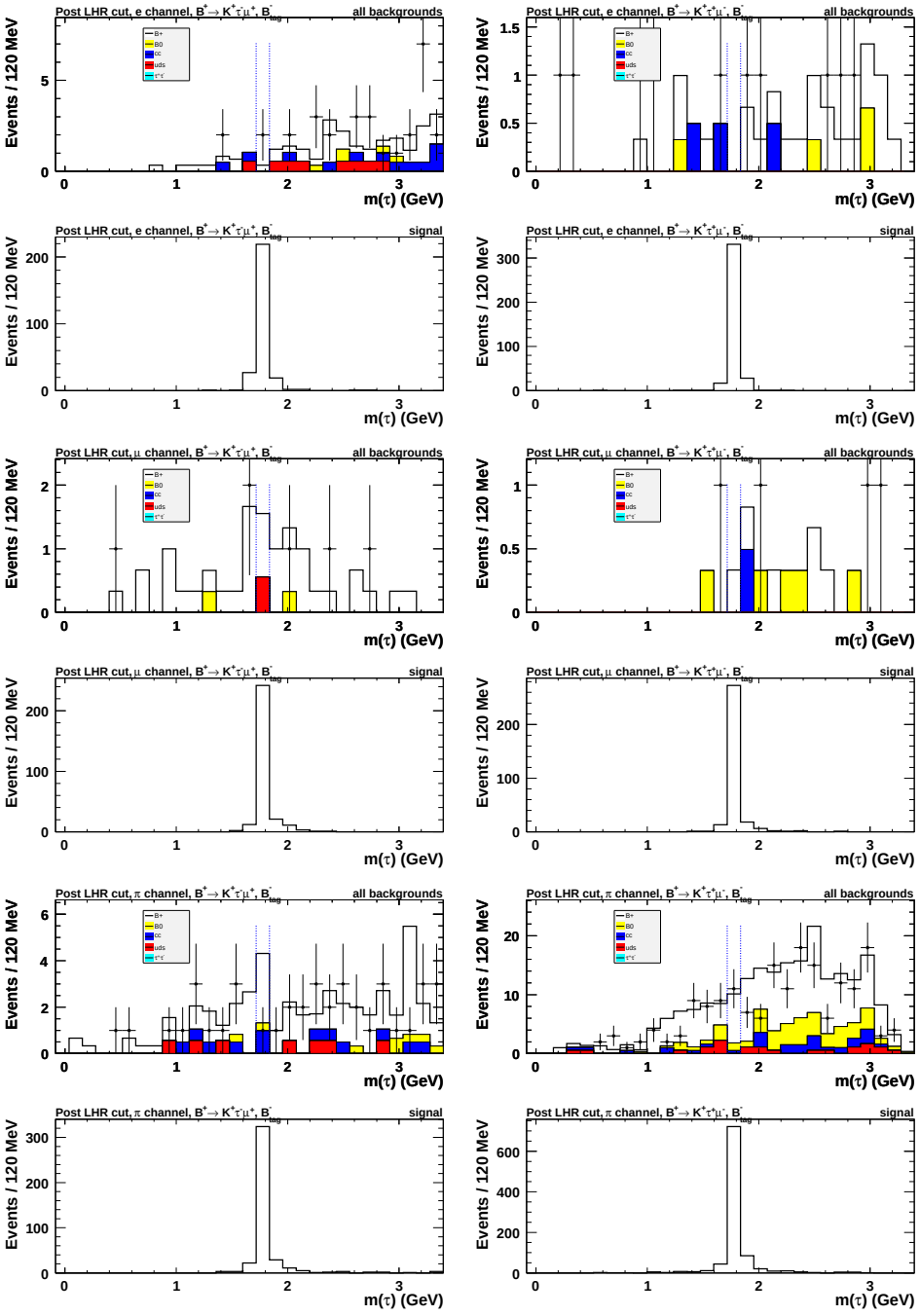

Figure 4.4: Unblinded $m(\tau)$ distributions after final event selection for "clean" (left) and "dirty" (right) $\boldsymbol{K\tau\mu}$ signal searches. Number of observed events consistent with SM expectations.

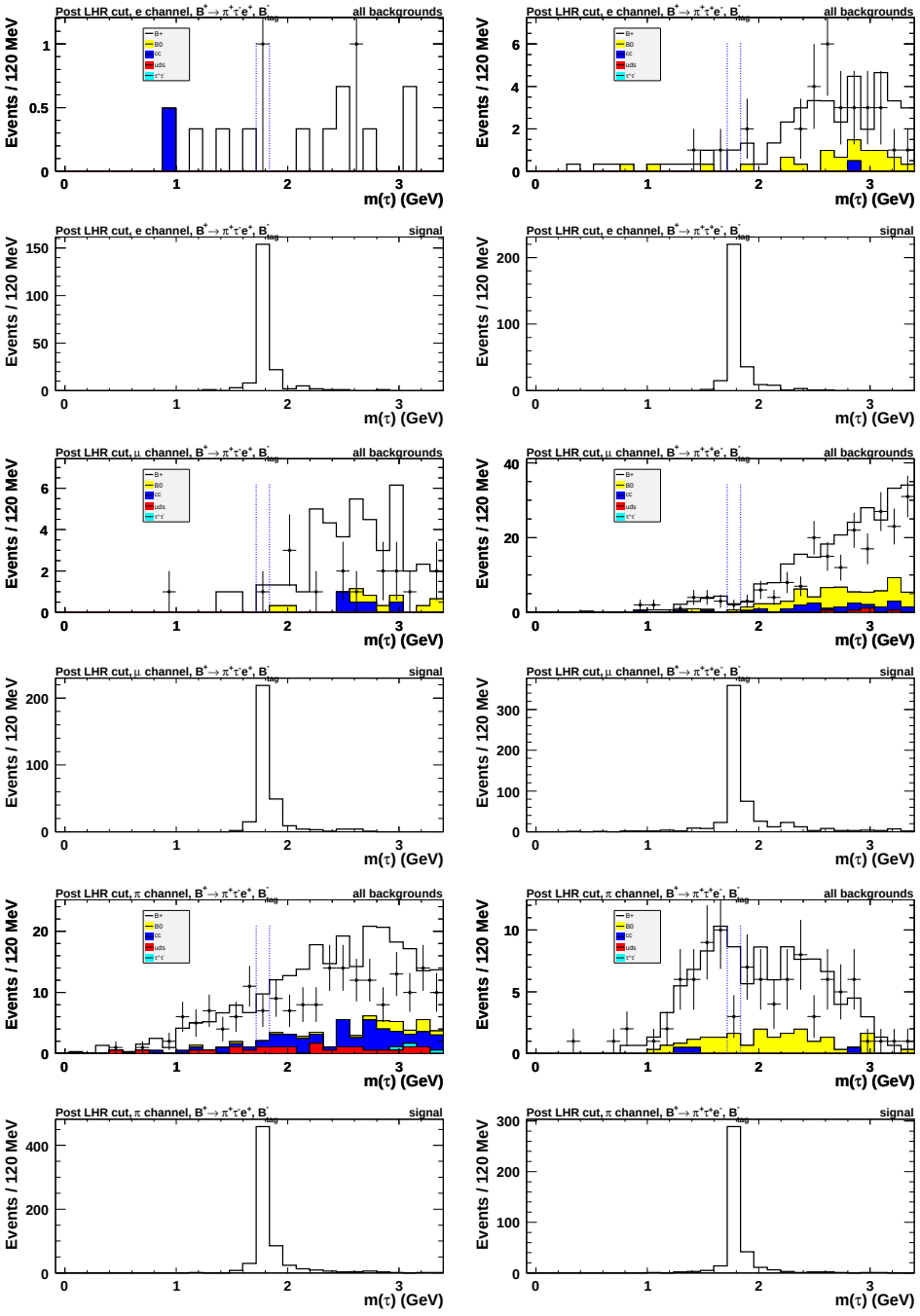

Figure 4.5: Unblinded $m(\tau)$ distributions after final event selection for "clean" (left) and "dirty" (right) $\boldsymbol{\pi\tau e}$ signal searches. Number of observed events consistent with SM expectations.

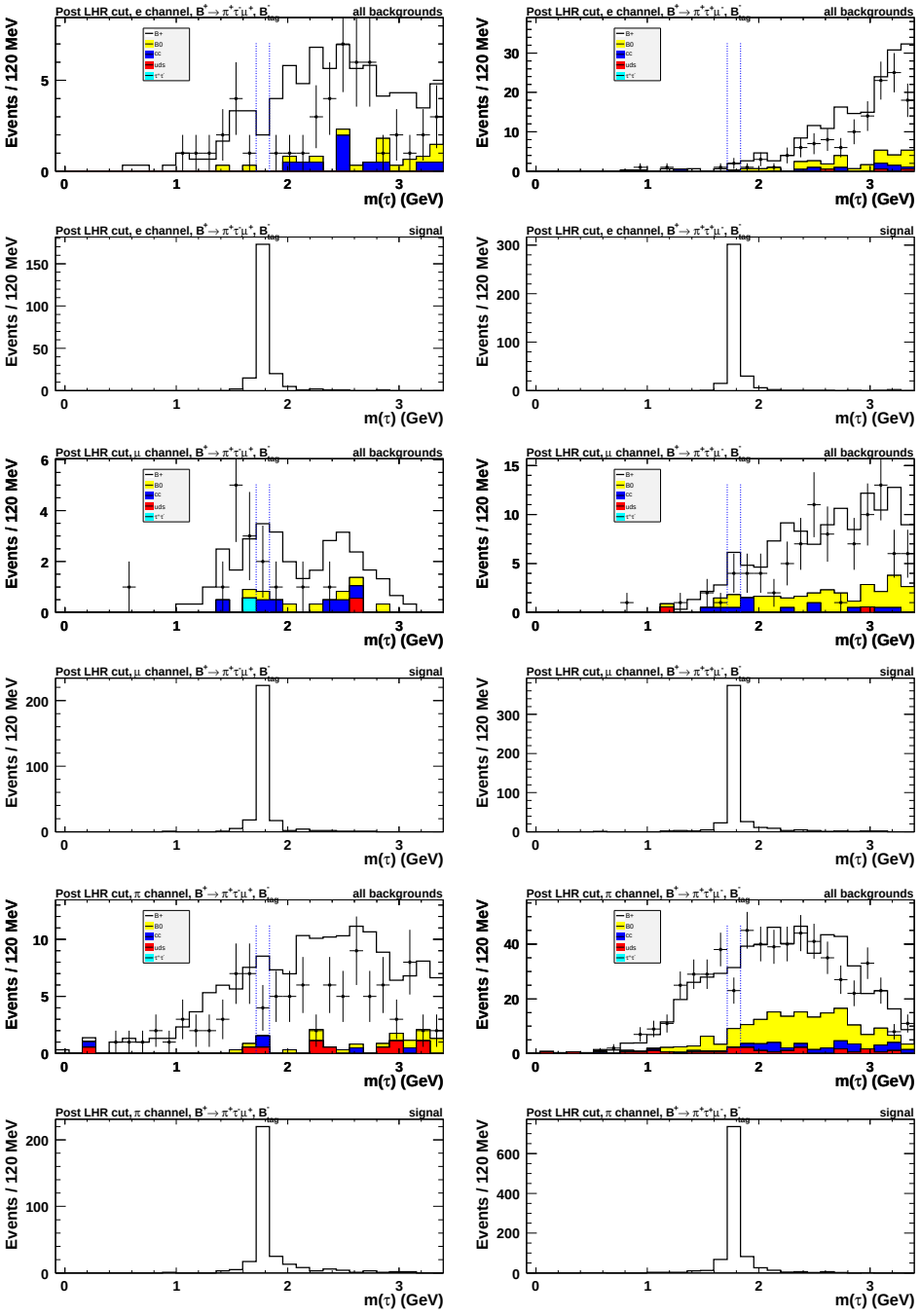

Figure 4.6: Unblinded $m(\tau)$ distributions after final event selection for "clean" (left) and "dirty" (right) $\boldsymbol{\pi\tau\mu}$ signal searches. Number of observed events consistent with SM expectations.

Channel	LHR cut	b_i sig.win. (data)	n_i sig.win. (data)	R. Barlow UL on $\mathcal{B}$ @ 90% CL	Feldman-Cousins UL on $\mathcal{B}$ @ 90% CL
	"Clean"	$\mathcal{B}(B^+ \to \pi^+\tau^-\mu^+, B^-_{\rm tag})$		$< 5.0 \times 10^{-5}$	$< 6.2 \times 10^{-5}$
electron	0.25	0.9 ± 0.6	0		
muon	0.50	1.1 ± 0.4	2		
pion	0.90	3.3 ± 0.9	4		
	"Dirty"	$\mathcal{B}(B^+ \to \pi^+\tau^+\mu^-, B^-_{\rm tag})$		$< 3.5 \times 10^{-5}$	$< 4.5 \times 10^{-5}$
electron	0.25	2.1 ± 0.5	2		
muon	0.50	3.6 ± 0.9	4		
pion	0.75	25.6 ± 2.6	23		
	"Clean"	$\mathcal{B}(B^+ \to \pi^+\tau^-e^+, B^-_{\rm tag})$		$< 6.9 \times 10^{-5}$	$< 7.4 \times 10^{-5}$
electron	0.25	0.05 ± 0.03	1		
muon	0.25	0.40 ± 0.16	1		
pion	0.25	6.02 ± 1.38	7		
	"Dirty"	$\mathcal{B}(B^+ \to \pi^+\tau^+e^-, B^-_{\rm tag})$		$< 0.5 \times 10^{-5}$	$< 2.0 \times 10^{-5}$
electron	0.50	1.0 ± 0.4	0		
muon	0.25	3.0 ± 1.2	2		
pion	0.75	5.7 ± 2.5	3		
	"Clean"	$\mathcal{B}(B^+ \to K^+\tau^-\mu^+, B^-_{\rm tag})$		$< 3.9 \times 10^{-5}$	$< 4.5 \times 10^{-5}$
electron	0.00	0.4 ± 0.2	2		
muon	0.25	0.3 ± 0.2	0		
pion	0.90	1.8 ± 0.8	1		
	"Dirty"	$\mathcal{B}(B^+ \to K^+\tau^+\mu^-, B^-_{\rm tag})$		$< 2.2 \times 10^{-5}$	$< 2.8 \times 10^{-5}$
electron	0.25	0.15 ± 0.05	0		
muon	0.90	0.18 ± 0.09	0		
pion	0.75	6.88 ± 1.53	11		
	"Clean"	$\mathcal{B}(B^+ \to K^+\tau^-e^+, B^-_{\rm tag})$		$< 3.4 \times 10^{-5}$	$< 4.3 \times 10^{-5}$
electron	0.00	0.57 ± 0.12	2		
muon	0.40	0.10 ± 0.04	0		
pion	0.50	1.48 ± 0.50	1		
	"Dirty"	$\mathcal{B}(B^+ \to K^+\tau^+e^-, B^-_{\rm tag})$		$< 0.8 \times 10^{-5}$	$< 1.5 \times 10^{-5}$
electron	0.25	0.8 ± 0.48	0		
muon	0.50	0.135 ± 0.06	0		
pion	0.50	4.62 ± 1.32	4		

Table 4.6: b_i is the expected background in data after optimized event selection. n_i is the number of actual observed events in data after unblinding. R. Barlow and Feldman-Cousins upper limits on signal branching fractions at the 90% confidence level are also given.

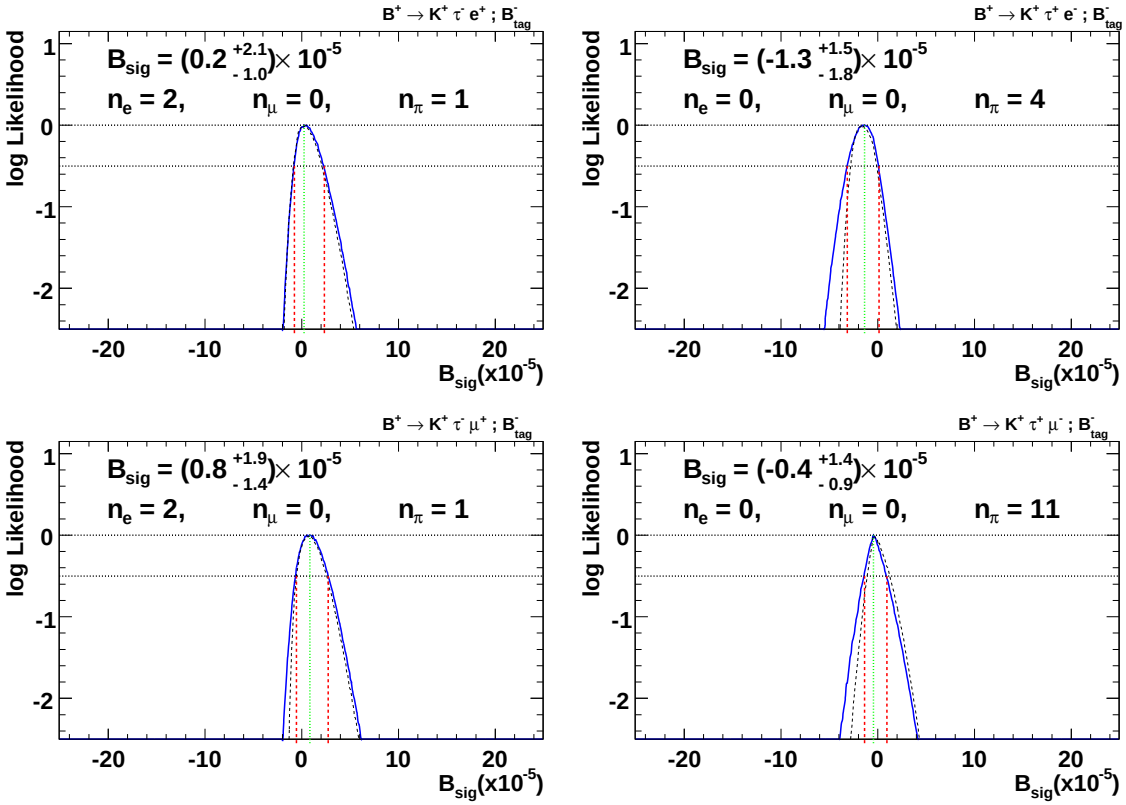

Figure 4.7: Log likelihood scan of signal branching fractions for $K\tau\ell$ signal searches, with central values and deviations of 0.5 given as positive and negative uncertainties.

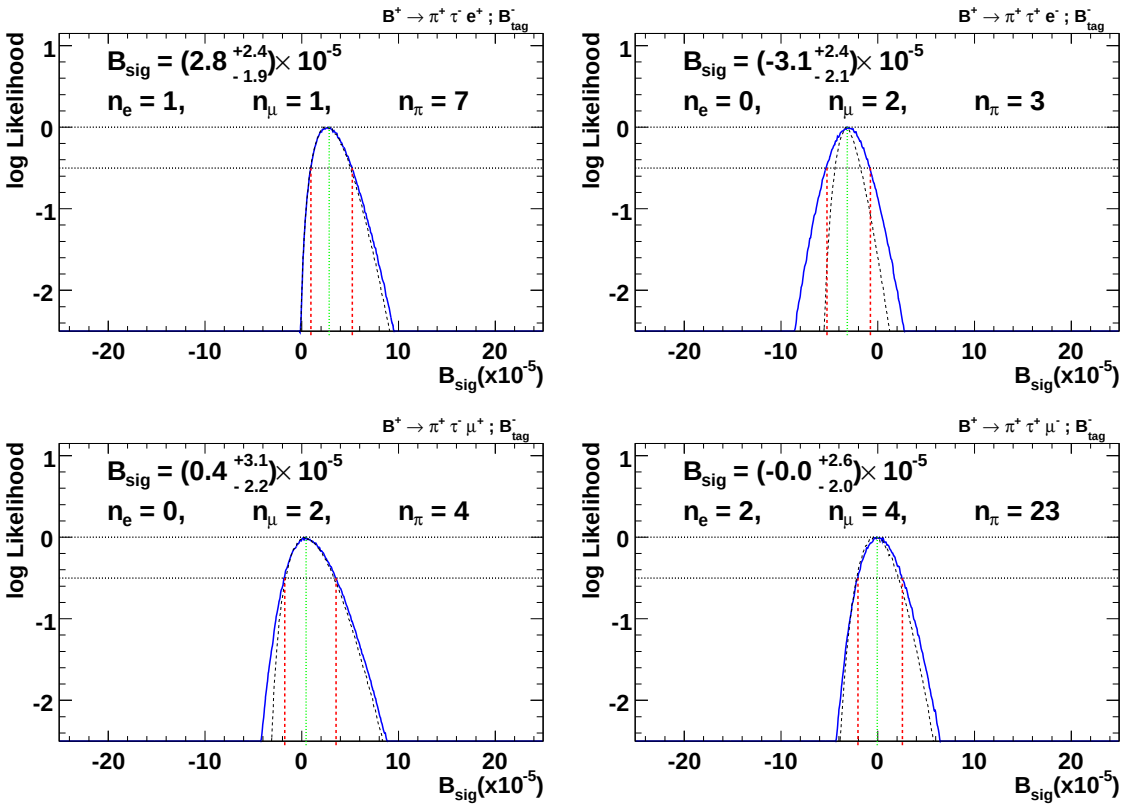

Figure 4.8: Log likelihood scan of signal branching fractions for $\pi\tau\ell$ signal searches, with central values and deviations of 0.5 given as positive and negative uncertainties.

Chapter 5

Conclusion

The Feldman-Cousins method for determining confidence intervals at the 90% upper limit on our signal search branching fractions are again provided in Table 5.1. Observe

Signal Search	Clean ($\times 10^{-5}$)	Dirty ($\times 10^{-5}$)
$\mathcal{B}(B^+ \to \pi^+ \tau \mu)$	< 6.2	< 4.5
$\mathcal{B}(B^+ \to \pi^+ \tau e)$	< 7.4	< 2.0
$\mathcal{B}(B^+ \to K^+ \tau \mu)$	< 4.5	< 2.8
$\mathcal{B}(B^+ \to K^+ \tau e)$	< 4.3	< 1.5

Table 5.1: Summary of Feldman-Cousins UL branching fractions at the 90% CL for "clean" (left) and "dirty" (right) searches.

dirty signal modes perform best, giving lower $\mathcal{B}$ UL at 90% CL. The search that provided the best sensitivity from the full *BABAR* dataset using the R. Barlow method came from the "dirty" $B \to \pi\tau e$ analysis with $< 0.5 \times 10^{-5}$, while the best sensitivity using the Feldman-Cousins approach came from the "dirty" $B \to K\tau e$ search with $< 1.5 \times 10^{-5}$ both at the 90% CL.

We put conservative constraints on New Physics parameters, using our "clean"

mode Feldman-Cousins ULs with the full *BABAR* dataset, corresponding to 471.9 million $B\bar{B}$ pairs. Using the Black *et al.* [17] estimation for determining NP energy scales between couplings of the third and second generation, and measured upper limit branching fractions of $\mathcal{B}(B^+ \to \pi^+\tau\mu) < 6.2$ and $\mathcal{B}(B^+ \to K^+\tau\mu) < 4.5$, we get bound on of $\Lambda_{\bar{b}s} > 15$ TeV and $\Lambda_{\bar{b}d} > 12$ TeV, respectively.

From Sher & Yuan [16], we can provide real experimental bounds on quark-type FCNCs and LFV Yukawa couplings between third and second generations, and third and first generations. You can compare our initial hypothetical bounds found in Table 1.2 with real experimental bounds in Table 5.2. Our measured upper limits improve bounds by an order to two orders of magnitude. Unfortunately, the resulting bounds on m_S are well within experimental energy scales and agree with no such observations. Future scheduled

Decay process	Measured upper limit	Bound	m_S (GeV)
$B^+ \to K^+\tau\mu$	4.5×10^{-5}	$\eta^4_{\mu\tau} < 4.5 \times (m_S/m_W)^4$	> 13.5
$B^+ \to \pi^+\tau\mu$	4.3×10^{-5}	$\eta^2_{e\tau}\eta^2_{\mu\tau} < 620 \times (m_S/m_W)^4$	> 1.0
$B^+ \to K^+\tau e$	6.2×10^{-5}	$\eta^2_{\mu\tau}\eta^2_{e\tau} < 4.3 \times (m_S/m_W)^4$	> 3.6
$B^+ \to \pi^+\tau e$	7.4×10^{-5}	$\eta^4_{e\tau} < 740 \times (m_S/m_W)^4$	> 5.5

Table 5.2: Measured bounds on flavor-changing couplings from three-body B decays estimated using the Sher & Yuan calculation [16], with measured *BABAR* sensitivity. Measured bounds provide method for determining mass of the scalar exchange particle, m_S, in Figure 1.1(a).

experiments, such as the Super B-factories in Italy or Japan, can improve constraints on New Physics by continuing to search for these decays.

Bibliography

[1] R. Wendell *et al.*, "Atmospheric neutrino oscillations analysis with sub-leading effects in Super-Kamiokande I, II, and III," submitted to Phys. Rev. D **,** arXiv:1002.3471v2 [hep-ph] 22 Apr 2010.

[2] B. T. Cleveland *et al.* (Homestake), "Measurement of the solar electron neutrino flux with the Homestake chlorine detector," Astro. Phys. J. **496**, 505 (1998); J. N. Abdurashitov *et al.* (SAGE Collaboration), "Measurement of the solar neutrino capture with gallium metal. III: Results for the 2002–2007 data-taking period," Phys. Rev.C **80**, 015807 (2009); W. Hampel *et al.* (GALLEX Collaboration), "GALLEX solar neutrino observations: results for GALLEX IV," Phys. Lett. B **447**, 127 (1999); W. Altmann *et al.* (GNO Collaboration), "Complete results for five years of GNO solar neutrino observations," Phys. Lett. B **616**, 174 (2005); K. Abe *et al.*, "Solar neutrino results in Super-Kamiokande-III," Phys. Rev. D **83**, 052010 (2011); B. Aharmim *et al.*, "Low-energy-threshold analysis of the Phase I and Phase II data sets of the Sudbury Neutrino Observatory," Phys. Rev.C **81**, 055504 (2010).

[3] A. Gando *et al.*, "Constraints of θ_{13} from a three-flavor oscillation analysis of reactor antineutrinos at KamLAND," Phys. Rev. D **83**, 052002 (2011).

[4] M. H. Ahn *et al.*, "Measurement of Neutrino Oscillation by the K2K Experiment," Phys. Rev. D **74**, 072003 (2006).

[5] A. Habig, "MINOS neutrino oscillation results," Mod. Phys. Lett. **A74**, 1219-1231 (2010).

[6] S. M. Bilenky *et al.*, "Neutrinoless Double-Beta Decay," Phys. Part. Nucl. **41**, 690 (2010).

[7] B. Aubert *et al.*, "Evidence for $D^0 - \bar{D}^0$ Mixing," submitted to Phys. Rev. Lett. **98**, 211802 (2007).

[8] S. L. Glashow, J. Iliopoulos, and L. Maiani, "Weak Interactions with Lepton-Hadron Symmetry∗," Phys. Rev. D **2**, 1285 (1970).

[9] T. P. Cheng and M. Sher, "Mass-matrix ansatz and flavor nonconservation in models with multiple Higgs doublets," Phys. Rev. D **35**, 3484 (1987).

[10] S. Glashow and S. Weinberg, "Natural conservation laws for neutral currents," Phys. Rev. D **15**, 1958-1965 (1977).

[11] http://pdglive.lbl.gov/.

[12] R. Cenci and J. M. Roney, "Search for lepton flavour violating decays $\tau^- \to \ell^- K^0_S$ and $\tau^- \to \ell^-(\rho^0, K^{*0}, \bar{K}^{*0}, \phi)$ at *BABAR* ," Nucl. Phys. B **189**, 154 (2009).

[13] J. P. Lees *et al.*, "Limit on τ lepton-flavor-violating decays into three charged leptons," Phys. Rev. D **81**, 111101(R) (2010).

[14] H. Georgi and S. L. Glashow, "Unity of All Elementary-Particle Forces," Phys. Rev. Lett. **32**, 438 (1974).

[15] P. Langacker, "Grand unified theories and proton decay," Phys. Rep. **72**, 185 (1981).

[16] M. Sher and Y. Yuan, "Rare B decays, rare τ decays, and grand unification," Phys. Rev. D **44**, 1461 (1991).

[17] D. Black, T. Han, H. He, and M. Sher, "$\tau - \mu$ flavor violation as a probe of the scale of new physics," Phys. Rev. D **66**, 053002 (2002).

[18] *BABAR* Collaboration, B. Aubert *et al.*, "Search for the decay $B^+ \to K^+\tau^\mp\mu^\pm$," Phys. Rev. Lett. **99**, 201801 (2007).

[19] O. Long, "Search for the forbidden decay $B^\pm \to K^\pm\tau\mu$," *BABAR* Analysis Document #1732 V09.

[20] CDF Collaboration, T. Aaltonen *et al.*, "Search for $B^0_s \to \mu^+\mu^-$ and $B^0 \to \mu^+\mu^-$ Decays with 2 fb^{-1} of $p\bar{p}$ Collisions," Phys. Rev. Lett. **100**, 101802 (2008).

[21] G. C. Branco *et al.*, "Theory and phenomenology of two-Higgs-doublet models," To be submitted to Phys. Rep. **,** (2011), arXiv:1106.0034v2 [hep-ph].

[22] http://news.cnet.com/2300-1008_3-6207233-11.html.

[23] http://www.slac.stanford.edu/BFROOT/www/Detector/Images/Images.html.

[24] *BABAR* Collaboration, B. Aubert *et al.*, "The *BABAR* Detector," "The *BABAR* Physics Book," SLAC-R-504 (1998).

[25] http://www.slac.stanford.edu/BFROOT/www/Detector/Images/Images.html.

[26] *BABAR* Collaboration, B. Aubert *et al.*, "The *BABAR* Detector," Nucl. Instrum. Methods Phys. Res., Sect. A479, 1-116 (2002), hep-ex/0105044.

[27] `Draft`: Update on the "The *BABAR* Detector," http://www.slac.stanford.edu/BFROOT/Detector/NIM_Update/.

[28] http://www.slac.stanford.edu/BFROOT/detector/online/archive/bbr-nfs01/www/babarrc/.

[29] http://www.slac.stanford.edu/BFROOT/www/Organization/PubBoard/OfficialPlots/.

[30] http://www.slac.stanford.edu/BFROOT/www/Organization/PubBoard/OfficialPlots/SVT/.

[31] C. Bozzi *et al.*, "The *BABAR* silicon vertex tracker," Nucl. Instrum. Methods Phys. Res., Sect. A435, 25-33 (1999).

[32] http://www.slac.stanford.edu/BFROOT/www/Organization/PubBoard/OfficialPlots/DCH/.

[33] I. Adam *et al.*, "The DIRC Particle Identification System for the *BABAR* Experiment," Nucl. Instrum. Methods Phys. Res., Sect. A538, 28 (2005), SLAC-PUB-10516.

[34] http://www.slac.stanford.edu/BFROOT/www/Organization/PubBoard/OfficialPlots/EMC/.

[35] M. Kocian *et al.*, "Performance and Calibration of the Crystal Calorimeter of the *BABAR* Detector," SLAC-PUB-10170.

[36] W. Menges *et al.*, "The *BABAR* Muon System Upgrade," IEEE Nucl. Sci. Symp. Conf. Rec. 5, , 1470 (2005), arXiv:physics/0609039v1.

[37] http://www.slac.stanford.edu/BFROOT/www/Organization/PubBoard/OfficialPlots/LST/.

[38] *BABAR* Note 586.

[39] Particle Data Group, D. E. Groom *et al.*, Eur. Phys. Jour. C **15**, 1 (2008).

[40] *BABAR* Collaboration, B. Aubert *et al.*, "Measurement of the Inclusive Charmless Semileptonic Branching Ratio of B Mesons and Determination of $|V_{ub}|$," Phys. Rev. Lett. **92**, 071802 (2004).

[41] http://www.slac.stanford.edu/BFROOT/www/Physics/Tools/Pid/UltimatePID/ultimate_PID_recip

[42] P. Ongmongkolkul, K. Mishra, A. Telnov, A. Gaz, "Particle Identification Using Error Correction Output Code Multiclass Classifier," *BABAR* Analysis Document #2199 V02 (2009).

[43] C. O. Vuosalo, A. V. Telnov, K. T. Flood, "Muon Identification Using Decision Trees," *BABAR* Analysis Document #1853 V03 (2010).

[44] http://www.slac.stanford.edu/BFROOT/www/Physics/Charged.html.

[45] R. Barlow, "A Calculator for Confidence intervals," Comput. Phys. Commun. **149**, 97 (2002), [arXiv:hep-ex/0203002].

[46] G. Feldman and R. Cousins, "A unified approach to the classical statistical analysis of small signals," Phys. Rev. **D57**, 3873 (1998).

Appendix A

The $m(K\pi)$ cut

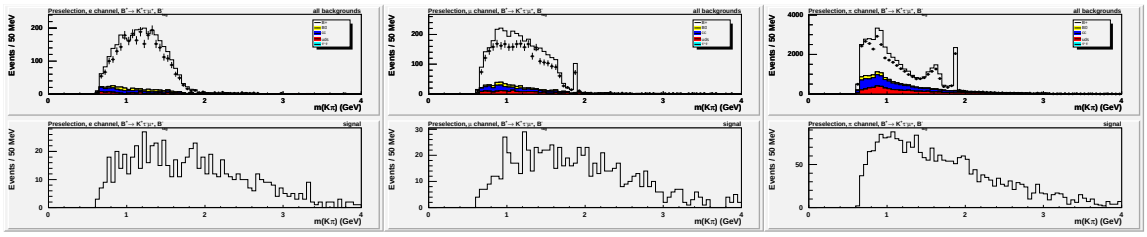

Figure A.1: **"Clean" $B^+ \to K^+\tau^-\mu^+; B^-_{\mathbf{tag}}$ mode**. The invariant mass of the kaon with the track of opposite charge, assuming that it's a pion for the **electron** (left), **muon** (middle), **pion** (right) channels for all backgrounds (top) and signal Monte Carlo (bottom). Points with error bars from on-resonance data (top). The $D^0 \to K^-\pi^+$ peak is clearly visible, except in the e channel (real e poorly faking π). Most of the B background has $m(K\pi)$ below the D^0 mass.

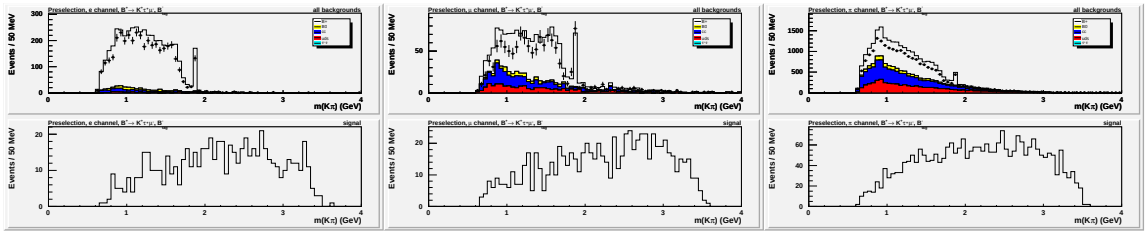

Figure A.2: **"Dirty" $B^+ \to K^+\tau^+\mu^-; B^-_{\mathbf{tag}}$ mode**. The invariant mass of the kaon with the track of opposite charge, assuming that it's a pion for the **electron** (left), **muon** (middle), **pion** (right) channels for all backgrounds (top) and signal Monte Carlo (bottom). Points with error bars from on-resonance data (top). The $D^0 \to K^-\pi^+$ peak is clearly visible in all channels. Relatively larger B backgrounds after the $m(K\pi)$ cut.

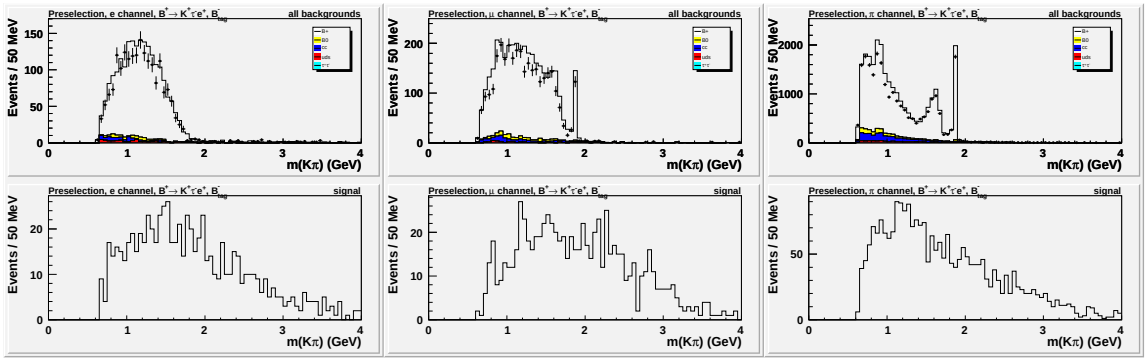

Figure A.3: **"Clean" $B^+ \to K^+\tau^-e^+; B^-_{\rm tag}$ mode**. The invariant mass of the kaon with the track of opposite charge, assuming that it's a pion for the **electron** (left), **muon** (middle), **pion** (right) channels for all backgrounds (top) and signal Monte Carlo (bottom). Points with error bars from on-resonance data (top). The $D^0 \to K^-\pi^+$ peak is clearly visible, except in the e channel. Most of the B background has $m(K\pi)$ below the D^0 mass.

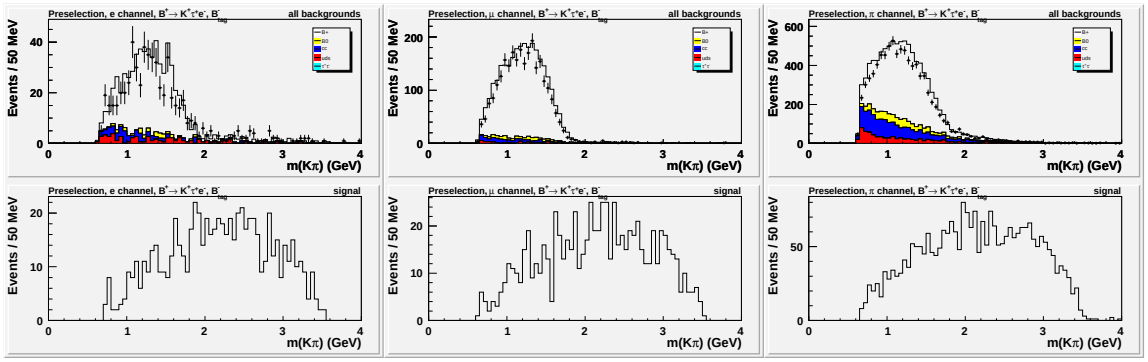

Figure A.4: **"Dirty" $B^+ \to K^+\tau^+e^-; B^-_{\rm tag}$ mode**. The invariant mass of the kaon with the track of opposite charge, assuming that it's a pion for the **electron** (left), **muon** (middle), **pion** (right) channels for all backgrounds (top) and signal Monte Carlo (bottom). Points with error bars from on-resonance data (top). The $D^0 \to K^-\pi^+$ peak is *not* visible (e poorly faking π). Most of the B background has $m(K\pi)$ below the D^0 mass, while signal is more symmetrically distributed.

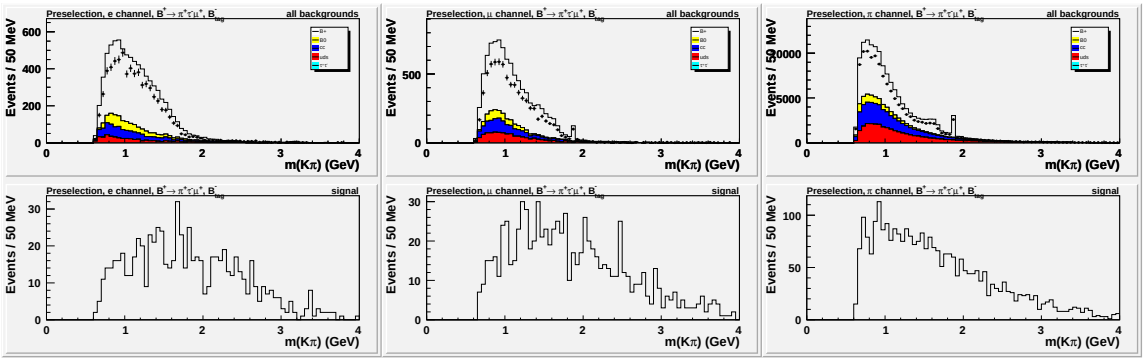

Figure A.5: **"Clean" $B^+ \to \pi^+\tau^-\mu^+; B^-_{\mathbf{tag}}$ mode**. The invariant mass of the kaon with the track of opposite charge, assuming that it's a pion for the **electron** (left), **muon** (middle), and **pion** (right) channels for all backgrounds (top) and signal Monte Carlo (bottom). Points with error bars from on-resonance data (top). The $D^0 \to K^-\pi^+$ peak is slightly visible, and not visible at all in the e channel. Most of the B background has $m(K\pi)$ below the D^0 mass. We lose signal efficiency but have better background rejection after the $m(K\pi)$ cut.

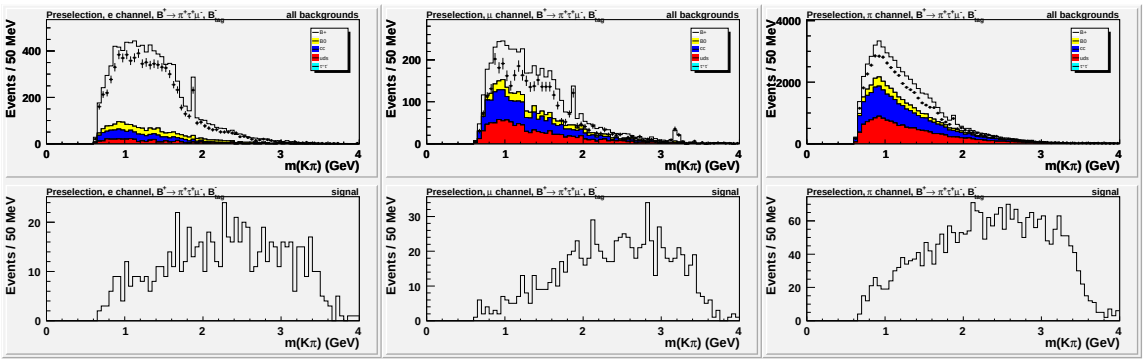

Figure A.6: **"Dirty" $B^+ \to \pi^+\tau^+\mu^-; B^-_{\mathbf{tag}}$ mode**. The invariant mass of the kaon with the track of opposite charge, assuming that it's a pion for the **electron** (left), **muon** (middle), and **pion** (right) channels for all backgrounds (top) and signal Monte Carlo (bottom). Points with error bars from on-resonance data (top). The $D^0 \to K^-\pi^+$ peak is only slightly visible in the μ channel, where a J/ψ peak seems to be present as well. Relatively larger B background after the $m(K\pi)$ cut, but higher signal efficiencies.

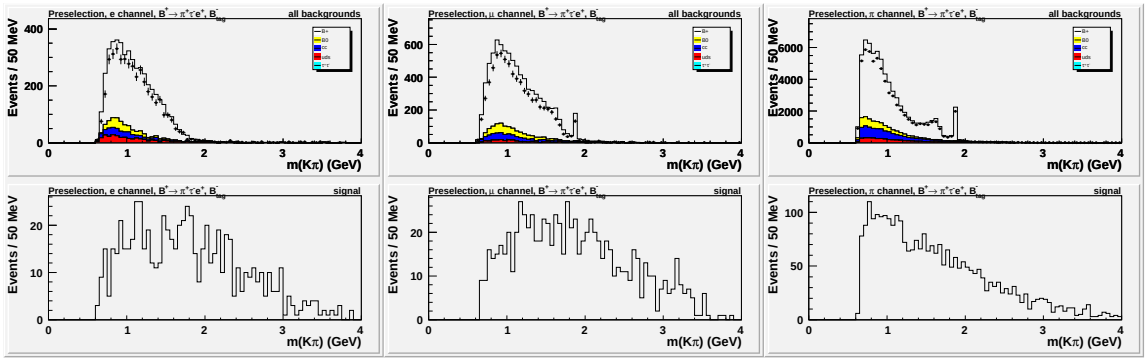

Figure A.7: **"Clean" $B^+ \to \pi^+\tau^-e^+; B^-_{\mathbf{tag}}$ mode**. The invariant mass of the kaon with the track of opposite charge, assuming that it's a pion for the **electron** (left), **muon** (middle), and **pion** (right) channels for all backgrounds (top) and signal Monte Carlo (bottom). Points with error bars from on-resonance data (top). The $D^0 \to K^-\pi^+$ peak is clearly visible, except in the e channel. Most of the B background has $m(K\pi)$ below the D^0 mass.

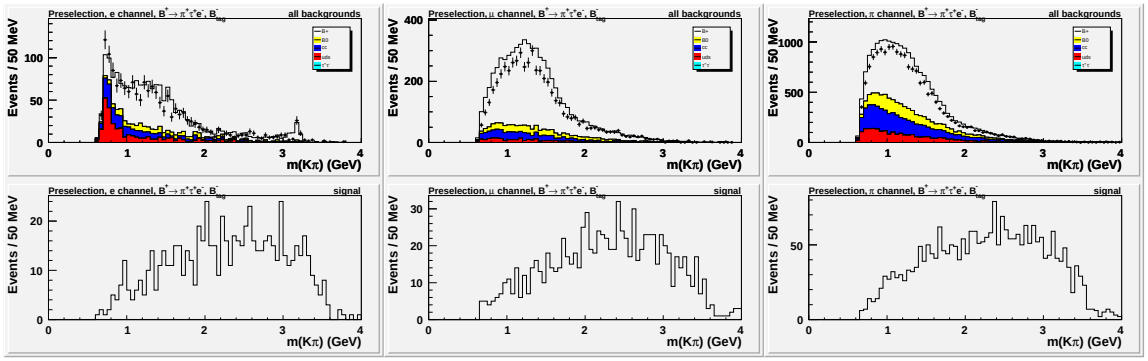

Figure A.8: **"Dirty" $B^+ \to \pi^+\tau^+e^-; B^-_{\mathbf{tag}}$ mode**. The invariant mass of the kaon with the track of opposite charge, assuming that it's a pion for the **electron** (left), **muon** (middle), and **pion** (right) channels for all backgrounds (top) and signal Monte Carlo (bottom). Points with error bars from on-resonance data (top). The $D^0 \to K^-\pi^+$ peak is *not* visible in any of the channels, but we seem to be faking some J/ψ decays in the e channel. Relatively large B background after the $m(K\pi)$ cut, with higher signal efficiencies.

Appendix B

The $m(\mu\mu)$ cuts

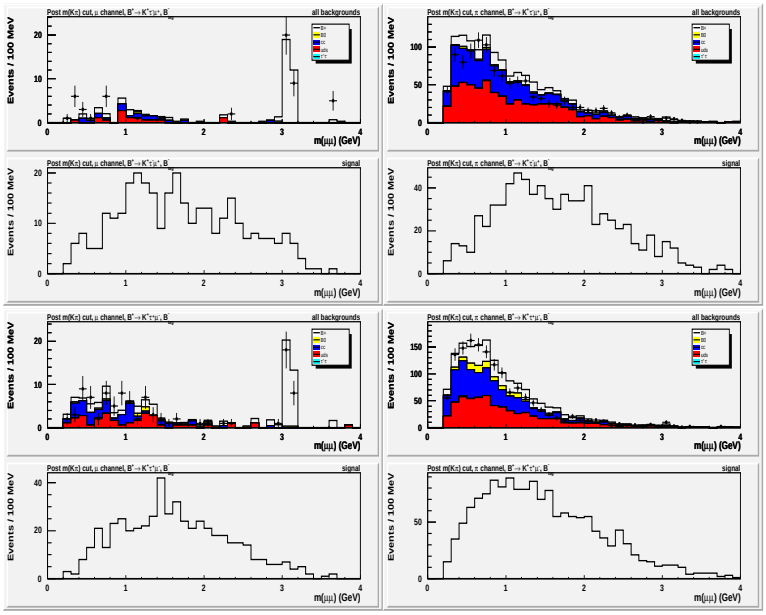

Figure B.1: Post $m(K\pi)$ cut for the invariant mass of the two non-kaon tracks assuming that both are muons for our **"clean" (top-two) and "dirty" (bottom-two) $K\tau\mu$ modes**, for the μ (left) and π (right) channels only. Points with error bars from on-resonance data (top). Observe a significant charmonium peak near the J/ψ resonance in the muon channels. Lower second and fourth distributions from signal MC.

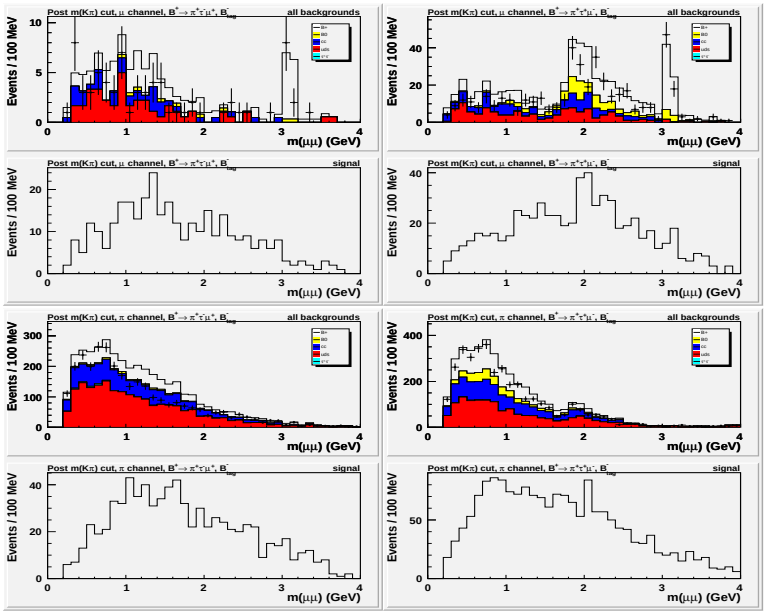

Figure B.2: Post $m(K\pi)$ cut for the invariant mass of the two non-primary-pion tracks assuming that both are muons for our **"clean" (top-two) and "dirty" (bottom-two) $\boldsymbol{\pi\tau\mu}$ modes**, for the μ (left) and π (right) channels only. Points with error bars from on-resonance data (top). Observe a significant charmonium peak near the J/ψ resonance in the muon channels. Lower second and fourth distributions from signal MC.

Appendix C

The $m(ee)$ cuts

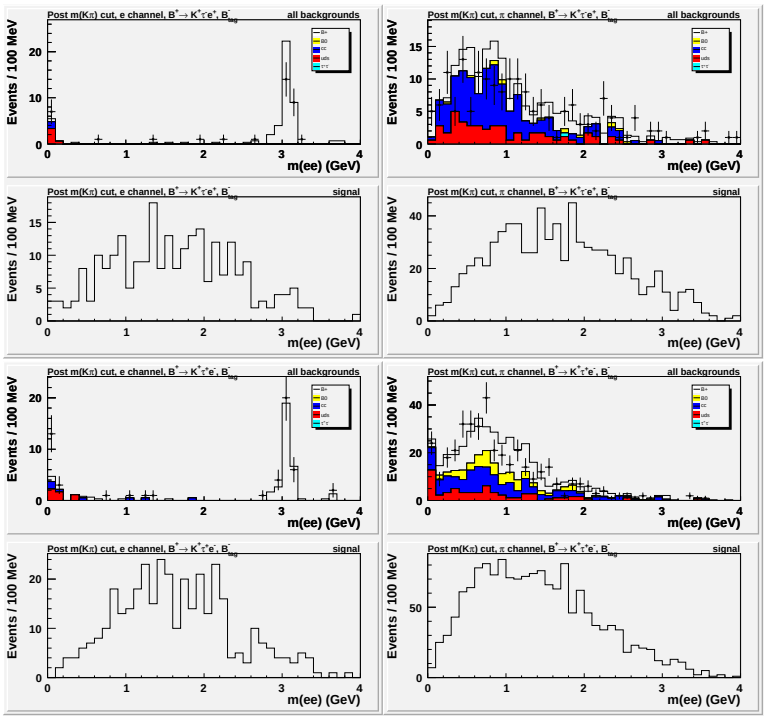

Figure C.1: Post $m(K\pi)$ cut for the invariant mass of the two non-kaon tracks assuming both are electrons for our **"clean" (top-two) and "dirty" (bottom-two) $K\tau e$ modes**, for the e (left) and π (right) channels only. Points with error bars in top first and third distributions from on-resonance data. Observe significant charmonium and γ-conversion peaks near the J/ψ resonance and zero in both e channels. Small rises near the $\psi(2s)$ resonance are also seen in the background distributions. Bottom second and fourth distributions from signal MC.

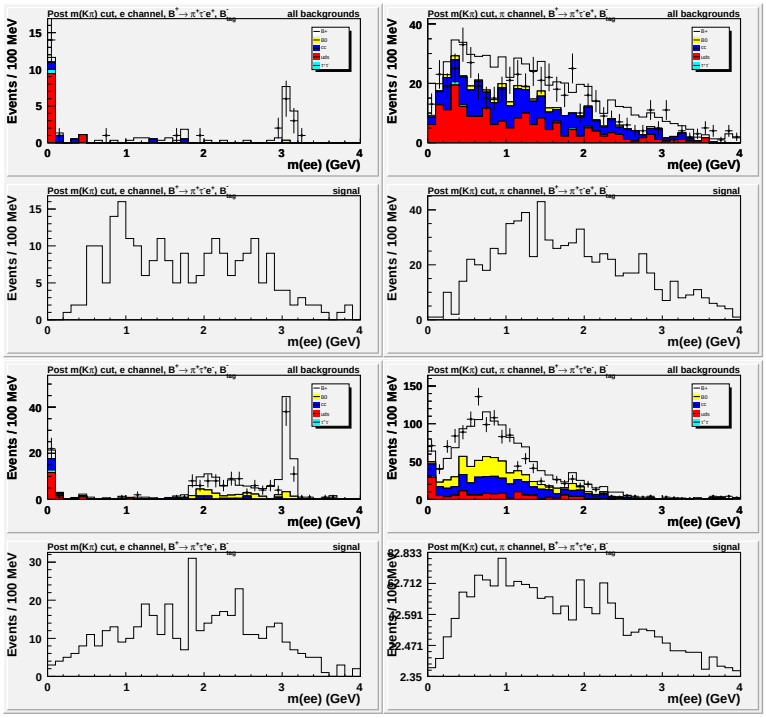

Figure C.2: Post $m(K\pi)$ cut for for the invariant mass of the two non-primary-pion tracks assuming both are electrons for our **"clean" (top-two) and "dirty" (bottom-two) $\boldsymbol{\pi\tau e^+}$ modes**, for the e (left) and π (right) channels only. Points with error bars in top first and third distributions from on-resonance data. Observe significant charmonium and γ-conversion peaks near the J/ψ resonance and zero in both e channels. Small rises near the $\psi(2s)$ resonance are also seen in the background distributions. Bottom second and fourth distributions from signal MC.

Appendix D

The B_{tag} m_{ES} cut

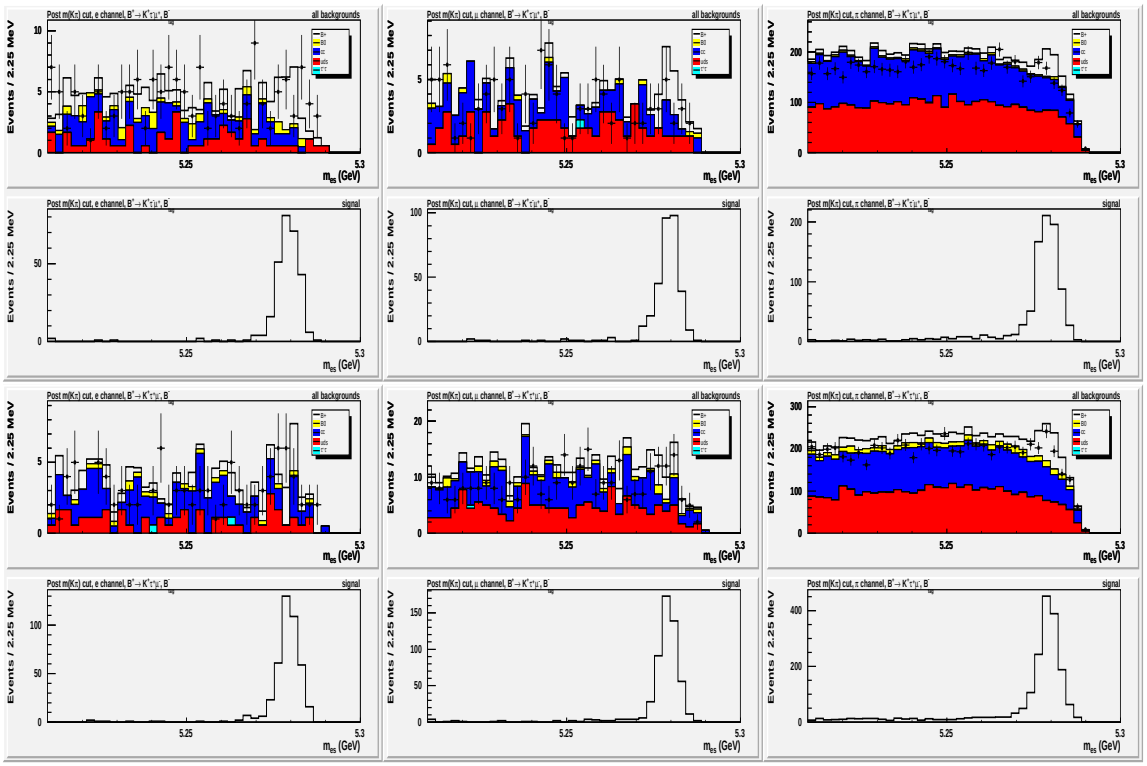

Figure D.1: Post $m(K\pi)$ cut for our **"clean" (top-two) and "dirty" (bottom-two) $K\tau\mu$ modes**. Distributions of $B_{\rm tag}$ $m_{\rm ES}$ for the **electron** (left), **muon** (middle), **pion** (right) channels. $B_{\rm tag}$ $m_{\rm ES} > 5.27$ GeV keeps most of our signal while removing most of the non-peaking background. Points with error bars from on-resonance data (top). Bottom plots from signal MC.

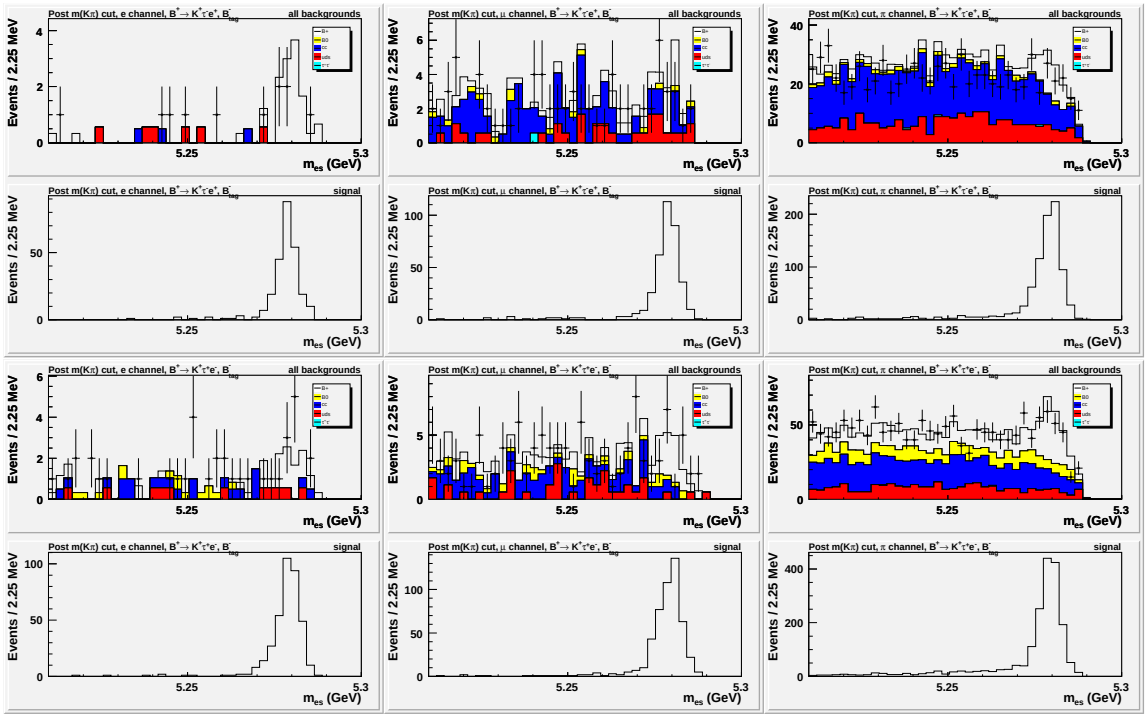

Figure D.2: Post $m(K\pi)$ cut for our **"clean" (top-two) and "dirty" (bottom-two) $K\tau e$ modes**. Distributions of $B_{\rm tag}$ $m_{\rm ES}$ for the **electron** (left), **muon** (middle), **pion** (right) channels. $B_{\rm tag}$ $m_{\rm ES} > 5.27$ GeV keeps most of our signal while removing most of the non-peaking background. Points with error bars from on-resonance data (top). Bottom plots from signal MC.

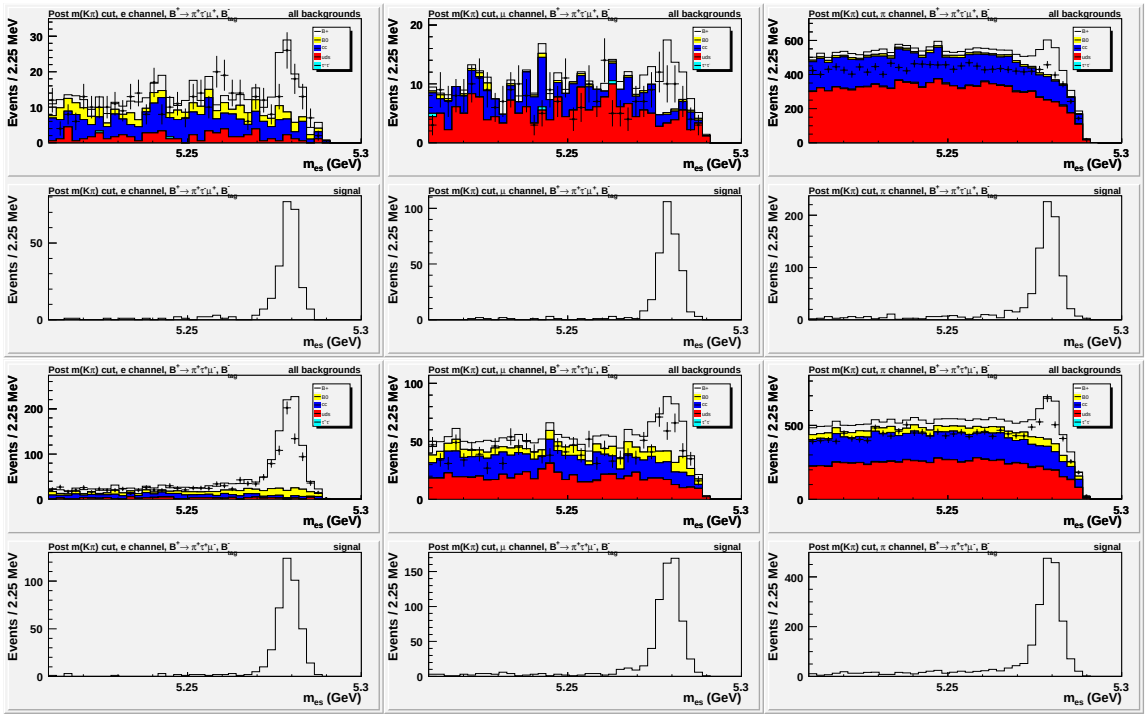

Figure D.3: Post $m(K\pi)$ cut for our **"clean" (top-two) and "dirty" (bottom-two) $\pi\tau\mu$ modes**. Distributions of $B_{\rm tag}$ $m_{\rm ES}$ for the **electron** (left), **muon** (middle), **pion** (right) channels. $B_{\rm tag}$ $m_{\rm ES} > 5.27$ GeV keeps most of our signal while removing most of the non-peaking background. Points with error bars from on-resonance data (top). Bottom plots from signal MC.

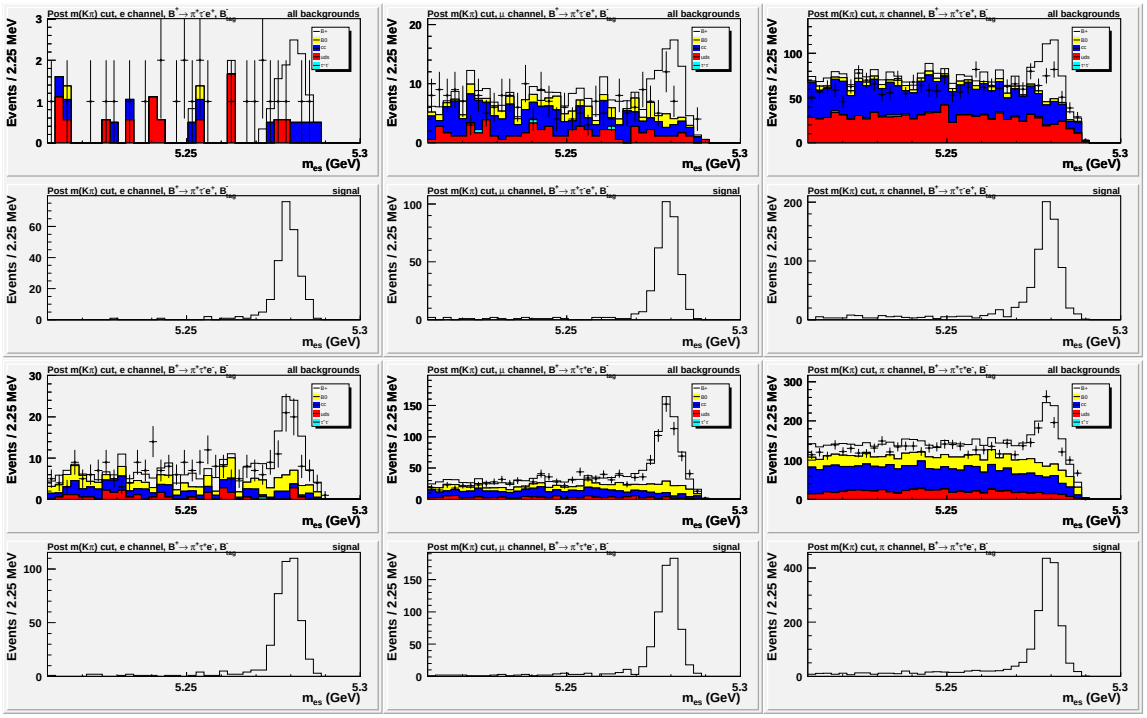

Figure D.4: Post $m(K\pi)$ cut for our **"clean" (top-two) and "dirty" (bottom-two) $\pi\tau e$ modes**. Distributions of $B_{\rm tag}$ $m_{\rm ES}$ for the **electron** (left), **muon** (middle), **pion** (right) channels. $B_{\rm tag}$ $m_{\rm ES} > 5.27$ GeV keeps most of our signal while removing most of the non-peaking background. The points with error bars in the top plots are the on-resonance data. Bottom plots from signal MC.

Appendix E

Pion PID level of the primary pion candidate ($\pi\tau\ell$ modes only)

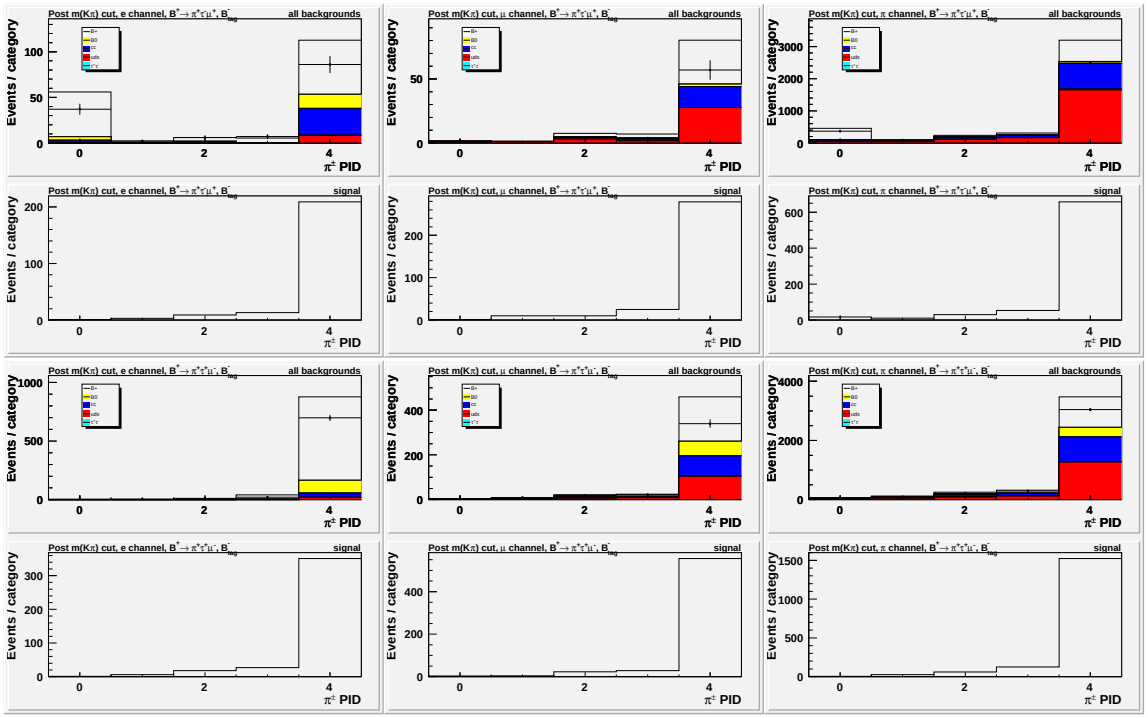

Figure E.1: Post $m(K\pi)$ cut for our **"clean" (top-two) and "dirty" (bottom-two) $\pi\tau\mu$ modes**. Distributions of pion PID level of the primary pion candidate for the **electron** (left), **muon** (center), and **pion** (right) channels. The bins correspond to passing at best the following PID lists: 1=`piKMVeryLoose`, 2=`piKMLoose`, 3=`piKMTight`, 4=`piKMVeryTight`. Points with error bars in the top first and third distributions from on-resonance data. Bottom second and fourth distributions from signal MC.

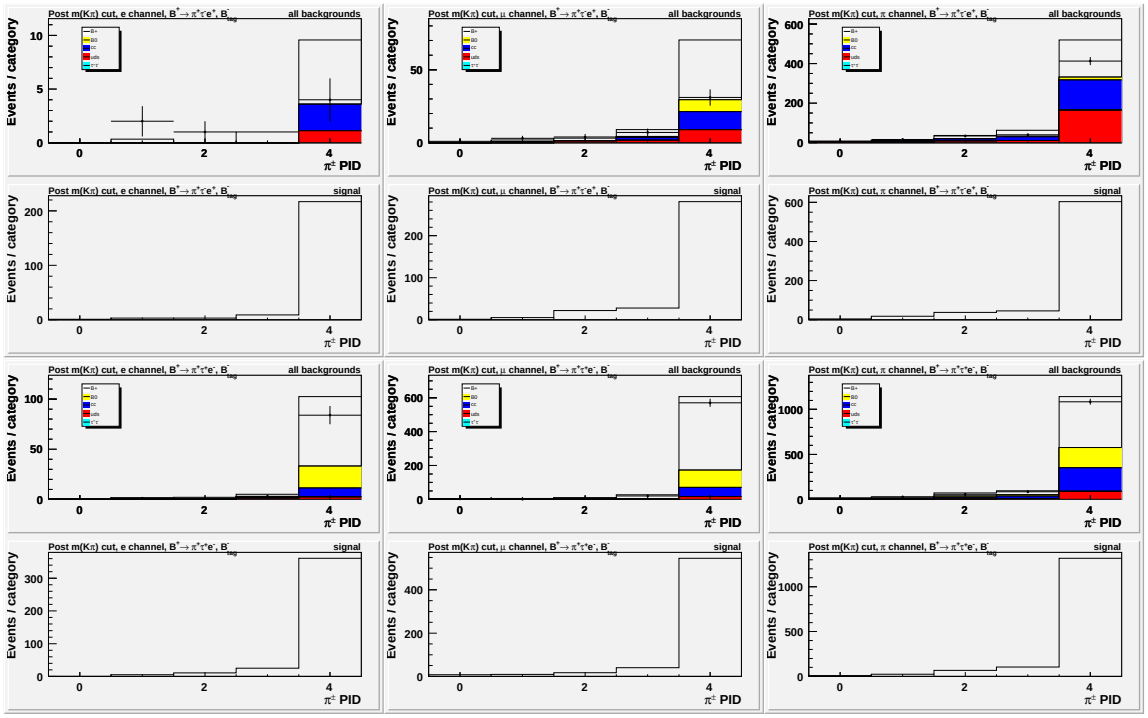

Figure E.2: Post $m(K\pi)$ cut for our **"clean" (top-two) and "dirty" (bottom-two) $\pi\tau e$ modes**. Distributions of pion PID level of the primary pion candidate for the **electron** (left), **muon** (center), and **pion** (right) channels. The bins correspond to passing at best the following PID lists: 1=`piKMVeryLoose`, 2=`piKMLoose`, 3=`piKMTight`, 4=`piKMVeryTight`. Points with error bars in the top first and third distributions from on-resonance data. Bottom second and fourth distributions from signal MC.

Appendix F

The $m(\tau)$ signal window

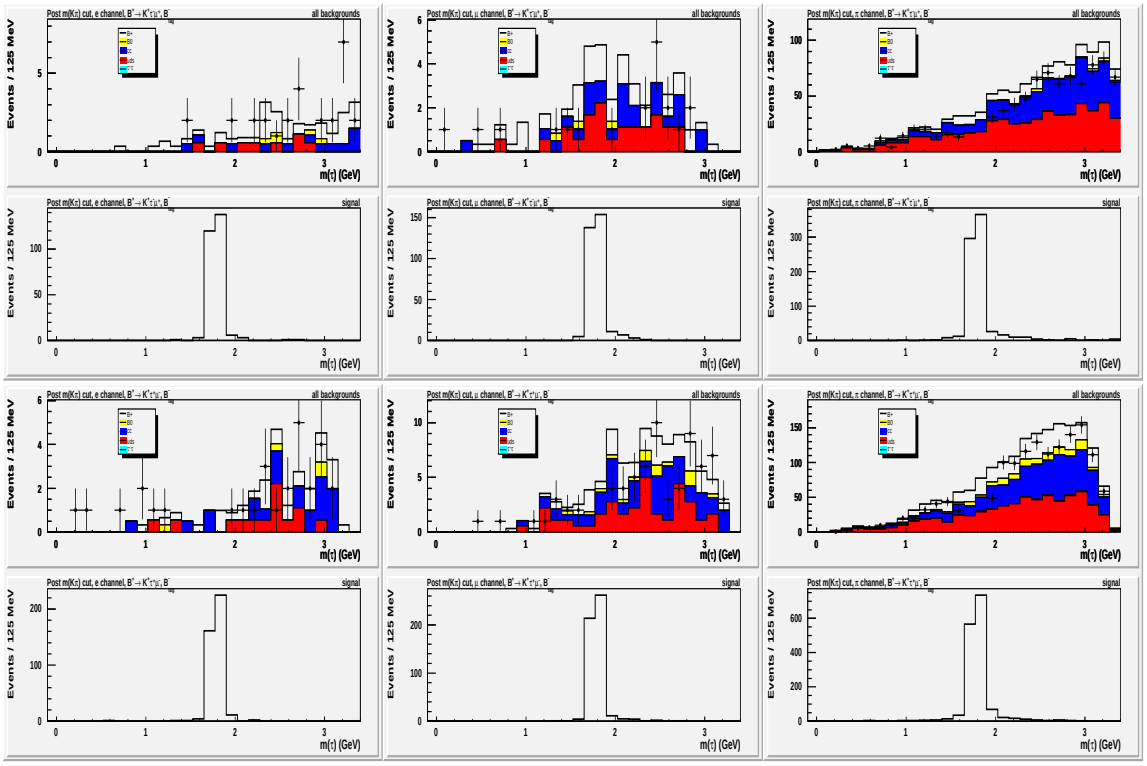

Figure F.1: Post $m(K\pi)$ cut for our **"clean" (top-two) and "dirty" (bottom-two)** $K\tau\mu$ **modes**. Distributions of the reconstructed tau mass for the **electron** (left), **muon** (middle), & **pion** (right) channels. Data blinded by removing events with $m(\tau)$ in the range [1.65,1.90] GeV, while background is broad and smooth distribution. Bottom second and fourth distributions from signal MC, where the signal peaks sharply at the tau mass.

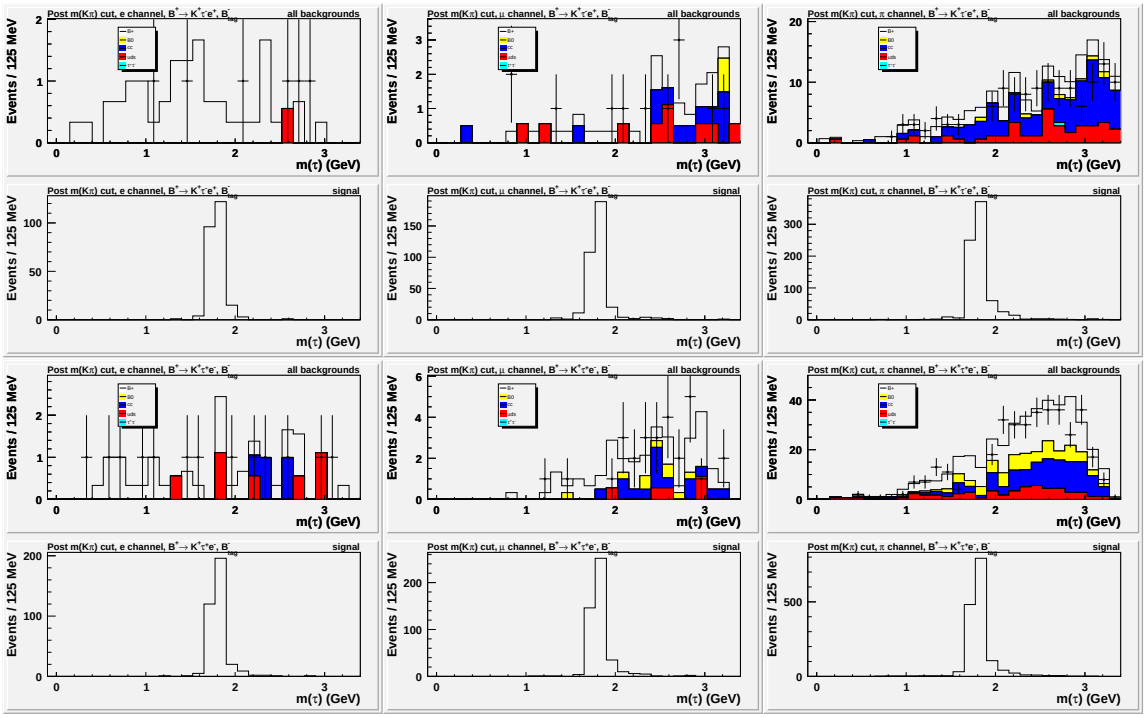

Figure F.2: Post $m(K\pi)$ cut for our **"clean" (top-two) and "dirty" (bottom-two) $K\tau e$ modes**. Distributions of the reconstructed tau mass for the **electron** (left), **muon** (middle), & **pion** (right) channels. Data blinded by removing events with $m(\tau)$ in the range [1.65,1.90] GeV, while background is broad and smooth distribution. Bottom second and fourth distributions from signal MC, where the signal peaks sharply at the tau mass.

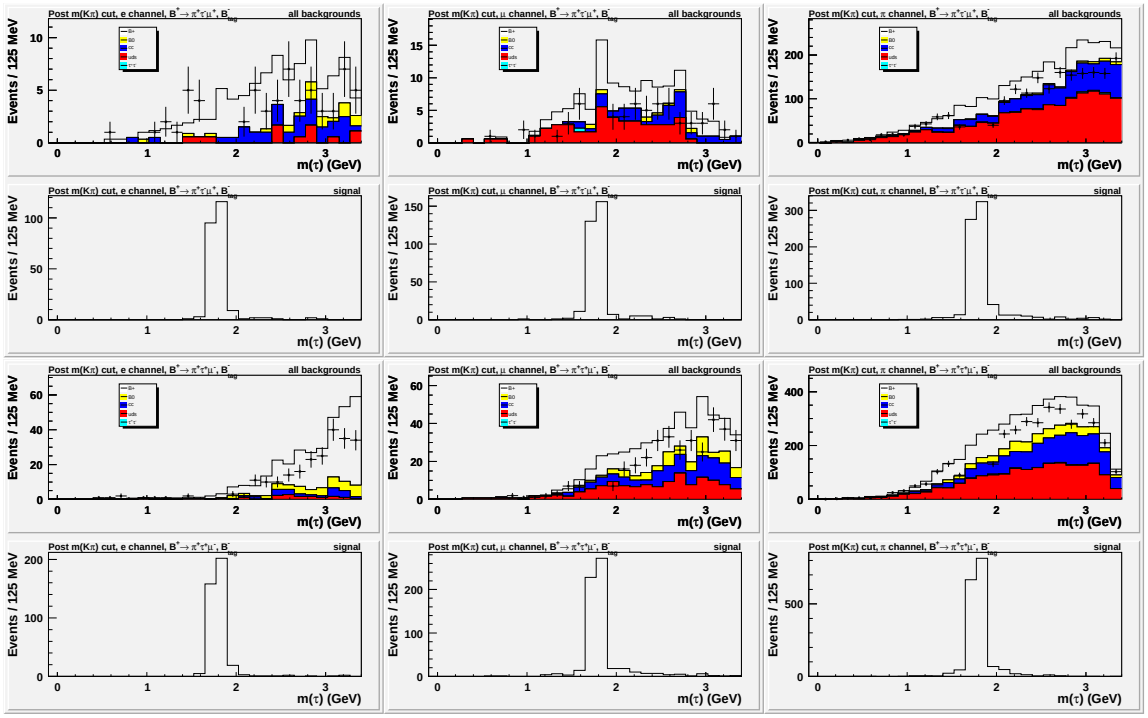

Figure F.3: Post $m(K\pi)$ cut for our **"clean" (top-two) and "dirty" (bottom-two) $\pi\tau\mu$ modes**. Distributions of the reconstructed tau mass for the **electron** (left), **muon** (middle), & **pion** (right) channels. Data blinded by removing events with $m(\tau)$ in the range [1.65,1.90] GeV, while background is broad and smooth distribution. Bottom second and fourth distributions from signal MC, where the signal peaks sharply at the tau mass.

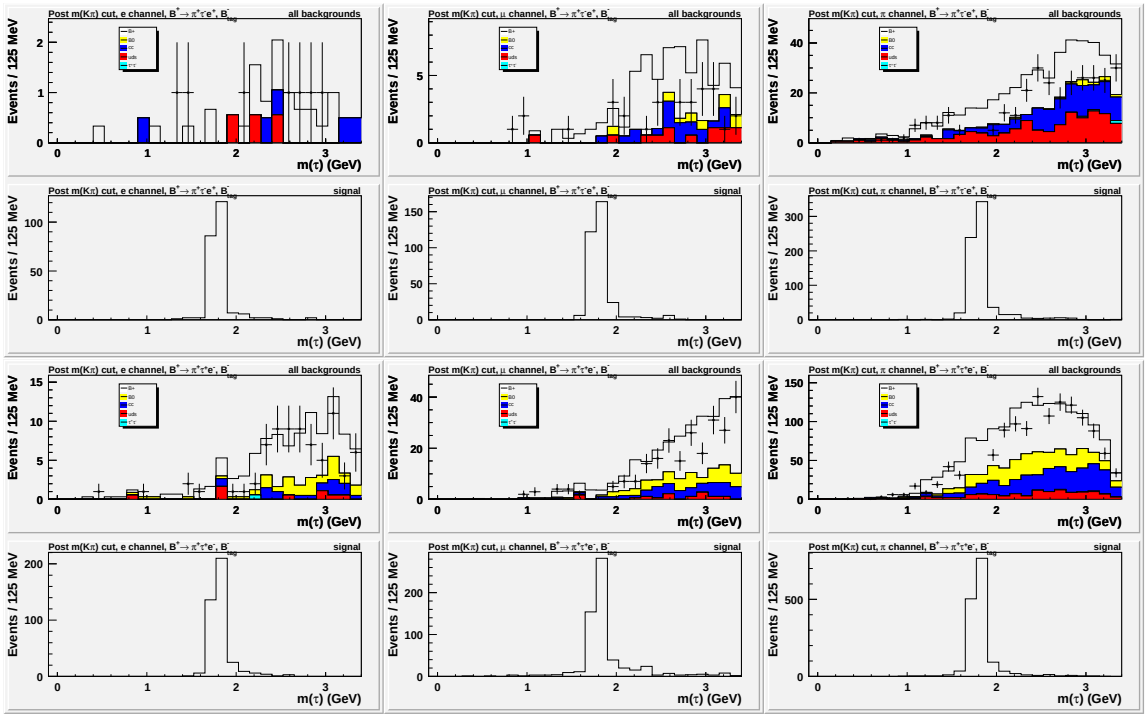

Figure F.4: Post $m(K\pi)$ cut for our **"clean" (top-two) and "dirty" (bottom-two) $\pi\tau e$ modes**. Distributions of the reconstructed tau mass for the **electron** (left), **muon** (middle), & **pion** (right) channels. Data blinded by removing events with $m(\tau)$ in the range [1.65,1.90] GeV, while background is broad and smooth distribution. Bottom second and fourth distributions from signal MC, where the signal peaks sharply at the tau mass.

Appendix G

Distributions of $\sum E_{\mathrm{cal}}$

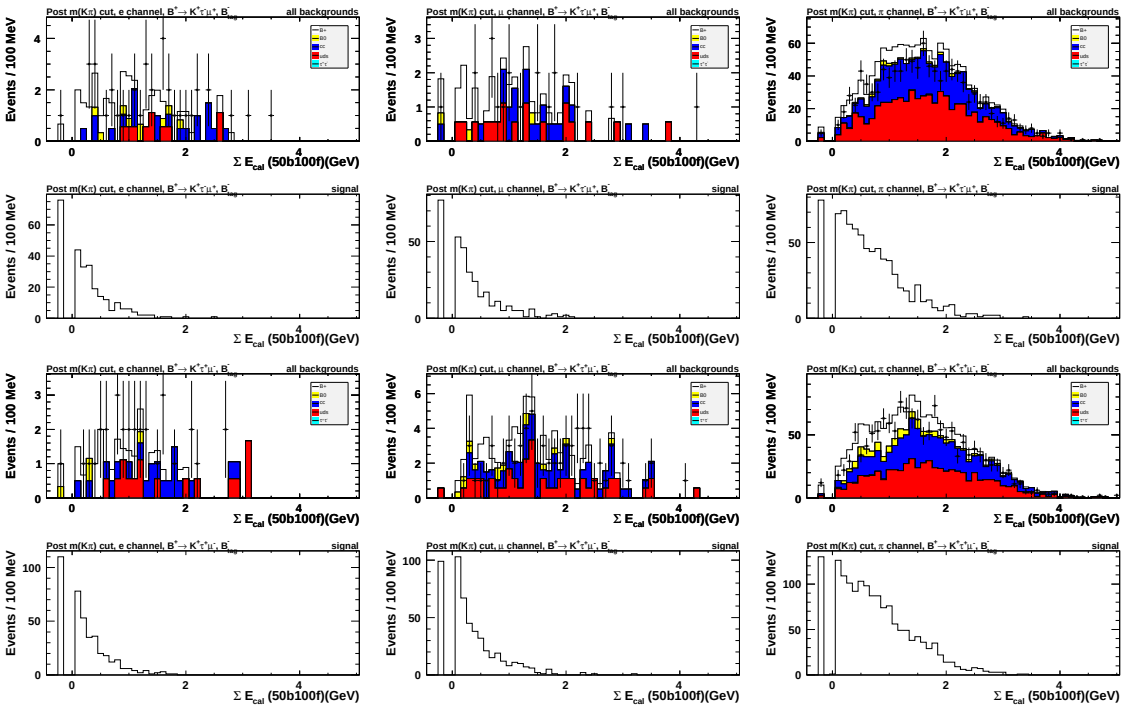

Figure G.1: Post $m(K\pi)$ cut for our **"clean" (top-two) and "dirty" (bottom-two) $K\tau\mu$ modes**. Distributions of the residual energy in the calorimeter, $\sum E_{\mathrm{cal}}$, with energy thresholds of 50 MeV in the barrel and 100 MeV in the endcaps for the **electron** (left), **muon** (middle), & **pion** (right) channels.

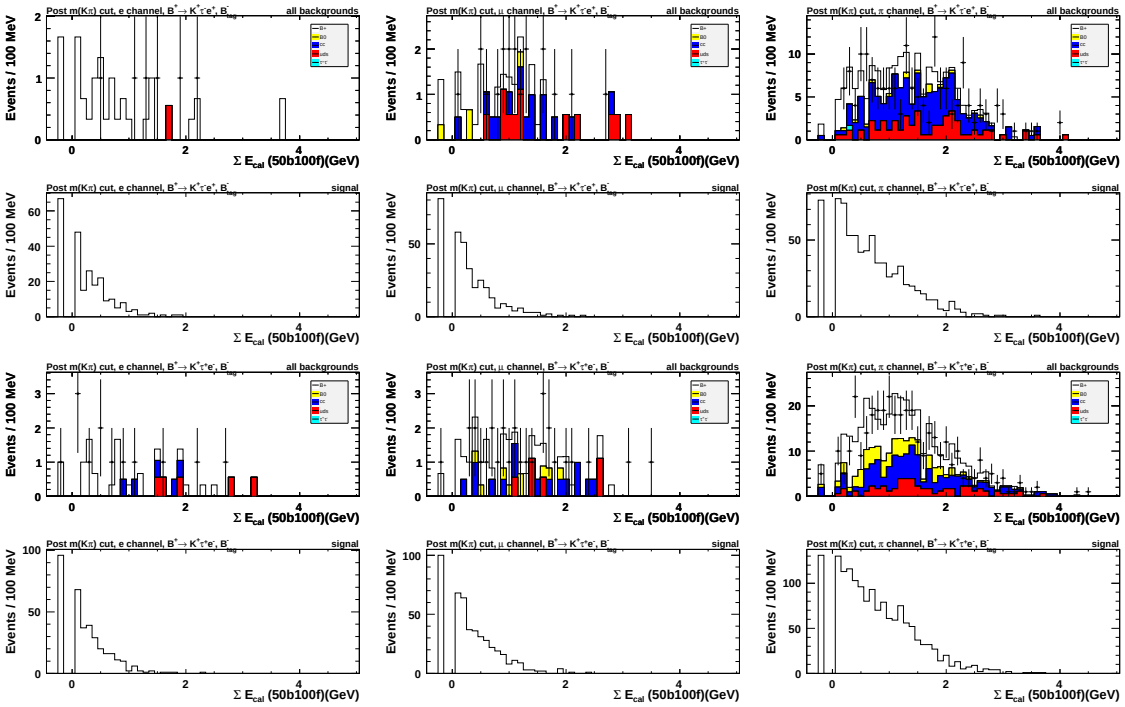

Figure G.2: Post $m(K\pi)$ cut for our **"clean" (top-two) and "dirty" (bottom-two) $K\tau e$ modes**. Distributions of the residual energy in the calorimeter, $\sum E_{\rm cal}$, with energy thresholds of 50 MeV in the barrel and 100 MeV in the endcaps for the **electron** (left), **muon** (middle), & **pion** (right) channels.

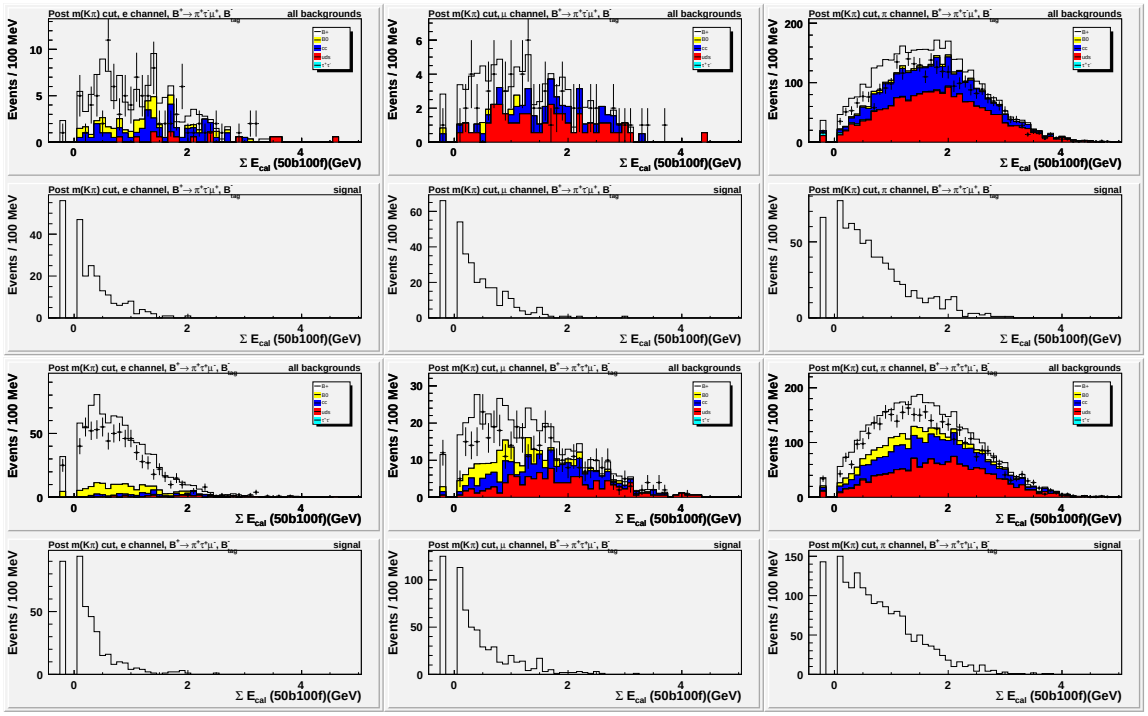

Figure G.3: Post $m(K\pi)$ cut for our **"clean" (top-two) and "dirty" (bottom-two) $\pi\tau\mu$ modes**. Distributions of the residual energy in the calorimeter, $\sum E_{\rm cal}$, with energy thresholds of 50 MeV in the barrel and 100 MeV in the endcaps for the **electron** (left), **muon** (middle), & **pion** (right) channels.

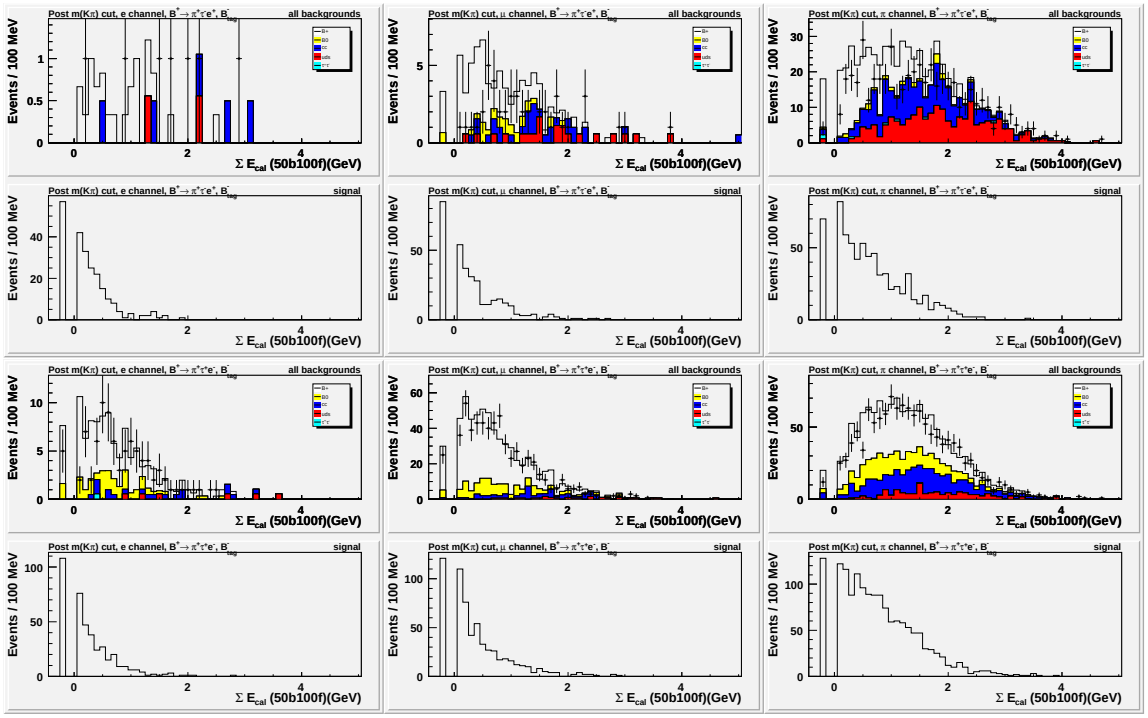

Figure G.4: Post $m(K\pi)$ cut for our **"clean" (top-two) and "dirty" (bottom-two) $\pi\tau e$ modes**. Distributions of the residual energy in the calorimeter, $\sum E_{\rm cal}$, with energy thresholds of 50 MeV in the barrel and 100 MeV in the endcaps for the **electron** (left), **muon** (middle), & **pion** (right) channels.

Appendix H

Distributions of $|cos(\theta_{\rm thr})|$

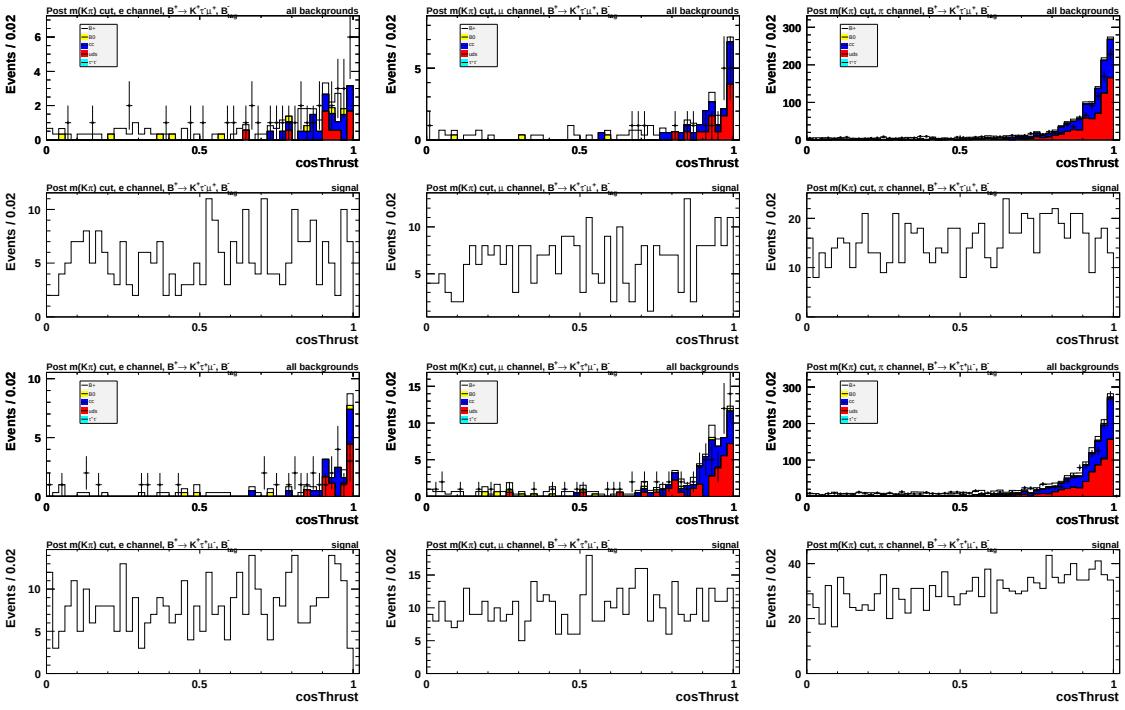

Figure H.1: Post $m(K\pi)$ cut for our **"clean" (top-two) and "dirty" (bottom-two) $K\tau\mu$ modes**. Distributions of the $|cos(\theta_{\rm thr})|$ for the **electron** (left), **muon** (middle), & **pion** (right) channels.

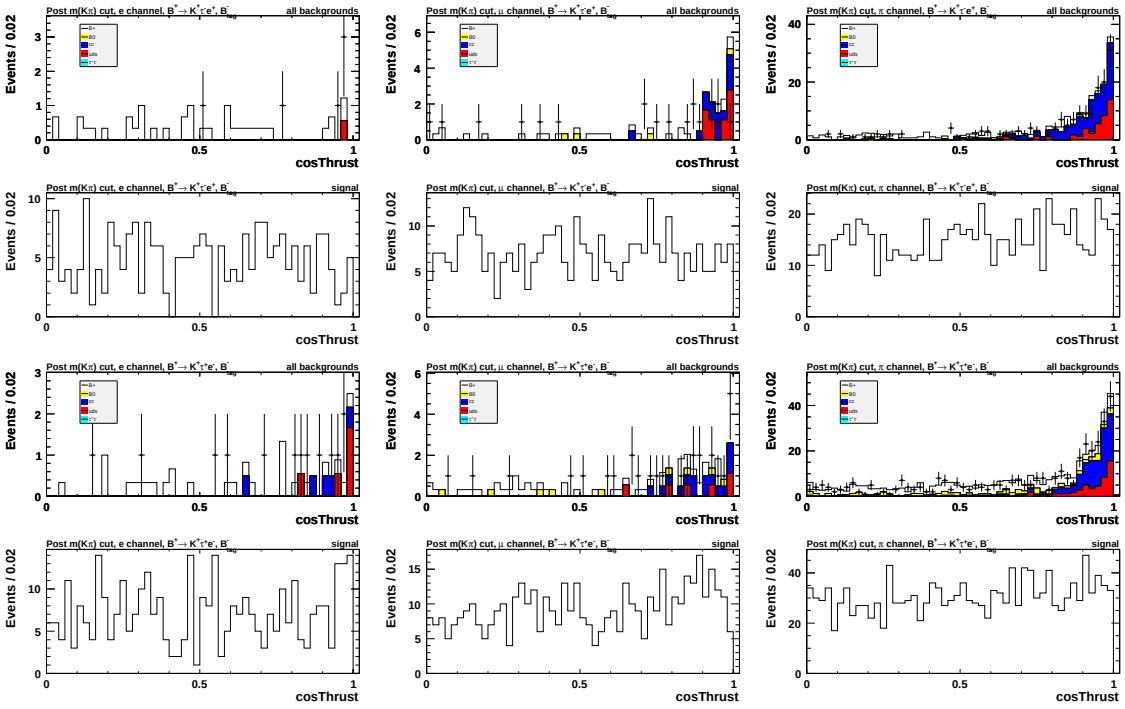

Figure H.2: Post $m(K\pi)$ cut for our **"clean" (top-two) and "dirty" (bottom-two) $K\tau e$ modes**. Distributions of the $|cos(\theta_{\rm thr})|$ for the **electron** (left), **muon** (middle), & **pion** (right) channels.

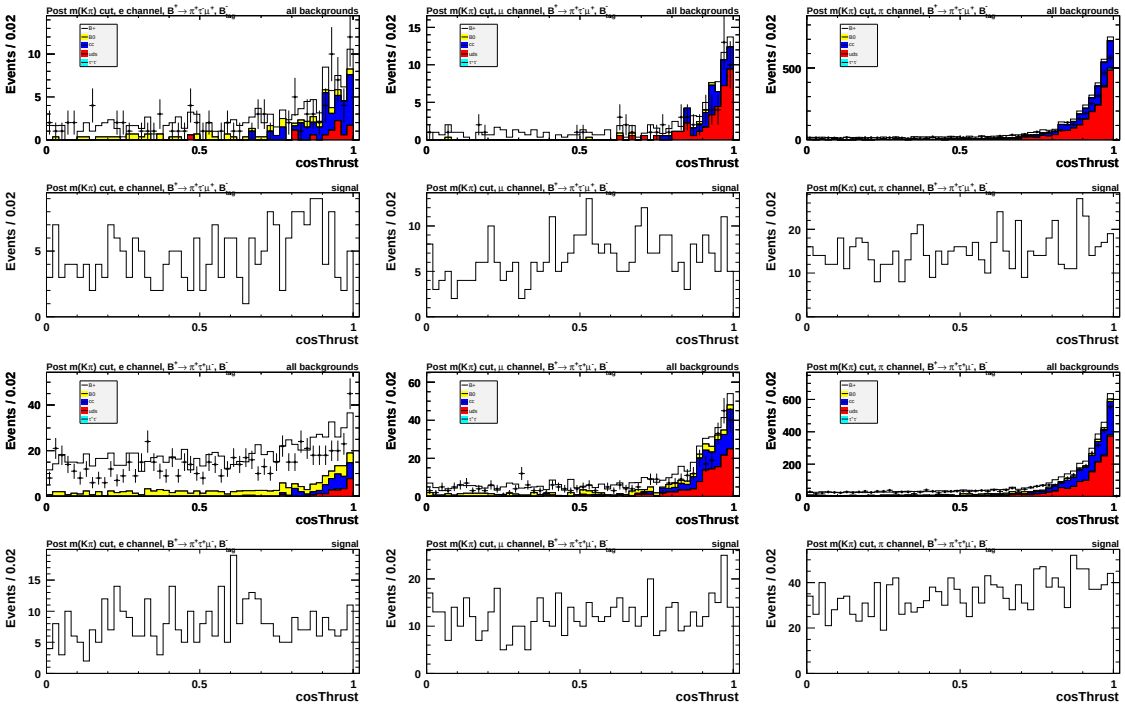

Figure H.3: Post $m(K\pi)$ cut for our **"clean" (top-two) and "dirty" (bottom-two) $\pi\tau\mu$ modes**. Distributions of the $|cos(\theta_{\rm thr})|$ for the **electron** (left), **muon** (middle), & **pion** (right) channels.

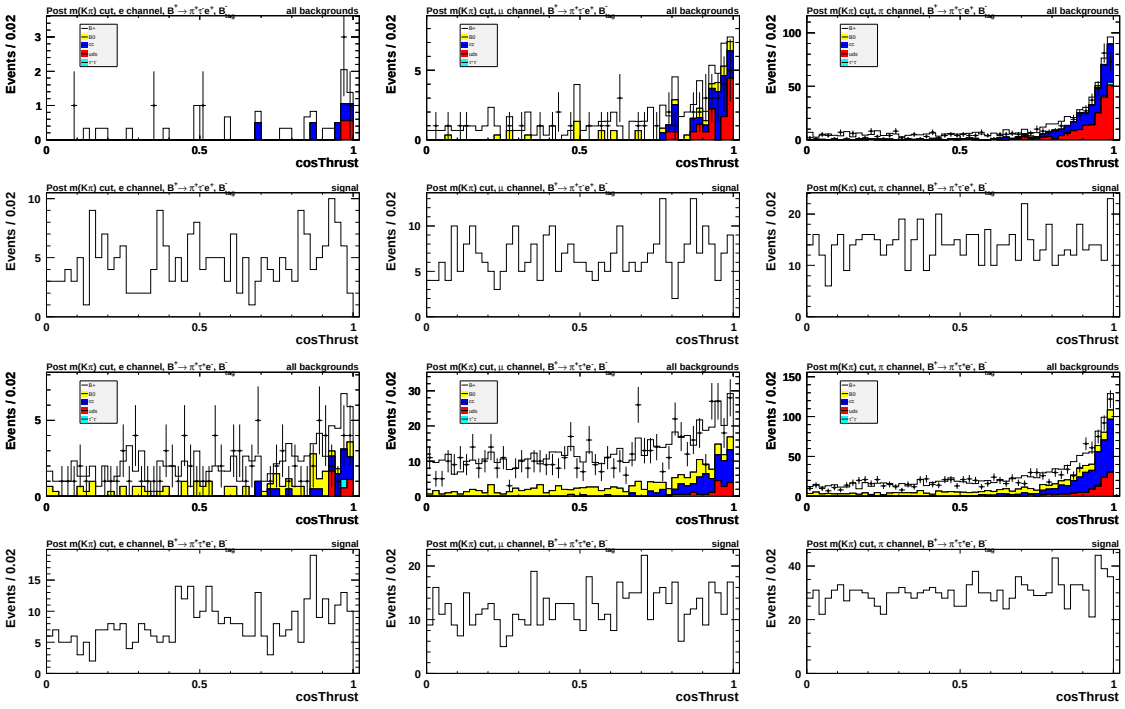

Figure H.4: Post $m(K\pi)$ cut for our **"clean" (top-two) and "dirty" (bottom-two) $\pi\tau e$ modes**. Distributions of the $|cos(\theta_{\rm thr})|$ for the **electron** (left), **muon** (middle), & **pion** (right) channels.

Appendix I

Parameterization of $\sum \boldsymbol{E}_{\mathbf{cal}}$ and $|\cos \boldsymbol{\theta}_{\mathbf{thr}}|$

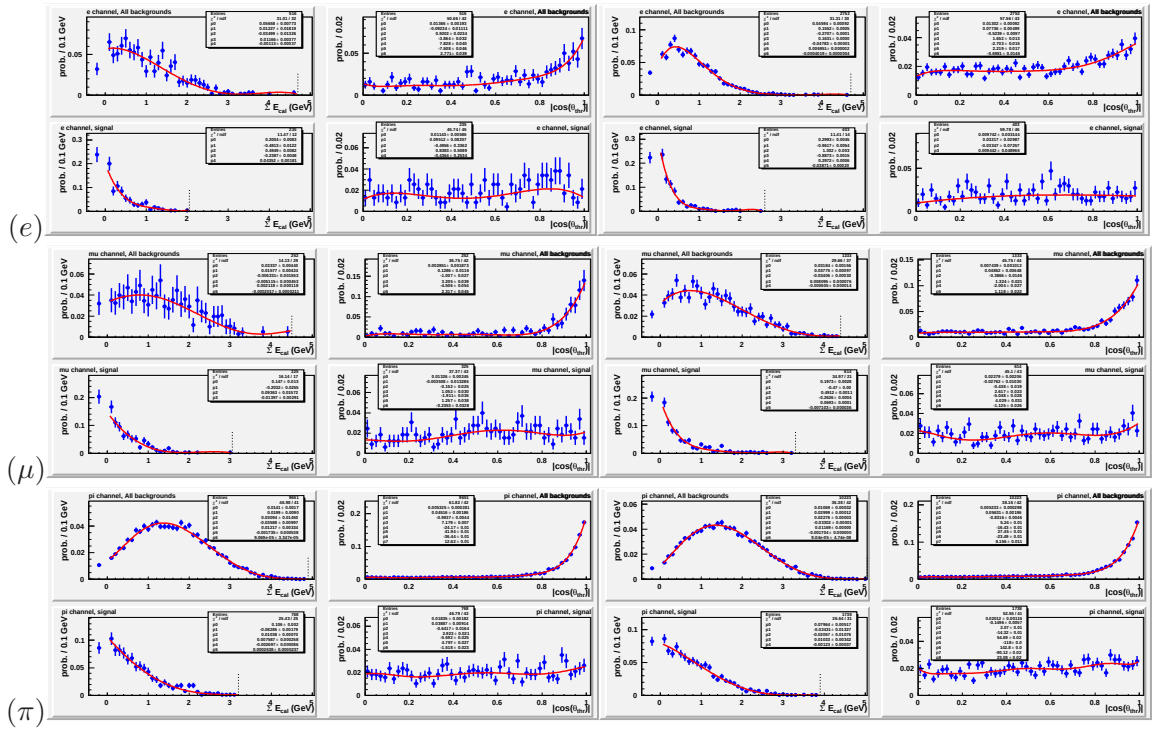

Figure I.1: $\boldsymbol{\pi\tau\mu}$ probability density functions of the $\sum E_{\rm cal}$ (columns 1 & 3) and $|\cos\theta_{\rm thr}|$ (columns 2 & 4) MC distributions for "clean" (left-two columns) and "dirty" (right-two columns) **electron** (top-two rows), **muon** (middle-two rows), and **pion** (bottom-two rows) channels.

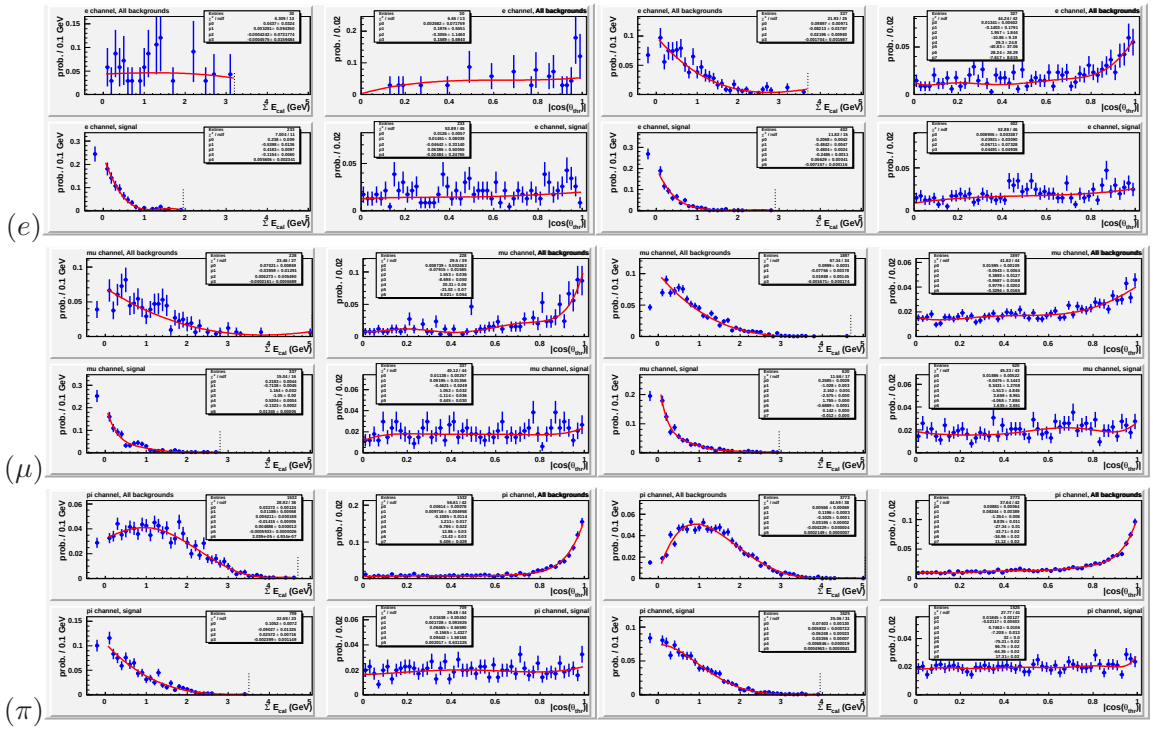

Figure I.2: $\boldsymbol{\pi\tau e}$ probability density functions of the $\sum E_{\rm cal}$ (columns 1 & 3) and $|\cos\theta_{\rm thr}|$ (columns 2 & 4) MC distributions for "clean" (left-two columns) and "dirty" (right-two columns) **electron** (top-two rows), **muon** (middle-two rows), and **pion** (bottom-two rows) channels.

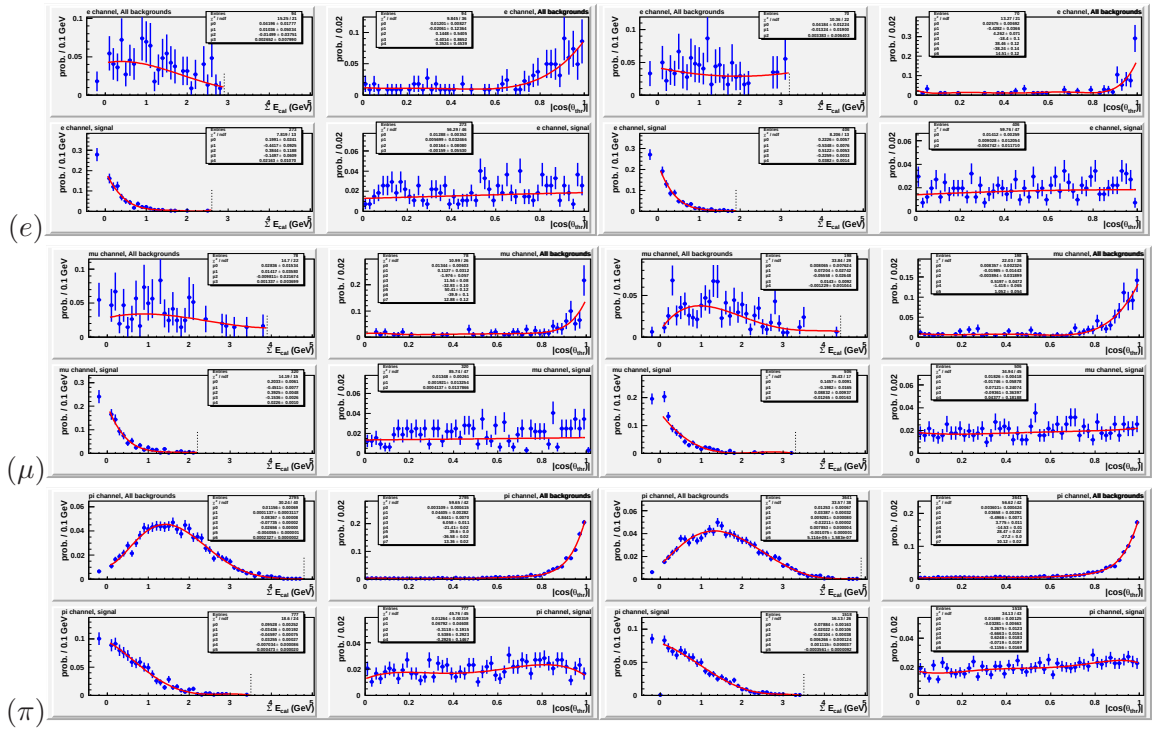

Figure I.3: $\boldsymbol{K\tau\mu}$ probability density functions of the $\sum E_{\rm cal}$ (columns 1 & 3) and $|\cos\theta_{\rm thr}|$ (columns 2 & 4) MC distributions for "clean" (left-two columns) and "dirty" (right-two columns) **electron** (top-two rows), **muon** (middle-two rows), and **pion** (bottom-two rows) channels.

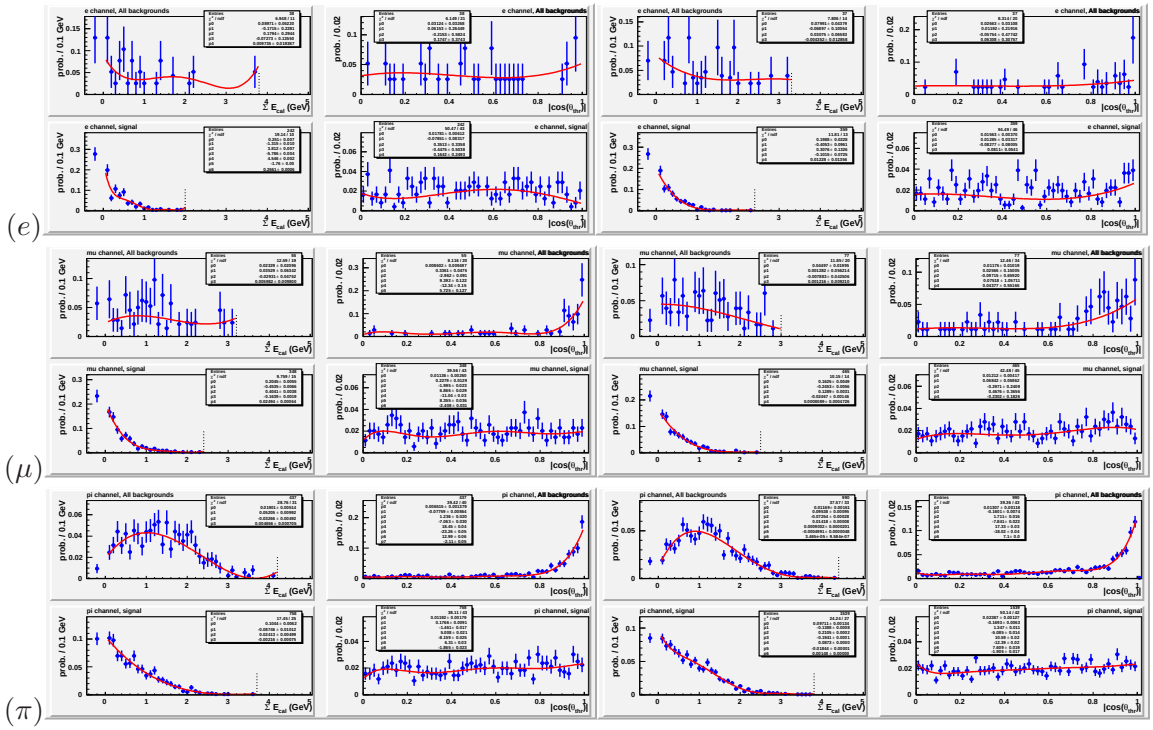

Figure I.4: $\boldsymbol{K\tau e}$ probability density functions of the $\sum E_{\rm cal}$ (columns 1 & 3) and $|\cos\theta_{\rm thr}|$ (columns 2 & 4) MC distributions for "clean" (left-two columns) and "dirty" (right-two columns) **electron** (top-two rows), **muon** (middle-two rows), and **pion** (bottom-two rows) channels.

Appendix J

Distributions of the primary lepton PID quality

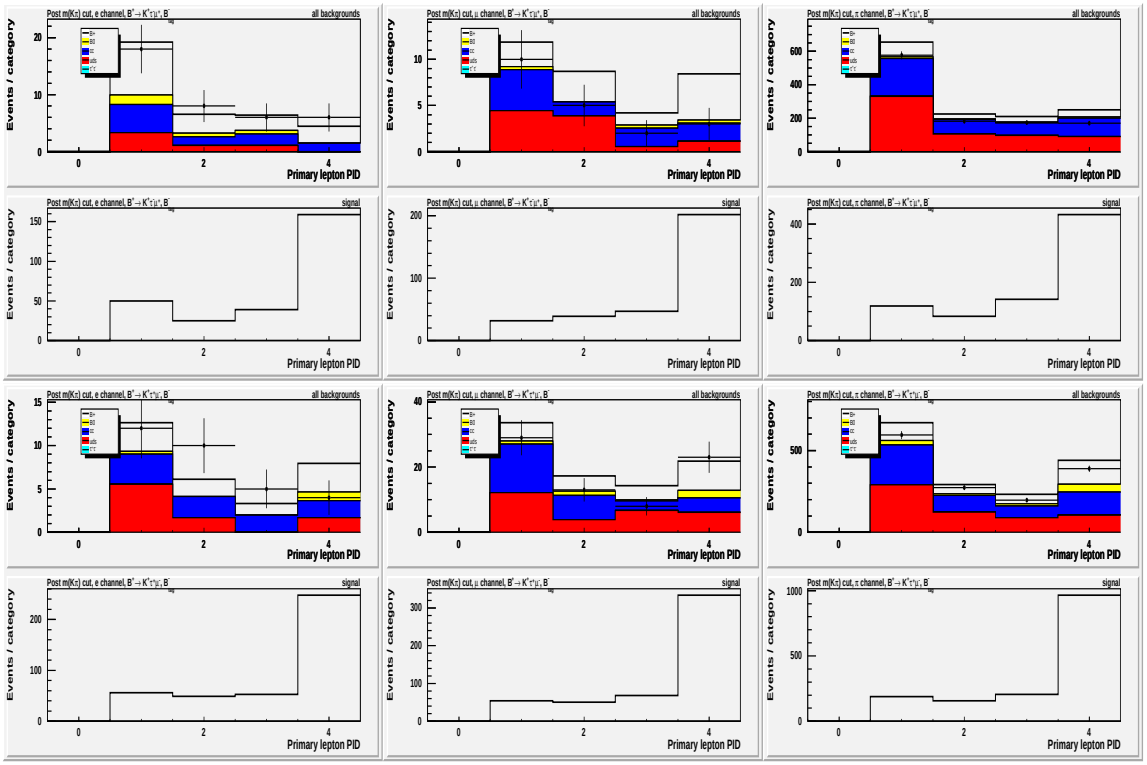

Figure J.1: $K\tau\mu$ distributions of muon PID level for the primary **muon** candidate in the "clean" (top-two) and "dirty" (bottom-two) **electron** (left), **muon** (center), and **pion** (right) channels. Bins correspond to the following PID quality: 1=`muBDTVeryLoose`, 2=`muBDTLoose`, 3=`muBDTTight`, 4=`muBDTVeryTight`.

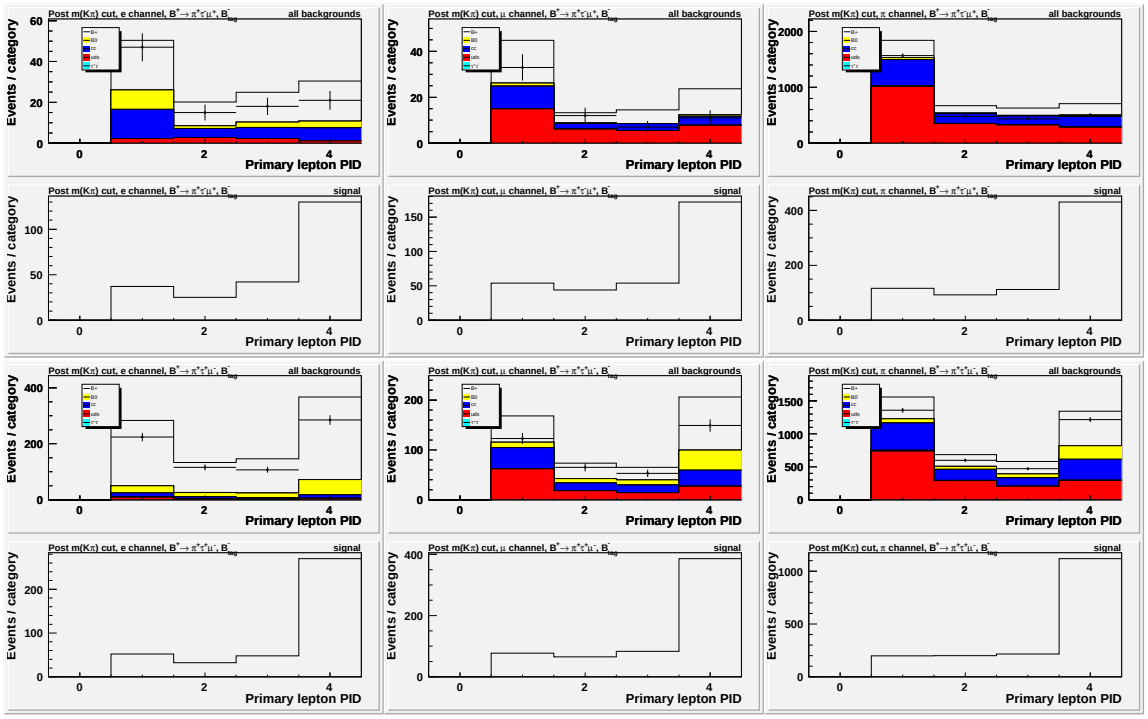

Figure J.2: $\boldsymbol{\pi\tau\mu}$ distributions of muon PID level for the primary **muon** candidate for the "clean" (top-two) and "dirty" (bottom-two) **electron** (left), **muon** (center), and **pion** (right) channels. Bins correspond to the following PID quality: 1=`muBDTVeryLoose`, 2=`muBDTLoose`, 3=`muBDTTight`, 4=`muBDTVeryTight`.

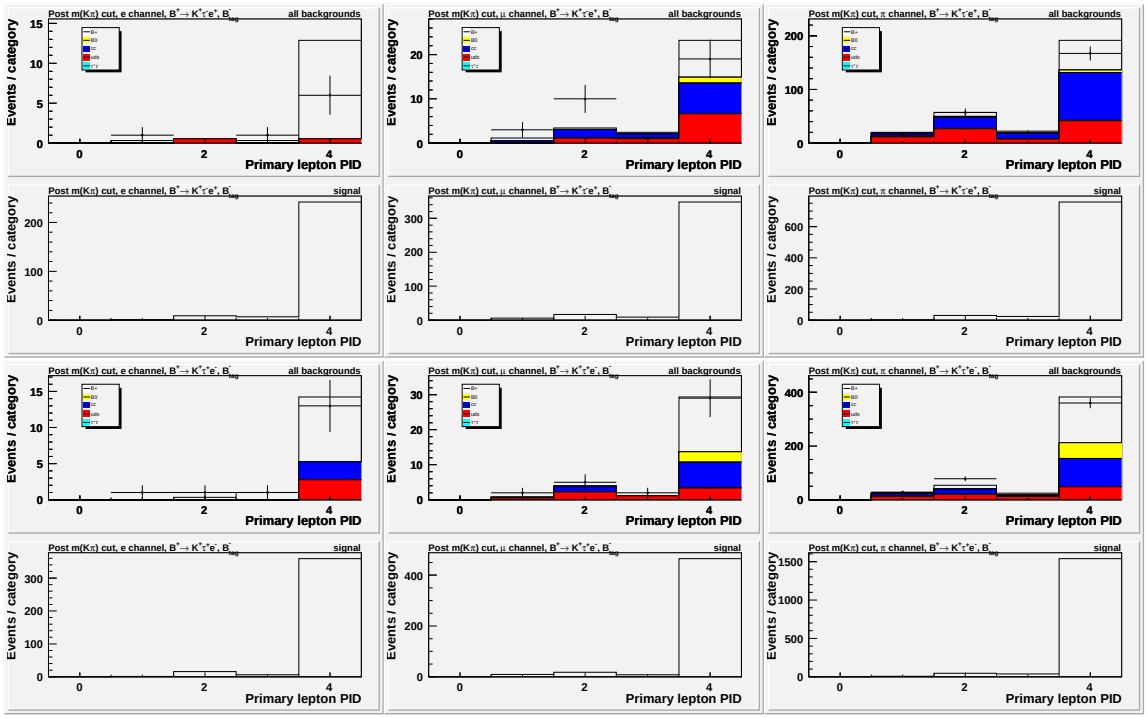

Figure J.3: $K\tau e$ distributions of electron PID level for the primary **electron** candidate for the "clean" (top-two) and "dirty" (bottom-two) **electron** (left), **muon** (center), and **pion** (right) channels. Bins correspond to the following PID quality: 1=`eKMVeryLoose`, 2=`eKMLoose`, 3=`eKMTight`, 4=`eKMVeryTight`.

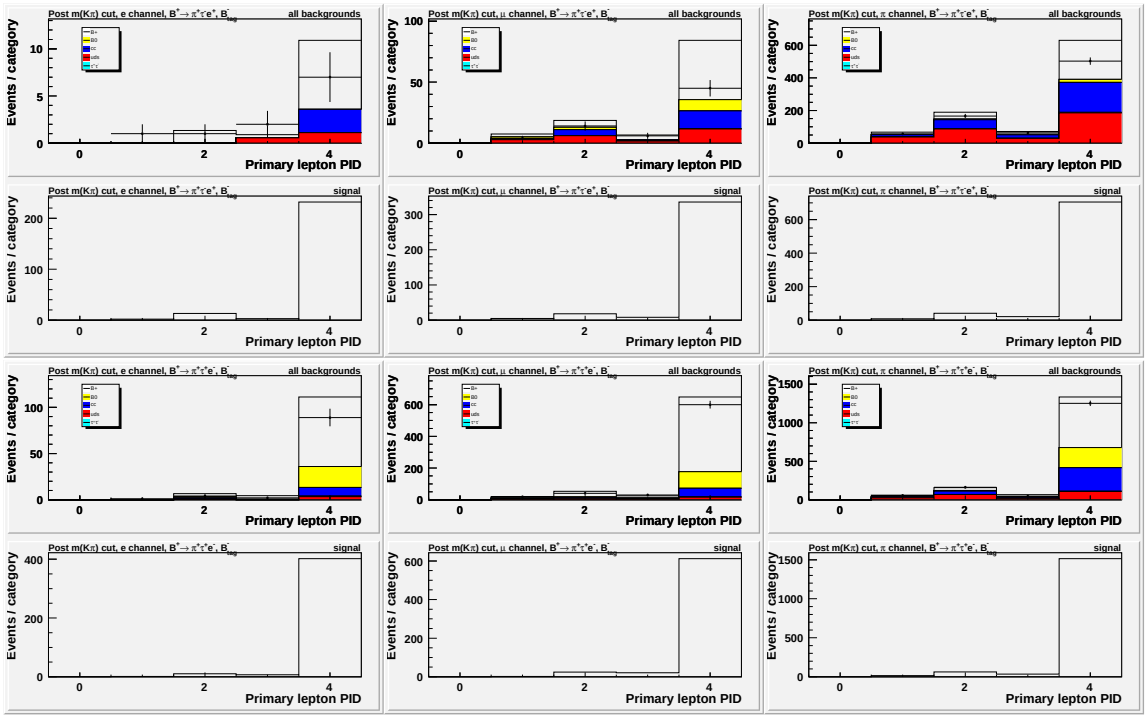

Figure J.4: $\pi\tau e$ distributions of electron PID level for the primary **electron** candidate for the "clean" (top-two) and "dirty" (bottom-two) **electron** (left), **muon** (center), and **pion** (right) channels. Bins correspond to the following PID quality: 1=`eKMVeryLoose`, 2=`eKMLoose`, 3=`eKMTight`, 4=`eKMVeryTight`.

Appendix K

Distributions of the secondary lepton PID quality

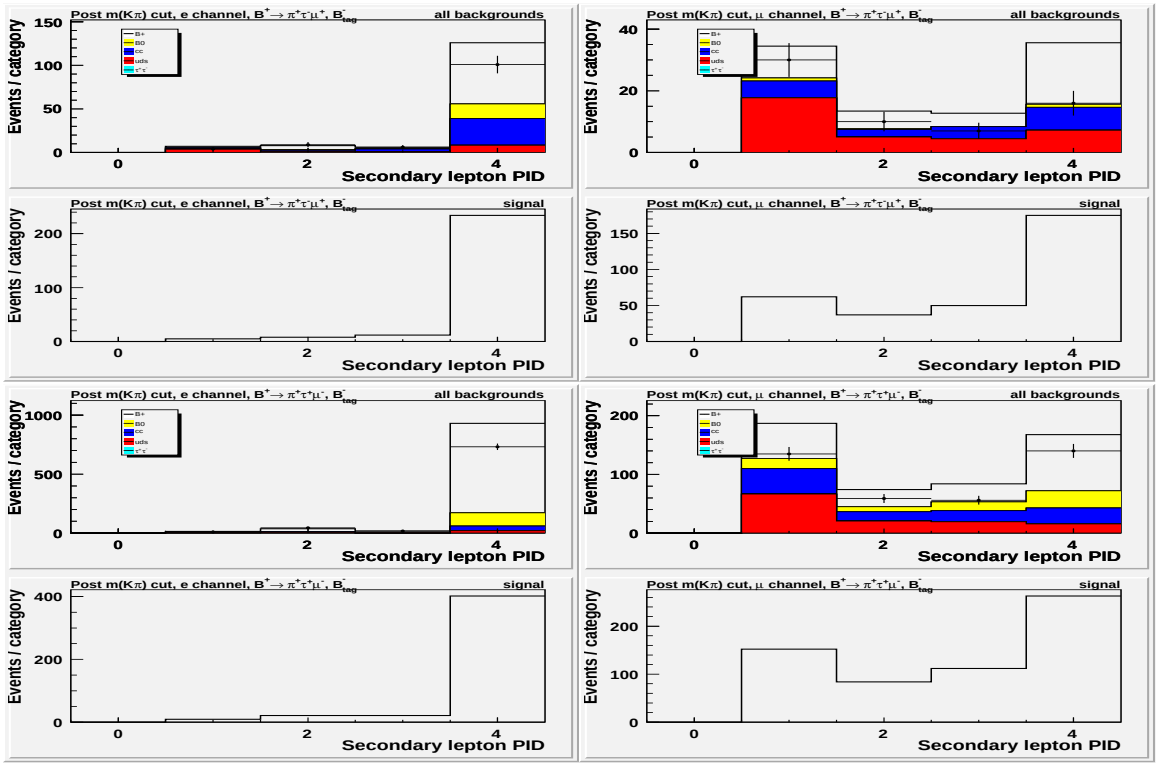

Figure K.1: $\boldsymbol{\pi\tau\mu}$ secondary lepton PID quality for "clean" (top-two) and "dirty" (bottom-two) **electron** (left) and **muon** (right) channels. The electron bins correspond to the following PID quality: 1=`eKMVeryLoose`, 2=`eKMLoose`, 3=`eKMTight`, 4=`eKMVeryTight`. The muon bins correspond to the following PID quality: 1=`muBDTVeryLoose`, 2=`muBDTLoose`, 3=`muBDTTight`, 4=`muBDTVeryTight`.

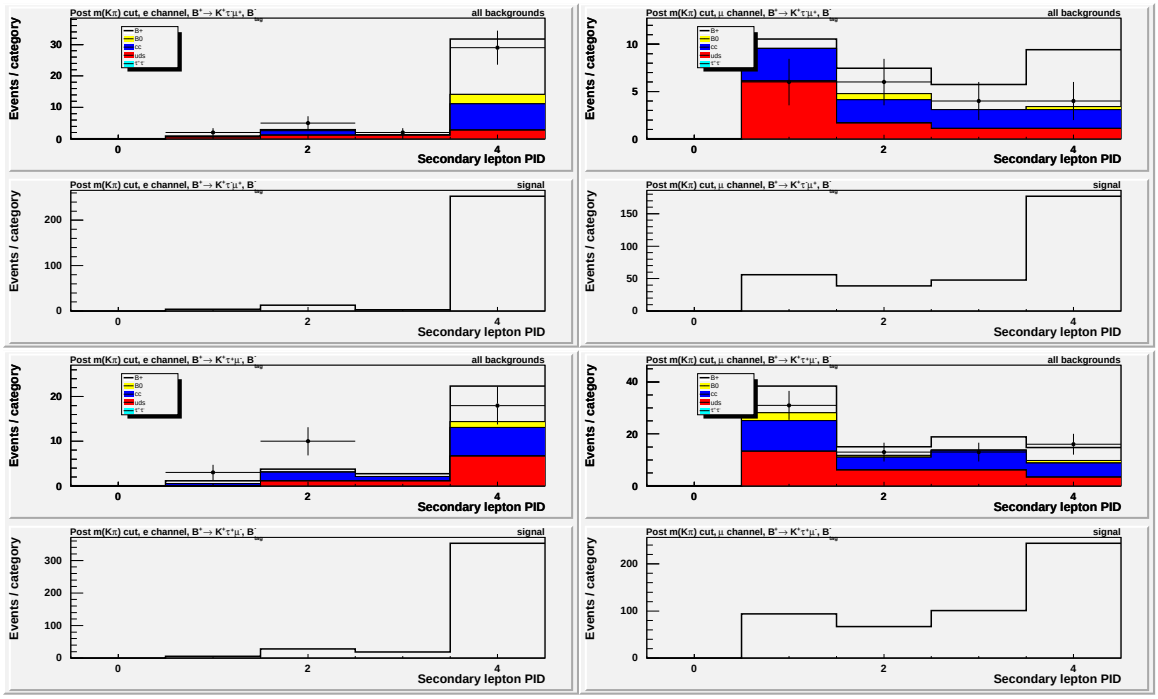

Figure K.2: $K\tau\mu$ secondary lepton PID quality for the "clean" (top-two) and "dirty" (bottom-two) **electron** (left) and **muon** (right) channels. The electron bins correspond to the following PID quality: 1=`eKMVeryLoose`, 2=`eKMLoose`, 3=`eKMTight`, 4=`eKMVeryTight`. The muon bins correspond to the following PID quality: 1=`muBDTVeryLoose`, 2=`muBDTLoose`, 3=`muBDTTight`, 4=`muBDTVeryTight`.

Appendix L

Likelihood ratio outputs

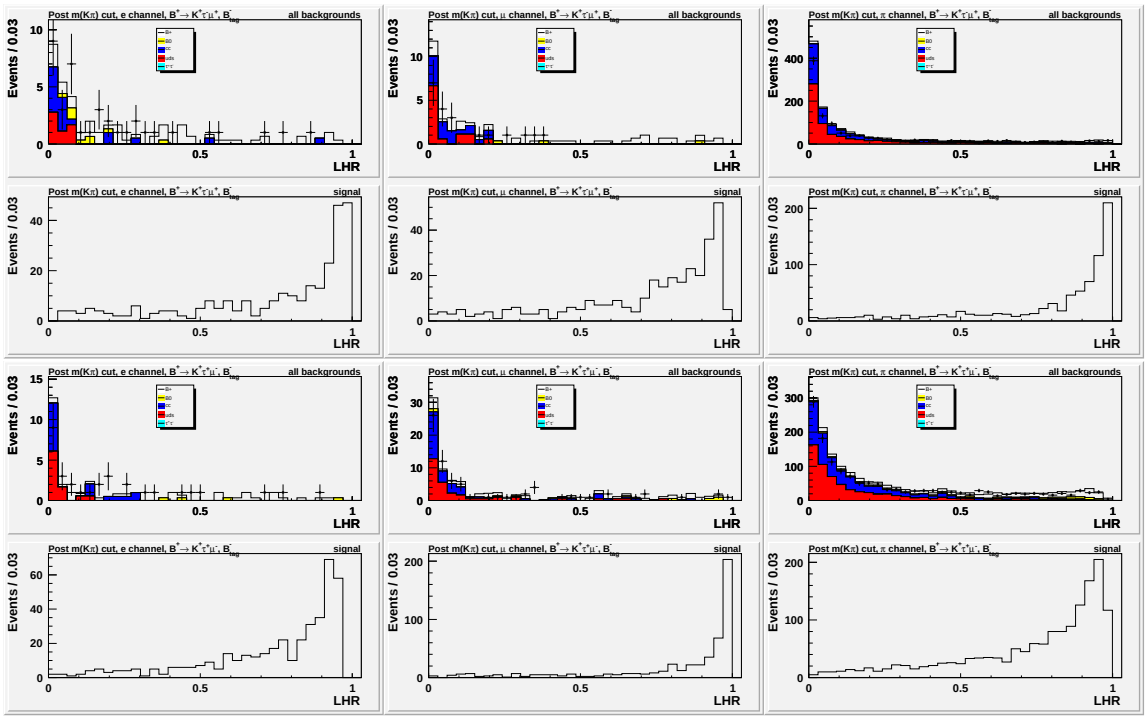

Figure L.1: Likelihood ratio for our "clean" (top-two) and "dirty" (bottom-two) $K\tau\mu$ modes, where $Q_\mu = -Q_{\rm tag}$ and $Q_\mu = Q_{\rm tag}$, respectively, for the **electron** (left), **muon** (center), and **pion** (right) channels. The points with error bars in the top first and third distributions are the on-resonance data. The bottom second and fourth distributions are from signal Monte Carlo. In the "clean" μ channel (top-middle), a minimum LHR cut of greater than 0.40 results in no more data. This will be a concern in the background estimation uncertainty, see section 4.1.3 Table 4.1.

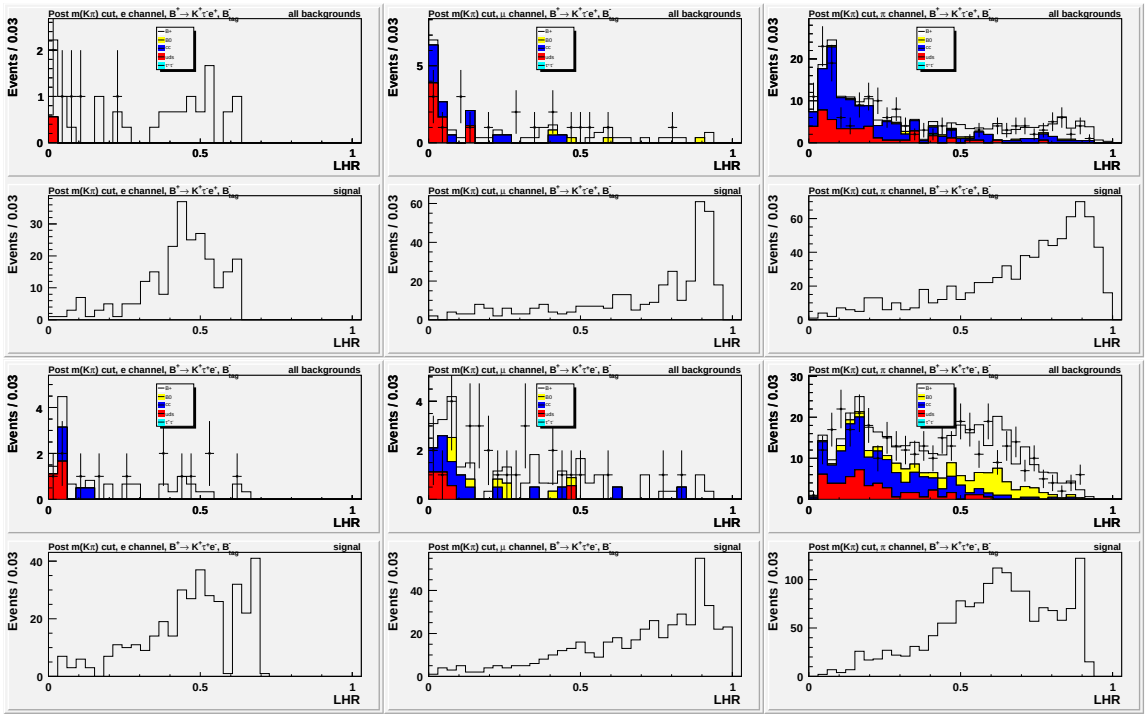

Figure L.2: Likelihood ratio for our "clean" (top-two) and "dirty" (bottom-two) $K\tau e$ modes, where $Q_e = -Q_{\rm tag}$ and $Q_e = Q_{\rm tag}$, respectively, for the **electron** (left), **muon** (center), and **pion** (right) channels. The points with error bars in the top first and third distributions are the on-resonance data. The bottom second and fourth distributions are from signal Monte Carlo. May need to assign systematic uncertainty to low statistics "clean" e channel (top-left) distributions. A minimum LHR cut of greater than 0.25 results in no more data, in this channel as well. This will be a concern in the background estimation uncertainty, see section 4.1.3 Table 4.1.

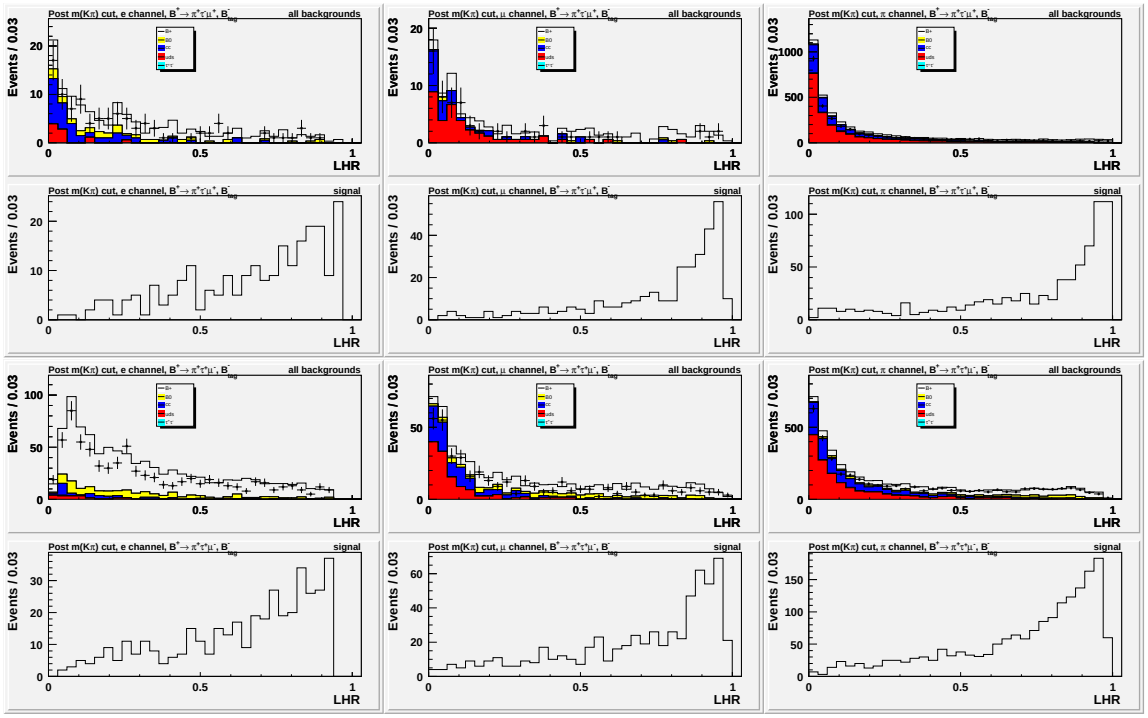

Figure L.3: Likelihood ratio for our "clean" (top-two) and "dirty" (bottom-two) $\boldsymbol{\pi\tau\mu}$ modes, where $Q_\mu = -Q_{\rm tag}$ and $Q_\mu = Q_{\rm tag}$, respectively, for the **electron** (left), **muon** (center), and **pion** (right) channels. The points with error bars in the top first and third distributions are the on-resonance data. The bottom second and fourth distributions are from signal Monte Carlo.

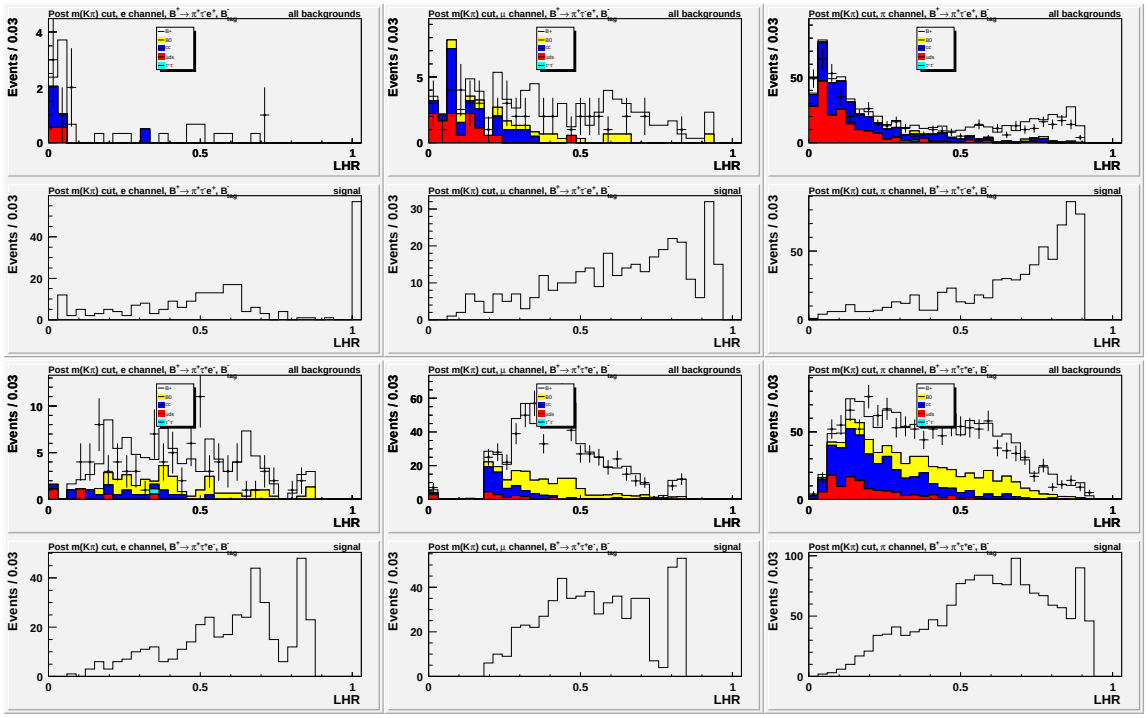

Figure L.4: Likelihood ratio for our "clean" (top-two) and "dirty" (bottom-two) $\boldsymbol{\pi\tau e}$ modes, where $Q_e = -Q_{\rm tag}$ and $Q_e = Q_{\rm tag}$, respectively, for the **electron** (left), **muon** (center), and **pion** (right) channels. The points with error bars in the top first and third distributions are the on-resonance data. The bottom second and fourth distributions are from signal Monte Carlo. May need to assign systematic uncertainty to low statistics "clean" e channel (top-left) distributions.

Appendix M

Δp^* vs. $B_{\rm tag}$ $m_{\rm es}$ scatter plots

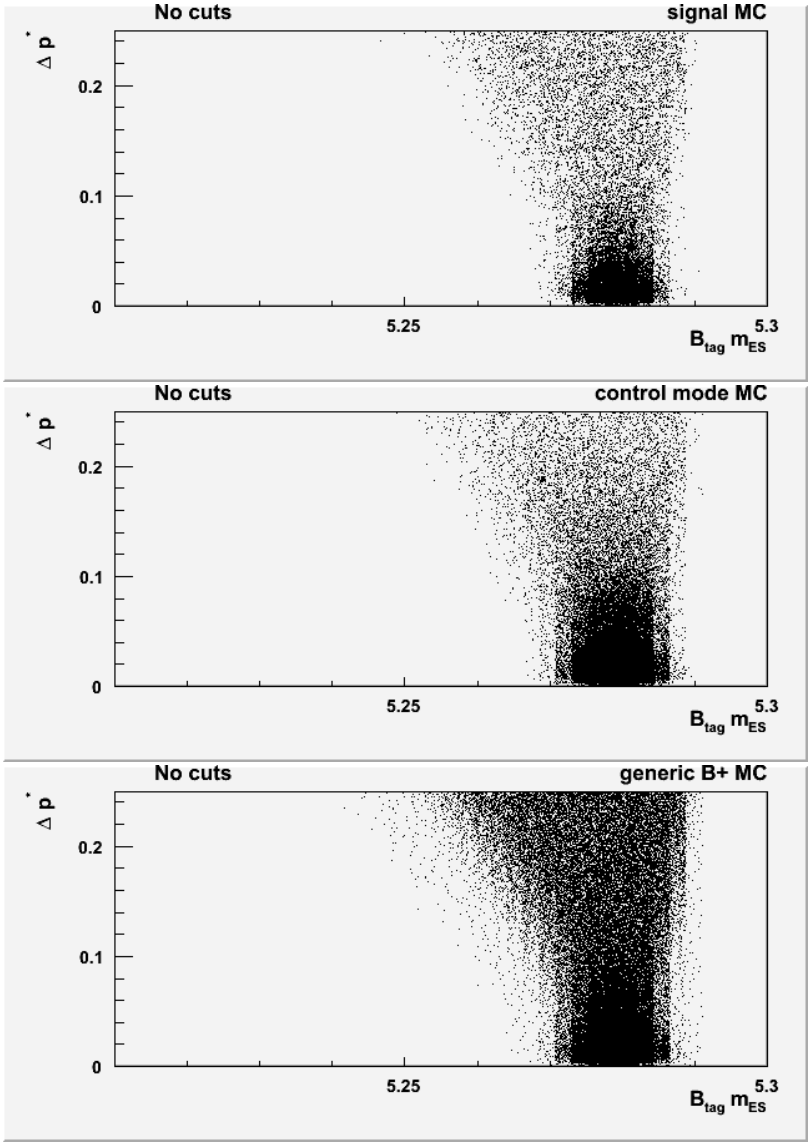

Figure M.1: Scatter plots of Δp^* vs. $B_{\rm tag}$ $m_{\rm es}$ for events with a signal decay (top), events with a $D^{(*)}e\nu$ decay (middle), and generic $B^{\pm}$ events (bottom). No strong correlation observed when no cuts are applied.

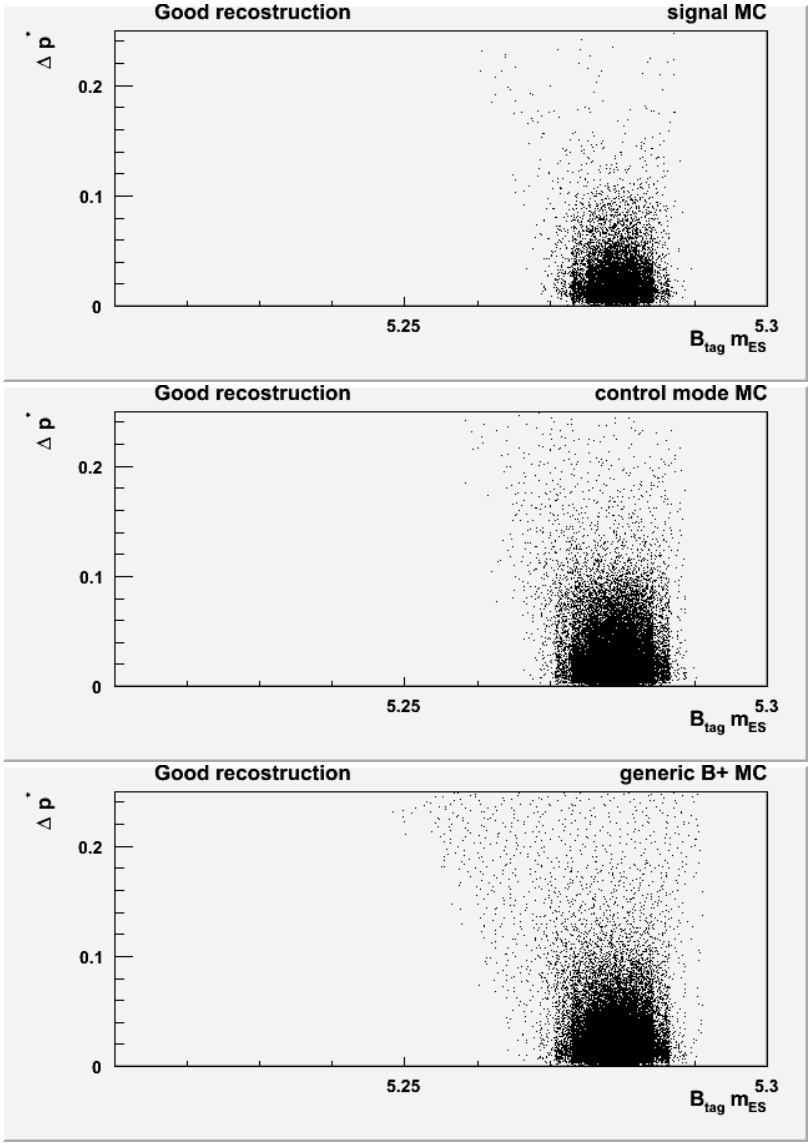

Figure M.2: Scatter plots of Δp^* vs. $B_{\rm tag}$ $m_{\rm es}$ for events with a signal decay (top), events with a $D^{(*)}e\nu$ decay (middle), and generic $B^{\pm}$ events (bottom). No strong correlation observed when the $B_{\rm tag}$ is properly reconstructed.

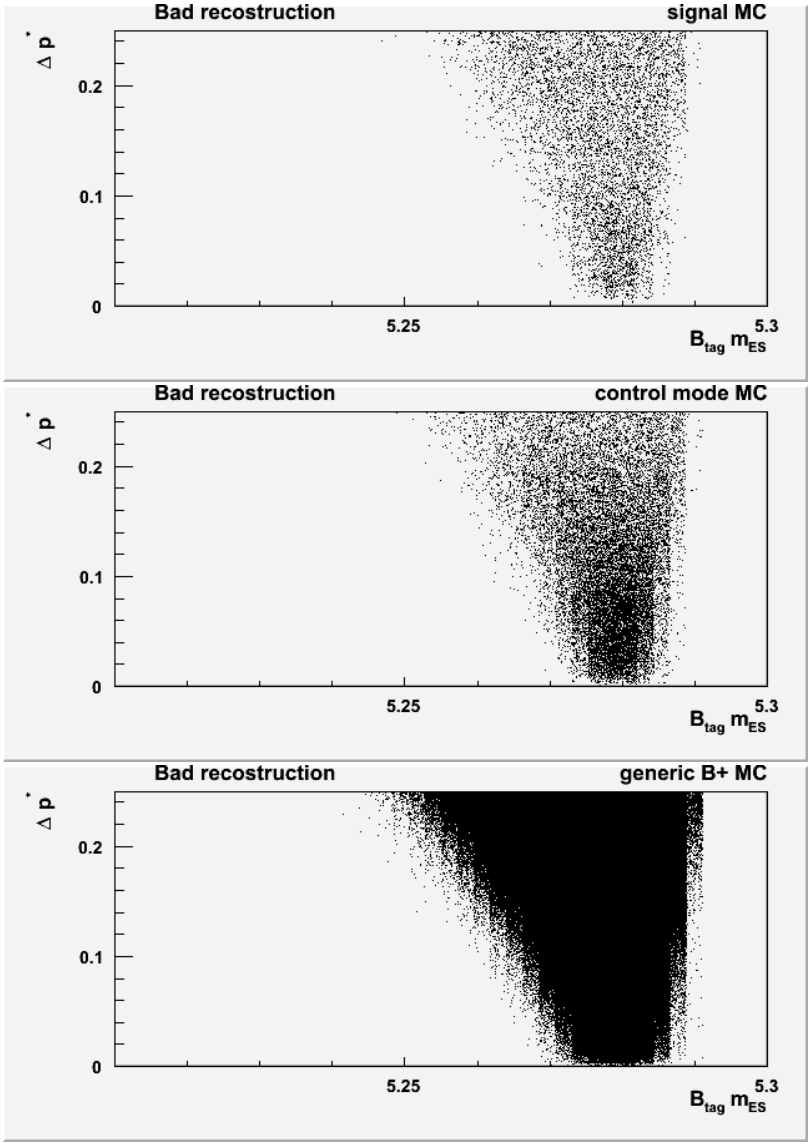

Figure M.3: Scatter plots of Δp^* vs. $B_{\rm tag}$ $m_{\rm es}$ for events with a signal decay (top), events with a $D^{(*)}e\nu$ decay (middle), and generic $B^{\pm}$ events (bottom). No strong correlation observed when the $B_{\rm tag}$ is not properly reconstructed.

Appendix N

Breakdown of signal efficiencies

Tables N.1, N.2, N.3, and N.4 give the absolute signal efficiency at various stages of the event selection for the pion modes. Tables N.5, N.6, N.7, and N.8 give the absolute signal efficiency at various stages of the event selection for the kaon modes.

has $B_{\rm tag}$ with $m_{\rm es} > 5.27$ GeV 120 MeV $m(\tau)$ signal window $\Delta p^* < 0.1$ GeV	$B^+ \to \pi^+\tau^-\mu^+, B^-_{\rm tag}$ ($Q_\mu = -Q_{\rm tag}$) SP mode 9209 generic $B_{\rm tag}$ decay 7373 signal events						
	electron		muon		pion		$\epsilon_{\rm total}$
and passes preselection	657	8.9%	739	10.0%	2109	28.6%	47.5%
and $m(K\pi) > 1.95$ GeV	256	3.5%	313	4.2%	726	9.8%	17.6%
and min $\tau_{\rm lep}$ PID veto	224	3.0%	313	4.2%	726	9.8%	17.1%
and the ($c\bar{c}$) vetoes	224	3.0%	309	4.2%	704	9.5%	16.8%
and the (p,K) vetoes	220	3.0%	304	4.1%	671	9.1%	16.2%
and no extra GTVL veto	219	3.0%	301	4.1%	668	9.1%	16.1%
and kaon PID veto	216	2.9%	292	4.0%	659	8.9%	15.8%
and K PID veto on primary π	216	2.9%	292	4.0%	659	8.9%	15.8%
and min primary π PID veto	216	2.9%	291	3.9%	646	8.8%	15.6%
and in $m(\tau)$ sig. win. [1.717,1.837] GeV	176	2.4%	244	3.3%	494	6.7%	12.4%
and optimal LHR cuts (0.25, 0.50, 0.90)	168	2.28%	211	2.86%	207	2.81%	7.95%

Table N.1: **"Clean" $\boldsymbol{\pi\tau\mu}$**: Breakdown of absolute signal efficiencies using signal MC.

has $B_{\rm tag}$ with $m_{\rm es} > 5.27$ GeV 120 MeV $m(\tau)$ signal window $\Delta p^* < 0.1$ GeV	$B^+ \to \pi^+\tau^+\mu^-, B^-_{\rm tag}$ $(Q_\mu = Q_{\rm tag})$ SP mode 9209 generic $B_{\rm tag}$ decay 7471 signal events						
	electron		muon		pion		$\epsilon_{\rm total}$
and passes preselection	648	8.7%	780	10.4%	2152	28.8%	47.9%
and $m(K\pi) > 1.95$ GeV	437	5.8%	569	7.6%	1518	20.3%	33.8%
and min $\tau_{\rm lep}$ PID veto	384	5.1%	569	7.6%	1518	20.3%	33.1%
and the $(c\bar{c})$ vetoes	384	5.1%	553	7.4%	1480	19.8%	32.4%
and the (p,K) vetoes	377	5.0%	547	7.3%	1439	19.3%	31.6%
and no extra GTVL veto	375	5.0%	545	7.3%	1431	19.2%	31.5%
and kaon PID veto	368	4.9%	537	7.2%	1403	18.8%	30.9%
and K PID veto on primary π	368	4.9%	537	7.2%	1403	18.8%	30.9%
and min primary π PID veto	367	4.9%	535	7.2%	1399	18.7%	30.8%
and in $m(\tau)$ sig. win. [1.717,1.837] GeV	308	4.1%	428	5.7%	1160	15.5%	25.4%
and optimal LHR cuts (0.25, 0.50, 0.75)	285	3.81%	359	4.81%	679	9.09%	17.71%

Table N.2: **"Dirty" $\pi\tau\mu$**: Breakdown of absolute signal efficiencies using signal MC.

has $B_{\rm tag}$ with $m_{\rm es} > 5.27$ GeV 120 MeV $m(\tau)$ signal window $\Delta p^* < 0.1$ GeV	$B^+ \to \pi^+\tau^-e^+, B^-_{\rm tag}$ $(Q_e = -Q_{\rm tag})$ SP mode 9209 generic $B_{\rm tag}$ decay 7427 signal events						
	electron		muon		pion		$\epsilon_{\rm total}$
and passes preselection	674	9.1%	793	10.7%	2292	30.9%	50.6%
OR passes presel w/ min $B_{\rm lep}$ PID veto	622	8.4%	728	9.8%	2112	28.4%	46.6%
and $m(K\pi) > 1.95$ GeV	238	3.2%	319	4.3%	688	9.3%	16.8%
and min $\tau_{\rm lep}$ PID veto	222	3.0%	319	4.3%	688	9.3%	16.5%
and the $(c\bar{c})$ vetoes	217	2.9%	319	4.3%	667	9.0%	16.2%
and γ conversion veto	217	2.9%	319	4.3%	666	9.0%	16.2%
and the (p,K) vetoes	210	2.8%	307	4.1%	607	8.2%	15.1%
and no extra GTVL veto	209	2.8%	305	4.1%	603	8.1%	15.0%
and kaon PID veto	205	2.8%	302	4.1%	593	8.0%	14.8%
and K PID veto on primary π	205	2.8%	302	4.1%	593	8.0%	14.8%
and min primary π PID veto	205	2.8%	302	4.1%	589	7.9%	14.8%
and in $m(\tau)$ sig. win. [1.717,1.837] GeV	163	2.2%	218	2.9%	451	6.1%	11.2%
and optimal LHR cuts (0.25, 0.25, 0.25)	145	1.95%	205	2.76%	424	5.71%	10.42%

Table N.3: **"Clean" $\pi\tau e$**: Breakdown of absolute signal efficiencies using signal MC.

has $B_{\rm tag}$ with $m_{\rm es} > 5.27$ GeV 120 MeV $m(\tau)$ signal window $\Delta p^* < 0.1$ GeV	$B^+ \to \pi^+\tau^+e^-, B^-_{\rm tag}$ $(Q_e = Q_{\rm tag})$ SP mode 9209 generic $B_{\rm tag}$ decay 7414 signal events						
	electron		muon		pion		$\epsilon_{\rm total}$
and passes preselection	674	9.1%	897	12.1%	2201	29.7%	50.9%
OR passes presel w/ min $B_{\rm lep}$ PID veto	635	8.6%	832	11.2%	2020	27.2%	47.0%
and $m(K\pi) > 1.95$ GeV	432	5.8%	576	7.8%	1373	18.5%	32.1%
and min $\tau_{\rm lep}$ PID veto	392	5.3%	576	7.8%	1373	18.5%	31.6%
and the $(c\bar{c})$ vetoes	383	5.2%	576	7.8%	1328	17.9%	30.8%
and γ conversion veto	380	5.1%	576	7.8%	1321	17.8%	30.7%
and the (p,K) vetoes	368	5.0%	567	7.6%	1286	17.3%	30.0%
and no extra GTVL veto	368	5.0%	564	7.6%	1281	17.3%	29.8%
and kaon PID veto	361	4.9%	554	7.5%	1269	17.1%	29.5%
and K PID veto on primary π	361	4.9%	554	7.5%	1269	17.1%	29.5%
and min primary π PID veto	361	4.9%	548	7.4%	1262	17.0%	29.3%
and in $m(\tau)$ sig. win. [1.717,1.837] GeV	272	3.7%	345	4.7%	968	13.1%	21.4%
and optimal LHR cuts (0.50, 0.25, 0.75)	213	2.87%	334	4.50%	270	3.64%	11.02%

Table N.4: **"Dirty" $\pi\tau e$**: Breakdown of absolute signal efficiencies using signal MC.

has $B_{\rm tag}$ with $m_{\rm es} > 5.27$ GeV 120 MeV $m(\tau)$ signal window $\Delta p^* < 0.1$ GeV	$B^+ \to K^+\tau^-\mu^+, B^-_{\rm tag}$ $(Q_\mu = -Q_{\rm tag})$ SP mode 7448 generic $B_{\rm tag}$ decay 7513 signal events						
	electron		muon		pion		$\epsilon_{\rm total}$
and passes preselection	642	8.5%	722	9.6%	2076	27.6%	45.8%
and $m(K\pi) > 1.95$ GeV	254	3.4%	308	4.1%	720	9.6%	17.1%
and the $(c\bar{c})$ vetoes	254	3.4%	301	4.0%	699	9.3%	16.7%
and the (p,K) vetoes	247	3.3%	297	4.0%	660	8.8%	16.0%
and no extra GTVL veto	246	3.3%	297	4.0%	657	8.7%	16.0%
and in $m(\tau)$ sig. win. [1.717,1.837] GeV	211	2.8%	256	3.4%	530	7.1%	13.3%
and Optimal LHR cuts (0.00, 0.25, 0.90)	211	2.81%	236	3.14%	306	4.07%	10.02%

Table N.5: **"Clean" $K\tau\mu$**: Breakdown of absolute signal efficiencies using signal MC.

has $B_{\rm tag}$ with $m_{\rm es} > 5.27$ GeV 120 MeV $m(\tau)$ signal window $\Delta p^* < 0.1$ GeV	$B^+ \to K^+\tau^+\mu^-, B^-_{\rm tag}$ $(Q_\mu = Q_{\rm tag})$ SP mode 7448 generic $B_{\rm tag}$ decay 7399 signal events						
	electron		muon		pion		$\epsilon_{\rm total}$
and passes preselection	584	7.9%	719	9.7%	2117	28.6%	46.2%
and $m(K\pi) > 1.95$ GeV	382	5.2%	478	6.5%	1319	17.8%	29.4%
and the $(c\bar{c})$ vetoes	382	5.2%	468	6.3%	1302	17.6%	29.1%
and the (p,K) vetoes	379	5.1%	465	6.3%	1262	17.1%	28.5%
and no extra GTVL veto	378	5.1%	464	6.3%	1261	17.0%	28.4%
and in $m(\tau)$ sig. win. [1.717,1.837] GeV	337	4.6%	408	5.5%	1051	14.2%	24.3%
and Optimal LHR cuts (0.25, 0.90, 0.75)	320	4.32%	263	3.55%	673	9.10%	16.98%

Table N.6: **"Dirty" $K\tau\mu$**: Breakdown of absolute signal efficiencies using signal MC.

has $B_{\rm tag}$ with $m_{\rm es} > 5.27$ GeV 120 MeV $m(\tau)$ signal window $\Delta p^* < 0.1$ GeV	$B^+ \to K^+\tau^-e^+, B^-_{\rm tag}$ $(Q_e = -Q_{\rm tag})$ SP mode 9656 generic $B_{\rm tag}$ decay 8196 signal events						
	electron		muon		pion		$\epsilon_{\rm total}$
and passes preselection	706	8.6%	746	9.1%	2159	26.3%	44.1%
and passes primary e PID requirement	659	8.0%	686	8.4%	1998	24.4%	40.8%
and $m(K\pi) > 1.95$ GeV	257	3.1%	317	3.9%	679	8.3%	15.3%
and min $\tau_{\rm lep}$ PID veto	237	2.9%	317	3.9%	679	8.3%	15.0%
and the $(c\bar{c})$ vetoes	234	2.9%	317	3.9%	668	8.2%	14.9%
and γ conversion veto	232	2.8%	317	3.9%	666	8.1%	14.8%
and the (p,K) vetoes	225	2.7%	313	3.8%	624	7.6%	14.2%
and no extra GTVL veto	225	2.7%	313	3.8%	624	7.6%	14.2%
and in $m(\tau)$ sig. win. [1.717,1.837] GeV	178	2.17%	252	3.07%	483	5.89%	11.14%
and Optimal LHR cuts (0.00, 0.40, 0.50)	178	2.17%	221	2.70%	394	4.81%	9.68%

Table N.7: **"Clean" $K\tau e$**: Breakdown of absolute signal efficiencies using signal MC.

has $B_{\rm tag}$ with $m_{\rm es} > 5.27$ GeV 120 MeV $m(\tau)$ signal window $\Delta p^* < 0.1$ GeV	$B^+ \to K^+\tau^+e^-, B^-_{\rm tag}$ $(Q_e = Q_{\rm tag})$ SP mode 9656 generic $B_{\rm tag}$ decay 8367 signal events						
	electron		muon		pion		$\epsilon_{\rm total}$
and passes preselection	670	8.0%	740	8.8%	2376	28.4%	45.2%
and passes primary e PID requirement	620	7.4%	681	8.1%	2181	26.1%	41.6%
and $m(K\pi) > 1.95$ GeV	388	4.6%	426	5.1%	1348	16.1%	25.8%
and min $\tau_{\rm lep}$ PID veto	338	4.0%	426	5.1%	1348	16.1%	25.2%
and the $(c\bar{c})$ vetoes	334	4.0%	426	5.1%	1333	15.9%	25.0%
and γ conversion veto	334	4.0%	426	5.1%	1329	15.9%	25.0%
and the (p,K) vetoes	327	3.9%	418	5.0%	1289	15.4%	24.3%
and no extra GTVL veto	324	3.9%	415	5.0%	1284	15.3%	24.2%
and in $m(\tau)$ sig. win. [1.717,1.837] GeV	254	3.04%	327	3.91%	977	11.68%	18.62%
and Optimal LHR cuts (0.25, 0.50, 0.50)	233	2.78%	268	3.20%	731	8.74%	14.72%

Table N.8: **"Dirty" $K\tau e$**: Breakdown of absolute signal efficiencies using signal MC.

Appendix O

Signal window optimization

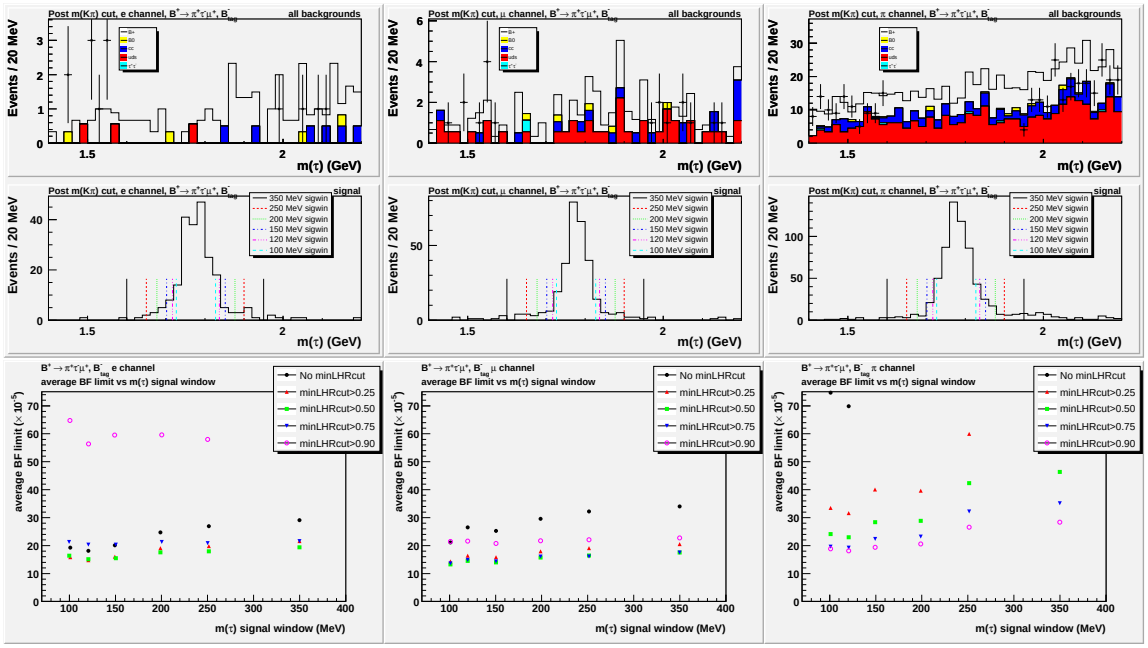

Figure O.1: **"Clean" $\pi\tau\mu$**: Top-two plots show a zoomed-in $m(\tau)$ distribution signal indicating our various signal window ranges with the bottom plots showing the expected average branching fraction upper limit vs. $m(\tau)$ signal window plots. The **electron** (left), **muon** (center), and **pion** (right) channels are shown. The on-resonance data is blinded with a 350 MeV signal window.

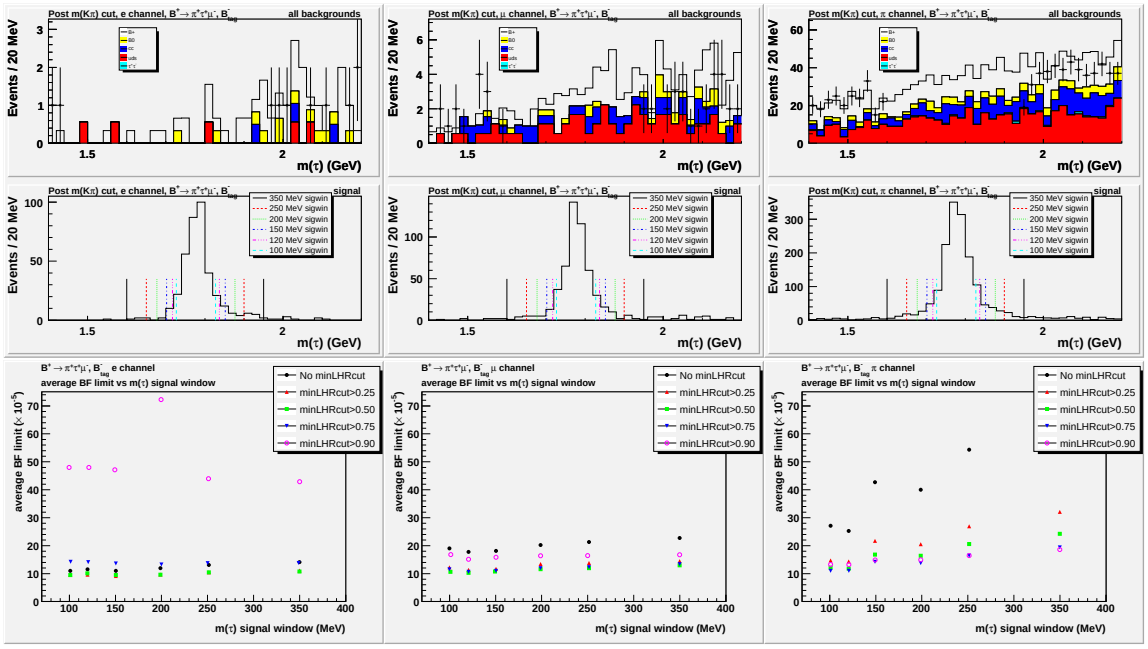

Figure O.2: **"Dirty" $\pi\tau\mu$**: Top-two plots show a zoomed-in $m(\tau)$ distribution signal indicating our various signal window ranges with the bottom plots showing the expected average branching fraction upper limit vs. $m(\tau)$ signal window plots. The **electron** (left), **muon** (center), and **pion** (right) channels are shown. The on-resonance data is blinded with a 350 MeV signal window.

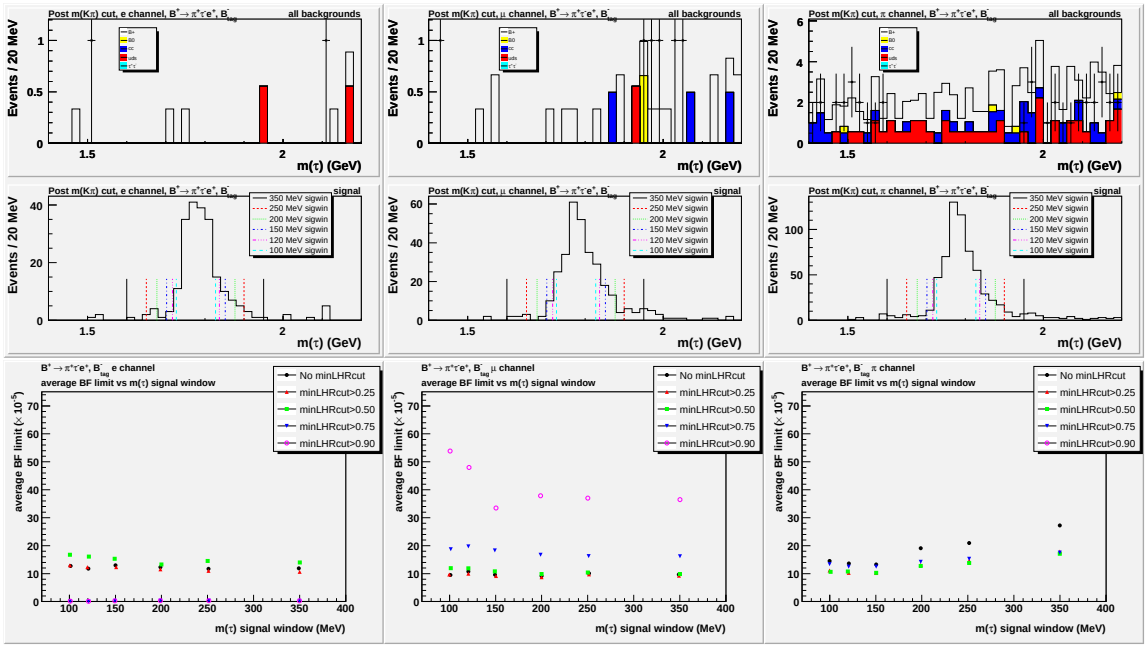

Figure O.3: **"Clean" $\pi\tau e$**: Top-two plots show a zoomed-in $m(\tau)$ distribution signal indicating our various signal window ranges with the bottom plots showing the expected average branching fraction upper limit vs. $m(\tau)$ signal window plots. The **electron** (left), **muon** (center), and **pion** (right) channels are shown. The on-resonance data is blinded with a 350 MeV signal window.

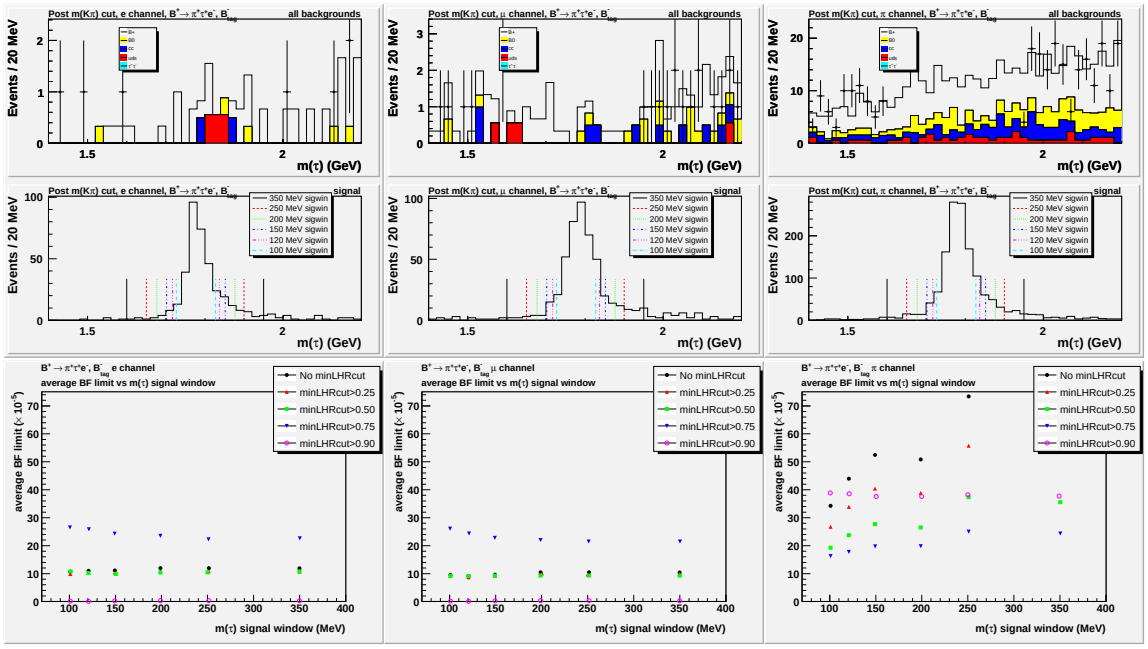

Figure O.4: **"Dirty" $\pi\tau e$**: Top-two plots show a zoomed-in $m(\tau)$ distribution signal indicating our various signal window ranges with the bottom plots showing the expected average branching fraction upper limit vs. $m(\tau)$ signal window plots. The **electron** (left), **muon** (center), and **pion** (right) channels are shown. The on-resonance data is blinded with a 350 MeV signal window.

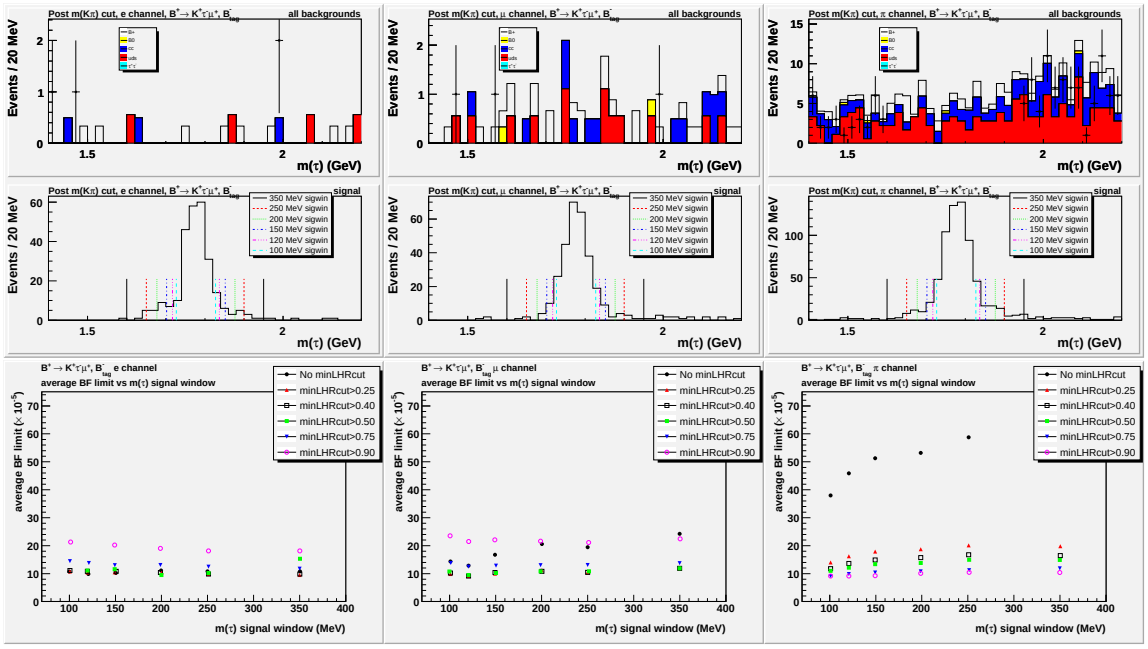

Figure O.5: **"Clean"** $K\tau\mu$: Top-two plots show a zoomed-in $m(\tau)$ distribution signal indicating our various signal window ranges with the bottom plots showing the expected average branching fraction upper limit vs. $m(\tau)$ signal window plots. The **electron** (left), **muon** (center), and **pion** (right) channels are shown. The on-resonance data is blinded with a 350 MeV signal window.

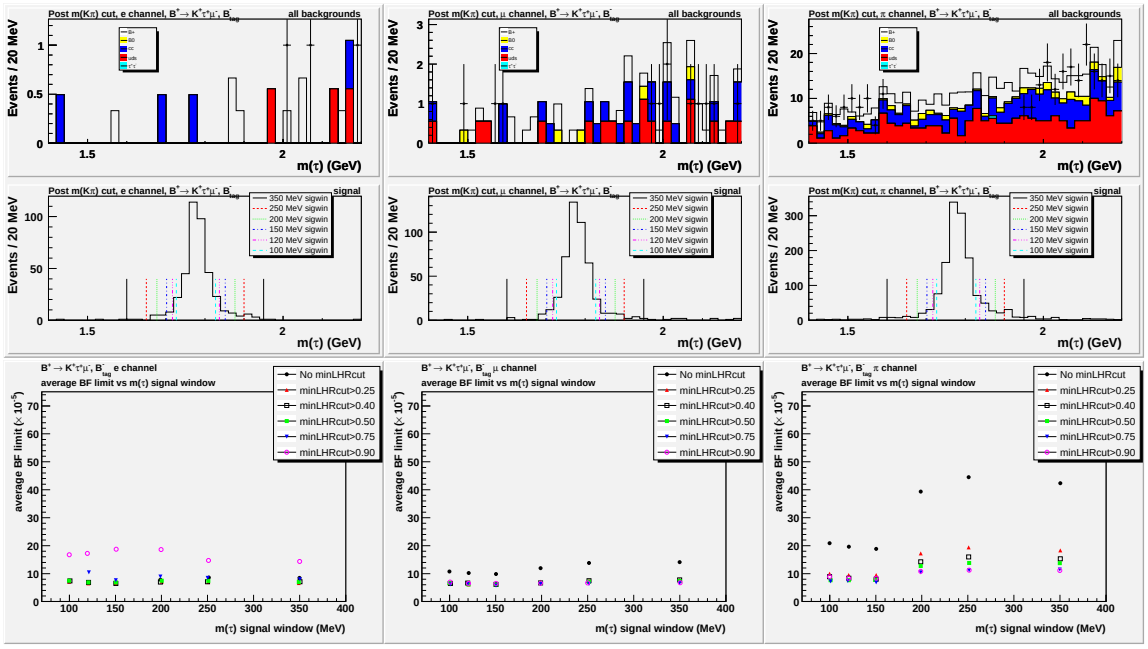

Figure O.6: **"Dirty"** $K\tau\mu$: Top-two plots show a zoomed-in $m(\tau)$ distribution signal indicating our various signal window ranges with the bottom plots showing the expected average branching fraction upper limit vs. $m(\tau)$ signal window plots. The **electron** (left), **muon** (center), and **pion** (right) channels are shown. The on-resonance data is blinded with a 350 MeV signal window.

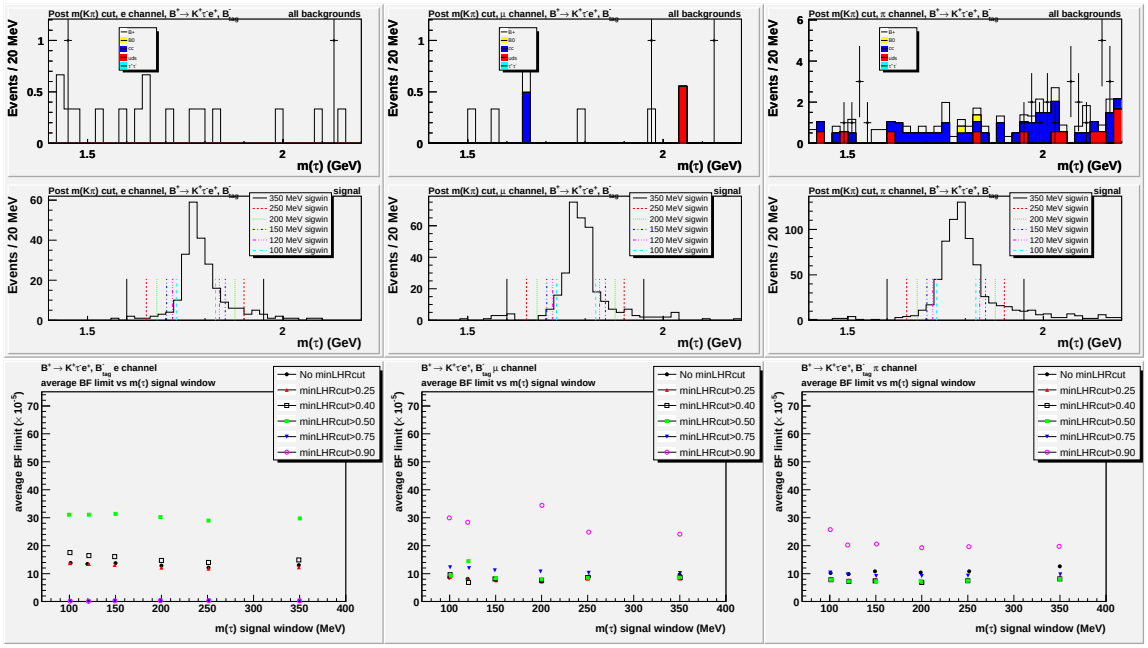

Figure O.7: **"Clean"** $K\tau e$: Top-two plots show a zoomed-in $m(\tau)$ distribution signal indicating our various signal window ranges with the bottom plots showing the expected average branching fraction upper limit vs. $m(\tau)$ signal window plots. The **electron** (left), **muon** (center), and **pion** (right) channels are shown. The on-resonance data is blinded with a 350 MeV signal window.

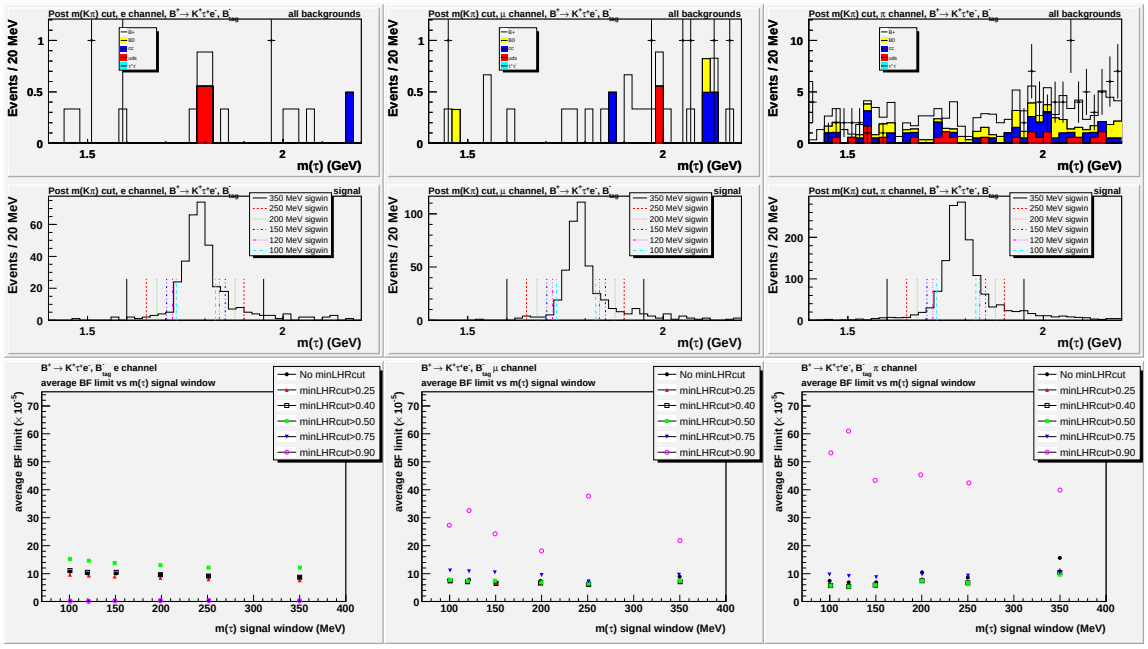

Figure O.8: **"Dirty"** $K\tau e$: Top-two plots show a zoomed-in $m(\tau)$ distribution signal indicating our various signal window ranges with the bottom plots showing the expected average branching fraction upper limit vs. $m(\tau)$ signal window plots. The **electron** (left), **muon** (center), and **pion** (right) channels are shown. The on-resonance data is blinded with a 350 MeV signal window.

Appendix P

Expected signal branching fraction limits

signal modes	Optimal $m(\tau)$ signal window (MeV)	Optimal likelihood ratio cuts	Barlow $\mathcal{B}_{sig} = (*10^{-5})$ 90% C.L. limit	
	e, μ, π	e, μ, π	mean	RMS
$B^+ \to \pi^+\tau^+e^-, B^-_{\rm tag}$	120, 120, 120	0.50, 0.25, 0.75	3.99	3.44
$B^+ \to \pi^+\tau^-e^+, B^-_{\rm tag}$	120, 120, 120	0.25, 0.25, 0.25	2.78	2.29
$B^+ \to \pi^+\tau^+\mu^-, B^-_{\rm tag}$	120, 120, 120	0.25, 0.50, 0.75	3.80	3.18
$B^+ \to \pi^+\tau^-\mu^+, B^-_{\rm tag}$	120, 120, 120	0.25, 0.50, 0.90	4.53	3.78
$B^+ \to K^+\tau^+e^-, B^-_{\rm tag}$	120, 120, 120	0.25, 0.50, 0.50	2.16	1.67
$B^+ \to K^+\tau^-e^+, B^-_{\rm tag}$	120, 120, 120	0.00, 0.40, 0.50	2.97	1.47
$B^+ \to K^+\tau^+\mu^-, B^-_{\rm tag}$	120, 120, 120	0.25, 0.90, 0.75	1.85	1.42
$B^+ \to K^+\tau^-\mu^+, B^-_{\rm tag}$	120, 120, 120	0.00, 0.25, 0.90	3.29	1.88

Table P.1: Summary of the multiple channel mean and RMS expected signal branching fraction upper limits at the 90% confidence level using the R. Barlow method. The best average limits for each signal decay mode are given optimized for our minimum likelihood ratio cuts and $m(\tau)$ signal window ranges. The Q_ℓ and $Q_{\rm tag}$ configured modes combine the three τ decay channels. The Poisson distributions of the expected limits for 500 experiments are found in Figure P.1.

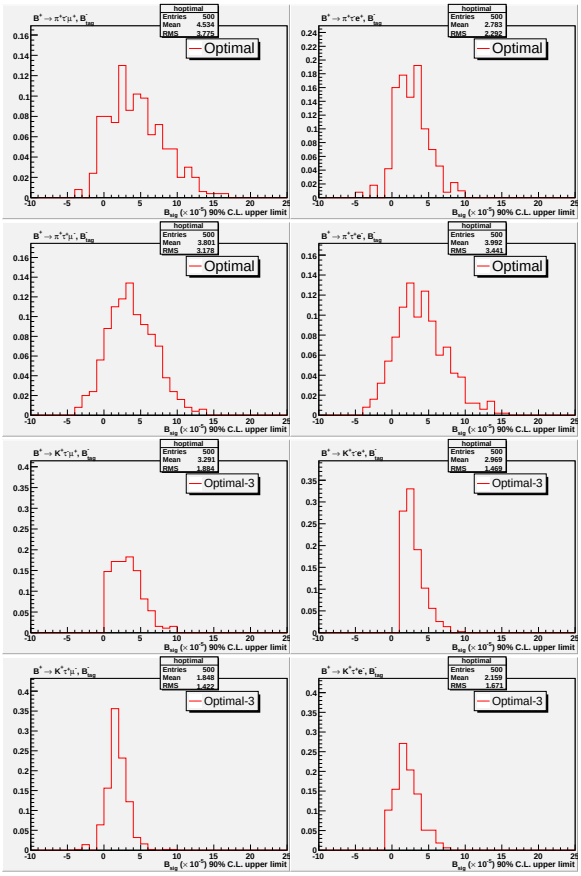

Figure P.1: RMS and means of expected signal branching fraction upper limits for optimized minimum likelihood ratio cuts and $m(\tau)$ signal windows. Histograms of the 90% confidence-level upper limit on the signal branching fraction for 500 generated sets of expected observed events assuming no signal combining each tau channel using the Barlow method.

Appendix Q

Signal $\sum E_{\rm cal}$ - Double Tag Systematic

We can conveniently extract a systematic variation on the signal $\sum E_{\rm cal}$ likelihood ratio input from our $B^- \to D^{(*)0}\ell\nu$; $D^0 \to K^-\pi^+$ control samples to build distributions composed of similar final states. This method of using a double tag sample as been done before, and we use it to obtain a reasonable systematic uncertainty on the signal $\sum E_{\rm cal}$ ($E_{\rm extra}$) likelihood ratio signal efficiency.

The nominal signal MC $\sum E_{\rm cal}$ distribution is modified by multiplying the normalized signal MC distribution by the ratio of normalized on-resonance to Monte Carlo control sample (double tag) distributions. The double tag sample reconstructs semi-leptonic B decays with appropriate ΔE requirements which can very closely mimic our signal MC $\sum E_{\rm cal}$ distribution for each τ decay channel. The on-resonance double tag, MC double tag, and signal MC samples require the same binning in order to properly scale the modified sys-

tematic signal MC distribution bin-by-bin. We compute the new systematic signal MC distributions using the formula below with propagated error:

$$\begin{aligned}
\mathcal{P}_{\substack{\text{syst}\\ \text{sig MC}}}\left(\sum E_{\text{cal}}\right) &= \left(\frac{\mathcal{P}_{\substack{\text{data}\\ \text{ctrl}}}(\sum E_{\text{cal}})}{\mathcal{P}_{\substack{\text{MC}\\ \text{ctrl}}}(\sum E_{\text{cal}})}\right)\mathcal{P}_{\substack{\text{sig}\\ \text{MC}}}\left(\sum E_{\text{cal}}\right); \\
\Delta\mathcal{P}_{\substack{\text{syst}\\ \text{sig MC}}} &= \mathcal{P}_{\substack{\text{syst}\\ \text{sig MC}}}\sqrt{\left(\frac{\Delta\mathcal{P}_{\substack{\text{data}\\ \text{ctrl}}}}{\mathcal{P}_{\substack{\text{data}\\ \text{ctrl}}}}\right)^2+\left(\frac{\Delta\mathcal{P}_{\substack{\text{MC}\\ \text{ctrl}}}}{\mathcal{P}_{\substack{\text{MC}\\ \text{ctrl}}}}\right)^2+\left(\frac{\Delta\mathcal{P}_{\substack{\text{sig}\\ \text{MC}}}}{\mathcal{P}_{\substack{\text{sig}\\ \text{MC}}}}\right)^2},
\end{aligned} \tag{Q.1}$$

where $\mathcal{P}(\sum E_{\text{cal}})$ are normalized extra energy distributions and $\Delta\mathcal{P}$ is the bin-by-bin uncertainty. Next, we normalize the new systematic signal MC $\sum E_{\text{cal}}$ distributions and fit it to determine new likelihood ratio input parameters for the signal shape. We use the new PDF parameters as our variation from nominal for each channel coherently. The deviation from our nominal LHR signal efficiency is our systematic error for this component.

Recall from Figure 3.14, we have our $B^- \to D^{(*)0}\ell\nu$; $D^0 \to K^-\pi^+$ control samples, which we then use for our double tag samples. We can cut around the ΔE distributions to build $\sum E_{\text{cal}}$ (E_{extra}) shapes to mimic our signal final state topologies. The e and μ channel signal MC shapes are in general similar, see middle and bottom plots in Figure Q.1, respectively from our "clean" $K\tau\mu$ example. The plot on top is built from the $B^- \to D^0\mu\nu$ double tag sample, requiring $\Delta E > -0.05$ GeV to remove most of the π^0's in the event reconstruction. Notice on-resonance data points and Monte Carlo distributions are in good agreement. We use the plot on top to determine the ratio of normalized on-resonance to Monte Carlo factors.

In Figure Q.2, we compare the $\sum E_{\text{cal}}$ shapes needed to generate the π channel systematic signal MC shape using our "clean" $K\tau\mu$ example again. In the top plot, we remove events a single π^0 in the reconstruction from D^{*0} events by excluding events in the range $\Delta E \in [-0.5, -0.05]$ GeV from our entire $B^- \to D^{(*)0}\mu\nu$ double tag sample. This is

done to reconstruct the offset peak at $\sum E_{\rm cal} = 0$ where there should be zero neutral pions and the log tail possibly from multiple π^0's. Again, notice that on-resonance data and the Monte Carlo distributions are in good agreement.

In Figure Q.3, the $\sum E_{\rm cal}$ distributions for our double tag systematic (left) computed using equation Q.1, and the associated PDFs (right) are shown for our three τ decay channels. We use these input parameters for each channel coherently to extract the systematic deviation in the LHR signal efficiency. We use the "clean" $K\tau\mu$ distributions as an example of the overall procedure. Other distributions can be presented, if requested.

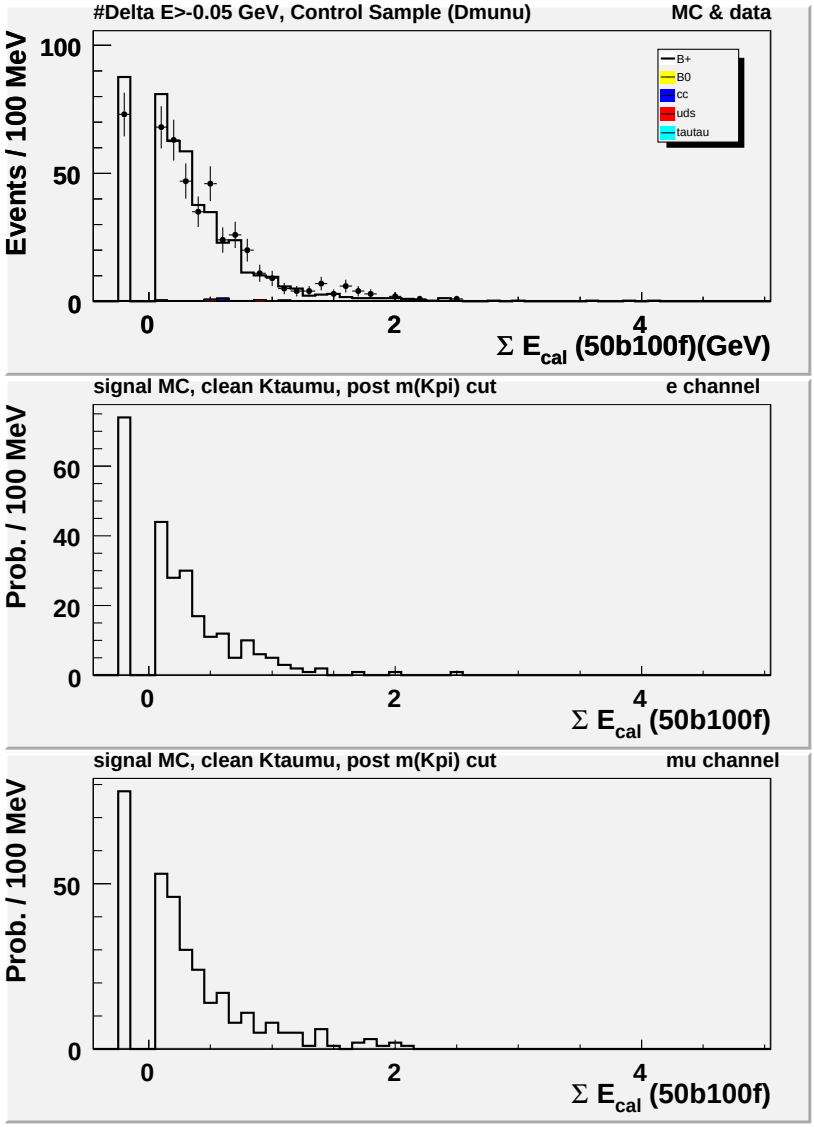

Figure Q.1: $\sum E_{\rm cal}$ ($E_{\rm extra}$) distributions used to compute double tag systematic in the LHR signal efficiency. The on-resonance data and MC distributions from the $D^{(*)0}\mu\nu$ control sample, after the $\Delta E > -0.05$ GeV requirement (top). Data and MC agreement is very good. The e and μ channel signal MC "clean" $K\tau\mu$ distributions are shown in the middle and bottom plots, respectively.

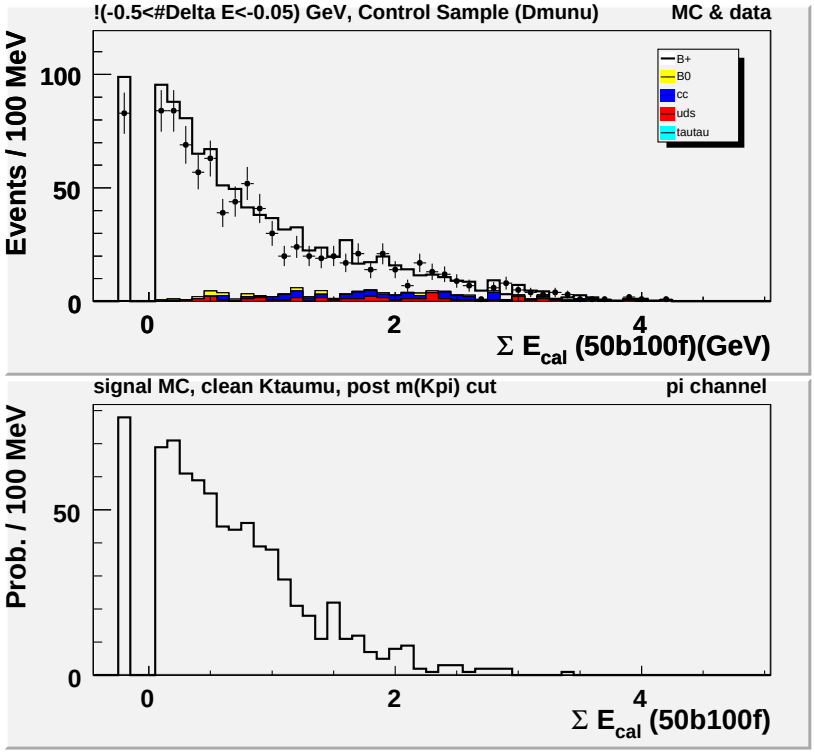

Figure Q.2: $\sum E_{\rm cal}$ ($E_{\rm extra}$) distributions used to compute double tag systematic in the LHR signal efficiency. The on-resonance data and MC distributions from the $D^{(*)0}\mu\nu$ control sample, after excluding events in the range $\Delta E \in [-0.5, -0.05]$ GeV (top). Data and MC agreement is very good. The π channel signal MC "clean" $K\tau\mu$ distribution is shown (bottom).

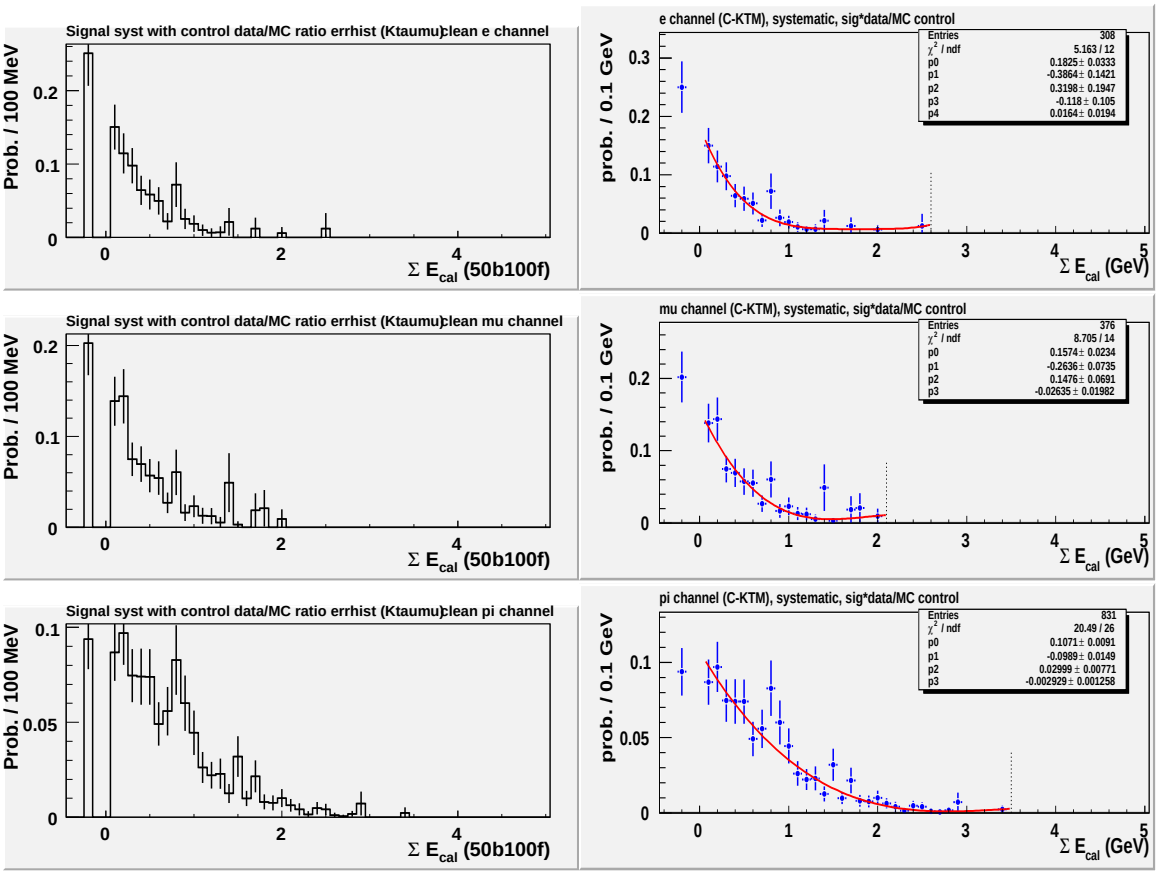

Figure Q.3: Modified signal $\sum E_{\rm cal}$ ($E_{\rm extra}$) systematic distributions with double tag control data/MC ratios for the "clean" $K\tau\mu$ e, μ, and π channels (left). The distributions with error bars are generated using equation Q.1. The associated PDFs with fit parameters are also shown (right).

Appendix R

K vs. π PID Efficiency Systematics - ΔE Fits

This additional systematic uncertainty must be considered because of our normalization of the signal branching fraction using the $D^{(*)0}\ell\nu$ control sample reconstruction. We add this systematic uncertainty in quadrature to our statistical uncertainty in our sensitivity, S, the denominator in equation R.1. For $B^+ \to K^+\tau\ell$ reconstructions, since the final state topology is similar, the signal sample hadron PID efficiency and control sample hadron PID efficiency cancel. In $B^+ \to \pi^+\tau\ell$ reconstructions, this is not the case. Recall our normalized signal branching fraction, equation 3.10, where here we substitute $N_{\pi\tau\ell}$ for $N_{\rm obs} - N_{\rm BG}$ - the number of observed events minus the number of expected background events:

$$\mathcal{B}_{\pi\tau\ell} = \frac{N_{\rm obs} - N_{\rm BG}}{N_{D\ell\nu}\left(\frac{\epsilon_{\rm tag}^{\pi\tau\ell}}{\epsilon_{\rm tag}^{D\ell\nu}}\right)\left(\frac{\epsilon_{\pi\tau\ell}}{\epsilon_{D\ell\nu}}\right)\left(\frac{1}{\mathcal{B}_{D\ell\nu}}\right)}. \tag{R.1}$$

The $\left(\frac{\epsilon_{\pi\tau\ell}}{\epsilon_{D\ell\nu}}\right)$ term does not cancel because of the kaon from the $D^0 \to K\pi$ decay. We account for this systematic uncertainty comparing kaon PID efficiency with pion PID efficiency, $\frac{\epsilon_{\rm KPID}}{\epsilon_{\pi{\rm PID}}}$, using the ratios of PID efficiencies also comparing on-resonance data and MC,

$$R_{\rm syst} = \frac{\epsilon^{\rm (onres)}_{\rm KPID}/\epsilon^{\rm (onres)}_{\pi{\rm PID}}}{\epsilon^{\rm (MC)}_{\rm KPID}/\epsilon^{\rm (MC)}_{\pi{\rm PID}}}. \tag{R.2}$$

Tables R.2 and R.3 give a detailed summary of the ΔE fit yields broken-down when kaon and pion PID are applied, kaon PID applied only, and when no hadron PID is applied to the kaon and pion candidates in the $D^0 \to K^-\pi^+$ reconstruction. Figures R.1, R.2, and R.3 show the ΔE fit yields when kaon and pion PID are applied, kaon PID applied only, and no hadron PID applied, respectively in the $D^{(*)0}\mu\nu$ reconstruction for separate D^0, $D^{(*)0}$, and D^{**} components (top). Projected fits with yields and shape parameters varied (bottom row) for Monte Carlo distributions (bottom left) and on-resonance distributions (bottom right) are also shown. Figures R.4, R.5, and R.6 show the same as above, except for $D^{(*)0}e\nu$ reconstructions.

The fraction of properly reconstructed D and D^* events, for the respective control modes, requiring Monte Carlo truth matched center-of-mass momentum differences, $\Delta p^* < 0.1$ GeV, is used to correct the MC and on-resonance fit yields. See Table R.1 for a summary of the correction factors. Note that $f_{\rm good}$ is consistent in the D reconstruction and in the D^* reconstruction regardless of the applied hadron PID criteria.

Mode	$N_{\rm rec}$	$N'_{\rm rec}$	$f_{\rm good}$
KaonPionPID applied			
$D\mu\nu$	1418	1292	$(91.1 \pm 0.8)\%$
$D^*\mu\nu$	4236	3660	$(86.4 \pm 0.5)\%$
KaonPID applied			
$D\mu\nu$	1423	1297	$(91.1 \pm 0.8)\%$
$D^*\mu\nu$	4247	3669	$(86.4 \pm 0.5)\%$
NoKpiPID applied			
$D\mu\nu$	1504	1370	$(91.1 \pm 0.8)\%$
$D^*\mu\nu$	4514	3886	$(86.1 \pm 0.5)\%$
KaonPionPID applied			
$De\nu$	1423	1283	$(90.2 \pm 0.8)\%$
$D^*e\nu$	4264	3607	$(84.6 \pm 0.6)\%$
KaonPID applied			
$De\nu$	1430	1289	$(90.1 \pm 0.8)\%$
$D^*e\nu$	4280	3622	$(84.6 \pm 0.6)\%$
NoKpiPID applied			
$De\nu$	1563	1412	$(90.3 \pm 0.7)\%$
$D^*e\nu$	4591	3879	$(84.5 \pm 0.5)\%$

Table R.1: Summary of fraction of properly reconstructed control sample events with various hadron PID criteria applied from $D^{(*)}\ell\nu$ reconstructions using generic $B^{\pm}$ MC samples. $N_{\rm rec}$ is the number of $D^{(*)}\ell\nu$ candidates reconstructed requiring control sample event selection. $N'_{\rm rec}$ is the same as $N_{\rm rec}$ with the additional $\Delta p^* < 0.1$ GeV requirement (see section on control samples). $f_{\rm good}$ is defined as $N'_{\rm rec}/N_{\rm rec}$.

Components	Fit yield (shape varied)	Fraction with $\Delta p^* < 0.1$ GeV	Corrected yield (shape varied)
	KaonPionPID applied		
$D\mu\nu$ (onres)	477 ± 38	0.911	435 ± 35
$D^*\mu\nu$ (onres)	1202 ± 49	0.864	1039 ± 42
other$_\mu$ (onres)	624 ± 31	-na-	-na-
$D\mu\nu$ (MC)	457 ± 56	0.911	416 ± 51
$D^*\mu\nu$ (MC)	1435 ± 64	0.864	1240 ± 55
other$_\mu$ (MC)	769 ± 35	-na-	-na-
	KaonPID applied		
$D\mu\nu$ (onres)	482 ± 37	0.911	439 ± 34
$D^*\mu\nu$ (onres)	1205 ± 49	0.864	1041 ± 42
other$_\mu$ (onres)	633 ± 32	-na-	-na-
$D\mu\nu$ (MC)	463 ± 53	0.911	422 ± 48
$D^*\mu\nu$ (MC)	1437 ± 61	0.864	1241 ± 53
other$_\mu$ (MC)	772 ± 35	-na-	-na-
	NoKpiPID applied		
$D\mu\nu$ (onres)	501 ± 40	0.911	456 ± 36
$D^*\mu\nu$ (onres)	1323 ± 51	0.861	1139 ± 44
other$_\mu$ (onres)	1055 ± 39	-na-	-na-
$D\mu\nu$ (MC)	467 ± 73	0.911	425 ± 66
$D^*\mu\nu$ (MC)	1553 ± 82	0.861	1337 ± 71
other$_\mu$ (MC)	1358 ± 44	-na-	-na-

Table R.2: Summary of ΔE fit results of on-resonance & MC $D^{(*)}\mu\nu$ samples with various hadron PID criteria applied. The projected fit yields onto on-resonance data were obtained from the fit yields in Appendix R. In the second column (shape varied), we varied yields and shape parameters (see text). We use the fit yields in the second column (shape varied) corrected for the fraction of Monte Carlo truth $B_{\rm tag}$ reconstructed for our corrected yields (last column). The corrected yields are added in Table 4.5

Components	Fit yield (shape varied)	Fraction with $\Delta p^* < 0.1$ GeV	Corrected yield (shape varied)
	KaonPionPID applied		
$De\nu$ (onres)	474 ± 46	0.902	427 ± 41
$D^*e\nu$ (onres)	1348 ± 58	0.846	1140 ± 49
other$_e$ (onres)	353 ± 28	-na-	-na-
$De\nu$ (MC)	467 ± 43	0.902	421 ± 39
$D^*e\nu$ (MC)	1476 ± 56	0.846	1249 ± 47
other$_e$ (MC)	471 ± 32	-na-	-na-
	KaonPID applied		
$De\nu$ (onres)	475 ± 46	0.901	428 ± 41
$D^*e\nu$ (onres)	1358 ± 58	0.846	1149 ± 49
other$_e$ (onres)	354 ± 29	-na-	-na-
$De\nu$ (MC)	470 ± 43	0.901	424 ± 39
$D^*e\nu$ (MC)	1483 ± 57	0.846	1255 ± 48
other$_e$ (MC)	472 ± 32	-na-	-na-
	NoKpiPID applied		
$De\nu$ (onres)	524 ± 50	0.903	473 ± 45
$D^*e\nu$ (onres)	1464 ± 62	0.845	1237 ± 52
other$_e$ (onres)	451 ± 30	-na-	-na-
$De\nu$ (MC)	475 ± 47	0.903	429 ± 42
$D^*e\nu$ (MC)	1641 ± 61	0.845	1387 ± 52
other$_e$ (MC)	622 ± 35	-na-	-na-

Table R.3: Summary of ΔE fit results of on-resonance & MC $D^{(*)}e\nu$ samples with various hadron PID criteria applied. The projected fit yields onto on-resonance data were obtained from the fit yields in Appendix R. In the second column (shape varied), we varied yields and shape parameters (see text). We use the fit yields in the second column (shape varied) corrected for the fraction of Monte Carlo truth $B_{\rm tag}$ reconstructed for our corrected yields (last column). The corrected yields are added in Table 4.5

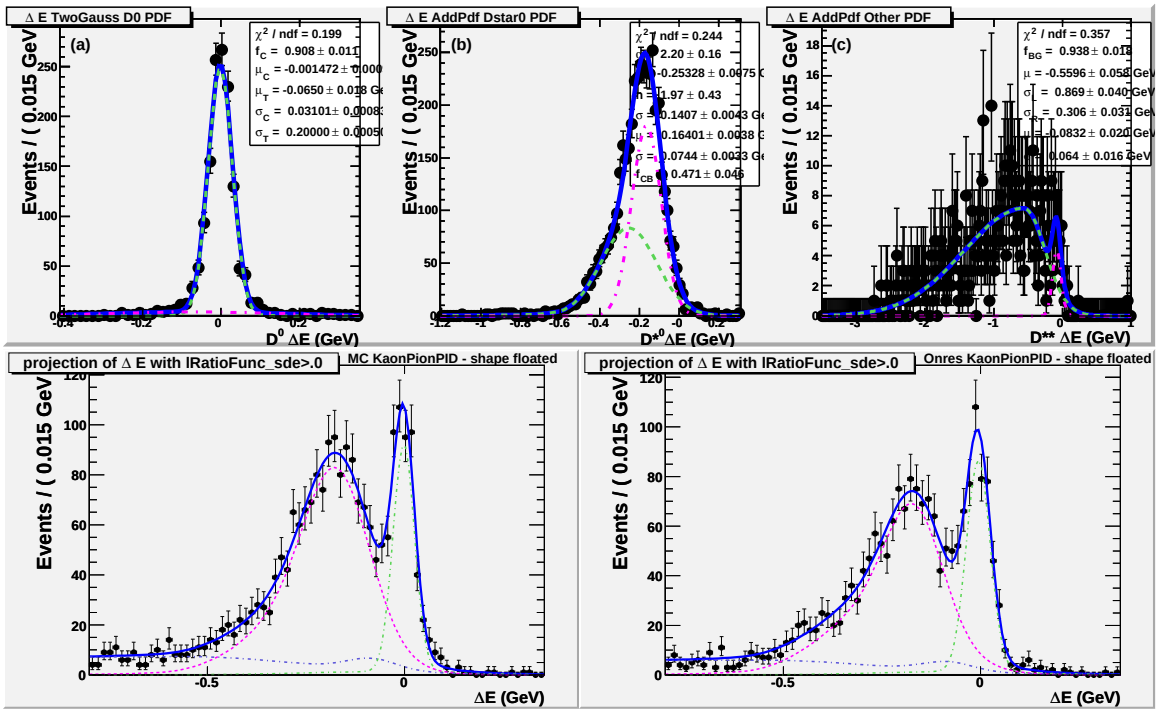

Figure R.1: Unbinned maximum likelihood fits with kaon and pion PID applied to obtain separate D^0 (left), $D^{(*)0}$ (middle), and D^{**} (right) fit components using our $D^{(*)}\mu\nu$ control modes from generic $B^{\pm}$ MC samples. Yield and shape parameters are allowed to vary when projected onto MC (left) & on-resonance (right) ΔE distributions. Yields found in Table R.2.

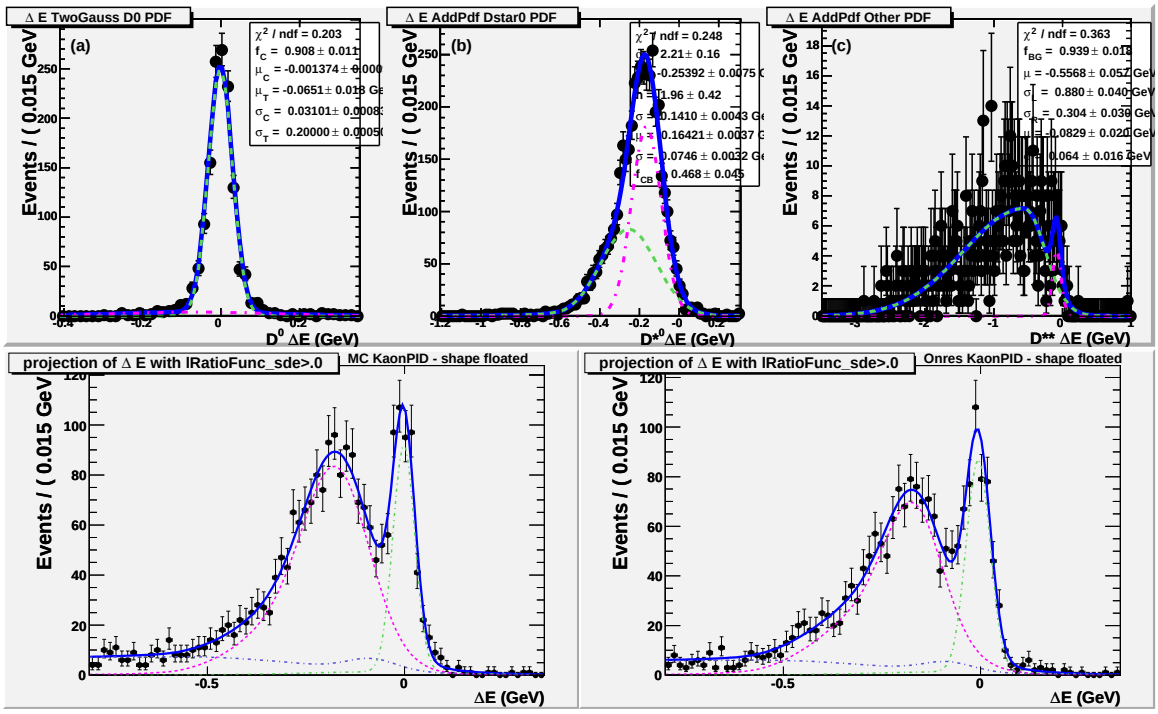

Figure R.2: Unbinned maximum likelihood fits with kaon PID applied only to obtain separate D^0 (left), $D^{(*)0}$ (middle), and D^{**} (right) fit components using our $D^{(*)}\mu\nu$ control modes from generic $B^{\pm}$ MC samples. Yield and shape parameters are allowed to vary when projected onto MC (left) & on-resonance (right) ΔE distributions. Yields found in Table R.2.

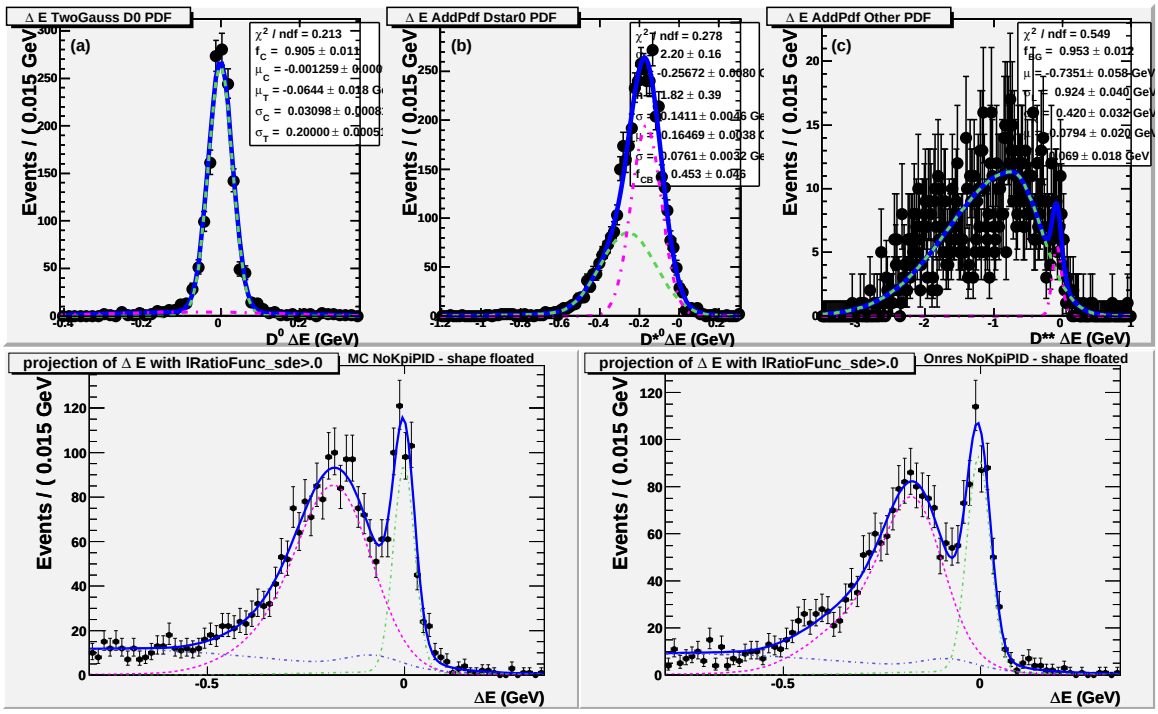

Figure R.3: Unbinned maximum likelihood fits with no hadron PID applied to obtain separate D^0 (left), $D^{(*)0}$ (middle), and D^{**} (right) fit components using our $D^{(*)}\mu\nu$ control modes from generic $B^{\pm}$ MC samples. Yield and shape parameters are allowed to vary when projected onto MC (left) & on-resonance (right) ΔE distributions. Yields found in Table R.2.

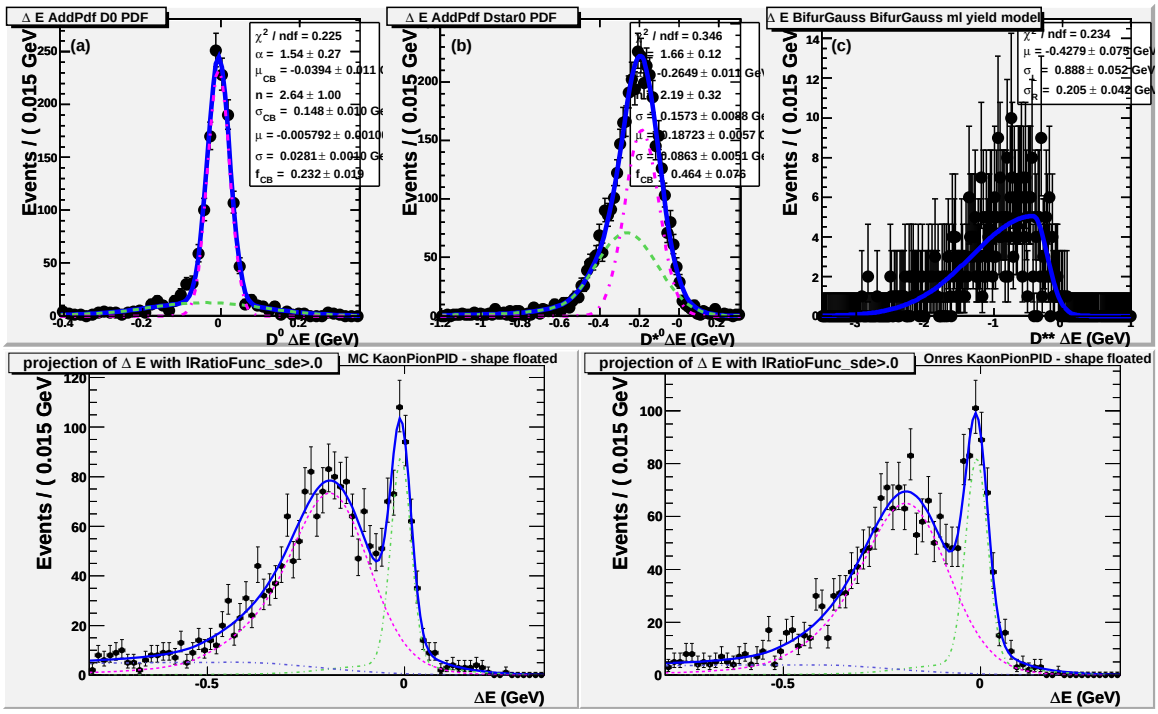

Figure R.4: Unbinned maximum likelihood fits with kaon and pion PID applied to obtain separate D^0 (left), $D^{(*)0}$ (middle), and D^{**} (right) fit components using our $D^{(*)}e\nu$ control modes from generic $B^{\pm}$ MC samples. Yield and shape parameters are allowed to vary when projected onto MC (left) & on-resonance (right) ΔE distributions. Yields found in Table R.3.

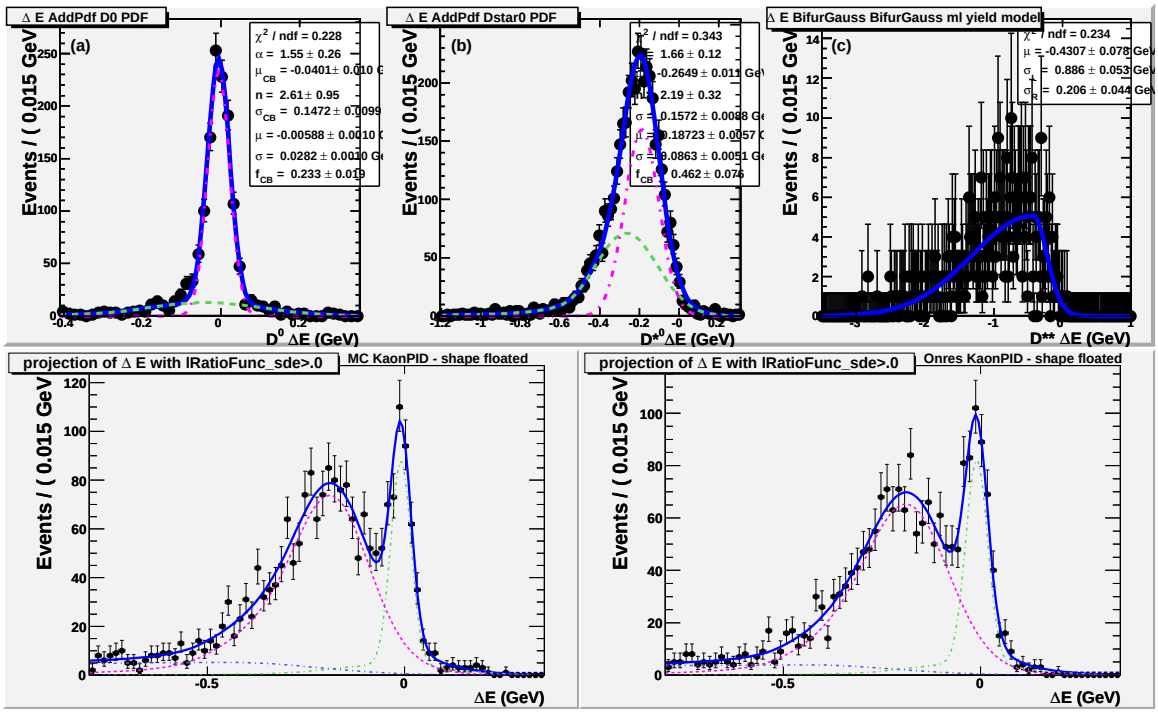

Figure R.5: Unbinned maximum likelihood fits with kaon PID applied only to obtain separate D^0 (left), $D^{(*)0}$ (middle), and D^{**} (right) fit components using our $D^{(*)}e\nu$ control modes from generic $B^{\pm}$ MC samples. Yield and shape parameters are allowed to vary when projected onto MC (left) & on-resonance (right) ΔE distributions. Yields found in Table R.3.

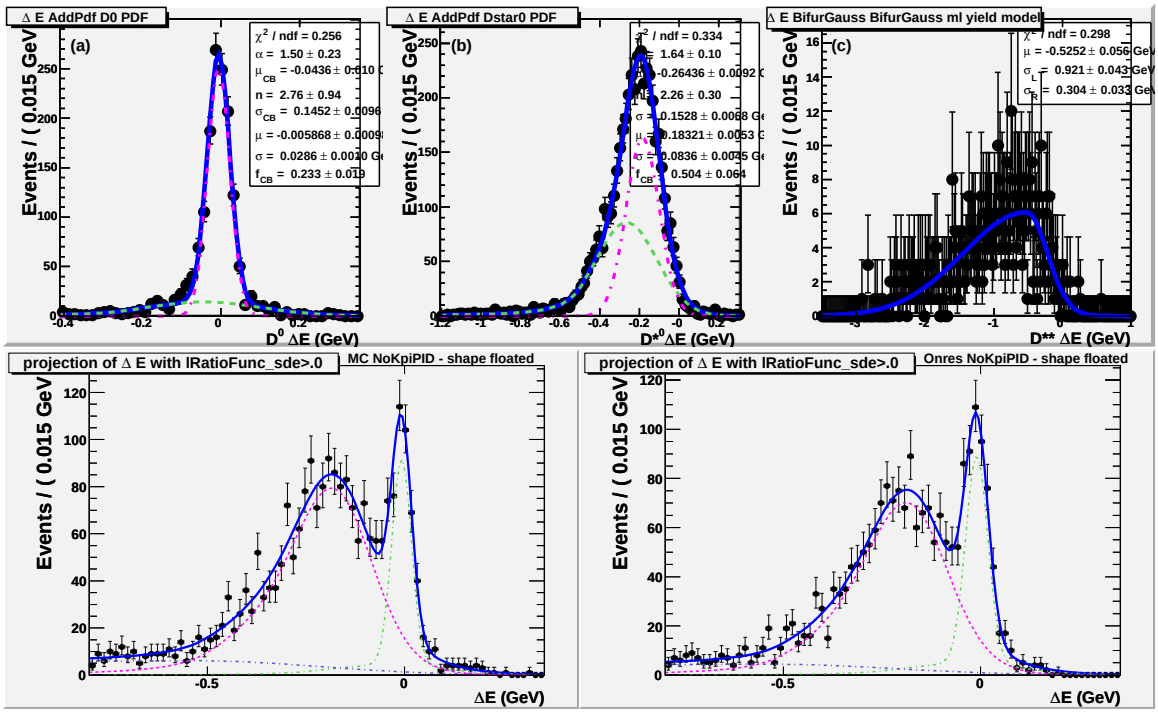

Figure R.6: Unbinned maximum likelihood fits with no hadron PID applied to obtain separate D^0 (left), $D^{(*)0}$ (middle), and D^{**} (right) fit components using our $D^{(*)}e\nu$ control modes from generic $B^{\pm}$ MC samples. Yield and shape parameters are allowed to vary when projected onto MC (left) & on-resonance (right) ΔE distributions. Yields found in Table R.3.